Solution-adaptive moving mesh solver for geophysical flows

Christian Kühnlein

München 2011

Solution-adaptive moving mesh solver for geophysical flows

Christian Kühnlein

Dissertation
an der Fakultät für Physik
der Ludwig–Maximilians–Universität
München

vorgelegt von
Christian Kühnlein
aus Nürnberg

München, Februar 2011

Erstgutachter: Prof. Dr. Ulrich Schumann
Zweitgutachter: Prof. Dr. George Craig
Tag der mündlichen Prüfung: 18.04.2011

Für meine Familie.

Abstract

Dynamical processes occurring in geophysical flows are characterised by the nonlinear interaction of various scales of motion. The accurate numerical representation of such flows is limited by the available number of mesh points covering the domain of interest. Numerical simulations applying uniformly distributed grid cells waste mesh points in regions of large motion scales whereas coexisting small-scale processes cannot be adequately resolved.
The current thesis offers the design, implementation, and application of an adaptive moving mesh algorithm for dynamically variable spatial resolution to the numerical simulation of nonlinear geophysical flows. For this purpose, the established geophysical flow solver EULAG was modified and extended. The non-hydrostatic, anelastic equations of EULAG are rigorously implemented in time-dependent generalised coordinates. This setting enables moving mesh adaptation by solving the equations in a straightforward approach developed in this thesis.

The methodological development of the new adaptive solver is divided into three tasks: (i) The flux-form Eulerian advection scheme MPDATA employed in EULAG was extended. For transport equations in conservative form, a mass conservation law enters naturally and implies a unique compatibility condition for the solution algorithm. Here, extensions of the Eulerian MPDATA integration were developed, implemented and tested to provide full compatibility with the generalised anelastic mass conservation law (GMCL) under adaptive moving meshes.
(ii) A machinery performing the numerical generation of an adaptive moving curvilinear mesh was designed and implemented in EULAG. For this purpose, an auxiliary set of parabolic moving mesh partial differential equations (MMPDEs) was employed to redistribute the existing mesh cells temporally. The solutions of the MMPDEs provide the mesh coordinates and the adaptation properties of the generated moving mesh (e.g. local mesh density) are controlled by a monitor function that varies horizontally and temporally. The form of the monitor function depends *inter alia* on the flow state.
(iii) An efficient coding of the mesh adaptation machinery was successfully incorporated into the computational framework of EULAG. For this task, the approximation of the advective contravariant mass flux in MPDATA was developed and implemented in EULAG so to minimise errors of the incompatibility with the GMCL.

The developed adaptive moving mesh solver was thoroughly investigated by simulating a number of relevant atmospheric problems. The advection of a passive tracer in a two-dimensional shear flow demonstrated the capability of the solver to automatically adapt the local resolution to the evolving small-scale filamentary structures. For this flow, the expected advantage of the mesh adaptation was achieved: the computing time (and the error) was reduced significantly by a factor of 26 (by 20%) compared to high-resolution uniform mesh computations. Another advantage of adaptive simulations is the appearance of new physical phenomena. Here, instabilities occurring at the interface of an idealised rising thermal with the ambient air could be simulated in much greater detail. The representation of the associated mixing processes is of direct relevance for simulating cumulus convection in realis-

tic atmospheric flows. There, the process of fine-scale mixing, i.e. entrainment and detrainment, between the cloudy and the ambient air could be better resolved by mesh adaptation.
The first application of the developed adaptive mesh solver in the three-dimensional parallelised modelling framework of EULAG to an idealised baroclinic wave life cycle demonstrated the accurate representation of the synoptic-scale flow (improved statistics) and the ability to resolve coexisting mesoscale processes. Focussing the adaptation to the developing frontal zone indicated the excitation of internal gravity waves which were nearly absent in simulations applying a uniform mesh with the same number of mesh points. As before, significant savings in computing time (at least a factor of 2) compared to equivalent results of a high-resolution uniform mesh computation were achieved for the three-dimensional simulations.

A cumbersome side-effect of the successful and efficient numerical simulations was the extremely time-consuming tuning of the adaptation parameters, especially of the monitor function. So far, only a very limited number of monitor functions were tested. Systematic research will yield improved specifications of the monitor function for distinct atmospheric flows. In summary, the results obtained in this thesis show the capability and potential of adaptive moving mesh methods to simulate multiscale atmospheric flows with higher numerical accuracy and a broader coverage of motion scales. However, the adaptive moving mesh method adds substantial user complexity to the modelling system EULAG.

Contents

Chapter 1

Introduction

The enormous range of scales of physical processes in geophysical flows together with their nonlinear interactions poses a formidable challenge for numerical modelling. Thanks to the steadily increasing computing power and advances in numerical modelling systems, realistic simulations of transient three-dimensional atmospheric and oceanic flows have become practical nowadays[1]. However, the current resources still do not allow to resolve many important multiscale phenomena accurately. For many problems of scientific and public interest, there is a demand to increase the resolution of current atmospheric and oceanic flow solvers by orders of magnitude.
For instance, consider tropical cyclone prediction: Here, the scales of the processes involved range from the large-scale tropical environment with $\sim \mathcal{O}(10^6 \text{-} 10^7)$ m, the scale the tropical cyclone itself $\sim \mathcal{O}(10^5 \text{-} 10^6)$ m, the scale of embedded phenomena like the eyewall and rainbands $\sim \mathcal{O}(10^3\text{-}10^4)$ m, while the boundary layer turbulence responsible for heat and moisture fluxes from the ocean is $\sim \mathcal{O}(10\text{-}10^2)$ m and smaller. These flow scales span (at least) seven orders of magnitude. Clearly, this resolution is far beyond that what can be achieved with the computing systems available today. The range of scales of the processes in tropical cyclone flows is by no means an exception. A similar complexity is encountered in many atmospheric modelling applications. Figure 1.1 shows a snapshot taken from a combined observational and numerical study of a CAT[2] event that occurred north to the Hawaiian islands over the Pacific ocean (Kühnlein, 2006). For this case, the atmospheric

[1]For instance, this becomes evident in the success story of daily numerical weather prediction, e.g. Kalnay et al. (1998).
[2]The term CAT especially refers to turbulence occurring several kilometers above the Earth's surface in an environment free of clouds and strong convective updrafts (Dutton and Panofsky, 1970). Among others, the prediction of the occurrence of CAT is important because of its hazard to airplanes, which is due to locally strong wind shears.

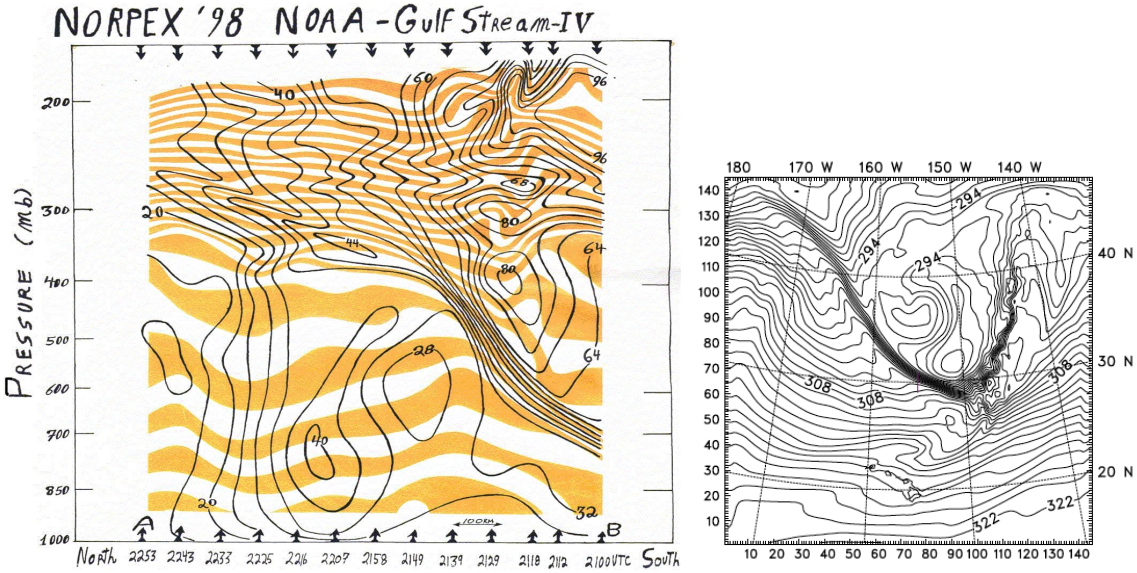

(a) (b)

Figure 1.1: (a) Vertical section as derived from dropsondes deployed along the flight track of the NOAA Gulfstream-IV (G-IV) research aircraft through a frontal system in the region of a mid-latitude cyclone during the North Pacific Experiment (NORPEX) 1998. Shown is potential temperature θ (K, orange-white shaded, $\Delta\theta = 2$ K) and horizontal velocity v_h (ms^{-1}, black contour lines, $\Delta v_h = 4$ ms^{-1}). (b) Horizontal section through the mid-latitude cyclone at $z = 4$ km of potential temperature θ (K, black contour lines, $\Delta\theta = 1$ K) as obtained from an attendant mesoscale numerical simulation. The short south-north-aligned violet line in about the centre of (b) over the front indicates the region along the vertical section shown in (a) where the G-IV research aircraft encountered moderate-to-severe CAT at the flight altitude of ≈ 12.5 km. The CAT encounter occurred in the region of the dropsonde deployed at 2118 UTC. See Kühnlein (2006) for further discussion. Courtesy of (a): M. A. Shapiro, NOAA.

flow comprises the excitation of internal gravity waves[1] from an intensifying frontal zone at mid-tropospheric levels. These internal gravity waves propagated upwards into the lower stratosphere, where they played a decisive role in the generation of strong localised bursts of CAT. Again, the processes involved range over a continuous spectrum of scales from the large-scale, i.e. synoptic- to planetary-scale, flow environment $\sim \mathcal{O}(10^6 \text{-} 10^7)$ m, cross-frontal scale $\sim \mathcal{O}(10^5)$ m, mesoscale internal gravity waves $\sim \mathcal{O}(10^4 \text{-} 10^5)$ m, embedded moist convection $\sim \mathcal{O}(10^3)$ m, down to microscales of the CAT $\sim \mathcal{O}(10 \text{-} 10^2)$ m.

Because of the complexity of the problem, numerical modelling is the only method to produce a nearly complete spatio-temporal prediction of nonlinear multiscale geophysical flows. In this thesis, an attempt to extend the capabilities of numerical models will be undertaken that offers the means to better cope with the large scale

[1]Internal gravity waves (sometimes called buoyancy waves) refer to internal oscillations in a stably stratified fluid where the force acting in the vertical direction is buoyancy due to Earth's gravity.

differences of the processes in geophysical flows.

Currently, the most common approach for the (horizontal) spatial discretisation in numerical models of the atmosphere is to employ uniform meshes. They are based on either a grid point/cell or spectral representation in the simulation domain. The restriction to distribute the grid points uniformly can be resolved by using an adaptive mesh method that applies finer or coarser mesh sizes in distinctive regions of interest. This means adaptive mesh methods provide variable spatial resolution over the simulation domain within a single numerical solver. As a result, a locally improved mesh resolution can be applied in limited regions without the requirement to increase the mesh resolution throughout the entire simulation domain. In particular, if a nonlinear physical flow problem involves local small-scale processes, an adaptive mesh focussing on (or zooming into) these regions represents a powerful means for the numerical simulation. The technique can be employed to resolve in a consistent manner local small-scale processes and the larger-scale flow at the same time. Usually, only a fraction of the computational expense (i.e. CPU and memory requirements) of a comparable simulation using a globally fine mesh will be required.

Adaptive meshes may be either static or dynamic. In the static case, a variable spatial resolution is defined in advance of the simulation and is then kept constant over the entire course of the integration. Thereby, the mesh adaptation regions must be known a priori and the static adaptation is thus best suited for stationary or quasi-stationary features, e.g. to better resolve flow interaction with topography or the storm track regions in the mid-latitudes of the Earth's atmosphere. In addition, static mesh adaptation can also be used to achieve an improved resolution in certain predefined geographical regions of interest, e.g. in the context of regional modelling. In fact, static adaptive meshes are employed in geophysical flow modelling for some time (Anthes, 1970), and have already been proven immensely beneficial for a variety of applications, see e.g. Fox-Rabinovitz et al. (1997); Dörnbrack et al. (1998); Sullivan et al. (1998); Dörnbrack et al. (2002); Lane et al. (2003); Kühnlein (2006); Laprise (2008); Abiodun et al. (2008); Rotunno et al. (2009). Traditionally, either mesh nesting (Clark and Farley, 1984) or mesh stretching (Anthes, 1970; Staniforth and Mitchell, 1978) techniques have been used. Latest developments also consider unstructured mesh techniques on the sphere, see e.g. Szmelter and Smolarkiewicz (2010b).

Dynamic mesh adaptation is a time-dependent generalisation of the static mesh adaptation approach. With a dynamic mesh, the spatial resolution or the discrete mesh geometry is not only variable in space over the simulation domain but is also

allowed to vary in time during the integration. The approach provides additional flexibility for the mesh adaptation in that the resolution can be adjusted locally in response to the evolution of the flow or to changing forcings. For instance, a dynamically adaptive mesh method technically enables to continuously track moving and transient features of significance with a locally improved resolution. These features may be tropical cyclones, fronts in a mid-latitude synoptic-scale flow environment, or a density current in an Alpine valley, just to name a few. Because the evolution of the features to be adapted is not known in advance, the dynamic mesh adaptation must functionally depend, either directly or indirectly, on the prognostic solution fields of the numerical flow solver. Therefore, the term *solution-adaptive mesh* method is appropriate and is used throughout this text. As an aside, it is obvious that flow solvers with a solution-adaptive (or dynamic) mesh capability are also suitable to employ static mesh adaptation.

Solution-adaptive mesh methods are relatively new and unexplored in the area of geophysical flow modelling. The first application in the context of atmospheric flows was reported by Skamarock et al. (1989) about two decades ago. They investigated solution-adaptive multiple component grids for numerical weather prediction applications. They combined a finite-difference solver for the hydrostatic primitive equations with the adaptive mesh technique developed by Berger and Oliger (1984), where fine (overlapping) component grids were placed automatically according to Richardson-type estimates of the truncation error in the coarse grid solution. The adaptive solver was successfully applied to test problems of barotropic cyclone advection and the baroclinic instability of an unstable jet flow.
In spite of a high level of research activity in recent years, see e.g. Jablonowski (2004); Nikiforakis (2009) [1], as yet, solution-adaptive mesh methods have not found widespread application. The great majority of efforts nowadays is still concerned with basic research in the methods themselves rather than with the study of physical problems or operational prediction using solution-adaptive mesh methods. A noteworthy exception is the numerical weather prediction modelling system OMEGA (Operational Multiscale Environment Model with Grid Adaptivity) (Bacon et al., 2000). The model has been applied in an operational forecast mode to the dispersion modelling of chemical tracers and hurricane prediction (Gopalakrishnan et al., 2002).
Major open research issues in solution-adaptive mesh methods are the definition of mesh refinement criteria, i.e. dynamic criteria that reliably indicate in which re-

[1] See also the DFG priority program Metström "http://metstroem.mi.fu-berlin.de".

gions of the domain a finer or coarser mesh is required. The formulation of sub-grid scale closure models that are applicable on (dynamically) adaptive meshes is a major issue, too. Furthermore, it is unclear how different mesh adaptation strategies – changing the number of mesh points, moving mesh points, and changing the order of the numerical approximation – should best be combined for geophysical applications (Weller et al., 2010).

1.1 Adaptive moving mesh methods

Most of the solution-adaptive mesh solvers being developed in the area of geophysical flows are based on so-called h-refinement methods, where the basic strategy is to insert or remove mesh points in order to adapt the resolution locally, see e.g. Jablonowski (2004); Behrens (2006). Recent examples of adaptive geophysical flow solvers based on h-refinement adaptive strategies are given by Hubbard and Nikiforakis (2003); Jablonowski et al. (2006); Läuter et al. (2007); St-Cyr et al. (2008); Weller (2009). These works investigated a variety of adaptive mesh techniques for applications on the sphere using benchmark flows of pure scalar advection and shallow-water equations with a view towards next-generation global weather and climate models.

In contrast, r-refinement methods, which are also known as continuous dynamic grid adaptation (CDGA) methods (e.g. Dietachmayer and Droegemeier, 1992) or *moving mesh methods* (e.g. Budd et al., 2009), keep the total number of mesh points fixed during the simulation but relocate the available mesh points to vary the resolution over the domain. Hence, r-refinement methods aim to minimise the error of the computations through an optimal distribution of the available mesh points. The idea of r-refinement methods is different from h-refinement methods, where a maximum of the error in the computations may be achieved through insertion of sufficient additional mesh points.

The area of moving mesh methods is a large research field of applied mathematics. The particular designs and implementations of moving mesh methods can differ significantly[1]. A complete overview of the variety of the published techniques is beyond the scope of this thesis. For an up-to-date overview and a discussion of the most common approaches, the interested reader is referred to the review article

[1]As applies to the field of h-refinement methods.

by Budd et al. (2009). In addition, a textbook solely devoted to the topic has been issued just recently (Huang and Russell, 2011), acknowledging the growing role of moving mesh methods play in modern computational modelling. Despite the increasing interest in moving mesh methods in recent years (Weller et al., 2010), they are in a relatively early stage of their development compared to the more matured h-refinement methods (Budd et al., 2009; Huang and Russell, 2011). In the following, aspects of moving mesh methods with particular relevance to the present thesis are addressed.

Numerical flow solvers that adopt solution-adaptive moving mesh methods consists of two main components. One component is the machinery used to move the mesh, i.e. the mesh generation component. The other component is the physical model of the governing flow equations and their discretisation on the moving mesh. A common principle for the mesh generation in moving mesh methods is to use generalised coordinate mappings from a transformed space $\mathbf{S}_t$ where the computational problem is solved (ideally chosen as a fixed regular computational mesh), into the physical space $\mathbf{S}_p$ where the actual geophysical flow problem is posed; hence the coordinate mappings $\mathbf{S}_t \rightarrow \mathbf{S}_p$ describe the adaptive (irregular) mesh in $\mathbf{S}_p$. Typically, the positions[1] of the mesh nodes in $\mathbf{S}_p$ are determined by solving (in computational space $\mathbf{S}_t$) an appropriate system of auxiliary partial differential equations. The latter are often referred to as *moving mesh equations*. A so-called monitor function is incorporated in the moving mesh equations to guide the evolution of the adaptive mesh in the physical domain. Typically, the monitor function is designed to give some measure of the local error of the flow computations (defined for instance in terms of numerical truncation error or based upon heuristic criteria of the simulated flow). One approach for the integration of the governing geophysical flow equations on moving meshes adopted here is to formulate and solve them in time-dependent generalised coordinates. However, note that many other approaches exist, see e.g. (Budd et al., 2009; Huang and Russell, 2011).

An advantage of moving mesh methods is that they allow to maintain the basic structure of a rectangular computational mesh during the simulation. There is no need to deal with the insertion or deletion of mesh points, an issue that always complicates the implementation of h-refinement methods, e.g. due to the requirement of some form of nested data structure. The conserved rectangular data structure in moving mesh methods also provides efficient numerical calculations and low memory

[1]Another possibility is to determine the mesh velocity instead of the mesh positions; e.g. Cao et al. (2003).

requirements. In addition, moving mesh methods are perfectly suited for parallel computational architectures, because they add little or no communication overhead compared to uniform mesh solvers. Favourable parallelisation characteristics are essential in the area geophysical flow modelling, where the use of supercomputers with hundreds to thousands of parallel processors has become reality nowadays, e.g. Prusa et al. (2008); Taylor et al. (2008).
The characteristic of a conserved rectangular data structure makes moving mesh methods the preferred technique to become part of existing established geophysical flow modelling systems. The latter traditionally rely on fixed rectangular computational meshes. In particular, this aspect is followed in the present thesis where a adaptive moving mesh scheme is introduced in the multiscale geophysical flow solver EULAG (Prusa et al., 2008).
Another aspect of moving mesh methods worth mentioning is their quasi-Lagrangian nature. In contrast to h-refinement methods, the mesh points can follow the flow, i.e. moving features like vortices or fronts, without the need for costly topological changes in the computational mesh geometry. In addition, if the discretisation of the governing geophysical flow equations is performed in time-dependent generalised coordinates, no interpolations of the prognostic variables are required under the mesh movement. If the mesh moves downwind, significantly larger time steps of the explicit numerical flow solver may be possible due to a less restrictive CFL stability condition. In contrast, a mesh movement against the wind requires to reduce the time step accordingly for the stability of the integration.
A shortcoming of moving mesh methods is that they are generally less flexible than h-refinement methods to adapt effectively to arbitrary flow features; see e.g. (Fiedler and Trapp, 1993; Piggott et al., 2005) for discusssions. For an illustrating example, imagine a frontal zone or a squall line stretching across the entire simulation domain between the boundaries. Then, a moving mesh method adapting to this front is able to improve the resolution across the elongated feature, though it cannot improve effectively the resolution along the feature. An improvement of the resolution along the adaptation feature during the simulation could be achieved by the dynamic insertion of additional mesh points, as possible in a h-refinement method.
As an aside, note that combinations of both methods in so-called rh-refinement methods do also exist, e.g. Szmelter et al. (1992); Lang et al. (2003); Piggott et al. (2005).

Solution-adaptive moving mesh methods have been used in number of physical disciplines, see Budd et al. (2009) for an overview. In atmospheric flow modelling, solution-adaptive moving mesh methods were first applied by Dietachmayer and

Droegemeier (1992). They employed the popular mesh generator of Brackbill and Saltzman (1982) to simulate a number of idealised test problems of meteorological significance. The test problems in Dietachmayer and Droegemeier (1992) included a kinematic frontogenesis flow governed by a single scalar advection equation, and a two-dimensional dry rising warm thermal in a neutrally-stratified quiescent atmosphere governed by the incompressible Boussinesq equations in vorticity-streamfunction formulation. The mesh adaptation was guided by means of simple criteria based on the first- and second-order derivatives of either the transported scalar (kinematic frontogenesis flow) or the potential temperature (rising thermal flow). Although their moving mesh solver provided very accurate results, they added that the solver was not competitive in terms of efficiency (i.e. execution time) against uniform mesh computations for the modelling problems considered.

The adopted mesh generator of Brackbill and Saltzman (1982) in Dietachmayer and Droegemeier (1992) formulated the mesh generation equations in a variational form to produce satisfactory mesh concentration in desired regions while maintaining relatively good orthogonality and smoothness. In a second publication (Dietachmayer, 1992), a (simplified) more efficient adaptive mesh generator was constructed that was built solely on the concept of equidistributing an error-indicating weighting function. The new mesh generator dispensed with the explicit requirements of smoothness and (near-)orthogonality of the mesh as in the approach of Brackbill and Saltzman (1982). Dietachmayer (1992) demonstrated the efficiency of the resulting solution-adaptive moving mesh solver for the modelling of interacting multiple vortices in a barotropic shallow water model in spherical coordinates. In particular, the showed that their integration using a solution-adaptive moving mesh is three times faster than a respective uniform mesh calculation in achieving a solution of a specified accuracy. Dietachmayer (1992) also concluded from their results that near-orthogonality of the mesh lines is not necessary for the successful implementation of the solution-adaptive moving mesh method. Dietachmayer added that solution accuracy in their solver is seriously degraded only if highly skewed mesh cells occur in conjunction with with rapid variation of the model fields, and this possibility may be avoided in many cases by smoothing the weight function that guides the mesh adaptation.

Shortly thereafter, two-dimensional and fully three-dimensional solution-adaptive moving mesh simulations of the dry rising thermal problem using the compressible flow equations were presented in Fiedler and Trapp (1993). They implemented a mesh generator similar to the one developed in Dietachmayer (1992). To achieve a higher efficiency, Fiedler and Trapp applied the mesh generator on a coarser mesh

than the mesh where the actual compressible flow equations were solved. The mesh refinement criterion was specified proportional to the magnitude of the buoyancy, in order obtain a higher resolution in the region of the rising thermal. They found that the integration using the solution-adaptive moving mesh is three times faster than a respective uniform mesh calculation, whereupon nearly equivalent results were obtained.
A more recent development is the two-dimensional solution-adaptive moving mesh scheme for scalar advection by Iselin et al. (2002). There development combines the mesh generator of Brackbill and Saltzman (1982) with the multidimensional positive definite advection transport algorithm (MPDATA). They applied the flux-form solver MPDATA to an advective transport equation (in time-dependent generalised coordinates) in a non-conservative form. Detailed numerical tests were performed to study the solution properties of MPDATA with uniform and solution-adaptive moving meshes using the problem of the advection of a cone-shaped passive tracer in a prescribed (solid-body) rotating velocity field. The mesh refinement was guided by a sum of first and second derivatives of the transported tracer field. For the problem considered, they found that the mesh adaptation scheme was far more efficient than the scheme using uniform meshes with similar accuracy. In a companion publication (Iselin et al., 2005), the scheme developed in Iselin et al. (2002) was then applied to regional-scale tracer advection over the United States, using a wind field as obtained from NCEP-NCAR reanalysis data. Their conclusion was that with the solution-adaptive moving mesh, results with about the same accuracy as a uniform mesh may be obtained using only a quarter of the mesh points of the uniform mesh.

It is mentioned at this point that the present thesis is concerned with the topic of using MPDATA under moving meshes for the integration of an advective transport equation (cast in time-dependent generalised coordinates) in conservation form. A general issue that appears when solving a scalar advective transport equation in conservation form is that the compatibility (or consistency) of the applied flux-form advection numerical solver (here MPDATA) with the associated mass conservation law must be ensured, see e.g. Lin and Rood (1996). For moving meshes, the mass conservation law takes on a compressible (i.e. time-dependent) form although the physical flow under consideration is assumed to be incompressible or anelastic (i.e. the mass conservation law in a symbolic (physical) representation has a time-independent form) (Prusa et al., 1996, 2001). This difference between time-dependent and time-independent generalised coordinates complicates the integration of advective scalar conservation laws in the first case, as a residual term due to the time-dependency of the mass conservation law may exists that is not accounted for

in the standard algorithm for static coordinates. The subject is known in the area of computational fluid dynamics under the term geometric conservation law (GCL) (Thomas and Lombard, 1979).

The previous works of Dietachmayer and Droegemeier (1992); Dietachmayer (1992); Fiedler and Trapp (1993); Iselin et al. (2002); Iselin et al. (2005) have suggested that solution-adaptive moving mesh methods are a useful and promising technique for the simulation of atmospheric flows. The complexity of the specific flow problems treated in these works is, however, relatively low compared to typical atmospheric flow modelling applications. Atmospheric flows contain a rich spectrum of processes including Rossby and internal gravity waves, various hydrodynamic instabilities (e.g. shear, symmetric, baroclinic, etc. instabilities), clouds, and diabatic processes, among others. It is currently not yet clear from the earlier studies of Dietachmayer and Droegemeier (1992); Dietachmayer (1992); Fiedler and Trapp (1993); Iselin et al. (2002); Iselin et al. (2005) whether solution-adaptive moving mesh methods can meet the demand of simulating correctly such processes. In addition, it has yet to be shown whether the use of adaptive moving mesh methods is justified for these flows in terms of the resulting efficacy gain in comparison to established modelling approaches.

1.2 Modelling framework and thesis approach

The Eulerian and semi-Lagrangian flow solver EULAG, see (Prusa et al., 2008) for a review, provides a proven multiscale modelling framework that accurately and efficiently simulates (geophysical) flows across a wide range of scales and for different scenarios. Among others, successful applications of EULAG have been documented for direct numerical simulation (DNS), large-eddy simulation (LES) and implicit large-eddy simulation (ILES) of turbulence, e.g. Margolin et al. (1999); Smolarkiewicz and Prusa (2002); Wedi and Smolarkiewicz (2006), cloud dynamics including microphysical processes, e.g. Grabowski and Smolarkiewicz (2002); Craig and Dörnbrack (2008), gravity wave dynamics, e.g. Smolarkiewicz and Margolin (1997); Doyle et al. (2010), sub-synoptic and synoptic scale weather phenomena, and global atmospheric flows, e.g. Smolarkiewicz et al. (2001). Furthermore, EULAG has proven its capability in simulating urban (Smolarkiewicz et al., 2007) and canopy (Dörnbrack et al., 2010) flows, flows past complex/moving boundaries (Ortiz and

Smolarkiewicz, 2006), and oceanic flows (Warn-Varnas et al., 2007)[1].

EULAG is based on semi-implicit non-oscillatory forward-in-time (NFT) numerics applied to solve the non-hydrostatic anelastic equations. Optionally, the advective transport is solved in either a flux-form Eulerian or an advective-form semi-Lagrangian representation – hence, the name EULAG. Previous efforts by Clark (1977); Smolarkiewicz and Clark (1986); Smolarkiewicz and Margolin (1993); Prusa et al. (1996); Smolarkiewicz and Margolin (1997); Smolarkiewicz and Prusa (2002); Prusa and Smolarkiewicz (2003); Wedi and Smolarkiewicz (2004); Smolarkiewicz and Prusa (2005) (see Prusa et al. (2008) for a more comprehensive list of references) were concerned with the design of the analytical and numerical framework of the model.

In particular, the recent work by Prusa and Smolarkiewicz (2003) established a generic framework for the implementation of a dynamic mesh adaptation capability via deforming coordinates. The foundation of the dynamic mesh adaptation capability is a time-dependent generalised coordinate transformation, implemented rigourously throughout the governing anelastic equations. One aspect of the modelling framework is the time-dependent vertical coordinate transformation that can be used to simulate – in the spirit of the classical terrain-following coordinate of Gal-Chen and Somerville (1975) – deforming lower (Prusa et al., 1996) and also upper (Wedi and Smolarkiewicz, 2004) domain boundaries. Another aspect of the modelling framework emphasised in Prusa and Smolarkiewicz (2003) is the use of time-dependent horizontal coordinate transformations for moving mesh adaptation. Prusa and Smolarkiewicz (2003) showed the potential of this aspect to improve the model representation of geophysical flows. They implemented a moving "nested" mesh by means of the time-dependent horizontal coordinate transformation to track a travelling stratospheric internal gravity wave packet with a uniform high resolution. The wave response of the internal gravity wave packet in the rotating stratified fluid was forced by a prescribed oscillating deflection of the lower domain boundary using the time-dependent vertical coordinate. The boundary deflection is thought to represent an idealised deformation of the tropopause. The moving "nested" high-resolution mesh tracking the wave packet was implemented via the numerical advection of a dense-mesh region with the prescribed velocity of the oscillating lower boundary deflection. The results of the "nested" mesh simulations showed excellent comparability with reference results obtained from uniform mesh simulations,

[1]Note, derivatives of EULAG have also been applied to simulations of visco-elastic waves in the human brain (Cotter et al., 2002), and solar convection (Elliott and Smolarkiewicz, 2002). Furthermore, current developments include extensions to MHD (magneto-hydrodynamics).

while using only a fraction of the computational expense. Another application in Prusa and Smolarkiewicz (2003) considered idealised global climate simulations of the benchmark test of Held and Suarez (1994). Prescribed (steady and unsteady) analytical stretching functions were employed to increase the meridional resolution either unimodal in the tropics or bimodal in the regions of the mid-latitude zonal jets. Although there was no consistent improvement in the climate statistics such as time-zonal averages, the adaptive mesh simulations outperformed uniform mesh simulations in terms of the flow symmetry about the equator and global statistics based upon the variation of the flow, e.g. the maximum value of the variation of potential temperature about its time-zonal average.

Despite the success, the applications in Prusa and Smolarkiewicz (2003) only exploited a relatively small capacity of the implemented time-dependent horizontal coordinate transformations in EULAG. Two main assumptions were made so far. First, only well-defined unimodal (i.e. single) or bimodal (i.e. double) targeted regions were considered for the moving mesh adaptation. Second, the moving mesh adaptation was prescribed in advance of the simulation. In particular, there was no dynamic interaction between the prognostic solution fields of the anelastic solver and the machinery that generates the adaptive moving mesh.

The promising results of Prusa and Smolarkiewicz (2003) represent the starting point for the present thesis. Here, the time-dependent generalised coordinate framework of EULAG as presented in Prusa and Smolarkiewicz (2003) is extended with a solution-adaptive moving mesh capability. The resulting scheme dispenses with the assumptions made so far. It enables to zoom with the mesh into multiple physical flow features at the same time. In addition, the moving mesh can dynamically interact with the simulated flow in EULAG. One main ingredient of the scheme is a set of *moving mesh equations* (see the previous Section 1.1) for the numerical generation of a dynamic curvilinear mesh. A time-space dependent monitor function in the moving mesh equations guides the mesh. With the approach, the monitor function can be specified proportional to some error-indicating quantity derived from prognostic solution fields in EULAG, e.g. velocity, temperature, water vapour mixing ratio, or any other quantity available in the model. If an appropriate error-indicating quantity can be determined for the flow considered, then the solution-adaptive moving mesh scheme can continuously self-adapt the mesh to improve the representation of the flow according to the error quantity's distribution. A simple heuristic example for such an error-indicating quantity may be to specify it proportional to the gradient of temperature in order to detect (temperature) fronts.

1.3 Overview of the thesis

The objective of the present thesis is to design, implement and assess a solution-adaptive moving mesh solver for the modelling of atmospheric (geophysical) flows. The solver, effectively incorporated into the computational framework of EULAG, is expected to enable a continuous spatiotemporal relocation of the mesh nodes during the integration according to predefined dynamic mesh refinement criteria that can depend on the prognostic solution fields.
Using the developed solver, the present thesis examines the question whether solution-adaptive moving mesh methods can be a viable alternative to uniform mesh atmospheric flow modelling approaches. In particular, the thesis investigates whether solution-adaptive moving mesh methods are able to significantly improve the efficacy of atmospheric flow simulations compared to uniform mesh computations.

Chapter 2 provides a review of the EULAG modelling framework. The emphasis is on the formulation of the underlying sound-proof anelastic thermo-fluid equations in the time-dependent generalised coordinates and the description of the numerical solution procedure. Furthermore, a detailed explanation of the Eulerian flux-form advection scheme MPDATA (which is employed in EULAG for the advective transport of all prognostic variables) will be given.

Chapter 3 addresses the numerical integration of the anelastic equations in time-dependent generalised coordinates. In particular, this part develops extensions to the Eulerian flux-form advection scheme MPDATA which are essential for an effective integration of the anelastic equations under (arbitrary, i.e. numerically-generated) moving meshes. The developed extensions aim at the compatibility of the flux-form MPDATA scalar advection transport with the associated anelastic mass continuity equation in time-dependent generalised coordinates. Scalar advection experiments are performed to investigate the subject. All numerical experiments in Chapter 3 are limited to prescribed oscillating meshes for simplicity.

Chapter 4 introduces the solution-adaptive moving mesh algorithm. The implemented machinery that performs the numerical generation of the solution-adaptive moving curvilinear mesh is described in detail. The main ingredient of the scheme developed is a set of parabolic moving mesh partial differential equations (MMPDEs)

(Huang and Russell, 1999), which are solved along with the anelastic equations in EULAG. Monitor functions in the MMPDEs guide the mesh adaptation. Subjects such as the specification of the monitor functions, balancing of various monitor function components, the choice of a relaxation time for the moving mesh adaptation, adaptation of the mesh at the boundaries of the simulation domain, and the efficient and robust numerical implementation of the MMPDE machinery, are dealt with. In addition, the final Section 4.4 is concerned with the effective incorporation of the MMPDE machinery into the computational framework of EULAG.

Chapter 5 is concerned with testing and validation of the more basic aspects of the developments of Chapters 3 and 4 using canonical two-dimensional modelling problems of relevance to atmospheric flows. A first test problem is the advection of a passive scalar in a prescribed time-varying shear flow. A second test problem is a dry rising warm thermal in a neutrally-stratified quiescent atmosphere. Both test problems used are well documented in the literature and have the advantage that they are relatively easily to perform and analyse. The final Section 5.3 is devoted specifically to the investigation of the compatibility issue thoroughly discussed in the previous Chapter 3.

In **Chapter 6**, the developed solution-adaptive moving mesh solver is eventually applied in the three-dimensional modelling framework of EULAG. For the first time, solution-adaptive moving mesh methods are used to simulate the life cycle of a synoptic-scale baroclinic wave instability. The adaptive solver's ability is investigated to capture the synoptic-scale baroclinic wave instability and coexisting mesoscale processes like internal gravity waves.

Chapter 7 summarises and concludes the thesis. Remarks concerning the developed solution-adaptive moving mesh solver and an outlook for future research are given.

Furthermore, a completely different topic is addressed in **Appendix B**. This part presents results from a numerical model investigation about the significance of the abbreviated representation of baroclinic vorticity production underlying the Boussinesq equations for the simulation of aircraft wake vortices in a stably stratified atmosphere.

Chapter 2

EULAG modelling framework

This chapter introduces the EULAG modelling system for geophysical flows. The model provides the framework for the implementation of the solution-adaptive moving mesh non-oscillatory forward-in-time (NFT) flow solver that is developed and applied in this thesis. The following presentation of EULAG focuses on aspects of particular relevance to this implementation. This includes a description of the underlying "sound-proof" anelastic equations followed by their analytical formulation in time-dependent generalised coordinates, see Section 2.1. Tensor identities that play an important role in the analytical and numerical formulation are also highlighted briefly. The numerical solution procedure is then described in Section 2.2. Finally in Section 3.1, a detailed description of the advection solver MPDATA, which is employed in EULAG, is also given. In the subsequent Chapter 3, an extension of the given MPDATA scheme will be developed that is essential for its use with solution-adaptive moving meshes.
The reader is referred to Prusa et al. (2008), and references therein, for a more comprehensive explanation of EULAG's historical development and present capabilities, including its performance on large-scale parallel computational architectures.

2.1 Analytical formulation

A straightforward explicit numerical discretisation of the fully compressible equations is prohibitively expensive in terms of the required computational effort – and overall difficult to implement (Klein, 2011) – for typical atmospheric and oceanic flow problems. The presence of fast acoustic modes in the solutions imposes a severe time-step restriction on the integration algorithm. In order to achieve a more efficient

solution, i.e. larger time steps, atmospheric flow solvers based on the compressible equations may adopt special time discretisation approaches. These approaches typically use some form of time splitting (Klemp and Wilhelmson, 1978; Klemp et al., 2007) or implicit-differencing (Tanguay et al., 1990; Cullen, 1990) schemes.
An alternative approach underlying the present model formulation is to employ analytically filtered subsets of the fully compressible equations, that do not contain the fast unimportant acoustic modes yet retain the slower relevant modes of internal gravity waves and advection. For general stratified atmospheres, these so-called "sound-proof" flow models comprise the anelastic systems of equations (Ogura and Phillips, 1962; Dutton and Fichtl, 1969; Wilhelmson and Ogura, 1972; Lipps and Hemler, 1982; Lipps, 1990; Bannon, 1996), and the pseudo-incompressible system of Durran (Durran, 1989, 2008).

Here, only the dry dynamical version of the EULAG model is presented. A higher complexity that arises from the inclusion of moist physics and explicit microphysical/chemical processes (Grabowski and Smolarkiewicz, 2002; Spichtinger and Gierens, 2009a,b; Sölch and Kärcher, 2010) is disregarded. The focus is on essential aspects regarding the formulation of the model equations in time-dependent generalised coordinates.

Anelastic thermo-fluid equations

Starting point is the physical representation of the non-hydrostatic Lipps and Hemler anelastic system (Lipps and Hemler, 1982; Lipps, 1990) , given in an extended perturbational form (Smolarkiewicz and Margolin, 1997; Smolarkiewicz et al., 2001)

$$\frac{D\mathbf{v}}{Dt} = -\nabla\pi' - \mathbf{g}\,\frac{\theta'}{\theta_b} - \mathbf{f}\times\mathbf{v}' + \mathbf{M} + \mathbf{D} + \mathbf{B} \tag{2.1a}$$

$$\frac{D\theta'}{Dt} = -\mathbf{v}\cdot\nabla\theta_e + \mathcal{H} + \mathcal{B} \tag{2.1b}$$

$$\nabla\cdot(\rho_b\mathbf{v}) = 0\ . \tag{2.1c}$$

The set of anelastic equations (2.1) describes, respectively, the three components of the momentum equation (2.1a), the thermodynamic equation (2.1b), and the anelastic mass continuity equation (2.1c). In (2.1), the operators ∇ and $\nabla\cdot$ symbolize gradient and divergence, while $D/Dt = \partial/\partial t + \mathbf{v}\cdot\nabla$ is the Lagrangian derivative, and $\mathbf{v}$ is the physical velocity vector. A vector representing gravitational accelera-

tion $\mathbf{g} = (0, 0, -g)^T$ occurs in the buoyancy term of Eq. (2.1a). The symbol $\mathbf{f}$ stands for the vector of the Coriolis parameter that arises due to the global rotation of the domain. The subscript b appearing with the density ρ and potential temperature θ refers to the basic state, a horizontally-homogeneous prescribed hydrostatic reference state, characteristic of the anelastic approximation, see Ogura and Phillips (1962); Clark and Farley (1984); Bacmeister and Schoeberl (1989). In addition to the basic state, a more general ambient (also called environmental) state, that can vary in the vertical as well as the horizontal direction, is denoted with the subscript e, and defined to satisfy a balanced subset of the system (2.1). Please consult Prusa et al. (2008) for a discussion of the ambient state and its benefits. All primed variables θ', $\mathbf{v}'$, and π' that appear in (2.1) correspond to deviations from the ambient state. Particularly, the symbol π' in the linearised pressure gradient term of (2.1a) denotes a density-normalised pressure perturbation (Smolarkiewicz and Margolin, 1997).

Additional source terms not explicitly stated in the system (2.1) are considered through the following symbols: $\mathbf{M}$ denotes metric forces due to the curvilinearity of the underlying physical system $\mathbf{S}_p$ (see below), among others. The terms in $\mathbf{D}$ and $\mathcal{H}$ symbolise viscous dissipation of momentum and diffusion of heat, respectively. The terms in $\mathbf{B}$ and $\mathcal{B}$ may represent wave-absorbing devices in the vicinity of the domain boundaries (Smolarkiewicz and Margolin, 1997), and/or fictitious body forces employed to model immersed boundaries (Smolarkiewicz et al., 2007).

Coordinate transformations

Let $\mathbf{S}_p$ denote the physical space where the actual problem is naturally posed. An irregular, possibly time-dependent, subdomain $\mathcal{D}_p \subseteq \mathbf{S}_p$ with an assumed tuple of coordinates $(t, \mathbf{x}) \equiv (t, x, y, z)$ in $\mathbf{S}_p$ can be mapped into a regular computational subdomain $\mathcal{D}_t \subseteq \mathbf{S}_t$ in a transformed space $\mathbf{S}_t$ with its own tuple of generalised coordinates $(\overline{t}, \overline{\mathbf{x}}) \equiv (\overline{t}, \overline{x}, \overline{y}, \overline{z})$:

$$(\overline{t}, \overline{\mathbf{x}}) \equiv (t, \mathcal{F}(t, \mathbf{x})) : \quad \mathcal{D}_p \rightarrow \mathcal{D}_t \ . \tag{2.2}$$

The general mapping (2.2) is understood here to be a diffeomorphism, i.e. $\mathcal{F}(t, \mathbf{x})$ is a bijective map between manifolds $\mathcal{D}_p$ and $\mathcal{D}_t$ that is at least C^2-continuously differentiable.[1]. The requirement that the coordinate mapping is bijective means

[1] As an aside, it is noted that the numerical formulation of EULAG even allows for discontinuities in the coordinate mapping to mimic nested grids, see Prusa and Smolarkiewicz (2003) for an example.

that there exists a one-to-one (invertible) relationship between the coordinates in $\mathcal{D}_p$ and the coordinates in $\mathcal{D}_t$, which ensures that the mesh cells are not folded, see e.g. Liseikin (1999)

In the present work, the physical coordinates $\mathbf{x} \in \mathbf{S}_p$ are assumed to be exclusively rectangular Cartesian. Note, however, that the general coordinate framework of EULAG, as presented in this chapter, allows the physical problem to be posed in any stationary orthogonal system $\mathbf{S}_p$. Cartesian, spherical and polar cylindrical physical coordinates are possible choices in the current implementation of the model (Prusa and Smolarkiewicz, 2003; Prusa and Gutowski, 2006; Prusa et al., 2008).

Transformed model equations

Using a tensorial description, e.g. Synge and Schild (1978), the anelastic equations (2.1) can be written with respect to $\mathbf{S}_t$ as (Prusa et al., 2001; Smolarkiewicz and Prusa, 2002; Prusa and Smolarkiewicz, 2003)

$$\frac{dv^j}{d\bar{t}} = -\widetilde{G}^k_j \frac{\partial \pi'}{\partial \overline{x}^k} + g\frac{\theta'}{\theta_b}\delta^j_3 - f^i\, v'^k \varepsilon_{jik} + M^j + D^j + B^j \tag{2.3a}$$

$$\frac{d\theta'}{d\bar{t}} = -\overline{v}^{s^k} \frac{\partial \theta_e}{\partial \overline{x}^k} + \mathcal{H} + \mathcal{B} \tag{2.3b}$$

$$\frac{\partial(\rho^* \, \overline{v}^{s^k})}{\partial \overline{x}^k} = 0 \ , \tag{2.3c}$$

where $i,\ j, k = 1,2,3$; and the Einstein summation convention applies, unless otherwise stated. The Kronecker Delta δ^j_3 in the momentum equation (2.3a) is 1 for $j = 3$, and 0 for $j \neq 3$. The Levi-Civita (permutation) symbol ε_{jik}, see e.g. Synge and Schild (1978), occurs in the Coriolis term to represent the cross product. Note that in (2.3a), advection of the physical velocity is retained; therefore v^j corresponds to the j-th component with respect to the system $\mathbf{S}_p$.[1]

In the system (2.3), a generalised density $\rho^* \equiv \rho_b \, \overline{G}$ is conveniently introduced as the product of the basic state density ρ_b and the Jacobian of the transformation $\overline{G}$ (defined below). For the sake of clarity, ρ^* represents a positive-definite variable that incorporates the effects of both, the physical volumetric variation due to background stratification contained in the time-independent prescribed physical density

[1]Note that the formulation in the physical velocity components (instead of the transformed dependent variables) avoids numerical complications due to the occurrence of metric terms that involve Christoffel symbols in the momentum equation; see the seminal works of Vinokur (1974); Viviand (1974); Clark (1977).

ρ_b, plus changes of the geometric volume through the Jacobian $\overline{G}$ of the underlying coordinate transformation, that may be time-dependent. In contrast to elastic (e.g. compressible, general shallow water) systems, the variable ρ^* is explicitly known in anelastic systems.

The operator $d/d\bar{t}$ is the total derivative given as

$$\frac{d}{d\bar{t}} = \frac{\partial}{\partial \bar{t}} + \overline{v}^{*k} \frac{\partial}{\partial \overline{x}^k} \ , \tag{2.4}$$

where $\overline{v}^{*k} := d\overline{x}^k/d\bar{t}$ is the contravariant velocity in the transformed system $\mathbf{S}_t$. The velocity $\overline{v}^{sk}$ occurring in the entropy (2.3b) and continuity (2.3c) equations is the so-called *solenoidal* velocity (Prusa et al., 2001) defined as

$$\overline{v}^{sk} := \overline{v}^{*k} - \frac{\partial \overline{x}^k}{\partial t} \ , \tag{2.5}$$

that reflects the advective velocity in an otherwise stationary curvilinear coordinate system $\mathbf{S}_t$. While numerous formulae may be derived to express the distinct forms of velocity (physical, contravariant, and solenoidal) in terms of the other, an especially convenient transformation that relates the physical and the solenoidal velocity directly, is given as

$$\overline{v}^{sk} = \widetilde{G}^k_j \, v^j \ . \tag{2.6}$$

The symbol $\widetilde{G}^k_j := \sqrt{g^{jj}} \, \partial \overline{x}^k / \partial x^j$ appearing in (2.6) and the pressure gradient term of (2.3a), denotes the renormalised elements of the Jacobian matrix (summation not implied over j), while the coefficients g^{jj} are the diagonal elements of the conjugate metric tensor of $\mathbf{S}_p$. The elements are $g^{jj} \equiv 1$ for Cartesian coordinates $\mathbf{x} \in \mathbf{S}_p$, as assumed in the present work. For the general case of non-Cartesian orthogonal coordinates $\mathbf{x}$, please refer to Prusa and Smolarkiewicz (2003).

The utilised form of the mass continuity equation (2.3c) is not the most general tensor-invariant representation under the time-dependent mapping (2.2). The latter reads

$$\frac{1}{\overline{G}} \frac{\partial (\rho^* \, \overline{v}^{*r})}{\partial \overline{x}^r} \equiv 0 \ , \tag{2.7}$$

where $r = 0,1,2,3$, $\bar{t} \equiv \overline{x}^0$, $t \equiv x^0$, and $\overline{v}^{*0} \equiv 1$, or similarly

$$\frac{1}{\overline{G}} \left(\frac{\partial \rho^*}{\partial \bar{t}} + \frac{\partial (\rho^* \, \overline{v}^{*k})}{\partial \overline{x}^k} \right) \equiv 0 \ . \tag{2.8}$$

However, under the given assumptions that (i) the coordinates $\mathbf{x} \in \mathbf{S}_p$ are stationary,

and (ii) the density obeys the functional dependence $\rho_b = \rho_b(\mathbf{x})$, the form (2.8) is analytically-equivalent to (2.3c), see Prusa et al. (2001) for a discussion. This allows to employ the form (2.3c) instead of (2.8) in the governing system (2.3). As a result, it simplifies the design of the numerical model (see Section 2.2), and improves the efficacy of the solution procedure under time-variable mappings. Notwithstanding the use of (2.3c) in the system (2.3), the general form of the mass continuity equation (2.8) has important implications for the design of the numerical solver under time-dependent generalised coordinates, see Chapter 3.

Given by (2.2) is the most general transformation of the coordinates in three dimensions. The specific mapping that underlies the current implementation of EULAG is given as

$$\mathcal{F}(t,\mathbf{x}) \equiv (\overline{x}(t,x,y), \overline{y}(t,x,y), \overline{z}(t,x,y,z)) \ . \tag{2.9}$$

In (2.9), the vertical mapping $\overline{z}(x,y,z,t)$ incorporates a time-variable generalisation (Wedi and Smolarkiewicz, 2004)[1] of the standard terrain-following coordinate by (Gal-Chen and Somerville, 1975), that takes on the form

$$\overline{z} = \mathcal{C}(\zeta) \qquad \zeta = \zeta(t,x,y,z) := H_0 \frac{z - z_s(t,x,y)}{H(t,x,y) - z_s(t,x,y)} \ , \tag{2.10}$$

where z_s and H describe the lower and upper boundary of the domain, respectively, and H_0 is a representative domain depth. The function $\zeta(t,x,y,z)$ realises a uniform mesh between z_s and H in the vertical, and the function $\mathcal{C}(\zeta)$ can conveniently be used to apply a prescribed stretching, i.e. variable resolution, of the coordinate ζ with height.

While the vertical mapping coded in EULAG is subject to (2.10), the horizontal mappings admit the most general transformation according to the functional dependence $\overline{x}(x,y,t)$ and $\overline{y}(x,y,t)$. In effect, the model formulation enables an arbitrary time-dependent adaptive deformation of the mesh in the horizontal plane, that is independent of height. Although this purely horizontal structure prevents full generality of the mesh adaptation in three dimensions, it meets/follows the basic hydrostatic nature of atmospheric and oceanic flows, while simplifying metric terms and respective coding design. Moreover, the computational overhead associated with the solution-adaptive moving mesh apparatus employed in the present work (see Chapter 4), is kept small in a typical three-dimensional setting.

[1]This work was conducted by N.P. Wedi as part of his dissertation thesis at the Ludwig-Maximilians-Universität München (Wedi, 2004).

From the specifications of the mapping $\mathcal{F}(t, \mathbf{x})$ in (2.9) and (2.10), the Jacobian of the transformation $\overline{G}$ attains a separable form

$$\overline{G} = G\,\overline{G}_0'\,\overline{G}_{xy} \ . \tag{2.11}$$

The symbol $\overline{G}_0'$ in (2.11) denotes Jacobian of the transformation (2.10)

$$\overline{G}_0' = \left(\frac{d\mathcal{C}}{d\zeta}\frac{\partial\zeta}{\partial\overline{z}}\right)^{-1} = \left(\frac{d\mathcal{C}}{d\zeta}\right)^{-1}\frac{H(t,x,y) - z_s(t,x,y)}{H_0} \ , \tag{2.12}$$

cf. Wedi and Smolarkiewicz (2004), while $\overline{G}_{xy}$ represents the Jacobian of the general transformation of the horizontal coordinates defined as

$$\overline{G}_{xy} = \left(\frac{\partial\overline{x}}{\partial x}\frac{\partial\overline{y}}{\partial y} - \frac{\partial\overline{x}}{\partial y}\frac{\partial\overline{y}}{\partial x}\right)^{-1} . \tag{2.13}$$

The choice of a possibly non-Cartesian physical system $\mathbf{S}_p$ is reflected in the Jacobian G, whereupon we have $G \equiv 1$ for the assumed Cartesian coordinates $\mathbf{x} \in \mathbf{S}_p$.

Tensor identities

Underlying the model formulation in the generalised coordinates are fundamental tensor identities (Prusa and Gutowski, 2006), where at least two deserve brief consideration here. Among these is the Kronecker-delta identity (Synge and Schild, 1978; Prusa and Gutowski, 2006)

$$\delta_s^r \equiv \frac{\partial\overline{x}^r}{\partial x^q}\frac{\partial x^q}{\partial\overline{x}^s} \ , \tag{2.14}$$

that states the reciprocity of the co- and contravariant base vectors describing the generalised system $\mathbf{S}_t$. Here, the indices $r, s, q = 0,1,2,3$, whereupon $\overline{t} \equiv \overline{x}^0$ and $t \equiv x^0$. Given the computed metric coefficients $\partial x^q/\partial\overline{x}^s$ in the model computational space $\mathbf{S}_t$ (where $x^s = x^s(\overline{x}^r)$), the identity (2.14) provides the relationships to determine the inverse metric coefficients $\partial\overline{x}^r/\partial x^q$, that are used in the transformed model variables.

Another identity that arises naturally with the equations in conservation law form, e.g. (2.18), is the multi-component tensor geometric conservation law (GCL)

$$\frac{G}{\overline{G}}\frac{\partial}{\partial\overline{x}^r}\left(\frac{\overline{G}}{G}\frac{\partial\overline{x}^r}{\partial x^s}\right) \equiv 0 \ ; \tag{2.15}$$

emphasised in Prusa et al. (2001); Prusa and Gutowski (2006). The GCL (2.15) represents a compact differential statement about the *conservation of space*, under the general mapping of the coordinates (2.2). For $s=1,2,3$ it relates the three-dimensional spatial variation in $\mathbf{S}_t$, of the inverse metric coefficients and the Jacobian determinants[1]. For $s=0$, it describes the conservation of volume (known to be equivalent to the Jacobian) according to

$$\frac{\partial(\overline{G}/G)}{\partial \bar{t}} + \frac{\partial}{\partial \overline{x}^k}\left(\frac{\overline{G}}{G}\frac{\partial \overline{x}^k}{\partial t}\right) = 0 \ , \tag{2.16}$$

i.e. it relates, in the transformed space $\mathbf{S}_t$, the divergence of the fluxes of volume in space with the changes of volume in time. The importance of satisfying the GCL on the level of discretisation with the solution of conservation law forms, was first shown by Thomas and Lombard (1979). In Chapter 3, this subject is discussed with regard to the nonlinear flux-form advection solver MPDATA in the framework of the present anelastic solver.

2.2 Numerical solution procedure

Each prognostic equation of the transformed anelastic system (2.3) is given in a Lagrangian representation

$$\frac{d\psi}{d\bar{t}} = R^{\psi} \ , \tag{2.17}$$

where $\psi = \psi(\bar{t}, \overline{\mathbf{x}})$ denotes the transported mass-specific variable, and R^{ψ} subsumes the appendant source terms. Alternatively, the same equations can be written in the analytically-equivalent flux-form Eulerian conservation law

$$\frac{\partial(\rho^* \psi)}{\partial \bar{t}} + \overline{\nabla} \cdot (\rho^* \, \overline{\mathbf{v}}^* \, \psi) = \rho^* R^{\psi} \ ; \tag{2.18}$$

given $\overline{\mathbf{v}}^* \equiv d\overline{\mathbf{x}}/d\bar{t}$ as the contravariant velocity vector, and $\overline{\nabla}\cdot$ the divergence operator with respect to the generalised coordinates $\overline{\mathbf{x}} \in \mathbf{S}_t$. Underlying the numerical model formulation is that the anelastic equations (2.3) can be optionally integrated in either the flux-form Eulerian (2.18) or the Lagrangian (2.17) representation[2]. A compact description of the unified Eulerian/semi-Lagrangian solution algorithm on a regular computational mesh $(\bar{t}^n, \overline{\mathbf{x}}_{\mathbf{i}})$, can be written as (Smolarkiewicz, 1991;

[1] From a geometrical point of view, the $s=1,2,3$ components of the GCL simply state that the surface enclosing a differential volume is closed.
[2] Hence, the name EULAG.

Smolarkiewicz and Margolin, 1993; Smolarkiewicz and Margolin, 1997, 1998)

$$\psi_{\mathbf{i}}^{n+1} = \mathcal{LE}_{\mathbf{i}}(\widetilde{\psi}) + 0.5\,\delta\bar{t}\,R^{\psi}|_{\mathbf{i}}^{n+1} \ , \tag{2.19}$$

whereupon $\mathcal{LE}_{\mathbf{i}}$ symbolically denotes a non-oscillatory[1] forward-in-time (NFT) advection transport scheme, and $\widetilde{\psi} \equiv \psi^n + 0.5\,\delta\bar{t}\,R^{\psi^n}$. Note, that the n, $n+1$ superscripts denote the time level, the subscript $\mathbf{i}$ denotes the spatial mesh vector index, and $\delta\bar{t} = \bar{t}^{n+1} - \bar{t}^n$ is the time step increment. In the Eulerian variant of the model, $\mathcal{LE}$ integrates the homogeneous conservation law (2.18) employing the second-order-accurate fully multidimensional advection algorithm MPDATA (see Section 2.3). In the semi-Lagrangian option, $\mathcal{LE}$ remaps the transported fields, which arrive at the grid points $(\bar{t}^{n+1}, \overline{\mathbf{x}}_{\mathbf{i}})$, back to the departure points of the flow trajectories $(\bar{t}^n,\ \overline{\mathbf{x}}_0(\bar{t}^{n+1},\ \overline{\mathbf{x}}_{\mathbf{i}}))$, using tensor-product application of one-dimensional advection schemes that are akin to MPDATA (Tremback et al., 1987; Smolarkiewicz and Pudykiewicz, 1992). Advecting the auxiliary field $\widetilde{\psi}$ (instead of the variable ψ^n alone) in the Eulerian FT scheme, compensates for $\mathcal{O}(\delta\bar{t})$ truncation errors proportional to the divergence of the advective flux of the source terms R^{ψ}, see Smolarkiewicz (1991); Smolarkiewicz and Margolin (1993) for an explanation. Simultaneously, it makes the Eulerian integration congruent to the trapezoidal approximation of the trajectory integral in the semi-Lagrangian scheme (Smolarkiewicz and Margolin, 1993; Smolarkiewicz and Margolin, 1997).

Restricting the anelastic set (2.3) to inviscid adiabatic dynamics for simplicity, i.e. $\mathbf{M}$, $\mathbf{D}$, $\mathcal{H}$, $\mathbf{B}$, $\mathcal{B}$ all set to zero, the template algorithm (2.19) represents a system that is fully implicit with respect to the dependent variables $\mathbf{v}$, π' and θ', while the explicit part in (2.19) consists of the advection operator $\widehat{\psi} := \mathcal{LE}(\widetilde{\psi})$. For the momentum equation (2.3a), the algorithm (2.19) results in

$$\mathbf{v}_{\mathbf{i}} = \widehat{\mathbf{v}}_{\mathbf{i}} - 0.5\,\delta\bar{t}\,(\widetilde{\mathbf{G}}\overline{\nabla}\pi')_{\mathbf{i}} + 0.5\,\delta\bar{t}\,\mathbf{F}_{\mathbf{i}}(\mathbf{v}, \widehat{\theta'}) \ , \tag{2.20}$$

with

$$\mathbf{F}_{\mathbf{i}}(\mathbf{v}, \widehat{\theta'}) \equiv -\frac{\mathbf{g}}{\theta_b}\left(\widehat{\theta'} - 0.5\,\delta\bar{t}\,((\widetilde{\mathbf{G}}^T\mathbf{v})\cdot\overline{\nabla}\theta_e)\right)_{\mathbf{i}} - (\mathbf{f}\times\mathbf{v}')_{\mathbf{i}} \tag{2.21}$$

accounting for the implicit treatment of buoyancy via the entropy equation (2.3b). Note that all superscripts indicating the $n+1$ time level have been dropped here, since there is no ambiguity. The symbol $\widetilde{\mathbf{G}}$ that appears in the utilised compact description, is identified with the renormalised Jacobi matrix $\widetilde{G}_j^k$, defined in Section 2.1.

[1]Non-oscillatory refers to the monotonicity of the solution, i.e. no spurious extrema are created by the numerical solution scheme, see e.g. Durran (1999) for a discussion.

Organising of (2.20) into explicit and implicit parts gives

$$\mathbf{v_i} = \widehat{\widehat{\mathbf{v}}}_\mathbf{i} - 0.5\,\delta\overline{t}\,(\widetilde{\mathbf{G}}\overline{\nabla}\pi')_\mathbf{i} + 0.5\,\delta\overline{t}\,\widetilde{\mathbf{F}}_\mathbf{i}(\mathbf{v})\ , \tag{2.22}$$

where $\widehat{\widehat{\mathbf{v}}}$ subsumes all known terms, and $\widetilde{\mathbf{F}}$ denotes the implicit remainder of (2.21). Provided that the underlying grid is co-located with respect to all prognostic variables[1], algebraic inversion of (2.22) leads to a unique expression for the vector $\mathbf{v_i}$. Then, the relation (2.6) leads to an expression for the solenoidal velocity of the form $\overline{\mathbf{v}}^s \equiv \widetilde{\mathbf{G}}^T \left[\widetilde{\widetilde{\mathbf{v}}} - (\mathbf{I} - 0.5\,\delta\overline{t}\,\widetilde{\mathbf{F}})^{-1}(\widetilde{\mathbf{G}}\overline{\nabla}\pi'')\right]$ with the definitions $\widetilde{\widetilde{\mathbf{v}}} := (\mathbf{I} - 0.5\,\delta\overline{t}\,\widetilde{\mathbf{F}})^{-1}\,\widehat{\widehat{\mathbf{v}}}$ and $\pi'' := 0.5\,\delta\overline{t}\,\pi'$. Finally, the solenoidal velocity $\overline{\mathbf{v}}^s$ is substituted into the anelastic mass continuity equation (2.3c) to obtain an elliptic equation for π''

$$\left\{-\frac{\delta\overline{t}}{\rho^*}\,\overline{\nabla}\cdot\left(\rho^*\,\widetilde{\mathbf{G}}^T\left[\widetilde{\widetilde{\mathbf{v}}} - (\mathbf{I} - 0.5\,\delta\overline{t}\,\widetilde{\mathbf{F}})^{-1}(\widetilde{\mathbf{G}}\overline{\nabla}\pi'')\right]\right)\right\}_\mathbf{i} = 0\ , \tag{2.23}$$

a complete development of which is given in the Appendix A of Prusa and Smolarkiewicz (2003). The applied normalisation by $(\delta\overline{t}/\rho^*)$ gives the residual errors of (2.23) the meaning of the divergence of a dimensionless velocity on the grid. The latter compares directly to the magnitude of the Courant and Lipschitz numbers (cf. Smolarkiewicz and Pudykiewicz (1992)), and facilitates the specification of physically meaningful accuracy thresholds $||(\delta\overline{t}/\rho^*)\overline{\nabla}\cdot(\rho^*\overline{\mathbf{v}}^s)|| < \epsilon$ (Smolarkiewicz and Margolin, 1994; Smolarkiewicz et al., 1997; Prusa and Smolarkiewicz, 2003). Multiplication by the factor (-1) assures the formal negative-definiteness of the elliptic operator (Smolarkiewicz and Margolin, 1994; Prusa and Smolarkiewicz, 2003). Note also, the scaling by $(1/\rho^*)$ acts as a preconditioner for deep atmospheres where ρ^*, respectively ρ_b, can vary several orders of magnitude over the vertical depth of the simulation domain.

Dirichlet boundary conditions along $\partial\mathcal{D}_t$ prescribed on the normal component of the solenoidal velocity, i.e. $\overline{\mathbf{v}}^s\cdot\overline{\mathbf{n}}$, which are subject to the integrability condition $\int_{\partial\mathcal{D}_t}\rho^*\overline{\mathbf{v}}^s\cdot\overline{\mathbf{n}}\,d\overline{\sigma} = 0$, imply the correct Neumann boundary conditions for π'' (Prusa and Smolarkiewicz, 2003). A preconditioned generalised conjugate residual GCR(k)[2] algorithm (Eisenstat et al., 1983; Smolarkiewicz and Margolin, 1994; Skamarock et al., 1997; Smolarkiewicz et al., 2004) is employed to solve the formulated elliptic boundary value problem. The solution to (2.23) is used to compute the updated solenoidal velocity. From this, the updated physical and contravariant velocity com-

[1] Arakawa A- or B-grids are possible options in the present model, see Smolarkiewicz and Margolin (1997).

[2] The generalized conjugate residual scheme is a type of non-symmetric Krylov subspace solver akin to the generalised minimum residual (GMRES) scheme (Saad, 1993).

ponents are obtained using the relations (2.6) and (2.5), respectively.

Note finally, that the additional source terms in the system (2.3) that represent the boundary forcings $\mathbf{B}$ and $\mathcal{B}$ are otherwise all treated implicitly in the solution scheme, see Smolarkiewicz and Margolin (1997); Prusa and Smolarkiewicz (2003); Smolarkiewicz et al. (2007). Moreover, possible nonlinear terms occurring in (2.3), e.g. metric terms arising with a spherical physical system $\mathbf{S}_p$ (Smolarkiewicz et al., 2001) or nonlinear pressure gradient terms that occur with the solution of Durran's pseudo-incompressible equations (as described in Smolarkiewicz and Dörnbrack (2008)), may use outer iteration of the system generated by (2.19). When incorporated, diabatic, viscous, and subgrid-scale forcings, are typically evaluated explicitly with first-order accuracy (Smolarkiewicz and Margolin, 1998; Prusa and Smolarkiewicz, 2003).

2.3 Advection solver MPDATA

The MPDATA scheme uses the upwind method in an iterative manner to achieve second-order accurate solutions to advective conservation laws. Given a regular upwind solution, MPDATA applies corrective upwind steps to reduce the error of the preceding solution. The basic idea is to employ error-compensative pseudo-velocities in the corrective steps that are derived on the basis of a truncation error analysis. Since this basic idea of MPDATA methods has been invented in the early 1980's by Piotr K. Smolarkiewicz (Smolarkiewicz, 1983), the technology has evolved into a broad class of complete flow solvers for general inelastic- and elastic-type conservation laws in curvilinear (Smolarkiewicz and Clark, 1986; Smolarkiewicz and Margolin, 1993; Smolarkiewicz and Margolin, 1998; Smolarkiewicz, 2006), and also arbitrary unstructured (Smolarkiewicz and Szmelter, 2005; Szmelter and Smolarkiewicz, 2006; Szmelter and Smolarkiewicz, 2010b,a) mesh frameworks.

MPDATA belongs to the class of nonlinear high-resolution schemes, e.g. Drikakis and Rider (2005), that offer solutions free of spurious oscillations, while maintaining second-order accuracy away from discontinuities for arbitrary flows. The particular nonlinear design of MPDATA (Rider, 2006) makes it a viable advection method for implicit large-eddy simulation (ILES) of high-Reynolds number turbulent flows (Margolin et al., 1999; Smolarkiewicz and Prusa, 2002; Smolarkiewicz and Prusa, 2002; Domaradzki et al., 2003; Domaradzki and Radhakrishnan, 2005; Rider, 2006; Prusa et al., 2008; Piotrowski et al., 2009). Therein, the large-scale turbulent mo-

tions are simulated explicitly, while the subgrid-scale modelling of turbulence is left to the self-adaptive dissipative nature of the truncation error terms in the advection scheme. This is in contrast to the typical LES approach where the effect of the subgrid-scale dynamics on the resolved scales is implemented by an explicit subgrid scale model, see for instance Schmidt and Schumann (1989); Nieuwstadt et al. (1991); Schumann (1996); Lesieur and Metais (1996). An option for ILES is of special relevance to geophysical flow simulations with possible adaptive meshing, where explicit modelling of subgrid-scale turbulence is difficult to implement effectively. Furthermore, the non-oscillatory character of the solution scheme per se represents an important ingredient of an accurate and robust mesh adaptation algorithm, especially when the mesh refinement is driven by the solution itself. In terms of the latter, note finally that MPDATA's special iterative error-reducing design can be exploited to derive a posteriori refinement indicators for mesh adaptation (Szmelter and Smolarkiewicz, 2006).

Derivation of the scheme

Here, the MPDATA solution scheme to a prototype advective conservation law in time-dependent generalised coordinates, which is given as the homogeneous version of the Eulerian transport equation (2.18)

$$\frac{\partial(\rho^*\psi)}{\partial\bar{t}} + \overline{\nabla}\cdot\left(\overline{\mathbf{v}}^*\rho^*\psi\right) = 0 \ , \tag{2.24}$$

is reviewed. Following the developments in Smolarkiewicz (1984); Smolarkiewicz and Margolin (1993); Smolarkiewicz and Prusa (2002) (see also the review publications Smolarkiewicz and Margolin (1998); Smolarkiewicz (2006)), the generalised advection conservation law (2.24) is discretised forward-in-time (FT) as

$$\frac{\rho^{*n+1}\psi^{n+1} - \rho^{*n}\psi^n}{\delta\bar{t}} + \overline{\nabla}\cdot\left(\hat{\mathbf{v}}^{n+1/2}\psi^n\right) = 0 \ , \tag{2.25}$$

where the superscripts correspond to the temporal levels, and again $\delta\bar{t} = \bar{t}^{n+1} - \bar{t}^n$ is the time step increment. Under the continuous divergence operator, the density ρ^* has been absorbed in an advective contravariant Jacobian-weighted mass flux vector $\hat{\mathbf{v}} := \rho^*\overline{\mathbf{v}}^*$. A truncation error analysis based on Taylor series expansions of all fields around the time level $\bar{t}^n$, shows that (2.25) approximates, to second-order accuracy

in time, the modified equation

$$\frac{\partial(\rho^*\psi)}{\partial\bar{t}} + \overline{\nabla}\cdot\left(\hat{\mathbf{v}}\,\psi\right) = -\overline{\nabla}\cdot\left[\frac{\delta\bar{t}^*}{2}\,\frac{1}{\rho^*}\hat{\mathbf{v}}\left(\hat{\mathbf{v}}\cdot\overline{\nabla}\psi\right)\right.$$
$$\left. + \frac{\delta\bar{t}^*}{2}\,\frac{1}{\rho^*}\,\hat{\mathbf{v}}\left(\frac{\partial\rho^*}{\partial\bar{t}} + \overline{\nabla}\cdot\hat{\mathbf{v}}\right)\psi\right] + \mathcal{O}(\delta\bar{t}^2)\;; \qquad (2.26)$$

given an $\mathcal{O}(\delta\bar{t}^2)$ estimate for $\hat{\mathbf{v}}^{n+1/2} = (\rho^*\overline{\mathbf{v}}^*)^{n+1/2}$ in (2.25). See Smolarkiewicz and Margolin (1993); Smolarkiewicz and Prusa (2002) for a thorough demonstration in the context of the inhomogeneous generalised transport equation (2.18). In contrast to the derivations in these earlier works Smolarkiewicz and Margolin (1993); Smolarkiewicz and Prusa (2002), a continuously varying time step $\delta\bar{t} = \delta\bar{t}(\bar{t})$ is assumed here. This leads to the modified equation (2.26) that is congruent with the one derived under a constant time step $\delta\bar{t}$, but with $\delta\bar{t}$ replaced by

$$\delta\bar{t}^* := \frac{\delta\bar{t}}{1 + 0.5\delta\bar{t}_{,t}}\;, \qquad (2.27)$$

in which $\delta\bar{t}_{,t} \equiv \partial(\delta\bar{t})/\partial\bar{t}$ denotes the time derivative of the time step (Smolarkiewicz et al., 2011). The solver's stability depends on the maximum of the Courant number $\sim ||\overline{\mathbf{v}}^*\delta\bar{t}/\delta\overline{\mathbf{x}}||$ in the solution domain. The larger the variability of the maximum Courant number $\mathcal{C}_{max}$ over the simulation time, the more significant are potential efficiency gains from the application of a variable time stepping procedure. In general, the observed maximum Courant numbers show a larger variability with solution-adaptive moving meshes than with computations on a static uniform mesh.

In order to arrive at a second-order accurate FT scheme for the homogeneous advection equation (2.24), one has to compensate, to at least $\mathcal{O}(\delta\bar{t}^2)$ accuracy, for all $\mathcal{O}(\delta\bar{t})$ terms on right-hand side (RHS) of (2.26). Within MPDATA, a first-order accurate $\mathcal{O}(\delta\bar{t}, \delta\overline{x})$ upwind solution is followed by a corrective upwind step that incorporates compensation of all truncation error terms $\sim\mathcal{O}(\delta\bar{t})$ on the RHS of (2.26), plus truncation errors $\sim\mathcal{O}(\delta\overline{x})$ that stem from one-sided upwind spatial differencing disregarded in the spatially continuous equation (2.25), and thus in (2.26); see Smolarkiewicz and Margolin (1998). This is accomplished by constructing error-compensative advective pseudo-velocities which are used in the corrective upwind steps (see Smolarkiewicz (1983) for an explanation of the basic methodology). The second truncation error term on the right-hand side (RHS) of (2.26) contains the generalized anelastic mass conservation law (GMCL) (3.2) which can be assumed to vanish, see the discussion in Section 3.1. The resulting advection algorithm attains

$\mathcal{O}(\delta\overline{t}^2, \delta\overline{x}^2)$ accuracy, for an arbitrary-variable velocity field $\hat{\mathbf{v}}$ and a (sufficiently smooth) time-dependent curvilinear mesh.

Implementation of the scheme

Next, the implementation of the scheme is described. As discussed in Smolarkiewicz and Prusa (2002), the solution update for a time-dependent ρ^*, can be written as a solution update for the algorithm that assumes a time-independent ρ^*, multiplied by the ratio (ρ^{*n}/ρ^{*n+1}). To see this, the semi-discretised equation (2.25) is recast into

$$\psi^{n+1} = \frac{\rho^{*n}}{\rho^{*n+1}} \left[\psi^n - \frac{\delta\overline{t}}{\rho^{*n}} \overline{\nabla} \cdot \left(\hat{\mathbf{v}}^{n+1/2} \psi^n \right) \right] , \tag{2.28}$$

where the expression in square brackets is formally independent of ρ^{*n+1}. Therefore, a second-order accurate MPDATA solution update for (2.24), under time-dependent mappings, can be written as

$$\psi_{\mathbf{i}}^{n+1} = \frac{\rho_{\mathbf{i}}^{*n}}{\rho_{\mathbf{i}}^{*n+1}} \mathcal{A}_{\mathbf{i}}(\psi^n, \hat{\mathbf{v}}^{n+1/2}, \rho^{*n}) = \frac{\rho_{\mathbf{i}}^{*n}}{\rho_{\mathbf{i}}^{*n+1}} \, \psi_{\mathbf{i}}^{(IORD)} , \tag{2.29}$$

in which $\mathcal{A}$ denotes the MPDATA scheme for time-independent ρ^*; viz. the same algorithm as used for time-independent, though curvilinear, coordinates. Specifically, $\mathcal{A}$ iterates for $k = 1, IORD$ the discrete flux-form

$$\psi_{\mathbf{i}}^{(k)} = \psi_{\mathbf{i}}^{(k-1)} - \frac{1}{\rho_{\mathbf{i}}^{*n}} \sum_{I=1}^{N} \left\{ F\left(\psi_{\mathbf{i}}^{(k-1)}, \psi_{\mathbf{i}+\mathbf{e}_I}^{(k-1)}, V_{\mathbf{i}+1/2\,\mathbf{e}_I}^{I\,(k)} \right) - F\left(\psi_{\mathbf{i}-\mathbf{e}_I}^{(k-1)}, \psi_{\mathbf{i}}^{(k-1)}, V_{\mathbf{i}-1/2\,\mathbf{e}_I}^{I\,(k)} \right) \right\} , \tag{2.30}$$

with $\mathbf{e}_I$ denoting the unit vector in the Ith of the N spatial dimensions, while integer and half integer indices correspond to the cell centers and edges, respectively. The superscript in parentheses denotes the number of inner MPDATA iterations, not the time levels. The upwind flux functions F in (2.30) can be stated in a symbolic form as

$$F\left(\psi_L, \psi_R, V\right) \equiv 0.5 \left(\left(V + |V|\right) \psi_L + \left(V - |V|\right) \psi_R \right) . \tag{2.31}$$

Then, the algorithm is initialised with the following quantities

$$\psi^{(0)} \equiv \psi^n , \qquad V^{I\,(1)} \equiv \overline{\lambda}^I \left(\rho^* \overline{v}^{*I}\right)^{n+1/2} , \qquad \overline{\lambda}^I \equiv \frac{\delta\overline{t}}{\delta\overline{x}^I} , \tag{2.32}$$

where $\delta\overline{x}^I$ are spatial mesh increments in the respective coordinate directions. Assumed here is the availability of a $\mathcal{O}(\delta\overline{t}^2)$ estimate for the generalised local Courant number $\overline{\lambda}^I (\rho^* \overline{v}^{*I})^{n+1/2}$ at the intermediate time level $\overline{t}^{\,n+1/2}$, see at the end of this

section for possible approximations. The functional dependence of the corrective pseudo-velocity for the $IORD > 1$ scheme can be written as

$$V^{I\,(k)} = V^{I}\left(\mathbf{V}^{(k-1)}, \psi^{(k-1)}, \overline{\nabla}\psi^{(k-1)}, \rho^{*n}\right) \ , \tag{2.33}$$

which also indicates the nonlinear character of the scheme. The particular implementation of the pseudo-velocities (2.33) for the basic MPDATA is given as (Smolarkiewicz, 1984; Smolarkiewicz and Clark, 1986)

$$\begin{aligned} V^{I\,(k)}_{\mathbf{i}+1/2\,\mathbf{e}_I} = & \left(\left| V^{I\,(k-1)}_{\mathbf{i}+1/2\,\mathbf{e}_I} \right| - \frac{\left(V^{I\,(k-1)}_{\mathbf{i}+1/2\,\mathbf{e}_I}\right)^2}{0.5\left(\rho^{*n}_{\mathbf{i}+\mathbf{e}_I} + \rho^{*n}_{\mathbf{i}}\right)} \right) \frac{\psi^{(k-1)}_{\mathbf{i}+\mathbf{e}_I} - \psi^{(k-1)}_{\mathbf{i}}}{\psi^{(k-1)}_{\mathbf{i}+\mathbf{e}_I} + \psi^{(k-1)}_{\mathbf{i}}} \\ & - \sum_{J=1;J\neq I}^{N} \left(\frac{V^{I\,(k-1)}_{\mathbf{i}+1/2\,\mathbf{e}_I} \overline{V^{J\,(k-1)}_{\mathbf{i}+1/2\,\mathbf{e}_I}}}{\left(\rho^{*n}_{\mathbf{i}+\mathbf{e}_I} + \rho^{*n}_{\mathbf{i}}\right)} \right) \\ & \times \frac{\psi^{(k-1)}_{\mathbf{i}+\mathbf{e}_I+\mathbf{e}_J} + \psi^{(k-1)}_{\mathbf{i}+\mathbf{e}_J} - \psi^{(k-1)}_{\mathbf{i}+\mathbf{e}_I-\mathbf{e}_J} - \psi^{(k-1)}_{\mathbf{i}-\mathbf{e}_J}}{\psi^{(k-1)}_{\mathbf{i}+\mathbf{e}_I+\mathbf{e}_J} + \psi^{(k-1)}_{\mathbf{i}+\mathbf{e}_J} + \psi^{(k-1)}_{\mathbf{i}+\mathbf{e}_I-\mathbf{e}_J} + \psi^{(k-1)}_{\mathbf{i}-\mathbf{e}_J}} \end{aligned} \tag{2.34}$$

and

$$\overline{V^{J\,(k-1)}_{\mathbf{i}+1/2\,\mathbf{e}_I}} := 0.25\left(V^{J\,(k-1)}_{\mathbf{i}+\mathbf{e}_I+1/2\,\mathbf{e}_J} + V^{J\,(k-1)}_{\mathbf{i}+1/2\,\mathbf{e}_J} + V^{J\,(k-1)}_{\mathbf{i}+\mathbf{e}_I-1/2\,\mathbf{e}_J} + V^{J\,(k-1)}_{\mathbf{i}-1/2\,\mathbf{e}_J} \right) \ ,$$

which consists of the aforementioned truncation error corrections for temporal (the first truncation error term $\sim \delta\bar{t}$ in the modified equation (2.26)) plus spatial differencing of the upwind scheme (Smolarkiewicz, 1984). The derived scheme (2.29)-(2.32) with (2.34) is fully second-order accurate and preserves the sign of the transported scalar field ψ. Note that in (2.34), the field ψ is assumed to be exclusively either non-negative or non-positive. In Smolarkiewicz and Margolin (1998), extensions for the applicability to scalar fields ψ of arbitrary sign are given. A variety of extending options to the presented MPDATA scheme exist, most of which are expressed in different specifications of the pseudo-velocity (2.33). Extensions employed in the present work include the "third-order accurate" scheme[1] (Smolarkiewicz and Margolin, 1998; Margolin and Smolarkiewicz, 1999), and the combination of MPDATA with the flux-corrected transport (FCT) technology (Zalesak, 1979; Smolarkiewicz and Grabowski, 1990) for applications that require a fully non-oscillatory solution. Furthermore, there is the two-step infinite-gauge "linearised" version of

[1]Note that strictly speaking, the "third-order accurate" scheme (2.33) contains a dependence on the second derivatives of ψ as well (Smolarkiewicz and Margolin, 1998).

MPDATA (Smolarkiewicz and Clark, 1986; Smolarkiewicz and Margolin, 1998) that is useful for the transport of fields ψ with variable signs, e.g. momentum components; cf. Smolarkiewicz and Margolin (1998) Section 3.2.

Advective velocity prediction

Finally, to complete the described algorithm, an $\mathcal{O}(\delta\bar{t}^2)$ estimate to the generalised contravariant mass flux vector $\hat{\mathbf{v}}^{n+1/2} = (\rho^*\overline{\mathbf{v}}^*)^{n+1/2}$ in (2.25) is required in order to achieve second-order accuracy of the MPDATA integration. A simple and efficient way is to employ linear extrapolation

$$(\rho^*\overline{\mathbf{v}}^*)^{n+1/2} = (1+\beta)\,(\rho^*\overline{\mathbf{v}}^*)^{n} - \beta\,(\rho^*\overline{\mathbf{v}}^*)^{n-1}\ , \tag{2.35}$$

where $\beta := 0.5\,(\bar{t}^{n+1} - \bar{t}^{n})/(\bar{t}^{n} - \bar{t}^{n-1})$ accounts for the variable time step (Smolarkiewicz and Szmelter, 2009). The linear predictor (2.35) preserves the solenoidal character of $\rho^*\overline{\mathbf{v}}^*$, a property that is especially advantageous in the anelastic model (Smolarkiewicz and Margolin, 1998). The approximation (2.35) is appropriate for the majority of applications, and is used almost exclusively in the present work. Nonlinear estimates for $(\rho^*\overline{\mathbf{v}}^*)^{n+1/2}$ based on a first-order solution of the underlying flow equations may also be used in lieu of (2.35), see Smolarkiewicz and Margolin (1993); Smolarkiewicz and Margolin (1998) for a complete discussion of the method.

Chapter 3

MPDATA extension for time-dependent coordinates

This chapter develops extensions to the flux-form Eulerian MPDATA integration of the anelastic equations in EULAG under moving meshes.
During the course of the implementation of the solution-adaptive moving mesh solver (see Chapter 4), significant errors in the MPDATA integration appeared that were completely absent from previous moving mesh applications based on MPDATA methods (Prusa and Smolarkiewicz, 2003; Wedi and Smolarkiewicz, 2004; Smolarkiewicz and Prusa, 2005; Wedi and Smolarkiewicz, 2005). It was found from a detailed study that these errors can be attributed to numerical inconsistencies of the MPDATA integration with the general form of the anelastic mass conservation law (2.8) in time-dependent generalised coordinates. The observed error magnitudes strongly depend on the rate and irregularity of the underlying mesh deformations during the adaptation process. In this regard, solution-adaptive numerically-generated meshes used in the present work typically suffer larger errors in the integration than analytically prescribed time-dependent meshes mostly employed in the previous works by Prusa and Smolarkiewicz (2003); Wedi and Smolarkiewicz (2004); Smolarkiewicz and Prusa (2005); Wedi and Smolarkiewicz (2005). In the later Section 5.3, specific examples for the occurrence of large solution errors due to the incompatibility of MPDATA will be given in the context of solution-adaptive moving mesh experiments.

3.1 Compatible scalar transport

A general issue that appears when solving a scalar advective transport equation in conservation form is that the *compatibility* (often also referred to as *consistency*) of the applied flux-form advection numerical solver with the associated mass conservation law must be ensured. Consistency means that for a spatially uniform transported scalar field ψ, the discretised form of the advective scalar conservation law degenerates to the discretised form of the associated mass conservation law, e.g. Lin and Rood (1996).

In the following sections, the MPDATA scheme for the integration of the scalar conservation law in time-dependent generalised coordinates (2.24), repeated here for convenience

$$\frac{\partial(\rho^*\psi)}{\partial\bar{t}} + \overline{\nabla}\cdot\left(\overline{\mathbf{v}}^*\rho^*\psi\right) = 0 \ , \tag{3.1}$$

will be revised. It will be shown that the original scheme in Chapter 2 is not fully compatible with the corresponding generalised anelastic mass conservation law (GMCL)

$$\frac{\partial\rho^*}{\partial\bar{t}} + \overline{\nabla}\cdot\left(\rho^*\overline{\mathbf{v}}^*\right) = 0 \ . \tag{3.2}$$

The general subject of the compatibility (or consistency) of advective scalar transport schemes with mass continuity was previously addressed in diverse contexts by Demirdzic and Peric (1988); Lin and Rood (1996); Schär and Smolarkiewicz (1996); Jöckel et al. (2001); Gross et al. (2002); Chou and Fringer (2009); Klein (2009).

In Section 2.3, a review of MPDATA scheme in time-dependent generalised coordinates was given. In the remaining chapter, a detailed theoretical and numerical analysis of the MPDATA scheme for the solution of the scalar conservation law (3.1) is conducted. The analysis will reveal extensions to the scheme that enable full compatibility with the GMCL (3.2) under arbitrary moving meshes. These extensions are essential for the use of MPDATA in the solution-adaptive moving mesh solver developed in this thesis.

3.2 MPDATA compatibility

MPDATA is based on a rigorous truncation error analysis for the FT discretisation (2.25). In Section 2.3, the derivation of the scheme was given, and its imple-

mentation was explained. Here, a systematic theoretical analysis of this scheme is conducted. For the first time, the compatibility with the GMCL (3.2) is rigorously taken into account.

Analysis of the scheme

The analysis of the MPDATA scheme is conducted for the advection of a uniform scalar field $\widetilde{\psi}$ in time-dependent generalised coordinates. Consider first the $IORD=1$ variant of the MPDATA scheme, i.e. the first-order accurate upwind scheme[1]. Insertion of the uniform field $\psi^n \equiv \widetilde{\psi}$ in the MPDATA scheme (2.29)-(2.32) results in

$$\psi_{\mathbf{i}}^{n+1} = \frac{\widetilde{\psi}}{\rho_{\mathbf{i}}^{*n+1}} \left\{ \rho_{\mathbf{i}}^{*n} - \sum_{I=1}^{\mathrm{N}} \overline{\lambda}^I \left((\rho^* \overline{v}^{*I})_{\mathbf{i}+1/2\mathbf{e}^I}^{n+1/2} - (\rho^* \overline{v}^{*I})_{\mathbf{i}-1/2\mathbf{e}^I}^{n+1/2} \right) \right\} . \tag{3.3}$$

This expression shows that the $IORD=1$ variant of MPDATA preserves a uniform transported field ψ if the following discrete implementation

$$\rho_{\mathbf{i}}^{*n+1} = \rho_{\mathbf{i}}^{*n} - \sum_{I=1}^{\mathrm{N}} \overline{\lambda}^I \left((\rho^* \overline{v}^{*I})_{\mathbf{i}+1/2\mathbf{e}^I}^{n+1/2} - (\rho^* \overline{v}^{*I})_{\mathbf{i}-1/2\mathbf{e}^I}^{n+1/2} \right) \tag{3.4}$$

of the GMCL (3.2) is satisfied. Then, the terms in the curly brackets of (3.3) are equal to $\rho_{\mathbf{i}}^{*n+1}$, which gives the desired result $\psi^{n+1} \equiv \widetilde{\psi} \equiv \psi^n$.

The generalised density ρ^* occurring in (3.4) at the various time levels is given by the product of the Jacobian $\overline{G}$ and the basic-state density ρ_b, which are both known diagnostic quantities in the anelastic system. In addition, the generalised contravariant mass flux $\rho^* \overline{v}^{*I}$ in (3.4) at the intermediate time level $\overline{t}^{n+1/2}$ in (3.4) is typically derived by using a predictor scheme as in (2.35). Therefore, all quantities entering the discrete GMCL (3.4) in the algorithm are predetermined and computed independently on the discrete mesh. It was found in the present study that the terms on the left and right hand sides of (3.4) are not necessarily equal in general within the framework of the anelastic solver EULAG. In fact, significant errors of the discrete GMCL (3.4) can occur for certain applications. These errors of the discrete GMCL (3.4) lead to errors in the MPDATA solution. Hence, special schemes have to be designed to satisfy (3.4). This will be the topic of the subsequent Section 3.3.

[1]Strictly speaking, the classical upwind scheme assumes the flux $\rho^* \overline{v}^{*\,I}$ at time level $\overline{t}^n$, and not at $\overline{t}^{n+1/2}$.

Next, the $IORD = 2$ variant of the MPDATA scheme is investigated. It is postulated that the discrete GMCL (3.4) is exactly satisfied. The operator $\mathcal{A}$ now executes (2.30) for two iterations. The first iteration is again the upwind scheme with the advective velocity $\overline{\mathbf{v}}^*$, and this is followed by a corrective upwind step using the pseudo-velocity (2.34) in (2.30). In the $IORD = 2$ scheme, the intermediate solution after completion of the first iteration is

$$\psi_{\mathbf{i}}^{(1)} = \frac{\widetilde{\psi}}{\rho_{\mathbf{i}}^{*n}} \left\{ \rho_{\mathbf{i}}^{*n} - \sum_{I=1}^{\mathrm{N}} \overline{\lambda}^I \left((\rho^* \overline{v}^{*I})_{\mathbf{i}+1/2\mathbf{e}^I}^{n+1/2} - (\rho^* \overline{v}^{*I})_{\mathbf{i}-1/2\mathbf{e}^I}^{n+1/2} \right) \right\} . \tag{3.5}$$

As ρ^* is time-dependent, a non-uniform intermediate solution $\psi^{(1)}$ which differs locally by a factor of ρ^{*n+1}/ρ^{*n} from the uniform field $\widetilde{\psi}$ is obtained. For the subsequent second MPDATA iteration, this intermediate value $\psi^{(1)}$ then generally yields a non-zero pseudo-velocity field $\mathbf{V}^{(2)}$ when it enters the formula (2.33). Altogether, the complete algorithm (2.29)-(2.33) for $IORD = 2$, does not maintain the uniform field $\widetilde{\psi}$. This analysis reveals that the default MPDATA scheme, as stated in Section 2.3, does not account for the transport compatibility with the GMCL (3.2). Moreover, this incompatibility of the scheme also holds if the postulated validity of the discrete GMCL (3.4) is abandoned. As discussed in the previous paragraph, even the $IORD = 1$ variant of the scheme does not maintain the uniform scalar field $\widetilde{\psi}$ in that case.

Extension of the scheme

MPDATA offers a variety of options extending the basic algorithm as presented in Section 2.3, see Smolarkiewicz (1984); Smolarkiewicz and Clark (1986); Smolarkiewicz and Margolin (1998). These options are generally expressed by different forms of the error-compensating pseudo-velocities in the scheme. Fundamentally, all pseudo-velocity formulae have in common that they can be derived on the basis of a rigorous truncation error analysis of the FT discretisation (2.25). None of the derived pseudo-velocity expressions and resulting schemes, however, admit an advective scalar transport that provides compatibility with the GMCL (3.4) in time-dependent generalised coordinates.

In the following, an heuristic argumentation is used to modify MPDATA for compatibility with the GMCL (3.4). The approach modifies the existing pseudo-velocity formulae in MPDATA to provide the preservation of a uniform scalar field ψ under arbitrary time-dependent generalised coordinates. These modified pseudo-velocity

formulae differ from the original ones derived from the formal truncation error analysis. However, as will be demonstrated by means of numerical tests, the MPDATA scheme with the modified pseudo-velocities maintains the second-order accuracy of the original scheme.

Assuming the validity of (3.4), the previous discussion revealed that the $IORD=1$ variant of MPDATA maintains a uniform field $\widetilde{\psi}$. A small modification of the functional arguments used to calculate the pseudo-velocity (2.33), retains the property for the $IORD>1$ variants as well. The preservation of a uniform field $\widetilde{\psi}$ with the general MPDATA scheme is achieved by using pseudo-velocity expressions that are isomorphic to the original ones, e.g. (2.34), but the value for the current iterate $\psi^{(k-1)}$ redefined as

$$\widehat{\psi}_{\mathbf{i}}^{(k-1)} := \psi_{\mathbf{i}}^{(k-1)} \left(\frac{\rho_{\mathbf{i}}^{*n}}{\rho_{\mathbf{i}}^{*n+1}} \right) \ , \tag{3.6}$$

so that the modified pseudo-velocity function (2.33) becomes

$$V^{I\,(k)} = V^I \left(\mathbf{V}^{(k-1)}, \widehat{\psi}^{(k-1)}, \overline{\nabla}\widehat{\psi}^{(k-1)}, \rho^{*n}, \rho^{*n+1} \right) \ . \tag{3.7}$$

This means the pseudo-velocity (3.7) is calculated with the full solution of the respective lower-order iteration according to (2.29) instead of using the intermediate solution $\psi^{(k-1)}$ from (2.30). Note, the modification applies only in the determination of the pseudo-velocity, while the transported quantities in the flux scheme (2.30) remain unchanged. Now, applying the scheme (2.29)-(2.32) and (3.7) with an initially uniform distribution $\psi^n \equiv \widetilde{\psi}$, yields a field

$$\widehat{\psi}_{\mathbf{i}}^{(1)} = \frac{\widetilde{\psi}}{\rho_{\mathbf{i}}^{*n+1}} \left\{ \rho_{\mathbf{i}}^{*n} - \sum_{I=1}^{\mathrm{N}} \overline{\lambda}^I \left((\rho^* \overline{v}^{*I})_{\mathbf{i}+1/2\mathbf{e}^I}^{n+1/2} - (\rho^* \overline{v}^{*I})_{\mathbf{i}-1/2\mathbf{e}^I}^{n+1/2} \right) \right\} \tag{3.8}$$

that enters the pseudo-velocity (3.7). This field $\widehat{\psi}^{(1)}$ is equal to the uniform solution of the complete $IORD=1$ variant of MPDATA. Because the pseudo-velocity expressions always calculates differences of the input field, i.e. now $\widehat{\psi}^{(1)}$, this results in a zero (i.e. with machine precision) corrective velocity $\mathbf{V}^{(2)}$. As a consequence, there is no further contribution to the flux divergence in (2.30), although the intermediate solution $\psi^{(1)}$ that enters (2.30) may be non-uniform. This property of the scheme continues to be valid for an arbitrary number of corrective iterations $IORD-1$. In summary, given the pseudo-velocity by the functional form (3.7) (instead of the original form (2.33)) and the validity of the discrete GMCL (3.4), the MPDATA scheme achieves exact preservation of a uniform advected field ψ, under arbitrary

time-dependent generalised coordinates.

As a final remark, note that in the case of time-independent coordinates, the newly proposed scheme (2.29)-(2.32) and (3.7) automatically reduces to the original algorithm for static coordinates. Then, the generalised density ρ^* is not a function of time $\bar{t}$, i.e. $\rho^{*n} \equiv \rho^{*n+1} \equiv \rho^*$, and consequently $\widehat{\psi}^{(k-1)} \equiv \psi^{(k-1)}$ in (3.6), giving identical expressions for either (3.7) or (2.33), respectively. For the uniform initial field $\widetilde{\psi}$, (3.5) or (3.8) then results in

$$\widehat{\psi}^{(1)}_{\mathbf{i}} \equiv \psi^{(1)}_{\mathbf{i}} \equiv \frac{\widetilde{\psi}}{\rho^*_{\mathbf{i}}} \left\{ \rho^*_{\mathbf{i}} - \sum_{I=1}^{\mathrm{N}} \overline{\lambda}^I \left((\rho^* \overline{v}^{s\,I})^{n+1/2}_{\mathbf{i}+1/2\mathbf{e}^I} - (\rho^* \overline{v}^{s\,I})^{n+1/2}_{\mathbf{i}-1/2\mathbf{e}^I} \right) \right\} . \tag{3.9}$$

Due to the anelastic divergence condition (2.3c), (3.9) shows $\widehat{\psi}^{(1)}_{\mathbf{i}} \equiv \psi^{(1)}_{\mathbf{i}} \equiv \widetilde{\psi}$. Therefore, the original and the newly proposed schemes allow for a mass-compatible advective transport under time-independent coordinates.

Asymptotic accuracy of MPDATA applying the redefined pseudo-velocities

The above considerations resulted in a modified version of MPDATA through an examination of the special case when the advected field ψ is uniform in space. Generally, the field ψ varies in space and in time, and it is necessary to examine whether the proposed modifications of the pseudo-velocity expressions as given by (3.7) retain the accuracy of the original form (2.33). Recall that the formal truncation error analysis results in a corrective pseudo-velocity of the form (2.33). The modified form (3.7) results solely from the requirement to integrate MPDATA consistently with the discrete GMCL (3.4). Therefore, basic numerical experiments will examine the asymptotic accuracy of the MPDATA solutions using the redefined pseudo-velocities (3.7) (referred to as scheme R in the following) versus applying the original form of the pseudo-velocities (2.33) (referred to as O).

For these numerical experiments, the one-dimensional advective conservation law (2.24) under assumption of a uniform basic-state density ρ_b and flow velocity u is solved with MPDATA in a domain $0 \leq x \leq 20$, subject to periodic boundary conditions, and in time $0 \leq t \leq T$. Here, all variables are dimensionless. A moving

mesh is analytically prescribed using the following mapping function[1]

$$X\,(\overline{X}, S_f) = 1/7\,\{\,\overline{X}\,(15 - 8S_f^{-1}) - \overline{X}^3\,(1 - S_f^{-1})(80 - \overline{X}\,(120 - 48\,\overline{X}\,))\}\ , \quad (3.10)$$

whereupon $0 \leq X, \overline{X} \leq 1$ are normalised physical and computational coordinates, respectively. The symbol S_f^{-1} represents a time-variable (inverse) mesh stretching factor. It is specified as $S_f^{-1}(t) = 1.0 - \gamma\,\sin^2(2\pi_c\,t/T_0)$, setting $\gamma = 0.75$ and an oscillation period $T_0 = 10$. Application of the mapping function (3.10) results in a discrete mesh with periodically increased resolution around the centre of the domain at $x = 10$. The smallest grid increment attained is one fourth of the increment size at uniform resolution in one cycle. Note, the above specification of the mesh movement in this configuration is solely for the purpose of solver validation.

The basic experimental design of the accuracy test follows that in Smolarkiewicz and Grabowski (1990). The constant-coefficient advection with the physical velocity $u(t, x) = 1.0$ under a static uniform mesh of Smolarkiewicz and Grabowski (1990) is extended here to a variable-coefficient advection with the contravariant velocity $\overline{u}^*$ due to the oscillating mesh (3.10). Note, here the mesh velocity $(\partial x/\partial \overline{t})$ is derived analytically from (3.10). The initial condition for the transported scalar field ψ in (2.24) is the Gaussian distribution

$$\psi(0, x) = \psi_0 \ + \ \frac{1}{\sigma\sqrt{2\pi_c}} \exp\left(\frac{-r^2}{2\sigma^2}\right)\ , \quad (3.11)$$

where $r = (x - x_0)$, and the parameters are set to $\sigma = 2$, $x_0 = 10$, $\psi_0 = 0$. An integral measure of the error is obtained at the final simulation time T by means of

$$E(\mathcal{C}_{max}, \delta\overline{x}) = \frac{1}{T}\left(\sum_{i=1}^{\mathrm{N}_x}(\psi_{_E}(T, x_i) - \psi(T, x_i))^2/\mathrm{N}_x\right)^{1/2}\ , \quad (3.12)$$

where $\psi_{_E}(T, x_i)$ and $\psi(T, x_i)$ are the analytical and numerical solution at position x_i. The spatial number of grid points is given by N_x. The described configuration is then reapplied to evaluate the asymptotic convergence of the algorithmic formulations O and R. For each of the formulations O and R, the error $E(\mathcal{C}_{max}, \delta\overline{x})$ is determined for a range of maximum Courant numbers $0.05 \leq \mathcal{C}_{max} \leq 0.95$ with increment $\Delta = 0.05$, and eight times successively refined spatial mesh increments $\delta\overline{x}$

[1]The adopted analytical mapping functions in this work belong to an entire suite of, mostly single-target, mesh adaptation functions that offer applicability for various geometrical configurations and boundary conditions. They were developed by J.M. Prusa in the framework of Prusa and Smolarkiewicz (2003); Prusa and Gutowski (2006).

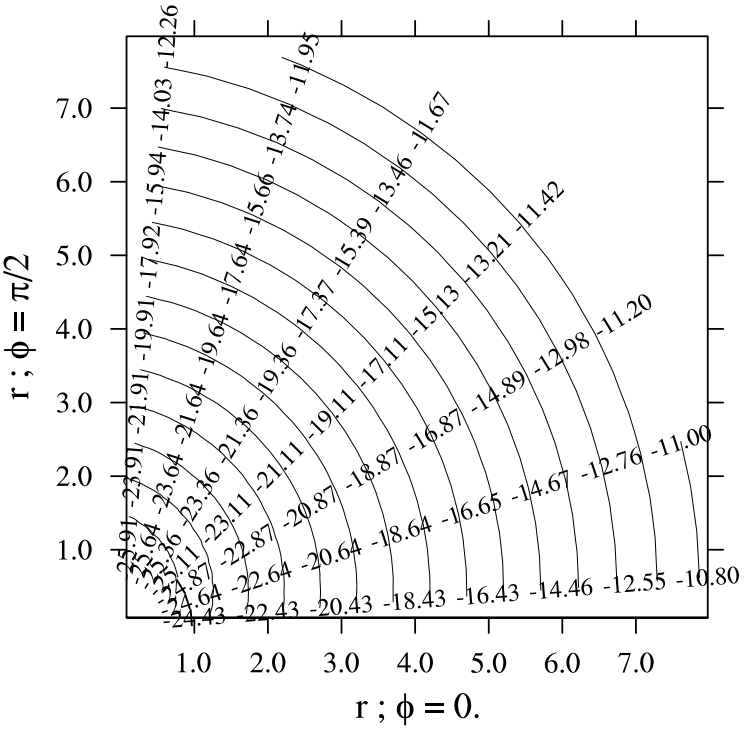

(a)

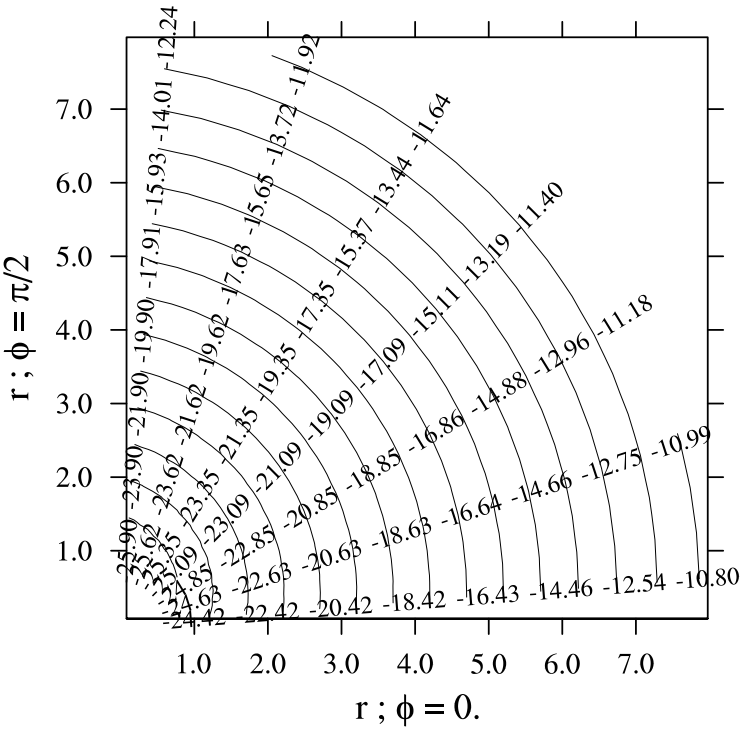

(b)

Figure 3.1: Examination of the asymptotic accuracy for the MPDATA solution under a moving mesh. Two different versions of MPDATA are compared: (a) Original form of the pseudo-velocities (2.33). (b) Redefined form of the pseudo-velocities with the application of the density-correction factor defined by (3.6) and (3.7). Isolines of $\log_2(E)$ in a polar system of coordinates that maps the varying spatial resolutions $\delta\overline{x}$ and Courant numbers $\mathcal{C}_{max}$ upon the radius r and the polar angle ϕ, respectively. Also given are rays of numerical values of $\log_2(E)$ along the radius r at constant Courant numbers $\mathcal{C}_{max} \in (0.05, 0.20, 0.35, 0.50, 0.65, 0.80, 0.95)$.

by a factor of 2, i. e. $\delta\overline{x} = (\delta\overline{x}_8/2^i)$ and $(i = 1, 8)$, while $\delta\overline{x}_8 = 0.4$ is the largest grid increment employed in the test. This specified configuration requires a total number of 152 simulations for every single formulation O and R. The resulting error surfaces are depicted in Figure 3.1. Displayed are isolines of $\log_2(E)$ in a polar system of coordinates, for which the radius and the polar angle are specified as $r = \log_2(\delta\overline{x}/\delta\overline{x}_8)$ and $\phi = \mathcal{C}_{max}\,(\pi_c/2)$, respectively.

Figure 3.1 demonstrates the obtained asymptotic accuracy of MPDATA using the original O (a) and the redefined R (b) pseudo-velocities. Numerical values of $\log_2(E)$ along rays of constant polar angle ϕ asymptotically decrease in increments of $\approx$ -2 as the resolution increases from $r = 8$ to $r = 1$. Recall that the size of the grid increment $\delta\overline{x}$ is halved for every output of $\log_2(E)$ along each ray, which proves $E \sim (\delta\overline{x}^2, \delta\overline{t}^2)$ for $\delta\overline{x}, \delta\overline{t} \to 0$.

Stability of MPDATA with the redefined pseudo-velocities

The stability properties of MPDATA using the redefined pseudo-velocities (3.7) is addressed briefly. Properly bounded generalised Courant numbers $|\mathbf{V}^{(1)}| \leq 1$ for the first upwind step ensure that the corrective pseudo-velocities remain bounded in the original scheme, see Smolarkiewicz (1984); Smolarkiewicz and Margolin (1998). Given the basic pseudo-velocity (2.34) in one dimension for simplicity (i.e. just the first line in the formula (2.34)), the bracketed expression with $|V^{1\,(1)}| \leq 1$ in (2.34) is restricted to the interval $[-1, 1]$. Then $|V^{1\,(2)}| \leq 1$ is assured if

$$A^{(1)}_{i+1/2} =: \frac{\psi^{(1)}_{i+1} - \psi^{(1)}_i}{\psi^{(1)}_{i+1} + \psi^{(1)}_i} \in [-1, 1]\ ; \tag{3.13}$$

see Smolarkiewicz (1984) for a more detailed discussion. Accordingly, the stability properties with the redefined pseudo-velocities (3.7) are maintained if

$$\widehat{A}^{(1)}_{i+1/2} =: \frac{\widehat{\psi}^{(1)}_{i+1} - \widehat{\psi}^{(1)}_i}{\widehat{\psi}^{(1)}_{i+1} + \widehat{\psi}^{(1)}_i} \in [-1, 1]\ . \tag{3.14}$$

Both conditions (3.13) and (3.14) are satisfied due to the positivity of the preceding upwind iteration and of the generalised density ρ^*.

3.3 Discrete generalised anelastic mass conservation

The previous Section 3.2 revealed in which way the MPDATA scheme can be modified to preserve (with machine precision) a uniform advected scalar field ψ under moving meshes. It was discovered that preserving the uniform scalar field requires the incorporation of the density correction factor (ρ^{*n}/ρ^{*n+1}) according to (3.6) in the MPDATA pseudo-velocities (3.7). However, it was also explained that a second factor is important to preserve the uniform scalar field – the validity of the discrete GMCL (3.4). It was shown that even the $IORD=1$ variant of the MPDATA scheme for the transport of the uniform field $\widetilde{\psi}$ as given in (3.3) only maintains the uniformity of $\widetilde{\psi}$ if the discrete GMCL (3.4) is satisfied.
Here, it is demonstrated that the validity of the discrete GMCL (3.4) is not ensured in the anelastic solver EULAG of Chapter 2. In the sub-Sections 3.3.1 and 3.3.2, two distinct methods are proposed to ensure validity of the discrete GMCL in the framework of the anelastic solver EULAG. Numerical experiments that evaluate the developments in this section and those of the previous Section 3.2 are presented in the subsequent Section 3.4.

The particular analytical and numerical formulation of the anelastic solver explained in Sections 2.1 and 2.2 implies explicit control over the residual error of the anelastic divergence constraint (2.3c), or similarly in a vector notation

$$\overline{\nabla}\cdot\,(\rho^{*}\overline{\mathbf{v}}^{s})=0\ . \tag{3.15}$$

The control over (3.15) is implemented by means of the exact projection for the solenoidal velocity $\overline{\mathbf{v}}^{s}$ underlying the elliptic boundary value problem (2.23). Given (3.15) together with the relation between the contravariant, solenoidal and mesh velocities (2.5), repeated here in the vector notation

$$\overline{\mathbf{v}}^{*}=\overline{\mathbf{v}}^{s}+\frac{\partial\overline{\mathbf{x}}}{\partial t}=:\overline{\mathbf{v}}^{s}+\overline{\mathbf{v}}^{g}\ , \tag{3.16}$$

the GMCL (3.2) results in

$$\frac{\partial\rho^{*}}{\partial\bar{t}}+\overline{\nabla}\cdot\,(\rho^{*}\overline{\mathbf{v}}^{g})=0\ . \tag{3.17}$$

This equation describes the advection of the generalised density ρ^{*} with the mesh velocity $\overline{\mathbf{v}}^{g}$ in transformed space $\mathbf{S}_{t}$. Equation (3.17) includes effects solely due to

the time-dependent (i.e. moving) coordinates and is formally independent of the physical flow. For a uniform basic-state density ρ_b, (3.17) is equivalent to the GCL (2.16). Hence, (3.17) can be considered as a generalised GCL for the anelastic system.
In summary, the anelastic solver of Section 2.2 implies control over the divergence constraint (3.15). The issue in the anelastic solver of Section 2.2 is that under moving meshes no control over errors of (3.17) is implemented. The errors of (3.17) result in errors of the GMCL (3.2).

In accordance with the discrete GMCL (3.4), the discrete representation of (3.17) is given as

$$\rho_{\mathbf{i}}^{*n+1} = \rho_{\mathbf{i}}^{*n} - \sum_{I=1}^{\mathrm{N}} \overline{\lambda}^I \left((\rho^* \overline{v}^{g\,I})^{n+1/2}_{\mathbf{i}+1/2\mathbf{e}^I} - (\rho^* \overline{v}^{g\,I})^{n+1/2}_{\mathbf{i}-1/2\mathbf{e}^I} \right) . \tag{3.18}$$

One may anticipate that the deviations or errors of the generalised GCL (3.18) depend strongly on the method to calculate the fluxes $(\rho^* \overline{\mathbf{v}}^g)^{n+1/2}$ at the local cell boundaries. In Section 4.4, the solution-adaptive moving mesh NFT flow solver is presented. There, a procedure for the calculation of the generalised contravariant fluxes $(\rho^* \overline{\mathbf{v}}^*)^{n+1/2}$ in MPDATA is proposed that is particularly advantageous for minimising the errors to (3.18). Unless otherwise noted, all simulations in this thesis employ the proposed method to approximate the generalised contravariant mass flux $(\rho^* \overline{\mathbf{v}}^*)^{n+1/2}$ in MPDATA. See Section 4.4 for the presentation of the procedure, and Sections 5.1 and 5.3 for associated test calculations.

The magnitude of the deviations from (3.18) and their impact on the error of the advection scheme depends strongly on the specific application. Basically, it was found in the numerical experiments performed for this thesis, that the deviations from the discrete generalised GCL (3.18) increase with a stronger, faster and more irregular deformation of the mesh. For general adaptive moving mesh applications, it is therefore required to incorporate explicit control over the deviations of the GCL (3.18) in order to avoid subsequent errors in the MPDATA solution. In the following two subsections, two distinct methods are presented for this purpose.

3.3.1 Diagnostic approach for the GMCL

In the discrete GMCL (3.4), the generalised densities ρ^{*n} and ρ^{*n+1} are diagnostic quantities that are predetermined from the knowledge of the mesh. Therefore, the only degree of freedom in the GMCL (3.4) within the solution algorithm is given by the contravariant fluxes $(\rho^*\overline{\mathbf{v}}^*)^{n+1/2}$ at the local cell boundaries, which are calculated to $\mathcal{O}(\delta\bar{t}^2)$ from either a linear or nonlinear predictor scheme, cf. (2.35) and Section 4.4. Motivated by the basic solution procedure that underlies the anelastic solver (see Section 2.2), a diagnostic approach based on a projection method (Chorin, 1968) is developed to ensure compatibility of the MPDATA integration with the GMCL. To the author's knowledge, the idea presented in the following has not been applied in this context before.

For compactness, the discussion is continued here by using the semi-discretised representation as in (2.25). Then, the form of the GMCL (3.2) consistent with the FT approximation of (2.25) becomes

$$\frac{(\rho^{*n+1}-\rho^{*n})}{\delta\bar{t}} + \overline{\nabla}\cdot\ (\rho^*\overline{\mathbf{v}}^*)^{n+1/2} = 0\ . \tag{3.19}$$

The idea is now that for prescribed quantities ρ^{*n} and ρ^{*n+1}, i.e. a given FT derivative of the generalised density ρ^*, the generalised contravariant mass flux $(\rho^*\overline{\mathbf{v}}^*)^{n+1/2}$ may be corrected to satisfy (3.19). Given a preliminary $\mathcal{O}(\delta\bar{t}^2)$ guess $\widehat{\mathbf{v}}$ at time $\bar{t}^{n+1/2}$ for $\hat{\mathbf{v}}=\rho^*\overline{\mathbf{v}}^*$, a potential ϕ is introduced according to

$$\left\{\hat{\mathbf{v}} = \widehat{\mathbf{v}} - \rho^*\ \widetilde{\mathbf{G}}^T\widetilde{\mathbf{G}}\overline{\nabla}\phi\right\}_{\mathbf{i}}^{n+1/2}\ . \tag{3.20}$$

Starting from $\mathbf{v}=\mathbf{v}_*-\widetilde{\mathbf{G}}\,\overline{\nabla}\phi$ for the physical velocity $\mathbf{v}$ (where $\mathbf{v}_*$ is a first guess for $\mathbf{v}$), (3.20) is found by insertion into the expression for the generalised contravariant mass flux $\rho^*\overline{\mathbf{v}}^*$, see e.g. Smolarkiewicz and Margolin (1994) for a related discussion. Ultimately, inserting (3.20) into (3.19) leads to an elliptic boundary value problem for ϕ of the form

$$\left\{-\frac{\delta\bar{t}}{\rho^{*n+1/2}}\ \left(\frac{(\rho^{*n+1}-\rho^{*n})}{\delta\bar{t}} + \overline{\nabla}\cdot\left(\widehat{\mathbf{v}}-\rho^*\ \widetilde{\mathbf{G}}^T\widetilde{\mathbf{G}}\ \overline{\nabla}\phi\right)^{n+1/2}\right)\right\}_{\mathbf{i}} = 0\ . \tag{3.21}$$

Again, multiplication by the factor $(-\delta\bar{t}/\rho^*)$ has been applied in (3.21) for numerical reasons, cf. the statements after the equation (2.23) in Section 2.2.
Unlike the elliptic problem (2.23) that arises in the solution of the anelastic system

(2.3), the problem (3.21) must be solved at the intermediate time level $\overline{t}^{n+1/2}$ in order to maintain the symmetry with regard to the FT derivative of ρ^*. By design of the FT model all fields except the generalised contravariant mass flux $\rho^*\overline{\mathbf{v}}^*$ exist at the full, i.e. non-staggered, time levels. This fact entails to derive the metric coefficients contained in $\widetilde{\mathbf{G}}$, the generalised density ρ^*, plus all variables needed in the specification of the boundary conditions for (3.21) at the intermediate time level $\overline{t}^{n+1/2}$ with second-order accuracy. Regarding the derivation of $\widetilde{\mathbf{G}}$ and ρ^* at $\overline{t}^{n+1/2}$, the reader is referred to the discussion in the last part of Section 4.4.

For compatibility of the advection algorithm, the formulated elliptic problem (3.21) is solved subject to either periodic or Dirichlet boundary conditions for the generalised contravariant mass flux $\rho^*\overline{\mathbf{v}}^*$ at the intermediate time level $\overline{t}^{n+1/2}$. Subsequent experiments will apply a GCR iterative solver (Eisenstat et al., 1983; Smolarkiewicz and Margolin, 1994) for (3.21). A physically meaningful stopping criterion for the GCR iterative solver in the solution of (3.21) is formulated as

$$\|r_{gmcl}\|_\infty = \left\| \frac{\delta\overline{t}}{\rho^{*n+1/2}} \left(\frac{(\rho^{*n+1}-\rho^{*n})}{\delta\overline{t}} + \overline{\nabla}\cdot(\rho^*\overline{\mathbf{v}}^*)^{n+1/2} \right) \right\|_\infty \leq \epsilon \; ; \tag{3.22}$$

please confer to the discussion after the equation (2.23) in Section 2.2 and the references given there. Note that throughout this thesis the error of the discrete GMCL (3.4) is quantified using (3.22).

3.3.2 Prognostic approach for the generalised GCL

Another approach that is adopted here aims to ensure compatibility with the discrete GMCL (3.4) using a prognostic procedure for the generalised density ρ^*. Specifically, the procedure employs the discrete generalised GCL (3.18) as an auxiliary prognostic equation to correct ρ^{*n+1} on the left-hand side (LHS) of (3.18). Note, the prognostic procedure actually leads to an over-specified mathematical problem in the framework of the present solver formulation where ρ^{*n+1} is a known quantity. In contrast, the diagnostic approach proposed in the preceding subsection corrects the generalised contravariant fluxes $(\rho^*\overline{\mathbf{v}}^*)^{n+1/2}$ which are given from the approximate predictor scheme. Nonetheless, the idea of the prognostic approach is obvious, as it directly satisfies (3.18) at every time step to machine precision by design. Because in the anelastic solver the divergence constraint (3.15) is controlled by the projection underlying the elliptic pressure equation (2.23), the described prognostic

procedure enforces the compatibility of MPDATA with the discrete GMCL (3.4).

If the basic-state density ρ_b in the anelastic system (2.3) is uniform, then (3.18) is identical to the discrete version of the GCL (2.16) as given by

$$\overline{G}_{\mathbf{i}}^{n+1} = \overline{G}_{\mathbf{i}}^{n} - \sum_{I=1}^{\mathrm{N}} \overline{\lambda}^{I} \left((\overline{G}\,\overline{v}^{g\,I})_{\mathbf{i}+1/2\mathbf{e}^{I}}^{n+1/2} - (\overline{G}\,\overline{v}^{g\,I})_{\mathbf{i}-1/2\mathbf{e}^{I}}^{n+1/2} \right) \ . \tag{3.23}$$

The basic idea of applying the discrete GCL in a prognostic manner along with the associated flux-form advection scheme to avoid errors introduced by a moving mesh was first proposed in Thomas and Lombard (1979). Nowadays, the procedure is fairly standard in computational fluid dynamics, see e.g. Drikakis and Rider (2005), although the detailed implementation can vary significantly with the formulation of the numerical solver. In the present work, the GCL (3.23) as discussed in Thomas and Lombard (1979) has been generalised to (3.18) in order to account for the non-uniform basic-state density ρ_b in the solution of the anelastic system (2.3).

Concerning the specific implementation of the prognostic approach, the contravariant fluxes $(\rho^{*}\overline{\mathbf{v}}^{*})^{n+1/2}$ in the generalised GCL (3.18) are always given from either the linear or nonlinear predictor schemes. Then, the obvious way applying the GCL (3.18) is to initialise the generalised density ρ^{*n} on the RHS with its diagnostic value at $\overline{t}^{0}$ and to integrate the equation for ρ^{*} in time, as given for instance in Chou and Fringer (2009). In fact, it has been found that this scheme is only applicable to simple moving meshes, e.g. the prescribed oscillating mesh applied in the experiments of the subsequent Section 3.4. Note, Chou and Fringer (2009) have also applied a simple oscillating mesh only. For complicated solution-adaptive numerically-generated moving meshes as considered in Chapter 5, it has been found that the scheme is not applicable in this form. The reason is that the prognostically-computed generalised density ρ^{*} from the GCL (3.18) may locally depart strongly from its diagnostic value after a certain integration time, and as a consequence, large errors are introduced in the MPDATA solution (not shown). In addition, the prognostic numerical scheme (3.18) does not assure the generalised density ρ^{*} to remain positive definite, which represents a severe issue for the stability of the overall MPDATA integration. The only implementation of the prognostic approach that has been found to provide stable and accurate solutions for general moving meshes is to reinitialise the generalised density ρ^{*n} on the RHS of the GCL (3.18) at every time step $\overline{t}^{n}$ with its known diagnostic value. This specific implementation is applied throughout the present thesis.

3.4 Scalar advection experiments with a prescribed moving mesh

Idealised two-dimensional scalar advection numerical experiments are performed to analyse and compare the various MPDATA implementations presented in Sections 3.2 and 3.3. Here, a oscillating moving mesh is prescribed using analytical functions for simplicity of the examination. Later in Section 5.3, the subject is further investigated in the context of general solution-adaptive numerically-generated moving meshes. Table 3.1 summarises the various schemes that are applied in the numerical experiments.

	Density-correction in MPDATA	Treatment of GCL/GMCL
OS	No	standard
OP	No	prognostic
RS	Yes	standard
RP	Yes	prognostic
RD	Yes	diagnostic

Table 3.1: Summary of the various MPDATA implementations compared in the numerical experiments. The first column states whether the density-correction factor (3.6) is applied in the redefined pseudo-velocities (3.7) of MPDATA (denoted as R), or the original form of the pseudo-velocities (2.33) is used (denoted as O). The second column describes the treatment of the errors associated with the discrete GMCL: either the use of the quantities ρ^{*n+1}, ρ^{*n} and $(\rho^*\overline{\mathbf{v}}^*)^{n+1/2}$ in the GMCL as obtained from the *standard* methods in the solution algorithm (denoted as S), the *diagnostic* approach based on a projection method (denoted as D), and the *prognostic* approach (denoted as P). See Sections 3.2 and 3.3 for the explanation of the various schemes.

Experimental design

The prototype conservation law (2.24) under the assumption of a uniform basic-state density ρ_b is solved in a two-dimensional domain $0 \leq x, y \leq 20$, subject to periodic boundary conditions in x and y, and for an integration time $0 \leq t \leq T$. Again, all variables are assumed to be dimensionless.

In order to test the solution behaviour of various MPDATA implementations under a moving mesh, an oscillating mesh is prescribed here using the mapping function

$$X\left(\overline{X}, \overline{Y}, S_f\right) = (1-\overline{Y}^2)^2 \left[S_f^{-1}\overline{X} + (1-S_f^{-1})\,\overline{X}^5\right] + \left(1-(1-\overline{Y}^2)^2\right)\overline{X} \quad (3.24)$$

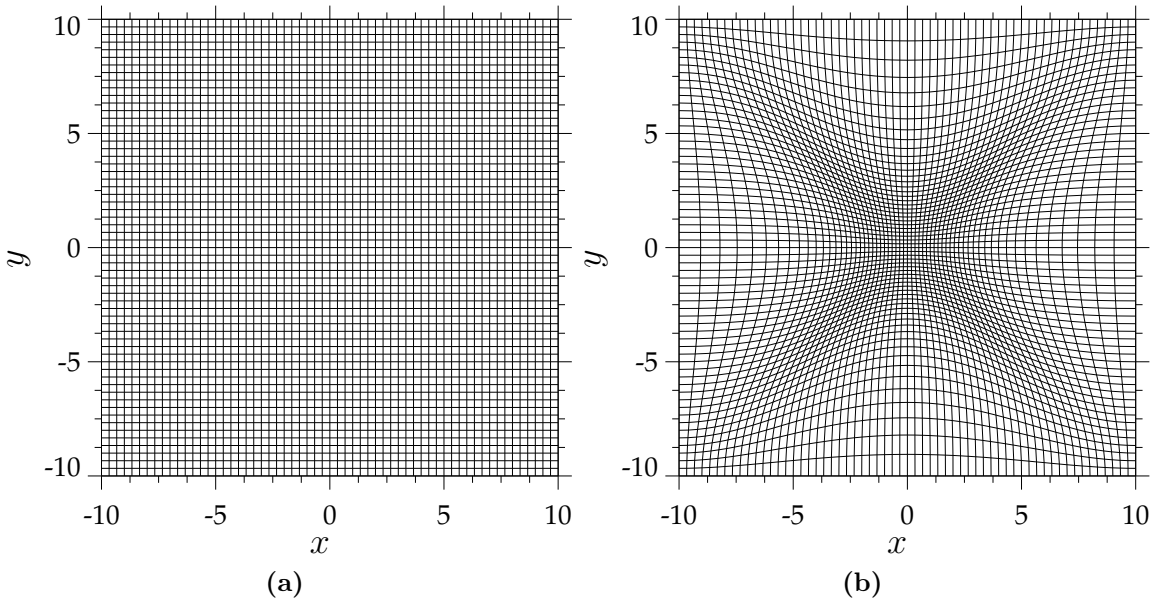

Figure 3.2: Illustration of the simple oscillating mesh defined by the mapping (3.24) analogously for the x and y coordinates. The figure in (a) shows the mesh in the initial uniform, i.e. undeformed, state, while (b) shows the mesh in the state of maximal deformation for $\gamma = 0.5$.

analogously for the normalised X and Y coordinates. The inverse mesh stretching factor S_f^{-1} is specified as $S_f^{-1}(t) = 1.0 - \gamma \sin^2(2\pi_c\, t/T_0)$, setting $\gamma = 0.5$ and an oscillation period $T_0 = 20$. Figure 3.2 shows an illustration of the resulting mesh.

In order to ensure the divergence constraint (3.15) to be satisfied with machine precision in discrete space over the entire course of the simulation, the components of the solenoidal velocity $\overline{\mathbf{v}}^s$ are evaluated in finite-difference space by means of a streamfunction χ according to

$$\overline{u}^s = \frac{1}{\rho^*}\frac{\partial \chi}{\partial \overline{y}}\ , \qquad\qquad \overline{v}^s = -\frac{1}{\rho^*}\frac{\partial \chi}{\partial \overline{x}}\ , \tag{3.25}$$

in all advection experiments that follow. For the present test, the streamfunction is specified as $\chi(t, x, y) = x + y$, equivalent to a uniform south-westerly flow field $\mathbf{v} \equiv (1, 1)^T$.

The mesh increments are chosen as $\delta\overline{x} = \delta\overline{y} = 0.4$, and the time step $\delta\overline{t}$ is continuously adapted to maintain a constant maximum Courant number of $\mathcal{C}_{max} = 0.5$.

scheme(-ϵ)	L_1	L_∞	$\|r_{gmcl}\|_\infty$	NIT	$\int \psi$
OS	2.08×10^{-4}	6.19×10^{-3}	3.84×10^{-6}	-	2.46×10^{-15}
OP	2.08×10^{-3}	6.15×10^{-3}	-	-	-1.22×10^{-9}
RS	1.61×10^{-5}	8.45×10^{-5}	3.84×10^{-6}	-	1.14×10^{-15}
RP	5.70×10^{-16}	5.77×10^{-15}	-	-	0.0
RD-10^{-6}	3.53×10^{-6}	8.21×10^{-6}	1.00×10^{-6}	1	-2.27×10^{-15}
RD-10^{-9}	4.66×10^{-8}	8.25×10^{-8}	1.00×10^{-9}	13	-1.89×10^{-16}
RD-10^{-12}	1.31×10^{-11}	3.45×10^{-11}	1.00×10^{-12}	66	5.69×10^{-16}
RD-10^{-15}	3.95×10^{-15}	1.73×10^{-14}	1.00×10^{-15}	177	0.0

Table 3.2: Comparison of the various schemes given in Table 3.1 for the advection of a uniform scalar field ψ under the oscillating mesh using the basic second-order accurate MPDATA. The number following the particular scheme RD in the first column indicates the prescribed convergence threshold ϵ of the GCR iterative solver for the elliptic equation (3.21) defined according (3.22). Second and third columns: L_1 and L_∞ error norms defined as deviations of the numerical $\psi(T, \mathbf{x})$ from the analytical solution $\widetilde{\psi}$ at the final simulation time $T = 20.0$. Fourth column: actual maximum value in the simulation of the GMCL error $\|r_{gmcl}\|_\infty$ (3.22). Fifth column: average number of GCR iterations NIT over the simulation time T. Sixth column: integral conservation measure $\langle\psi\rangle/\langle\psi_{t=0}\rangle - 1$ for the transported scalar ψ at $T = 100.0$.

Advective transport of a uniform scalar distribution

A first test inspects the compatibility of the various schemes of Table 3.1 through their ability to preserve a uniform scalar field ψ under the oscillating mesh (3.24). The initial scalar field in the solution of the conservation law (2.24) is specified as $\psi(0, x, y) \equiv \widetilde{\psi} \equiv 1.0$. Table 3.2 displays the associated simulation results obtained using the basic second-order accurate MPDATA, i.e. one corrective upwind step, without FCT enhancement.

The comparison in Table 3.2 show that the largest deviations from the uniform scalar distribution are generated with OS and OP, indicated by the relatively largest L_1 and L_∞ error norms. The scheme OS represents the original algorithmic implementation of the MPDATA integration as applied in previous works[1]. In the scheme OP, the original form of the pseudo-velocities in MPDATA is combined with the prognostic correction for the generalised density ρ^* to enforce validity of the GMCL. The results for OP fully support the theoretical analysis of Section 3.2, where it was demonstrated that even with the validity of the discrete GMCL (3.4) the original form of the pseudo-velocities in MPDATA does not allow to exactly maintain a uniform transported scalar field ψ.

[1]As an aside, recall that the revised predictor scheme for the generalised contravariant mass flux $(\rho^*\overline{\mathbf{v}}^*)^{n+1/2}$ developed in Section 4.4 is applied in all schemes of Table 3.1.

The scheme RS that applies the redefined pseudo-velocities in MPDATA as developed in Section 3.2, provides L_1 and L_∞ error norms that are more than one order of magnitude lower than with the original scheme OS.

If the application of the redefined pseudo-velocities in MPDATA is combined with the prognostic approach to enforce validity of the GMCL in RP, then the L_1 and L_∞ error norms in Table 3.2 indicate preservation of the uniform transported field ψ at the order of machine precision $\sim 10^{-15}$. This result is also in complete agreement with the formula (3.8) derived in the theoretical analysis of Section 3.2.

In the algorithmic implementation RD, the application of the redefined pseudo-velocities in MPDATA is combined with the developed diagnostic approach for the GMCL. The number following the descriptor RD in the first column of Table 3.2 indicates the prescribed convergence threshold ϵ of the GCR(1) iterative solver applied to the elliptic equation (3.21), as defined according (3.22). As can be seen, the L_1 and L_∞ error magnitudes with the algorithmic implementation RD decrease persistently with a tighter convergence threshold ϵ. In fact, preservation with machine precision of the uniform transported field ψ can be achieved with NIT $= 177$ GCR(1) iterations, although such a high accuracy is generally not necessary (see below in Table 3.3). The observed error behaviour with the scheme RD is again in complete agreement with the formula (3.8) and the general discussion provided in Section 3.2.

Advective transport of a Gaussian scalar distribution

A second test inspects the various schemes of Table 3.1 for the advective transport of a general scalar field ψ, given here as a Gaussian scalar distribution. For this purpose, the preceding doubly-periodic experimental test setup with the prescribed oscillating mesh is retained, but the scalar field ψ is initialised by the function (3.11) with $r^2 = (x - x_0)^2 + (y - y_0)^2$, and the parameters set to $\sigma = 2$, $x_0 = y_0 = 10$, $\psi_0 = 1$.

Table 3.3 presents the results computed using the second-order accurate MPDATA with FCT enhancement. The values of the L_2 error norm in the second column are about twice as large for OS when compared to all other schemes RS, RP, and RD. A factor of the larger L_2 error with the scheme OS is revealed by the values for the quantity $(\min(\psi) - \psi_0)$, displayed in the third column of Table 3.3. The results for the scheme OS show a noticeable negative deviation from zero, and this deviation is significantly larger compared to all other schemes. A negative deviation

scheme(-ϵ)	L_2	$\min(\psi)-\psi_0$	$\|r_{gmcl}\|_\infty$	NIT	$\int \psi$
OS	4.62×10^{-4}	-3.70×10^{-2}	3.84×10^{-6}	-	0.0
RS	2.43×10^{-4}	-1.87×10^{-4}	3.84×10^{-6}	-	-9.35×10^{-16}
RP	2.42×10^{-4}	4.00×10^{-7}	-	-	-2.77×10^{-7}
RD-10^{-6}	2.42×10^{-4}	-2.39×10^{-5}	3.18×10^{-7}	1	9.35×10^{-16}
RD-10^{-9}	2.42×10^{-4}	3.68×10^{-7}	1.00×10^{-9}	13	9.37×10^{-15}
RD-10^{-12}	2.42×10^{-4}	4.00×10^{-7}	1.00×10^{-12}	66	1.12×10^{-15}
RD-10^{-15}	2.42×10^{-4}	4.00×10^{-7}	1.00×10^{-15}	177	-5.61×10^{-16}

Table 3.3: Advection of a Gaussian scalar distribution under the prescribed oscillating mesh using the second-order accurate MPDATA with FCT enhancement. The schemes tested are OS, RS, RP (see Table 3.1) and RD, where again the number following RD indicates the prescribed convergence threshold of the elliptic solver in the solution of (3.21). Second column: standard L_2 error norm at the final simulation time $T = 100.0$. Third column: domain minimum value of the numerical solution ψ minus the basic-state value $\psi_0 = 1.0$ at $T = 100.0$. Fourth column: actual maximum value of the GMCL residual error $\|r_{gmcl}\|_\infty$ defined by (3.22) which occurred in the simulation. Fifth column: average number of GCR(1) iterations over the simulation time T. Sixth column: integral conservation measure $\langle\psi\rangle/\langle\psi_{t=0}\rangle - 1$ for the transported scalar ψ at $T = 100.0$. Again, the mesh parameters are $\gamma = 0.5$ and $T_0 = 20.0$.

scheme(-ϵ)	L_2	$\min(\psi)$	$\|r_{gmcl}\|_\infty$	NIT	$\int \psi$
OS	3.71×10^{-4}	4.20×10^{-5}	3.84×10^{-6}	-	-3.42×10^{-15}
RS	3.70×10^{-4}	4.21×10^{-5}	3.84×10^{-6}	-	-4.37×10^{-15}
RP	3.70×10^{-4}	4.21×10^{-5}	-	-	-1.32×10^{-5}
RD-10^{-6}	3.70×10^{-4}	4.21×10^{-5}	3.18×10^{-7}	1	-2.72×10^{-15}
RD-10^{-9}	3.70×10^{-4}	4.21×10^{-5}	1.00×10^{-9}	13	-3.07×10^{-15}
RD-10^{-12}	3.70×10^{-4}	4.21×10^{-5}	1.00×10^{-12}	66	-4.96×10^{-15}
RD-10^{-15}	3.70×10^{-4}	4.21×10^{-5}	1.00×10^{-15}	177	-3.42×10^{-15}

Table 3.4: As in Table 3.3, but the results here are for the advection of the Gaussian scalar distribution with a zero background $\psi_0 = 0$ in (3.11).

in the $(\min(\psi)-\psi_0)$ from zero is also present in the results for the schemes RS and RD-10^{-6}, even though with smaller magnitudes. For all these schemes OS, RS, and RD-10^{-6}, the negative deviation of $(\min(\psi)-\psi_0)$ from zero indicates the failure of the applied FCT methodology to provide the monotonicity of the solution.

In contrast, the scheme RP, and the schemes RD with a convergence threshold lower equal than $\epsilon = 10^{-9}$, achieve full monotonicity of the solution. Simultaneously, these schemes give the lowest L_2 error values. However, it is observed that the particular scheme RP based on the prognostic approach (Section 3.3.2) suffers conservation errors of the transported scalar ψ, as given last column of Table 3.3.

Table 3.4 presents results from the same experiment as performed for the results

shown in Table 3.3, but with a zero background value $\psi_0 = 0$ of the transported scalar field ψ in (3.11). In contrast to the results of Table 3.3, the values for the L_2 error norms given here exhibit no significant difference between the different schemes. This is although the magnitudes of the residual errors $\|r_{gmcl}\|_\infty$ are identical in Table 3.3 and 3.4. The reason for this behaviour is found by inspecting the minimum values of the transported scalar variable ψ, given in the third column of Table 3.4. Due to the sign-preserving property of MPDATA, similar negative deviations from zero as observed in Table 3.3 for the quantity $(\min(\psi) - \psi_0)$, are not present here. Again, the particular scheme RP based on the prognostic approach for the GCL suffers conservation errors, while all other schemes provide conservation of the transported variable ψ with machine precision.

Further discussion and conclusions

As a consequence of the previous results, it can be stated that the incompatibility of the MPDATA advective transport with the GMCL not only affects the property of the algorithm to preserve a uniform field ψ (Table 3.2) but also the more general property of the solution monotonicity (Table 3.3). Note, the failure of the FCT methodology to provide the solution monotonicity in MPDATA originates from the loss of the monotonicity-preserving character of the underlying upwind scheme, which is due to the incompatibility with the GMCL (3.2). This conclusion has been verified on the basis further numerical experiments (not shown). In addition, the presented results highlight the general aspect of the MPDATA scalar transport (Smolarkiewicz and Szmelter, 2005) that the solution monotonicity requires compatibility with mass continuity, i.e. here with the GMCL (3.2), while the sign-preserving property of the scheme does not, cf. Tables 3.3 and 3.4).

As demonstrated, the MPDATA implementations RP and RD, which have been developed in this thesis, can be employed to ensure the required compatibility of the MPDATA scalar transport with the GMCL (3.2). The prognostic approach in the scheme RP and the diagnostic approach in the scheme RD with a convergence threshold lower equal than $\epsilon = 10^{-9}$ provide accurate solutions free of spurious (i.e. unphysical) extrema under the oscillating mesh.

However, an issue observed with the application of the implemented prognostic approach (the scheme OP and RP) is that, although in flux-form, the MPDATA integration is not exactly conservative anymore, cf. the last column in Tables 3.2, 3.3, and 3.4. Due to this shortcoming, the scheme RD is to choose over RP in the

context of the general moving mesh solver.

Unfortunately, it was not possible within the time frame of the present thesis to complete the development and testing of the diagnostic approach (Section 3.3.1) for application in the general framework of the anelastic NFT solver EULAG. Open research issues in the solution of (3.21) are the accurate formulation of Neumann boundary conditions for general flows and arbitrary moving meshes, the implementation of the associated integrability condition, along with the development of customised preconditioning of the applied GCR iterative solver. All this work is currently ongoing and will be presented elsewhere in the near future. Note, in the remaining thesis, the scheme RP based on the prognostic approach (Section 3.3.2) is used as a temporary solution to provide the required compatibility of the MPDATA integration in the context of the solution-adaptive moving mesh solver (Chapter 4). The observed conservation issue with RP is insignificant for the conducted examination in this thesis.

In Section 5.3, the subject of the compatibility of MPDATA with the GMCL is further investigated in the context of solution-adaptive numerically-generated moving meshes. There, it will be demonstrated that the magnitudes of the errors introduced by the incompatibility of the original MPDATA scheme with the GMCL are typically substantially larger than under the simple prescribed oscillating meshes considered above.

Chapter 4

Solution-adaptive moving mesh algorithm

The previous two chapters dealt with the integration of the anelastic equations (2.3) in time-dependent generalised coordinates. Given this particular model formulation, the discrete mesh can in principle be moved arbitrarily in physical space over the course of the integration, while only being subject to the regularity assumptions of the coordinate mappings (2.2) and (2.9). This capability of the model opens avenues for spatio-temporal adaptation of the mesh to increase the numerical resolution in certain sensitive regions in response to the simulated flow. In general, the use of such a *solution-adaptive moving mesh* solver can be motivated by a variety of problem-dependent conditions. Of course, the basic conception behind the approach is to reduce the errors inherent to the discrete numerical approximation of the governing continuous flow equations.

In this chapter, the implementation of the developed solution-adaptive moving mesh NFT flow solver is presented. The discussion begins in Sections 4.1 and 4.2 with the introduction of the basic mathematical apparatus underlying the present adaptive moving mesh solver. Practical aspects regarding the implementation and use of the method are discussed afterwards in Section 4.3. The last part given in Section 4.4 explains the implementation of the mesh adaptation component into the computational framework of EULAG. Therein, an algorithmic sequence of the NFT flow solver EULAG is proposed that is advantageous for applications with solution-adaptive meshes. The suggested algorithmic structure allows to incorporate the MPDATA-related developments from Chapter 3. Furthermore, it paves the way for a particularly accurate evaluation of the advective contravariant velocities under solution-adaptive moving meshes, which is also presented here.

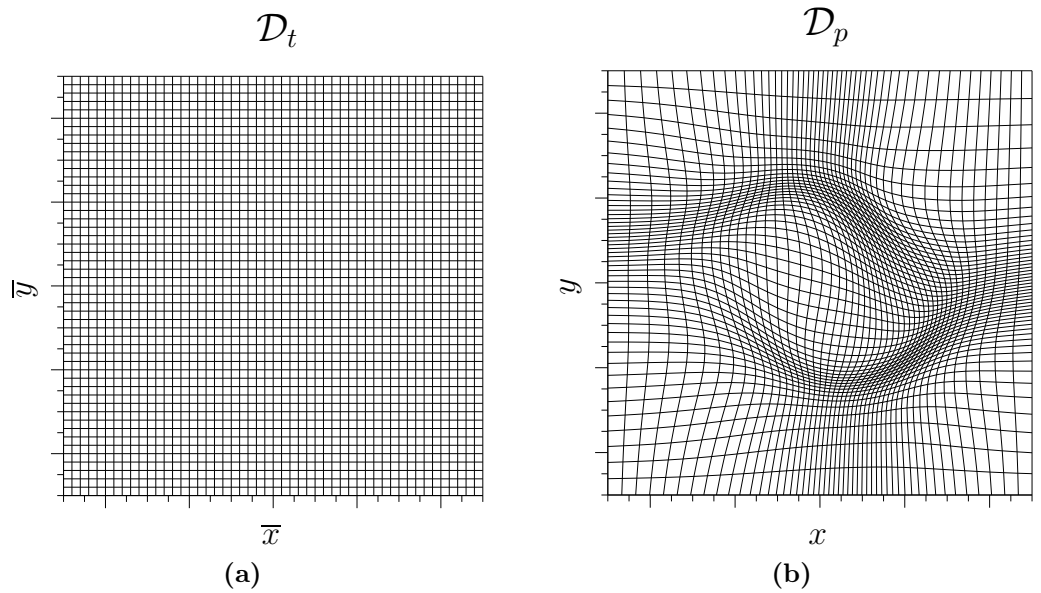

Figure 4.1: Representative mesh mapping from the computational domain $\mathcal{D}_t$ (a) into the physical domain $\mathcal{D}_p$ (b).

4.1 Conceptual approach

The solution-adaptive mesh technique in this work is based on the particular class of r-refinement (i.e. relocation- or redistribution- refinement) methods, which are also named *moving mesh methods*. These methods continuously redistribute the mesh points in space to obtain a finer resolution in sensitive regions of the evolving flow. Inherent in the method is that the the number of mesh points and their connectivity do not change during the adaptation process. This is a basic requirement for the applicability of the mesh adaptation technique in the EULAG flow solver (see Chapter 2), which relies on a conserved (structured) data arrangement.

The objective of moving mesh methods is to construct a well-defined discrete mesh $\mathcal{D}_p^h$ on the physical domain $\mathcal{D}_p$, that has the desired solution-adaptive properties. To achieve this, the approach usually resorts to the classical concept of coordinate mappings (cf. also Section 2.1): Given the fixed regular mesh geometry $\mathcal{D}_t^h$ on the computational domain $\mathcal{D}_t$ as a reference, the time-dependent irregular adaptive mesh $\mathcal{D}_p^h$ on the physical domain $\mathcal{D}_p$ is described by means of a coordinate mapping

$$(t, \mathbf{x}) \equiv (\overline{t}, \mathcal{M}(\overline{t}, \overline{\mathbf{x}})) : \quad \mathcal{D}_t \rightarrow \mathcal{D}_p \ , \tag{4.1}$$

so that the function $\mathcal{M}(\overline{t}, \overline{\mathbf{x}})$ determines the mesh. This idea is exemplified in Fig-

ure 4.1, where the mapping function $\mathcal{M}(\overline{t}, \overline{\mathbf{x}})$ assumes the general two-dimensional form $\mathcal{M} \equiv (x(\overline{x}, \overline{y}), y(\overline{x}, \overline{y}))$, at a particular time t. It is now obvious that the main task of r-adaptive mesh generation is to find the appropriate mapping function $\mathcal{M}$ that specifies $\mathcal{D}_p^h$. The following sections discuss the mathematical apparatus to manage this task.

4.2 Variational formulation

Modern methods of grid generation based on a mapping of coordinates (4.1) often rely on a variational approach. This method is attractive because it allows to combine various constraints that may be imposed to generate the mesh. For example, such constraints may concern mesh properties like smoothness, orthogonality, alignment, and adaptivity with respect to certain refinement indicators, all of which have a direct consequence on the efficacy of the employed numerical solution scheme (e.g. the advection solver MPDATA). The principal task is to chose appropriately defined functionals that incorporate the desired properties of the coordinate mappings specifying the mesh. Then, optimisation leads to a "compromise" mesh that combines the various properties involved. Typically, the corresponding Euler-Lagrange equations that minimise the constructed functionals are solved to obtain the mesh mapping. The books of Knupp and Steinberg (1994); Liseikin (1999) discuss the topic in detail.

A functional that leads to a particularly robust system of mesh equations can be formulated over the physical domain $\mathcal{D}_p$ as (Winslow, 1981; Dvinsky, 1991; Huang and Russell, 1999; Huang, 2001b)

$$\mathcal{I}[\overline{\mathbf{x}}] = \frac{1}{2} \int_{\mathcal{D}_p} \sum_{k=1}^{\mathrm{N}} (\nabla \overline{x}^k)^T \, M^{-1} \, \nabla \overline{x}^k \, d\mathbf{x} \; , \tag{4.2}$$

where k numbers the spatial dimensions N, and $(\ )^T$ is the transpose. The symbol M in (4.2) denotes the so-called monitor function, a $\mathrm{N} \times \mathrm{N}$ symmetric positive definite matrix, that is assumed to depend on the physical coordinates $\mathbf{x}$ and on time t. It is remarked that in the application of the mesh functional (4.2) a computational space $\mathbf{S}_t$ with non-positive Riemann curvature tensor and a convex boundary of the domain $\partial\mathcal{D}_t$ is assumed. These properties are important for the existence and uniqueness of the generated mesh mappings (Dvinsky, 1991; Li et al., 2001). By assuming a non-positive Riemann curvature tensor of $\mathbf{S}_t$, the functional (4.2) is not

directly applicable to mesh generation in spherical geometries. An approach for the generation of moving meshes on the sphere which is based on perturbed harmonic mappings is presented in Di et al. (2006). As an aside, variational mesh generation is also used to construct quasi-uniform meshes on the spherical surface for global atmospheric modelling (Rančić et al., 1996; Purser and Rančić, 1998).

In the functional (4.2), it is the matrix M that specifies the local metric, i.e. shape and size, of the mesh geometry. In the solution-adaptive moving mesh solver, the monitor function M is typically defined to be proportional to some error indicator of the numerically-computed physical flow solution. See further below in Section 4.3 for a discussion and the detailed implementation in the present solver. From the functional (4.2), the mesh is found by the solution of the corresponding Euler-Lagrange equations, given as the stationary points

$$\frac{\delta \mathcal{I}(\overline{x}^k)}{\delta \overline{x}^k} = 0 \qquad k = 1, \mathrm{N} \tag{4.3}$$

in the function space $\overline{x}^k$ [1].

4.3 Moving mesh partial differential equations

Atmospheric and oceanic flows exhibit a strongly transient and non-linear behaviour. An effective solution-adaptive mesh method for these applications should manage to follow the permanently evolving multiscale flow features in an efficient and robust manner. For these demands, it is useful to incorporate explicit control over time scale of the moving mesh adaptation in the solver. With this approach, the continuous mesh movement can be adjusted by the physical time scale representative to the problem under consideration. The following approach proposed by Huang et al. (1994); Huang and Russell (1999) has been found appropriate for this purpose. Instead of applying the condition (4.3) to derive elliptic mesh PDEs from the functional $\mathcal{I}(\overline{\mathbf{x}})$, the modified gradient flow equations

$$P \frac{\partial \overline{x}^k}{\partial t} = -\frac{\delta \mathcal{I}(\overline{x}^k)}{\delta \overline{x}^k} \qquad k = 1, \mathrm{N} \tag{4.4}$$

are used to obtain so-called moving mesh partial differential equations (MMPDEs) of parabolic type. Therein, a scaling function P plays the role of the diagonal

[1] $\delta / \delta \overline{x}^k$ is meant to be a variational derivative, see e.g. Gelfand and Fomin (1963).

preconditioner that improves the solution properties of the MMPDEs and the overall solution-adaptive moving mesh flow solver. Among others, the function P allows to explicitly specify the time scale of the mesh adaptation, which is extremely valuable for the general efficiency and robustness of the method. The ensuing subsection deals with the specification of the scaling function P. Here, the discussion continues with the derivation of the MMPDEs as employed in the solution-adaptive moving mesh NFT flow solver.

The gradient flow equations (4.4) with the functional (4.2) result in a particular set of MMPDEs (Huang and Russell, 1999)

$$P\,\frac{\partial \overline{x}^k}{\partial t} = \nabla \cdot \left(M^{-1} \nabla \overline{x}^k \right) \;, \qquad k = 1, \mathrm{N} \;. \tag{4.5}$$

In (4.5), all partial derivatives are taken with respect to the physical coordinates, i.e. $\nabla \equiv (\partial / \partial x^j)$. For a practical application, the roles of the dependent and independent variables are interchanged in (4.5). This leads to the final form of the MMPDEs (Huang, 2001a; Lang et al., 2003) employed in the numerical solver. In two dimensions ($\mathrm{N} \equiv 2$), they are given as

$$P(\mathbf{x}, M)\,\frac{\partial \mathbf{x}}{\partial \overline{t}} = \sum_{i,j=1,2} D_{ij}(\mathbf{x}, M) \frac{\partial^2 \mathbf{x}}{\partial \overline{x}^i \partial \overline{x}^j} + \sum_{i=1,2} C_i(\mathbf{x}, M) \frac{\partial \mathbf{x}}{\partial \overline{x}^i} \tag{4.6}$$

with the coefficients

$$D_{ij}(\mathbf{x}, M) = \nabla \overline{x}^i \cdot M^{-1} \nabla \overline{x}^j \;, \qquad C_i(\mathbf{x}, M) = -\nabla \overline{x}^i \cdot \left(\sum_{k=1,2} \frac{\partial M^{-1}}{\partial \overline{x}^k} \nabla \overline{x}^k \right) \;.$$

The MMPDEs (4.6) are solved in the computational space $\mathbf{S}_t$ in conjunction with the physical model equations (2.3). The solution of (4.6) provides positions of the mesh $\mathbf{x}(\overline{t}, \overline{\mathbf{x}})$ in the physical space $\mathbf{S}_p$, in line with general definition of the transformation (4.1). The coefficients D_{ij} and C_i of (4.6) depend on the monitor function M. The specification of the monitor function M in turn couples the MMPDEs to the physical solutions. The following subsections elaborate on the solution procedure of the MMPDEs (4.6) including the specification of the monitor function M. The algorithmic implementation in the context of the complete solution-adaptive mesh NFT flow solver is finally described in Section 4.4.

Scaling of the MMPDEs

For the solution of the MMPDEs (4.6) along with the actual physical problem (2.3), it is beneficial to apply a scaling to them. For this purpose, following Huang (2001a) the function P is specified here as

$$P(\mathbf{x}, M) = \Theta \sqrt{(D_{11})^2 + (D_{22})^2 + (C_1)^2 + (C_2)^2} \; . \tag{4.7}$$

The symbol Θ represents a mesh relaxation time ($\Theta > 0$) which is employed as a smoothing parameter of the mesh motion. The parameter Θ allows explicit control over the time scale of the MMPDE solution towards the steady state with respect to a given monitor function M. Basically, the smaller (larger) the mesh relaxation time Θ, the faster (slower) reacts the mesh. The idea behind the incorporated relaxation time Θ in the MMPDEs is that the mesh needs not to be solved for a completely steady (equidistributed) state with respect to M at every time step, but rather has to evolve just as fast as to capture the essential features of the physical flow solution.

The appropriate value for the mesh relaxation time Θ is not straightforwardly identified for a given flow configuration, particularly for complex multidimensional applications considered with the present solver. It was found that the choice for Θ is influenced not only by the problem physics, but also by the configuration of the solution-adaptive moving mesh solver itself, e.g. the specification of the monitor function M. Overall, the literature on MMPDE methods provides virtually no information on this issue. Generally, Θ must be chosen small enough to ensure that the mesh can follow the temporal evolution of the flow or the mesh adaptation features in appropriate manner. However simultaneously, if the value of Θ is chosen too small for a particular setup, then unnecessary large stiffness is introduced in the numerical solver which requires more computational effort for the integration. Furthermore, it is also not clear at this time whether and how to apply a dynamical change of Θ during the simulation; only recently in Soheili and Stockie (2008) this has been applied for the first time to idealised one-dimensional problems. For the conducted experiments in the present work, the mesh relaxation time Θ had yet to be found on a trial-and-error basis for each flow problem and with Θ kept constant over the course of the simulation. See the test applications in Chapters 5 and 6.

The second factor in (4.7) aims to improve the numerical solution properties of the MMPDEs through spatial balancing of the RHS of (4.6) by the norm of its diagonal coefficients. This results in a more uniform size $\sim \mathcal{O}(1)$ of the coefficients D_{ij} and C_i in (4.6) over the solution domain, thereby leading to a numerically

better-conditioned MMPDE (Huang, 2001a). Another important aspect is that the applied normalisation makes the MMPDEs invariant with respect to the scalings $\mathbf{x} \rightarrow \gamma\,\mathbf{x}$ and $M \rightarrow \gamma\,M$, $\forall\ \gamma > 0$ (Huang, 2001a). Given a computational domain $\mathcal{D}_t$ of standard size, the MMPDEs consequently acquire more consistent solution properties under different sizes of the physical domain $\mathcal{D}_p$ and/or monitor functions M. By definition, all applications in this work use a unit square computational domain $\mathcal{D}_t$ in (4.1).

Monitor function

The most decisive part in the application of the MMPDEs to specific physical problems is the appropriate choice of the monitor function M. The monitor function M couples the MMPDEs to the physical flow equations, and its specification aims at the construction of a mesh that is at all times well adapted to the evolving physical flow solution. The design of monitor functions for the purpose of automatic mesh refinement is an open research area, and this applies particularly to the area of geophysical flows. In general, the better one understands the physical processes of the simulated problem, the easier is it to design an effective monitor function. As an example, the evolution of tropical cyclones is known to depend critically on the processes in the inner-core region, e.g. Wang (2002); Rotunno et al. (2009), especially in the eyewall surrounding the centre of the vortex where substantial low-level radial convergence occurs. Hence, it would be desirable to have a relatively high resolution, i.e. a large mesh density, in this region of a simulated tropical cyclone and design the monitor function accordingly. Other aspects in the construction of the adaptive mesh may concern properties like smoothness and orthogonality, or the directional alignment of the mesh with certain flow features. All these considerations may be incorporated in the definition of the monitor function M, see e.g. Brackbill (1993); Huang and Russell (1997); Cao et al. (1999) for discussions.

The functional form of M used in the present work is given as a diagonal matrix Winslow (1981)

$$M = \begin{bmatrix} q & 0 \\ 0 & q \end{bmatrix}\ , \tag{4.8}$$

where $q = q(t, \mathbf{x})$ is a strictly positive scalar weighting function. The particular diagonal form of the monitor function (4.8) realises a non-directional, i.e. isotropic, refinement of the mesh coordinates relative to the distribution of the scalar weighting function q. As already mentioned above, the mesh adaptation could be extended

to directional, i.e. anisotropic, alignment with particular solution features by using a different form of the monitor function M, see e.g. Brackbill (1993); Huang and Russell (1997); Cao et al. (1999).

With the use of (4.8), the local size of the mesh cells tends to be inversely proportional to the relative size of the scalar weighting function q over the physical domain $\mathcal{D}_p$. Consider the one-dimensional version of the functional (4.2)

$$\mathcal{I}[\overline{x}] = \frac{1}{2} \int_{\mathcal{D}_p} \frac{1}{q} \left(\frac{\partial \overline{x}}{\partial x} \right)^2 dx \ , \tag{4.9}$$

with the corresponding Euler-Lagrange equation given as

$$\frac{\partial}{\partial x} \left(\frac{1}{q} \frac{\partial \overline{x}}{\partial x} \right) = 0 \tag{4.10}$$

or equivalently

$$\frac{\partial \overline{x}}{\partial x} = q \, \mathrm{C} \ ; \tag{4.11}$$

where C is a constant. Because $\partial \overline{x} / \partial x$ is a measure of a local mesh density in the physical domain $\mathcal{D}_p$, the relation (4.11) simply states that a higher numerical resolution is associated with a locally large weighting function q. This is a form of the so-called equidistribution principle after de Boor (1974). In more than one dimension, no comparable theoretical statement to (4.11) is known for the functional (4.2). However, the considered functional (4.2) with the monitor function (4.8) is a direct multidimensional generalisation of (4.9). This suggests that a behaviour of the mesh adaptation kind of similar to the one-dimensional case (4.11) can be expected in higher dimensions. Indeed, this was studied by means of a variety of idealised solution-adaptive moving mesh experiments in Cao et al. (2003). Therein, it was demonstrated that the functional (4.2) with (4.8) provides a mesh roughly satisfies the general equidistribution condition $q \, \overline{G}_{xy} \approx \mathrm{C}^{-1}$, wherein $\overline{G}_{xy}$ denotes the Jacobian of the transformation (2.13).

Given a local mesh refinement indicator $\Phi(t, \mathbf{x}) \geq 0$, i.e. some measure for the local error in the flow computation that indicates where a finer mesh is required, the basic specification for q that is adopted here is

$$q(t, \mathbf{x}) = 1 + \frac{\beta}{1 - \beta} \frac{\Phi}{\langle \Phi \rangle} \ . \tag{4.12}$$

The symbol $\langle \cdot \rangle$ in (4.12) defines the domain average according to

$$\langle \Phi \rangle = \frac{1}{A} \int_{\mathcal{D}_p} \Phi(t, \mathbf{x}) \, d\mathbf{x} \ , \tag{4.13}$$

wherein A denotes the area of the two-dimensional plane of the domain $\mathcal{D}_p$ in which the mesh adaptation is applied. The parameter $0 \leq \beta < 1$ in (4.12) allows user-specified control over the strength of the adaptation (Huang, 2001a). For the choice $\beta = 0$, the weighting function q is unity, and a uniform non-adapted mesh results. The larger the parameter β, the stronger is the adaptation of the mesh with respect to the refinement indicator $\Phi(t, \mathbf{x})$. The applied normalisation of Φ by the domain average $\langle \Phi \rangle$ (Beckett et al., 2002) conveniently makes the weighting function q a dimensionless quantity. Furthermore, the normalisation provides a more uniform distribution of the mesh points for the time-space-dependent error measure Φ, in that a certain mesh point density (depending on the choice of β) is maintained in less sensitive areas, i.e. where $\Phi \to 0$.

The actual specification of the refinement indicator Φ is crucial for the success of the solution-adaptive moving mesh flow solver. The choice of Φ may be motivated by a variety of aspects that include physical criteria related to the flow problem under consideration, numerical error estimates based on the applied discretisation of the governing flow equations, or heuristically-derived error proxies (Behrens, 2006). Within the present study, mesh adaptation is restricted to physical and heuristically-derived mesh refinement indicators[1]. A heuristic error proxy could be the gradient of a transported scalar variable in an advection problem that is supposed to be indicative of large solution errors, see Section 5.1. Mesh refinement driven by physical criteria may use vorticity to detect strong shear layers or the gradient of temperature to detect fronts, see Sections 5.2 and 6.1 for example applications. The possibilities for the specification are diverse and often depend strongly on the problem under consideration. Solution-adaptive mesh algorithms may be based on pure numerical error estimates, see Szmelter and Smolarkiewicz (2006) in the context of MPDATA transport methods. See also Behrens (2006) and the given references therein for a more general discussion. Moreover, using adjoint-based mesh refinement indicators, e.g. Power et al. (2006); Dwight (2008); Mani and Mavriplis (2010), is a noteworthy approach particularly for complex nonlinear geophysical flow applications. In geophysical flows, the local evolution of the dynamical fields may be influenced strongly by processes occurring large distances away in the system Weller et al.

[1]Note that physical and heuristically-derived refinement criteria cannot always be strictly distinguished from each other.

(2010). Adjoint-based techniques have the ability to provide the associated sensitivity information for specific quantities of interest. The obtained spatial sensitivity distribution can be used to design criteria for the mesh refinement. It is finally also indicated that another aspect highly relevant to the solution-adaptive mesh simulations of geophysical flows is the coupling of the mesh refinement to the sub-grid scale processes and their parameterisations in the numerical model. Just as an example, exploiting criteria based on sub-grid scale information from a convective parameterisation may prove beneficial to detect the initiation of moist convection in certain regions. In general, the ideal mesh refinement indicator reliably detects important and unimportant regions of the particular flow evolution throughout the simulation and is also computationally inexpensive to derive.

Balancing of various monitor components

In complex dynamical applications, it may often be desirable or required to combine different aspects for the refinement indicator Φ. For instance, one can imagine to rely on numerical and physical error indicators at the same time. Another option could be to combine indicators based on thermodynamic fields, e.g. entropy or moisture variables, with indicators that are derived from the flow field, e.g. vorticity or divergence. Again, the actual possibilities are diverse. In the majority of the cases, the values of the different refinement indicators will not be in the same range, and proper balancing of the various components is necessary to achieve an effective solution-dependent adaptation of the mesh.

Let Φ_l be the l-th refinement indicator and $l = (1, L)$, where L is the number of the various refinement aspects involved. A direct expansion of (4.12) for $L > 1$, is to sum over the individual components q_p as follows

$$q(t, \mathbf{x}) = \sum_{l=1}^{L} q_l(t, \mathbf{x}) = \sum_{l=1}^{L} \left[1 + \frac{\beta}{1-\beta} \frac{\Phi_l}{\langle \Phi_l \rangle} \right] \ . \tag{4.14}$$

The disadvantage of the implementation (4.14) is that one component Φ_l with a large maximum value but a relatively small average $\langle \Phi_l \rangle$, may dominate the other components (van Dam, 2009). An additional normalisation of each component by its maximum value in the domain $\mathcal{D}_p$, i.e. $(q_l / \max_{\mathcal{D}_p}(q_l))$ in (4.14), leads to an improved

and better balanced weighting function (van Dam, 2009)

$$q(t,\mathbf{x}) = \sum_{l=1}^{L} q_l(t,\mathbf{x}) = \sum_{l=1}^{L} \left[\frac{\langle \Phi_l \rangle + \gamma\, \Phi_l}{\langle \Phi_l \rangle + \gamma \max_{\mathcal{D}_p}(\Phi_l)} \right] , \qquad \gamma := \frac{\beta}{1-\beta} . \quad (4.15)$$

Note that for $L=1$, (4.15) is equivalent to (4.12), because the normalisation by the domain maximum does not alter the MMPDEs due to the scaling invariance property ($M \rightarrow \gamma\, M \;\; \forall\, \gamma > 0$).

An application of the solution-adaptive moving mesh solver that uses a combination of mesh refinement indicators based on the gradient of potential temperature and vorticity of the flow field will be given in Section 5.2.

Smoothing of the monitor function

The computed monitor function M is often quite irregular. As a consequence, using the computed monitor function M directly has a detrimental effect on the solution properties on the MMPDEs as well as the overall solution-adaptive solver. Therefore, some amount of smoothing is applied to the monitor function M, which is common practice in moving mesh methods, e.g. Dorfi and Drury (1987); Huang (2001a); Huang and Russell (2001); Lang et al. (2003). Here, a local averaging procedure is adopted

$$M^{(k+1)}(t,\mathbf{x}_0) = \frac{\int_{\mathcal{U}(\overline{\mathbf{x}}_0)} M^{(k)}(t,\mathbf{x})\, d\overline{\mathbf{x}}}{\int_{\mathcal{U}(\overline{\mathbf{x}}_0)} d\overline{\mathbf{x}}} \quad \forall\, \mathbf{x}_0 \in \mathcal{D}_p,\;\; (k=1,K) \;, \quad (4.16)$$

where $\mathcal{U}(\overline{\mathbf{x}}_0) \subset \mathcal{D}_t$ denotes the union of the direct neighbouring mesh points having $\overline{\mathbf{x}}_0$ (which is the image point to $\mathbf{x}_0$) as one of their vertices (Huang and Russell, 2001). Basically, a larger number of smoothing passes K facilitates the solution of the MMPDEs, and the associated anelastic solver. Because the smoothing of the monitor function M is effectively equivalent to a smoothing of the mesh itself, a larger K simultaneously results in a weaker adaptation. Furthermore, the smoothing of the monitor function M spreads out the regions of mesh refinement and provides a more gradual change in the local size of the mesh cells. An optimal choice of K obviously depends on the considered problem and the specification of the monitor function M. Typical numbers in the context of the present solver are $K \approx 15$.

Boundary conditions

The solution of the MMPDEs (4.6) requires the specification of appropriate boundary conditions. At non-periodic horizontal boundaries (e.g. open boundaries or rigid walls) of the anelastic solver, Dirichlet-type conditions are specified for $\mathbf{x}$. It was found that keeping the mesh coordinates $\mathbf{x}$ fixed and uniform along the boundary of the domain $\partial\mathcal{D}_p$ results in undesired deformations of the mesh for refinement in the vicinity to $\partial\mathcal{D}_p$. A consistent movement of the mesh coordinates on the domain boundary $\partial\mathcal{D}_p$ with the mesh coordinates in the inner part of the domain could successfully be achieved by the implementation of one-dimensional boundary MMPDEs as applied in Huang and Russell (1997); Huang (2001a). With this procedure, one-dimensional MMPDEs for the distribution of the mesh points $\mathbf{x}$ on individual segments Γ_p of the boundary $\partial\mathcal{D}_p$ (typically between fixed corner points), are solved prior to (4.6). The one-dimensional analogue to (4.6) reads

$$p(s,\mu)\,\frac{\partial s}{\partial \overline{t}} = \mu\,\frac{\partial^2 s}{\partial \overline{s}^2} + \frac{\partial \mu}{\partial \overline{s}}\,\frac{\partial s}{\partial \overline{s}}\;, \tag{4.17}$$

where the arc-length coordinates s and $\overline{s}$ parameterise the physical Γ_p and the associated computational Γ_t boundary segments, respectively. The one-dimensional scalar-valued monitor function μ in (4.17) is computed as the projection $\mu(t,s) = \mathbf{t}^T M\,\mathbf{t}$ of the matrix-valued monitor function M along the boundary $\partial\mathcal{D}_p$, where $\mathbf{t}$ is the local tangent vector to $\partial\mathcal{D}_p$. The scaling parameter $p(s,\mu)$ in (4.17) is given as

$$p(s,\mu) = \Theta\,\sqrt{\mu^2 + \left(\partial\mu/\partial\overline{s}\right)^2}\;, \tag{4.18}$$

in which the mesh relaxation time Θ usually adopts the same value as in the solution of the associated two-dimensional equation (4.6).

Periodic boundaries are another choice in the anelastic solver, which are consistently implemented in the solution scheme of the MMPDEs (4.6); see Figure 6.1 for an illustration.

Moving mesh algorithm

Solution-adaptivity of the mesh within the physical flow solver presented in Chapter 2 is accomplished through an algorithmic coupling with the MMPDEs. Here, the adopted solution approach integrates the physical set of anelastic equations (2.3) and the coupled MMPDEs (4.6) in a successive manner for each time step. This

alternate solution procedure is in contrast to a simultaneous integration of the MMPDE and the underlying physical equations. In the latter approach, a single implicit system for the overall solution-adaptive model is formulated and eventually solved by specifically designed numerical methods, see Lang et al. (2003) for an implementation. The present development extends the established multiscale geophysical flow solver EULAG with the solution-adaptive moving mesh capability, whereupon the MMPDEs are treated in a single algorithmic entity that adheres to the main physical solver. During the model integration, the mutual coupling between the various modules always exists through the monitor function M and the mesh positions $\mathbf{x}$. The numerical solution of the MMPDEs is described next, whereas the ensuing section discusses the incorporation of the developed MMPDE algorithm into the framework of the geophysical NFT flow solver EULAG.

Numerical solution of the MMPDEs

The principal requirements for the numerical solution procedure of the MMPDEs (4.6) are robustness and efficiency. The formal accuracy of the mesh computation is of minor concern because it is not a determining factor for the accuracy of the physical solution that is computed on the mesh. This constitutes a virtue of the alternate solution approach adopted here. First- and second-order implicit temporal discretisations are chosen for the integration of the MMPDEs (4.6) and (4.17), as they offer stable solutions, independent of the size of the scaling parameters P and p, respectively. Specifying a spatial differential operator $\mathcal{L}$ in (4.6) as

$$\mathcal{L}(\mathbf{x}) \equiv P^{-1} \left(\sum_{i,j=1,2} D_{ij}(\mathbf{x}, M) \frac{\partial^2 \mathbf{x}}{\partial \overline{x}^i \partial \overline{x}^j} + \sum_{i=1,2} C_i(\mathbf{x}, M) \frac{\partial \mathbf{x}}{\partial \overline{x}^i} \right) \ , \tag{4.19}$$

the implemented temporal discretisation is given as

$$\frac{\mathbf{x}^{n+1} - \mathbf{x}^n}{\delta \bar{t}} = a\, \mathcal{L}(\mathbf{x}^{n+1}) + b\, \mathcal{L}(\mathbf{x}^n) \ , \tag{4.20}$$

which optionally allows for the backward Euler ($a = 1,\ b = 0$) or the trapezoidal Crank-Nicolson ($a = b = 0.5$) scheme. In the practical implementation, the coefficients D_{ij} and C_i in (4.19) are freezed at the time level n. Standard central differences are used to discretise all spatial partial derivatives. Given either Dirichlet or periodic boundary conditions for $\mathbf{x}$, the resulting algebraic problem is solved by the generalised conjugate residual GCR scheme (Eisenstat et al., 1983; Smolarkiewicz and Margolin, 1994; Smolarkiewicz et al., 2004). A convergence threshold for the

iterative GCR algorithm can be based simply on some norm of the residual error to (4.20). However, a more meaningful convergence criterion with regard to the underlying mesh generation problem is obtained by considering the difference between successive GCR iterations ν for the solutions ϕ^ν and relate them to the characteristic extensions L of the physical domain $\mathcal{D}_p$. Specifically, it is proposed here to use

$$\| \phi^{\nu+1} - \phi^\nu \|_\infty < \epsilon \, \mathrm{L} \, , \qquad \phi = x^i \tag{4.21}$$

as a stopping criterion for the iterative GCR scheme in the MMPDE solution. The criterion (4.21) is applied in combination with a criterion based on some norm of the residual error[1]. A value of $\epsilon = 10^{-7}$ in (4.21) has been employed successfully throughout all experiments of largely varying scales L (see the Sections 5 and 6) performed in this work.

The described MMPDE solution procedure is fully embedded in the parallel coding structure of the EULAG flow solver. Note finally, the discretisation given above applied to the one-dimensional boundary MMPDEs (4.17) results in a tridiagonal system of algebraic equations, which is solved by the Thomas algorithm, see e.g. Durran (1999).

4.4 Solution-adaptive moving mesh NFT solver

This section demonstrates the algorithmic implementation of the overall solution-adaptive moving mesh NFT flow solver. It is explained in which way the MMPDE machinery of Section 4.3, is incorporated into the solution procedure of the physical anelastic NFT flow solver of Chapters 2 and 3. The discussion focuses on the Eulerian MPDATA scheme for advection in (2.19).

Implementation of the algorithm

A flowchart illustrating the algorithmic sequence of the basic parts that compose the solver is shown in Figure 4.2. Given the current set of model solutions Ψ^n and the mesh $\mathbf{x}^n$ at the time level $\overline{t}^n$, the time loop begins with the execution of the mesh adaptation module. This involves the evaluation of the monitor function M^n (typically a function of the present solutions Ψ^n), and the subsequent integration

[1]Note, the combination of (4.21) with a criterion based on a residual error norm is required because (4.21) can fail if the iterative solver stalls.

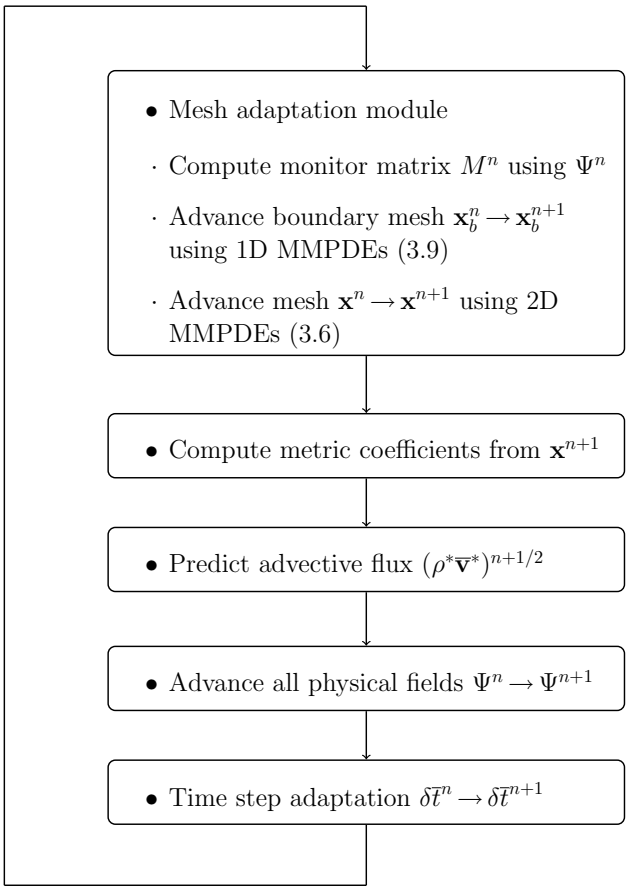

Figure 4.2: Flowchart showing a full time-loop coding sequence of the basic parts that compose the solution-adaptive moving mesh Eulerian NFT flow solver.

of the MMPDEs for the solution-adapted mesh points $\mathbf{x}^{n+1}$ at the time level $\overline{t}^{n+1}$ [1]. Having obtained the mesh $\mathbf{x}^{n+1}$, the corresponding metric variables that specify the adapted mesh geometry, e.g. elements of the Jacobian matrix, are computed. This step also includes an update of all known background and ambient fields in the anelastic equations (2.3) to the new positions $\mathbf{x}^{n+1}$. At this stage of the model algorithm, the required advective momentum vector $\hat{\mathbf{v}}^{n+1/2}$ at the intermediate time level $\overline{t}^{n+1/2}$ in the MPDATA solution (see Section 2.3) is determined. In adaptive simulations, this part intertwines with the numerical procedure for the computation of the mesh velocity $\overline{\mathbf{v}}^g$ (3.16). In the next subsection, it is elaborated how the procedure is best incorporated into the velocity predictor for $\hat{\mathbf{v}}^{n+1/2}$. The algorithm proceeds by advancing all physical model fields $\Psi^n \rightarrow \Psi^{n+1}$ based on the solution procedure described in Section 2.2. In order to improve the efficiency of the model integration, the time step $\delta\overline{t}$ is adapted to an optimal size (according to the

[1]For relatively large time steps $\delta\overline{t}$ of the physical solver, e.g. with the semi-Lagrangian advection scheme, sub-steps in the MMPDE integration may be required for an efficient solution.

underlying stability criterion) by the end of each time loop.

The described algorithmic structure offers the flexibility to incorporate the MPDATA-related developments as presented in Section 3.1. This essentially requires that the mesh adaptation $\mathbf{x}^n \rightarrow \mathbf{x}^{n+1}$ is performed prior to the execution of the advection scheme, i.e. prior to the advancement of the model fields $\Psi^n \rightarrow \Psi^{n+1}$ as shown in Figure 4.2. Only with such a procedure, diagnostically derived generalised densities ρ^{*n} and ρ^{*n+1} are known within MPDATA as needed for the application of the generalised density correction factor (3.6). Note, in the default EULAG the mesh adaptation is performed after the execution of the advection scheme (not shown). This shortcoming with the developments of Section 3.1 initiated a redesign of the model's coding structure in the context of the present work. Furthermore, another aspect of this redesigned coding structure is that it allows for a more accurate computation of the advective contravariant velocities $\hat{\mathbf{v}}^{n+1/2}$ in MPDATA under time-dependent generalised coordinates, which is explained in the last part of this section. Compared to the default EULAG, the coding structure of Figure 4.2 requires at least the storage of one additional three-dimensional field for the generalised density ρ^*.

It shall be finally remarked, that the time step adaptation has the potential to significantly (~ 10 - 20 percent, but strongly depending on the application) increase the efficiency of the solution-adaptive moving mesh applications. Despite this benefit, one should be aware that variable time stepping, at least in the author's experience, introduces small additional errors absent in comparable constant time step computations.

Advective velocity prediction in the solution-adaptive mesh solver

As explained in Section 2.3, MPDATA requires an $\mathcal{O}(\delta\bar{t}^2)$ approximation to the advective generalised contravariant mass flux vector $\hat{\mathbf{v}}^{n+1/2} = (\rho^*\overline{\mathbf{v}}^*)^{n+1/2}$ at the intermediate time level $\bar{t}^{n+1/2}$. Here, the procedure of predicting $(\rho^*\overline{\mathbf{v}}^*)^{n+1/2}$ in the solution-adaptive moving mesh solver is considered.

Under a time-dependent mesh geometry, the default procedure is to evaluate the solenoidal $\overline{\mathbf{v}}^s$ (2.6) and the mesh velocity $\overline{\mathbf{v}}^g$ (see the subsequent paragraph) both at the time level $\bar{t}^n$. Using the relation (2.5), the generalised contravariant mass flux $(\rho^*\overline{\mathbf{v}}^*)^n$ is formulated according to

$$(\rho^*\overline{\mathbf{v}}^*)^n = (\rho^*\overline{\mathbf{v}}^s)^n + (\rho^*\overline{\mathbf{v}}^g)^n \ . \tag{4.22}$$

Given $(\rho^*\overline{\mathbf{v}}^*)^n$ and $(\rho^*\overline{\mathbf{v}}^*)^{n-1}$ from the previous time step, the linear predictor scheme

$$(\rho^*\overline{\mathbf{v}}^*)^{n+1/2} = (1+\beta)\,(\rho^*\overline{\mathbf{v}}^*)^n - \beta\,(\rho^*\overline{\mathbf{v}}^*)^{n-1}\ , \tag{4.23}$$

cp. (2.35), is employed to obtain an $\mathcal{O}(\delta\bar{t}^2)$ approximation for $(\rho^*\overline{\mathbf{v}}^*)^{n+1/2}$. Similarly, nonlinear predictor schemes may be used instead of (4.23) to calculate $(\rho^*\overline{\mathbf{v}}^*)^{n+1/2}$, cf. Smolarkiewicz and Margolin (1993); Smolarkiewicz and Margolin (1998).

The MPDATA solution in a time-dependent mesh geometry requires to evaluate the mesh velocity $\overline{\mathbf{v}}^g$ in (4.22). In the solution-adaptive moving mesh solver, the positions $\mathbf{x}$ and the velocity of mesh, i.e. $\partial\mathbf{x}/\partial\bar{t}$, are not known analytically during the integration. Rather, they have to be determined numerically at each time step. Within the algorithm displayed in Figure 4.2, the mesh adaptation module at the beginning of the time loop generates the mesh positions $\mathbf{x}^{n+1}$. At this point, a centred[1] second-order finite-difference around the time level $\bar{t}^n$ can be used to compute $(\partial\mathbf{x}/\partial\bar{t}\,)^n$, namely

$$\left(\frac{\partial\mathbf{x}}{\partial\bar{t}}\right)^n = \frac{(\mathbf{x}^{n+1}-\mathbf{x}^{n-1})}{2\delta\bar{t}}\ , \tag{4.24}$$

where a constant time step $\delta\bar{t}$ is assumed for simplicity of the exposition. The mesh velocity $(\overline{\mathbf{v}}^g)^n = (\partial\overline{\mathbf{x}}/\partial t\,)^n \in \mathbf{S}_t$, and hence $(\rho^*\overline{\mathbf{v}}^g)^n$ in (4.22), are subsequently derived by means of the Kronecker-delta relations (2.14) and the mesh geometry $\mathbf{x}^n$.

Revised procedure for predicting advective velocities

A revised procedure for the approximation of $(\rho^*\overline{\mathbf{v}}^*)^{n+1/2}$ in the framework of the solution-adaptive moving mesh NFT flow solver (Figure 4.2) is proposed. The method evaluates $\rho^*\overline{\mathbf{v}}^g$ straightforwardly at the intermediate time level $\bar{t}^{n+1/2}$, and applies the predictor scheme only to the part with the solenoidal velocity $\overline{\mathbf{v}}^s$. The detailed procedure is as follows: After completion of the mesh adaptation module in the algorithm of Figure 4.2, the mesh velocity $(\partial\mathbf{x}/\partial\bar{t})$ is evaluated as

$$\left(\frac{\partial\mathbf{x}}{\partial\bar{t}}\right)^{n+1/2} = \frac{\mathbf{x}^{n+1}-\mathbf{x}^n}{\delta\bar{t}}\ . \tag{4.25}$$

[1]With variable time stepping, the finite difference is not symmetric about $\bar{t}^n$, and appropriate difference formulae have to be used to retain second-order accuracy, see e.g. Ferziger and Peric (2001).

Then, then $(\overline{\mathbf{v}}^g)^{n+1/2}$ and the generalised density $\rho^{*n+1/2}$ are obtained from the Kronecker-delta relations (2.14) and the mesh geometry $\mathbf{x}^{n+1/2}$ approximated by [1]

$$\mathbf{x}^{n+1/2} = 0.5 \left(\mathbf{x}^{n+1} + \mathbf{x}^{n} \right) \ . \tag{4.26}$$

This procedure yields an $\mathcal{O}(\delta\overline{t}^2)$ approximation for $(\rho^*\overline{\mathbf{v}}^g)^{n+1/2}$ at the intermediate time level $\overline{t}^{n+1/2}$. As $(\rho^*\overline{\mathbf{v}}^g)^{n+1/2}$ is already known, only the flux with the solenoidal velocity $(\rho^*\overline{\mathbf{v}}^s)^{n+1/2}$ is obtained from the application of the respective linear or non-linear predictor schemes. With the former scheme, i.e. analogous to (4.23), it uses

$$(\rho^*\overline{\mathbf{v}}^s)^{n+1/2} = (1+\beta)\,(\rho^*\overline{\mathbf{v}}^s)^{n} - \beta\,(\rho^*\overline{\mathbf{v}}^s)^{n-1} \ . \tag{4.27}$$

After that, the contravariant fluxes $(\rho^*\overline{\mathbf{v}}^*)^{n+1/2}$ are computed at $\overline{t}^{n+1/2}$ as

$$(\rho^*\overline{\mathbf{v}}^*)^{n+1/2} = (\rho^*\overline{\mathbf{v}}^s)^{n+1/2} + (\rho^*\overline{\mathbf{v}}^g)^{n+1/2} \ , \tag{4.28}$$

which completes the procedure.

The explained scheme (4.25)-(4.28) for the computation of $(\rho^*\overline{\mathbf{v}}^*)^{n+1/2}$ features a number of advantages compared to (4.22)-(4.24). From a practical point of view, the initialisation of (4.25)-(4.26) is straightforward. Moreover, the numerical evaluation of the mesh velocity $(\partial\mathbf{x}/\partial\overline{t}\,)$ under variable time steps uses the simple derivative (4.25), in the spirit of FT schemes. Most importantly, the application of the procedure (4.25)-(4.28) leads to a more accurate solution of the MPDATA scheme under time-dependent generalised coordinates. An important aspect of the procedure (4.25)-(4.28) thereby is that it achieves round-off error compliance with the GCL (3.18) for a uniform background density ρ_b and time-dependent coordinate transformations of the one-dimensional form $\mathcal{F}(t,\mathbf{x}) = (\overline{x}(t,x), \overline{y}(t,y), \overline{z}(t,z))$ in (2.2). This property is due to the centred evaluation of the mesh velocity and all metric terms with respect to $\overline{t}^n$ and $\overline{t}^{n+1}$. The latter together with the commutativity of the discrete numerical derivatives for the metric terms provides the particular round-off error compliance with the GCL (3.18). Although this does not hold for more general coordinate mappings and a non-uniform background density ρ_b, the procedure provides minimisation of the errors with respect to the GCL (3.18) also for arbitrary time-dependent coordinate mappings. Note, the procedure (4.22)-(4.24) has no similar property and normally shows significantly larger errors in terms of the compliance with the GCL (3.18). The accuracy of the procedure

[1] Note that optionally $\rho^{*n+1/2} = 0.5\,(\rho^{*n+1} + \rho^{*n})$ may be used, which simplifies the procedure within the general anelastic solver.

(4.25)-(4.28) against (4.22)-(4.24) will be investigated by means of solution-adaptive moving mesh experiments in the subsequent Sections 5.1 and 5.3. It is anticipated here, that these experiments will show the procedure (4.25)-(4.28) to be superior over (4.22)-(4.24). Therefore, unless otherwise noted, all simulations in this work employ the procedure (4.25)-(4.28) for the calculation of the generalised contravariant mass flux $(\rho^*\overline{\mathbf{v}}^*)^{n+1/2}$, with the mesh velocity $\overline{\mathbf{v}}^g$ evaluated straightforwardly at $\overline{t}^{n+1/2}$.

Chapter 5

Two-dimensional solution-adaptive moving mesh test simulations

The previous two Chapters 3 and 4 are concerned with the design and implementation of the solution-adaptive moving mesh NFT flow solver based on MPDATA advective transport methods. As with any new modelling approach, basic validation and testing of its consistence is crucial. This task is best performed initially in a simple configuration for flow problems that are straightforward to analyse.
In the present chapter, two-dimensional prototype versions of the solution-adaptive moving mesh solver are created and applied that resemble the numerical formulation of the anelastic NFT flow solver EULAG. Two canonical flow test problems are considered for the prototype solvers. The first model problem in Section 5.1 is the advection of a passive scalar in a prescribed time-varying shear flow. This model problem provides an ideal first test because of the simplicity to handle only a single linear hyperbolic physical conservation law and the availability of an exact solution. Despite its simplicity, it is of relevance to dispersion modelling of chemical tracers in (large-scale) atmospheric and oceanic flows. A second model problem considered in Section 5.2 is the nonlinear evolution of a dry rising warm thermal in a neutrally-stratified quiescent atmosphere. Here, this non-hydrostatic flow is modelled on the basis of the anelastic equations[1]. The anelastic equations are also employed in EULAG. Although the nonlinear rising thermal flow does not have an exact solution, it allows for a quick analysis of well-defined solution features like the representation of the amplitude of the rising thermal and the temperature gradients

[1]Actually, the incompressible Boussinesq flow equations are applied here. These, however, represent a direct subset of the anelastic equations.

along its edges. An accurate representation of these solution features in the simple configuration adopted here is of direct relevance for the numerical modelling of cumulus convection in realistic atmospheric flows.

The present chapter is concerned with the question of whether the basic conceptual formulation of the solution-adaptive moving mesh solver developed in Chapters 3 and 4 works in practice. This is confirmed by applying the adaptive solver to the two-dimensional model problems given above. Both model problems feature strongly varying lengths scales in the evolving flow, and the adaptive solver is assessed with regard to its performance against the uniform mesh solver. For instance, it is investigated whether the adaptive mesh solver is able to achieve a significantly better representation of the multiscale flow than the uniform mesh solver with the same number of grid points. If the improvement in the solution quality is of significant size, then this is an argument for the usefulness of the adaptive solver.
In addition, basic aspects of the adaptive solver are investigated in the present chapter. Among others, one of these aspects is the adaptation of the mesh points at the domain boundary. In the moving mesh solver, one-dimensional MMPDEs for the mesh adaptation at the boundaries are combined with the two-dimensional MMPDEs for the mesh adaptation in the inner part of the domain. Here, it is demonstrated that the boundary mesh adaptation occurs consistently with the adaptation of the mesh points in the inner part of the domain.
Another aspect is whether the adaptive solver can cope with strong mesh adaptations required to resolve fine structures in the flow. For example, the rising thermal flow simulation in Section 5.2 demands strong adaptations at the sharp interface of the thermal with the ambient air. The integration of the underlying anelastic equations involves the solution of the elliptic boundary value problem for the pressure variable at each time step; see Equation (2.23) in Section 2.2. The variation of the size of the coefficients in the elliptic pressure equation is related to the metric of the underlying mesh. It is unclear in advance whether the convergence properties of the iterative solver applied to solve the elliptic pressure equation are seriously degraded as a result of strong adaptations of the mesh. Fortunately, it can be shown that this is not the case.
Two different schemes for the approximation of the advective generalised contravariant mass flux $\hat{\mathbf{v}}^{n+1/2} = (\rho^* \overline{\mathbf{v}}^*)^{n+1/2}$ in MPDATA under a moving mesh are proposed in the last part of Section 4.4. Here, the scalar advection problem in Section 5.1 is used to assess the different schemes. The analysis can easily be performed due to the existence of an exact solution for the considered scalar advection problem.
It is also noted that the formulation of the adaptive anelastic solver for the sim-

ulation of the rising thermal in Section 5.2 will assume the two-dimensional mesh adaptation in the vertical plane. This formulation differs from the current formulation of EULAG, where the solution-adaptive mesh adaptation is restricted to the horizontal plane. Here, it is demonstrated, in the simplified though sufficiently complex configuration of the rising thermal, that such an extension could be of value for the simulation small-scale flows in EULAG as well.
In Chapter 3, the issue of the compatibility of the MPDATA advection scheme with the generalised anelastic mass conservation law (GMCL) is discussed. There, extensions of MPDATA for its use under moving meshes were developed. However, the associated numerical test and validation experiments in Section 3.4 were restricted to prescribed oscillating moving meshes and the model problem of scalar advection in a uniform velocity field. In the final Section 5.3 of the present chapter, the subject is further investigated in the context of solution-adaptive numerically-generated moving meshes. Here, both the scalar advection problem and the rising thermal flow problem are used for the examination.

The use of the simplified two-dimensional prototype solvers in the present chapter allows for a straightforward code handling and fast execution times. This has been of value during the elaborate development and testing phase of the solution-adaptive moving mesh solver. As mentioned above, the prototype solvers resemble the analytical and numerical formulation of EULAG. Therefore, all aspects discussed in the present chapter are of direct relevance to the application of the adaptive solver in the full framework of the three-dimensional modelling system EULAG.

5.1 Scalar advection

In this section, the problem of scalar advection in a predefined velocity field is considered. This relatively straightforward configuration allows to validate the developed solution-adaptive moving mesh NFT solver by means of known analytical solutions. The particular model setup follows that in Blossey and Durran (2008). The setup describes an initially cosine-squared-shaped hill of the advected scalar variable ψ that is elongated into a fine-scale filamentary structure by the acting of a deformational flow field. The flow field reverses its magnitude in time to recover the initial condition after one period T. The scalar advection configuration is of relevance to tracer dispersion modelling of chemical constituents in large-scale atmospheric and oceanic flows, where a high local resolution is typically essential to resolve filamentary structures that may develop; see e.g. Behrens et al. (2000) and references therein.

Description of the model and experimental design

The scalar advection problem treated here is based on the single homogeneous conservation law (2.24), repeated here for completeness

$$\frac{\partial(\rho^*\psi)}{\partial\bar{t}} + \overline{\nabla}\cdot(\overline{\mathbf{v}}^*\rho^*\psi) = 0 \ , \tag{5.1}$$

assuming an incompressible fluid with a constant density ρ_b. All variables in the present problem are dimensionless. The extensions of the model domain $\mathcal{D}_p$ are -0.5 $\leq x, y \leq$ 0.5. The model implements a fully general time-dependent transformation of the coordinates $\mathcal{D}_p \rightarrow \mathcal{D}_t$ in the horizontal plane according to the functional relationship $\mathcal{F} = (\overline{x}(t,x,y), \overline{y}(t,x,y))$ in (2.2).

A time-dependent shear flow that is periodic over the integration time $T = 1.0$, is prescribed by means of the streamfunction (Blossey and Durran, 2008)

$$\begin{aligned}\chi(t,x,y) = \frac{4\pi_c}{T}\left\{\frac{r^2}{2} + \cos\left(\frac{2\pi_c t}{T}\right)\left[\frac{r^2}{2} + \frac{1}{96}\log(1 - 16r^2 + 256r^4)\right.\right. \\ -\frac{1}{48}\log(1+16r^2) \\ \left.\left. -\ \frac{\sqrt{3}}{48}\arctan\left(\frac{-1+32r^2}{\sqrt{3}}\right)\right]\right\},\end{aligned} \tag{5.2}$$

where $r = \sqrt{x^2 + y^2}$. Given the specification (5.2), the solenoidal velocity $\overline{\mathbf{v}}^s$ in the transformed space $\mathbf{S}_t$ is evaluated on the discrete mesh from (3.25). Note again, instead of defining the velocity field $\mathbf{v}$, this procedure ensures compliance with the divergence constraint (3.15) throughout the integration period T. Again following Blossey and Durran (2008), the initial scalar field ψ is described as

$$\psi(0,x,y) = 0.5 + \begin{cases} \left(\dfrac{1+\cos\left(\pi_c \tilde{r}\right)}{2}\right)^2, & \tilde{r} \leq 1 \\ 0 & \tilde{r} > 1, \end{cases} \tag{5.3}$$

where $\tilde{r} = 5\sqrt{(x+0.2)^2 + y^2}$. A zero gradient of the scalar variable ψ is supposed at the model boundaries.

Fully general two-dimensional solution-dependent adaptation of the mesh by the MMPDEs (4.6) is applied in the model plane of $\mathcal{D}_p$, whereby the underlying mapping $\mathcal{D}_t \rightarrow \mathcal{D}_p$ in (4.1) exhibits the general form $\mathcal{M} = (x(\overline{t}, \overline{x}, \overline{y}), y(\overline{t}, \overline{x}, \overline{y}))$. One-dimensional MMPDEs (4.17) are solved for the distribution of the mesh points along each the four boundary segments of $\mathcal{D}_p$. The mesh relaxation time Θ in the solution of the MMPDEs in (4.7) is set to $\Theta = 1.6 \times 10^{-2}$.
The monitor function of the form M (4.8) is based on a single mesh refinement indicator Φ in (4.12) (or equivalently Φ_1 for $L = 1$ in multi-component form (4.15)), specified to be proportional to the gradient of the transported scalar variable ψ. In particular, it is defined as

$$\Phi(t, \mathbf{x}) = \|\nabla \psi\| \tag{5.4}$$

where $\|\cdot\|$ refers to the Euclidean vector norm. The use of (5.4) may be explained by the heuristic argumentation that relatively large solution errors in the advection scheme occur in regions where ψ shows its greatest variations (compare for instance the first truncation error term on the RHS of the modified equation (2.26)); see also Skamarock et al. (1989). The parameter β in (4.12), that controls the strength of the mesh adaptation, is set to $\beta = 0.7$. The smoothing procedure (4.16) of the computed monitor function uses a number of $K = 15$ passes.

All results in the present section are obtained using the developed MPDATA extension RP (see Table 3.1). In addition, the "third-order accurate" version of the MPDATA scheme with FCT enhancement (Smolarkiewicz and Grabowski, 1990) is applied. The simulations are performed using variable time stepping and a constant maximum Courant number $\mathcal{C}_{max} = 0.5$. Regarding the "third-order accurate" version of MPDATA, it is remarked that in the author's experience this variant of MPDATA

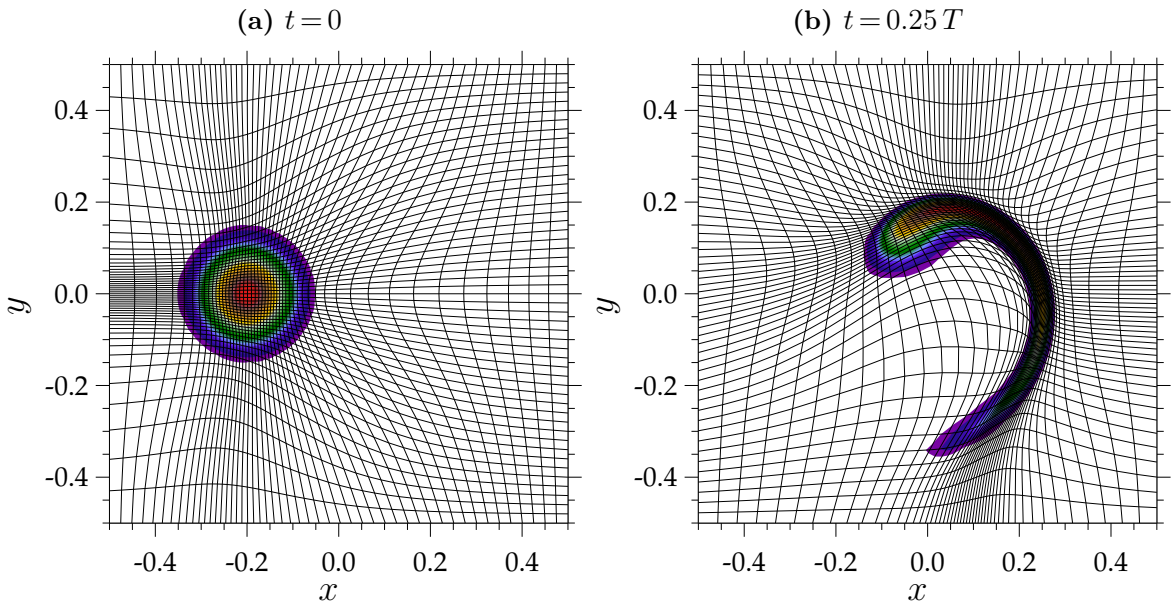

Figure 5.1: MPDATA integration of the scalar advection problem with a solution-adaptive mesh; at the initial time (a), and at $0.25\,T$ (b). Indicated are contours of the transported scalar variable ψ (shaded; warmer colours correspond to larger value of ψ), overlaid by the solution-adaptive mesh (black solid lines).

especially minimises the truncation errors introduced by the coordinate transformations of the generalised coordinates, particularly for strongly deformed meshes. All computations here are conducted in a single processor computing environment.

Results and discussion

Figure 5.1a shows the scalar field ψ superimposed by the adaptive moving mesh at the initial time $t = 0$ of the model integration. As can been seen, the mesh at $t = 0$ is already finer resolved in the region of high values of $\|\nabla\psi\|$. This is achieved by reapplying the MMPDE integration procedure to the initial distribution of the scalar ψ given by (5.3), until the desired degree of adaptation is attained (typically until a steady state of the mesh movement). Figure 5.1(b) displays the situation after $0.25\,T$. At this stage of the simulation, the circularly-symmetric zone of nonzero ψ values from $t = 0$ is stretched into a thin elongated structure. Large local gradients of ψ exist transverse to the elongation direction, and the solver automatically provides a finer mesh there. This locally fine mesh is essential to resolve the large gradients in the transported field ψ. In the rest of the domain, a much coarser resolution is basically found, but highly anisotropic mesh cells exist in some parts as a result from the strong adaptations.

The continuous adaptation of the mesh runs stable over the entire course of the simulation. The mesh points on the boundary of the domain are adapted uniformly with the mesh points in the inner part of the domain. As can be identified in Figure 5.1(b), the solver can handle the extreme deformations and stretching of the mesh while simultaneously producing accurate results; see below in Figure 5.2. In terms of the mesh deformations, the ratio of the smallest to the largest mesh cell area at $t = 0.25\,T$ is $1/64$. Note, even smaller ratios of $1/130$ with $\beta = 0.85$ have been simulated for the present test. These however did not significantly reduce the error but increased the wall clock time $\mathrm{T_w}$ of the simulation due to a smaller time step necessary for $\mathcal{C}_{max} = 0.5$ under a locally finer spatial mesh.

Figure 5.2 investigates the efficacy of the solution-adaptive moving mesh solver for the present scalar advection experiment. The final result at $t = T$ of the solution-adaptive moving mesh solver is compared to results obtained using a static non-adaptive uniform mesh, i.e. using the same model but the mesh adaptation by the MMPDE machinery deactivated. Due to the temporal periodicity of the prescribed flow field, the exact solution at the final simulation time $t = T$ is equal to the initial distribution of the scalar, which means $\psi(0, x, y) \equiv \psi(T, x, y)$.

The result from a static uniform mesh run with a total number of $\mathrm{N}_c = 50^2$ mesh cells (or a mesh increment size of $\delta\overline{x} = \delta\overline{y} = 0.02$) is shown in Figure 5.2(a). Using the same number mesh cells, the solution-adaptive moving mesh solver in Figure 5.2(c) provides substantial improvement compared to the simulation with the static uniform mesh in Figure 5.2(a). The L_2 and L_∞ error norms of the static mesh run in Figure 5.2(a) are one order of magnitude larger than of the solution-adaptive mesh run in Figure 5.2(c). The solution-adaptive moving mesh run very accurately reproduces the amplitude and the shape of the cosine-squared hill in the solution field of ψ. In addition, the results of another static uniform mesh run with a total number of $\mathrm{N}_c = 250^2$ mesh cells is given in Figure 5.2(b). Although the number of mesh cells N_c in this static uniform mesh run is increased by a factor of 25, it shows, respectively, ~ 1.4 and ~ 1.7 times larger L_2 and L_∞ error norms than in the solution-adaptive moving mesh simulation of Figure 5.2(c).

Despite the presence of very large gradients in the transported field ψ, all simulations provide a numerical solution that is completely free of spurious oscillations. For the solution-adaptive moving mesh simulation, this requires compatibility of the MPDATA scheme with the GMCL (3.2). Here, this has been achieved by applying the MPDATA implementation RP as developed in Section 3.1. Note, with the original implementation of MPDATA, i.e. the scheme OD of Section 3.1, spurious

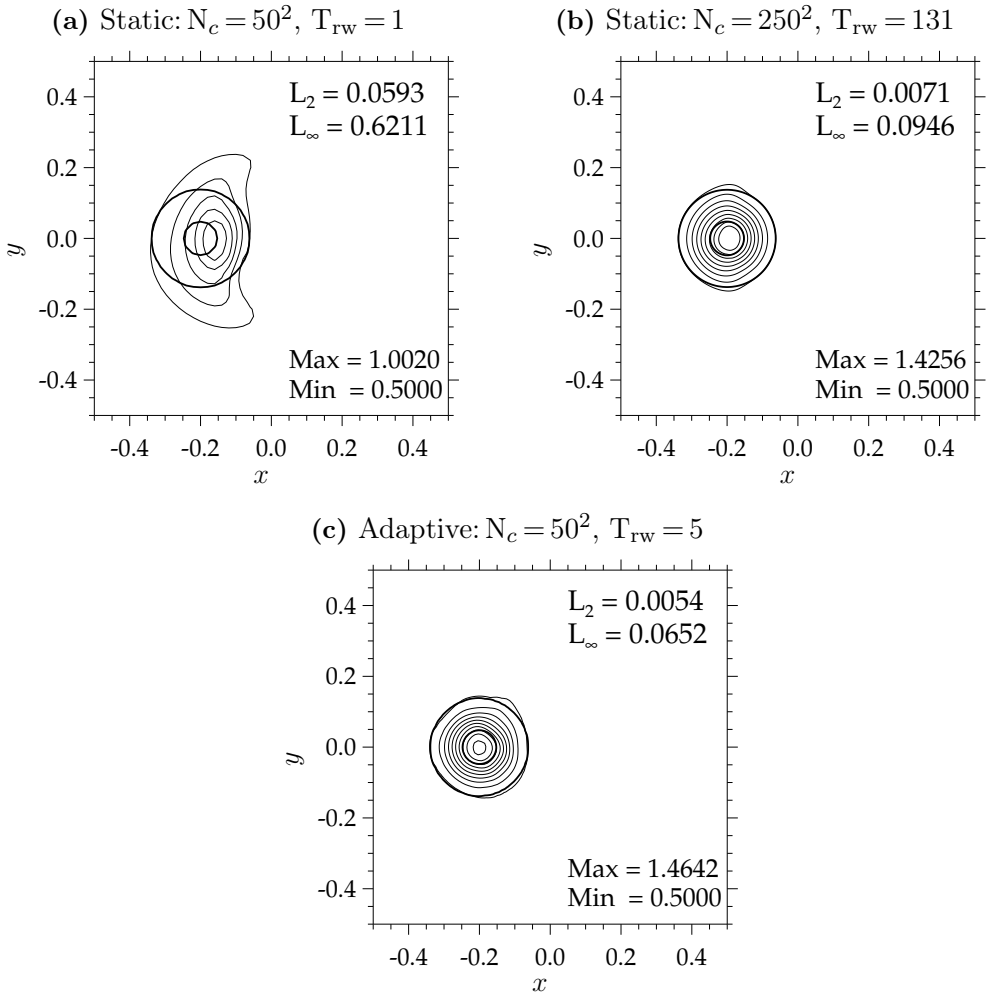

Figure 5.2: Comparison of results from the MPDATA integration of the scalar advection problem with a static uniform mesh (a,b), against the integration that uses solution-adaptive meshing (c). Shown are contours of the numerical solution for the scalar field ψ at the final integration time $t = T$ (thin solid lines; contours from 0.55 to 1.45 at intervals of 0.1). The exact analytical solution is overlaid (heavy solid lines; shown are only the contour values of 0.55 and 1.25). Domain maximum and minimum values of the approximate numerical solution for ψ, plus standard L_2 and L_∞ error norms, are given in the lower and upper right parts of the figure, respectively. The symbol N_c refers to the number of discrete mesh cells, and T_{rw} is the relative wall clock time of the computations with respect to the low-resolution standard static uniform mesh run that uses $N_c = 50^2$ in (a).

extrema of significant magnitude would result here. This will be demonstrated in the discussion of Section 5.3; see the Figure 5.8 therein.

The relative computational effort of the three different simulations is given by the variable T_{rw} in Figure 5.2. For the two-dimensional pure advection problem considered here, the solution-adaptive moving mesh simulation in Figure 5.2(c) requires a factor of 5 larger wall clock time T_w for the simulation than the static uniform mesh

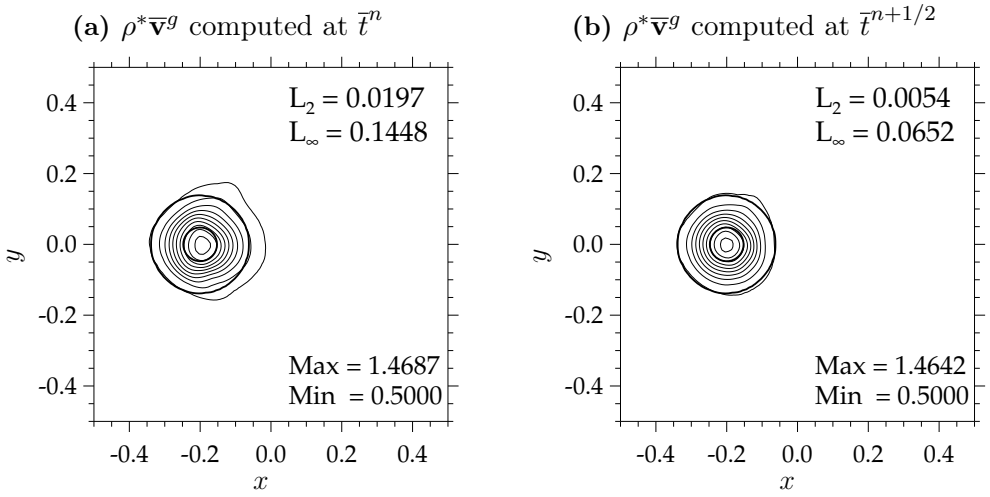

Figure 5.3: Comparison of results from solution-adaptive moving mesh simulations of the scalar advection problem with two different procedures of approximating the generalised contravariant mass flux $(\rho^*\overline{\mathbf{v}})^{*n+1/2}$ in MPDATA (see Chapter 4.4): (a) Using the procedure (4.22)-(4.24), i.e. with $\rho^*\overline{\mathbf{v}}^g$ evaluated at $\overline{t}^n$. (b) Using the procedure (4.25)-(4.28), i.e. with $\rho^*\overline{\mathbf{v}}^g$ evaluated at $\overline{t}^{n+1/2}$. Otherwise as in Figure 5.2.

computation with the same number of mesh cells in Figure 5.2(a). The computational overhead of the solution-adaptive moving mesh run over the static uniform mesh run in Figure 5.2(a) results from the processing of the MMPDE machinery, plus the use of smaller time steps with $\mathcal{C}_{max} = 0.5$ due to the finer spatial resolution. However, the solution-adaptive moving mesh run in Figure 5.2(c) requires a factor of 26 less wall clock time T_w than the fine resolution static uniform mesh run in Figure 5.2(b). Altogether, this demonstrates the extremely high efficacy of the solution-adaptive moving mesh solver for the present configuration.

Advective velocity prediction in the solution-adaptive mesh solver

In Section 4.4, the procedure for approximating the generalised contravariant mass flux $(\rho^*\overline{\mathbf{v}}^*)^{n+1/2}$ in the solution-adaptive mesh NFT flow solver was considered. Figure 5.3 compares the results for the two different schemes discussed, using the present scalar advection problem. In Figure 5.3(a), the linear predictor scheme is applied to the contravariant fluxes $\rho^*\overline{\mathbf{v}}^*$ with generalised mesh mass flux $\rho^*\overline{\mathbf{v}}^g$ evaluated at the full time level $\overline{t}^n$. In contrast, the results in Figure 5.3(b) are obtained with the linear predictor scheme applied only to the fluxes with the solenoidal velocity $\rho^*\overline{\mathbf{v}}^s$, while the mesh flux $\rho^*\overline{\mathbf{v}}^g$ is evaluated straightforwardly at the intermediate time level $\overline{t}^{n+1/2}$; see Chapter 4.4 for the detailed implementation of the two different procedures. Note that for proper comparability, both simulations in Figure 5.3(a)

and Figure 5.3(b) have used the procedure of Figure 5.3(b) to start off the algorithm for the first time step.

Using the revised procedure in Figure 5.3(b) yields, respectively, ~ 3.6 and ~ 2.2 times lower magnitudes of the L_2 and L_∞ error norms over the results in Figure 5.3(a). While the obtained maximum amplitude of the ψ field is about the same with both procedures, the solution field of ψ in Figure 5.2(a) appears less symmetric and shows larger dissipative errors than in Figure 5.2(b).

Although both schemes are formally of second-order accuracy, the comparison shown in Figure 5.3 clearly indicates a superior solution quality for the revised procedure adopted in (b) over that in (a). As explained in the last paragraph of Section 4.4, a key aspect for the improved results with the revised procedure (b) is the favourable discrete evaluation of the mesh velocity in regard to the compliance with the GCL (3.18). For a further demonstration of this point, please refer to the discussion of Section 5.3; particularly the comparison of Figure 5.9(c) and Figure 5.9(d) therein.

5.2 Nonlinear evolution of a rising thermal

Here, the two-dimensional flow of the rising warm thermal in a neutrally-stratified environment is considered.

Description of the model and experimental design

The two-dimensional domain $\mathcal{D}_p$ is assumed in the vertical x-z-plane, whereas the physical dimensions of $\mathcal{D}_p$ are specified as $0 \leq x, z \leq L_0$ with $L_0 = 1200\,\mathrm{m}$. A special setup of the solver is considered. In contrast to the formulation of the default EULAG solver explained in Chapter 2.1, the solver here implements a fully general time-dependent mapping of the coordinates $\mathcal{D}_p \rightarrow \mathcal{D}_t$ according to the functional relationship $\mathcal{F} = (\overline{x}(t,x,z), \overline{z}(t,x,z))$ in (2.2). Therefore, arbitrary two-dimensional moving mesh adaptation can be applied in the vertical plane of the thermal flow, which is presently not possible in the three-dimensional solver EULAG.

The governing transformed model equations in Eulerian flux-form for an assumed inviscid adiabatic nonrotating fluid are written as

$$\frac{\partial(\rho^* u)}{\partial \overline{t}} + \overline{\nabla} \cdot (\overline{\mathbf{v}}^* \rho^* u) = -\rho^* \widetilde{G}_1^1 \frac{\partial \pi'}{\partial \overline{x}} - \rho^* \widetilde{G}_1^3 \frac{\partial \pi'}{\partial \overline{z}} \tag{5.5a}$$

$$\frac{\partial(\rho^* w)}{\partial \overline{t}} + \overline{\nabla} \cdot (\overline{\mathbf{v}}^* \rho^* w) = -\rho^* \widetilde{G}_3^1 \frac{\partial \pi'}{\partial \overline{x}} - \rho^* \widetilde{G}_3^3 \frac{\partial \pi'}{\partial \overline{z}} + \rho^* g \frac{\theta'}{\theta_b} \tag{5.5b}$$

$$\frac{\partial(\rho^* \theta')}{\partial \overline{t}} + \overline{\nabla} \cdot (\overline{\mathbf{v}}^* \rho^* \theta') = -\rho^* \overline{\mathbf{v}}^s \cdot \overline{\nabla} \theta_e \tag{5.5c}$$

$$\overline{\nabla} \cdot (\rho^* \, \overline{\mathbf{v}}^s) = 0 \; . \tag{5.5d}$$

For the small-scale rising thermal flow, the basic-state density is specified with a uniform value of $\rho_b = 1.0\,\mathrm{kg\,m^{-3}}$. The basic-state and ambient-state potential temperature fields are set to $\theta_b = \theta_e = 300\,\mathrm{K}$. Note, with these definitions the anelastic equations (5.5) reduce to the classical Boussinesq set of flow equations (Spiegel and Veronis, 1960); see also Klein (2009). The gravitational acceleration is given as $g = 9.80665\,\mathrm{m\,s^{-2}}$. Boundary conditions at the top and bottom boundaries of the model domain are assumed to be rigid free-slip walls for velocity, while a zero normal flux is applied for θ'. Periodicity is specified for all variables at the lateral boundaries of the domain.

Relative to the neutrally-stratified environment θ_e, an initial thermal anomaly for

the prognostic variable θ' is prescribed as

$$\theta'(0,x,z) = \begin{cases} \delta\theta \left(\dfrac{1+\cos\left(\pi_c \tilde{r}\right)}{2} \right)^2, & \tilde{r} \leq 1 \\ 0 & \tilde{r} > 1 \end{cases} \tag{5.6}$$

with

$$\tilde{r} = 5 \sqrt{\left(\frac{x}{L_0} - 0.5 \right)^2 + \left(\frac{z}{L_0} - 0.2 \right)^2}$$

and the amplitude $\delta\theta = 1\,\mathrm{K}$. The initial flow is at rest $u = w = 0\,\mathrm{m\,s^{-1}}$. Similar setups as the one described here have been previously discussed by Carpenter et al. (1990); Smolarkiewicz and Grabowski (1990); Robert (1993), and in the context of solution-adaptive moving meshing by Dietachmayer and Droegemeier (1992); Fiedler and Trapp (1993).

Fully general solution-dependent moving mesh adaptation by the MMPDEs (4.6) is applied in the vertical plane of $\mathcal{D}_p$, whereby the mesh mapping function (4.1) adopts the form $\mathcal{M} = (x(\bar{t},\bar{x},\bar{z}), z(\bar{t},\bar{x},\bar{z}))$. One-dimensional MMPDEs (4.17) are solved for the distribution of the mesh points along the bottom and top boundary segments of the domain $\mathcal{D}_p$. The mesh relaxation time Θ in (4.7) is set to $\Theta = 60\,\mathrm{s}$.

For the present examination, the mesh adaptation will be based on feature-dependent physical considerations. The dynamics of the rising thermal flow are solely driven by the spatial variation of buoyancy and its advection. In addition, the flow evolution is characterised by localised shear layers and their instabilities. One may argue that the quality of the flow solution obtained with the numerical solver depends critically on the accurate representation of these effects. Therefore, particular mesh refinement indicators Φ_l in (4.15) are specified proportional to the gradient of potential temperature perturbation

$$\Phi_1(t,x,z) = \|\nabla\theta'\| \tag{5.7}$$

and the curl of the physical flow field

$$\Phi_2(t,x,z) = \|\nabla \times \mathbf{v}\|\,, \tag{5.8}$$

i.e. vorticity, where again $\|\cdot\|$ in (5.7) and (5.8) refers to the Euclidean vector norm. Note that although concise symbolic mathematical expressions for the differential operators have been used in (5.7) and (5.8), it is noted that these expressions are evaluated in component form with respect to the transformed coordinates $\overline{\mathbf{x}}$. The

parameter β in (4.15), that controls the strength of the mesh adaptation, is set to $\beta = 0.75$. The smoothing procedure of the monitor function M by (4.16) uses a number of $K = 25$ passes.

As addressed above, the integration procedure of the equation set (5.5) follows that given in Section 2.2. The preconditioned GCR(3) iterative solver is applied to solve the resulting elliptic pressure equation with a convergence threshold specified as $\| (\delta\bar{t}/\rho^*) \, \overline{\nabla} \cdot (\rho^* \overline{\mathbf{v}}^s) \|_\infty < \epsilon = 10^{-5}$. An implicit Richardson preconditioner (see Smolarkiewicz et al. (2004)) with an successive number of 7 iterations is used. As in the scalar advection experiments presented in the previous section, all results in the present section are obtained using the developed MPDATA extension RP (see Table 3.1). Also, the "third-order accurate" variant of the MPDATA advection scheme with FCT enhancement is applied. The integration procedure adopts variable time stepping with a constant maximum Courant number $\mathcal{C}_{max} = 0.5$, while the first two time steps use a constant size of $\delta\bar{t} = 0.5\,\mathrm{s}$. In all simulations that follow, an evolution of the rising thermal over 600 s of integration time is considered. The computations here are conducted in a single processor computing environment.

Results and discussion

Figure 5.4 shows a time sequence of a rising thermal flow simulation using the developed solution-adaptive moving mesh NFT flow solver. Displayed is the solution field of the potential temperature perturbation θ' superimposed by the solution-adaptive moving mesh. In the simulation shown, the domain consists of $\mathrm{N}_c = 94^2$ number of discrete mesh cells. Furthermore, the simulation uses a combination of the mesh refinement indicators (5.7) and (5.8) in the multi-component scalar weighting function (4.15) with $L = 2$. As in the scalar advection problem of the previous section, the MMPDE machinery has again been applied at the initial time $t = 0\,\mathrm{s}$ to adapt the mesh with respect to the specified monitor function M until a steady state is attained. This is seen in Figure 5.4(a), where a strongly refined mesh is provided in the region of the prescribed thermal anomaly. Because the initial flow is at rest and therefore has zero vorticity, the mesh adaptation at this stage is only based on the gradient of potential temperature via (5.7). This changes with the start of the simulation. As the warm thermal begins to rise, thin layers of large vorticity develop along its lateral and rear faces with the environment (not shown). In the consecutive evolution of the flow, these thin vorticity sheets lead to instabilities and a subsequent growth of fine-scale eddies, see for instance Figure 5.4(e) at the simulation time $t = 500\,\mathrm{s}$. Afterwards at $t = 600\,\mathrm{s}$ in Figure 5.4(f), the thermal breaks

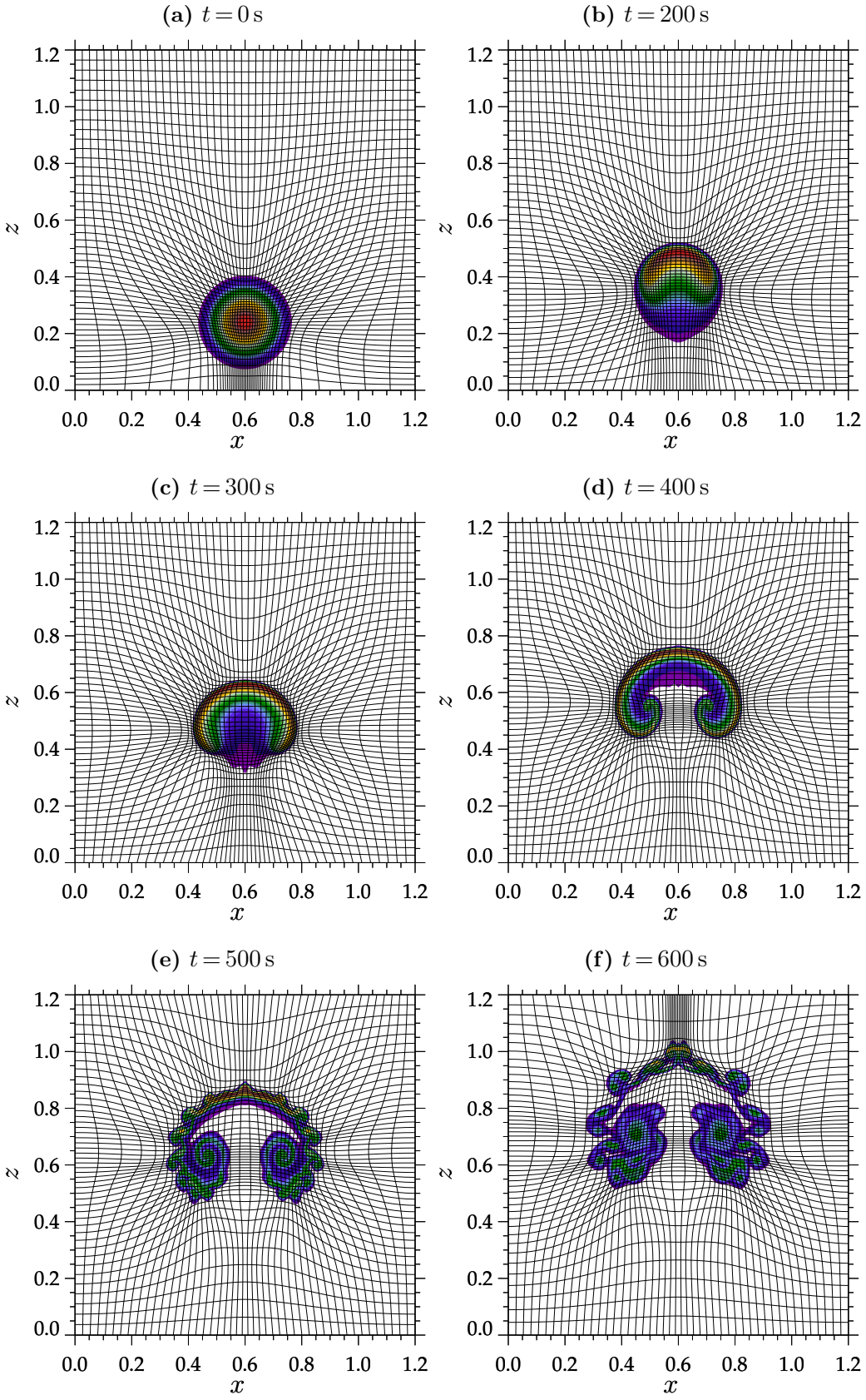

Figure 5.4: Mesh adaptation sequence from a rising thermal flow simulation shown in the full domain. Indicated are contours of potential temperature perturbation θ' (shaded; warmer colours correspond to a higher temperature), overlaid by the solution-adaptive mesh (solid lines; only every 2nd mesh line is drawn). Horizontal distance x and height z are given in km.

up into more irregular vortical motions.

Over the entire course of the simulation, the solution-adaptive moving mesh NFT flow solver continuously provides an increased local numerical resolution in the relevant region of the rising thermal and particularly along the unstable interface between the thermal and the ambient air. The gradients of the solution fields along the edges of the rising thermal are locally very large; e.g. see Figure 5.4(c) and Figure 5.4(d); which, according to the mesh refinement indicators (5.7) and (5.8), leads to a sharp structure of the monitor function M (not shown). As a consequence of this sharp structure in the monitor function M in that region, a comparatively large number of $K = 25$ smoothing passes of M (instead of the typical numbers $K \approx 15$) is applied to obtain a more gradual, i.e. a smoother, change of the resolution.

Nevertheless, the overall changes in the local mesh size over the domain are quite large; typical values of the ratio of the smallest to the largest mesh cell area is 1/30. Despite the presence of these strong mesh adaptations, the solution-adaptive moving mesh NFT flow solver runs stable and efficiently. For the applied convergence threshold $\| (\delta\overline{t}/\rho^*)\, \overline{\nabla} \cdot (\rho^* \overline{\mathbf{v}}^s) \|_\infty < \epsilon = 10^{-5}$ in the iterative solution of the underlying elliptic pressure equation, an average number of 10 GCR iterations was required. A comparable simulation with a static, i.e. non-adaptive, uniform mesh takes an average number of 4 GCR iterations. This difference is quite acceptable considering the spatial and temporal variability of the coefficients in the elliptic pressure equation (cf. (2.23)) introduced by the solution-adaptive mesh geometry. It is added that for a lower number of $K \approx 15$ smoothing passes of the monitor function M, an average number of 25 GCR iterations may be required in the iterative solution of the elliptic pressure equation. Again, although large gradients are present in the solution variables, no spurious oscillations are produced by the numerical solver. Furthermore, the design of the flow configuration is perfectly symmetric about the middle vertical axis of the domain, and this symmetry is maintained in all prognostic solution variables with the order of 10^{-6}. [1] It is added here, that the symmetry of the prognostic variables is related to the convergence threshold ϵ (4.21) of the GCR iterative solver applied in the solution of the MMPDEs (4.6). This means that the symmetry depends on how accurately the positions of the solution-adaptive moving mesh are determined. Note, the symmetry of the obtained prognostic variables in the static uniform mesh simulations is at the order of machine precision.

Figure 5.5 compares, after an integration time of $t = 350\,\mathrm{s}$, the computed results for

[1] This is true whether the imposed periodic boundary conditions or non-periodic, i.e. rigid walls, are assumed in the horizontal.

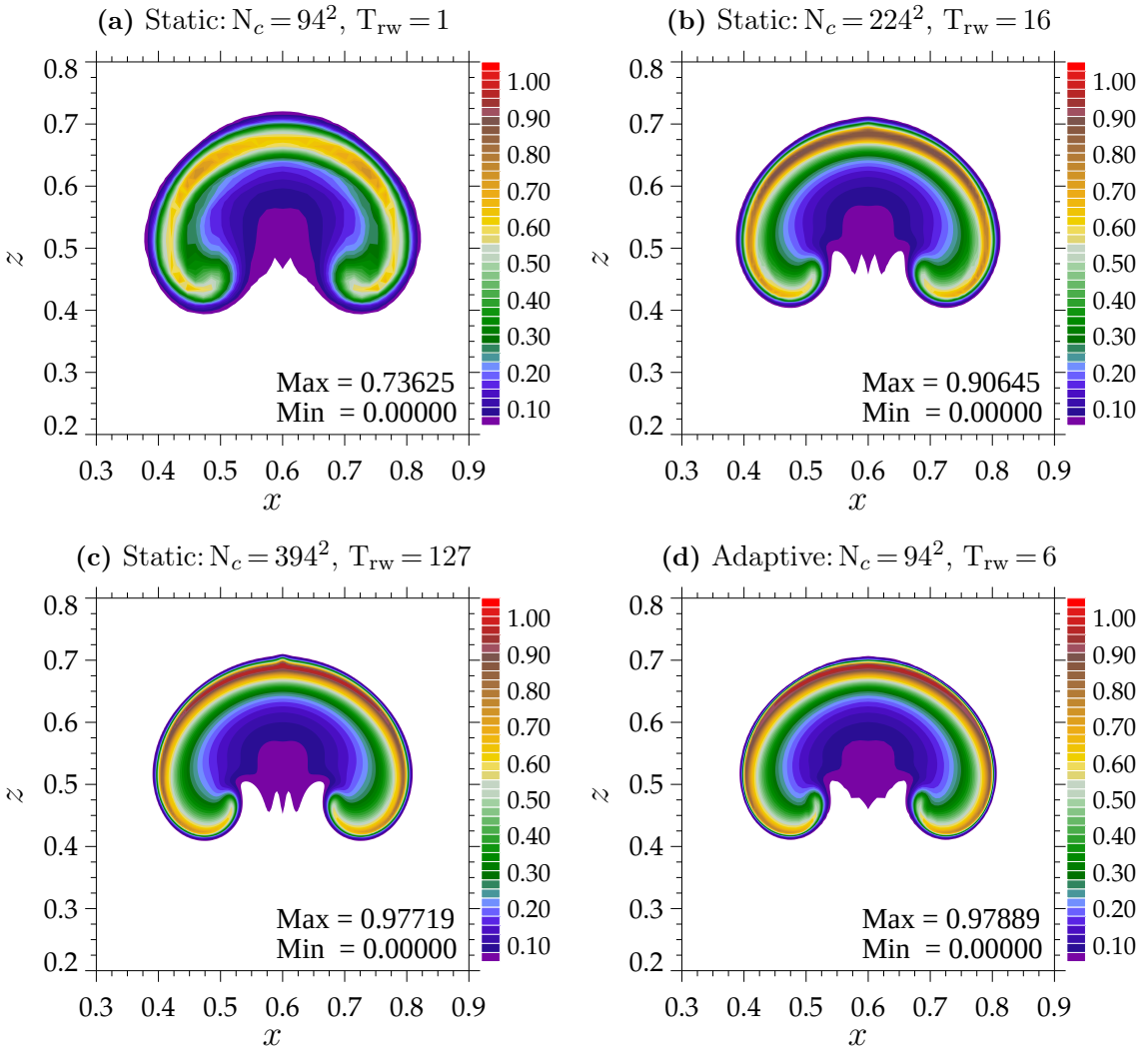

Figure 5.5: Comparison of results from rising thermal flow simulations with a static uniform (non-adaptive) mesh of various resolutions (a)-(c) against the integration that employed solution-adaptive meshing (d), all at the simulation time $t = 350\,\mathrm{s}$. Shown are contours of potential temperature perturbation θ' (K, shaded). Domain maximum and minimum values of θ' are given in the lower right part of the figure. The symbol N_c refers to the number of mesh cells, and T_{rw} is the relative wall clock time with respect to the low-resolution static uniform mesh run with $N_c = 94^2$ in (a). Horizontal distance x and height z are given in km.

the θ' field from the solution-adaptive moving mesh run against non-adaptive static uniform mesh runs of various resolutions. At this stage of the simulation, the rising thermal is still in a laminar phase of its evolution. The initially circular thermal has been stretched into a thin structure by the action of horizontal variations in the buoyancy field, i.e. $\partial\,(g\,\theta'/\vartheta)/\partial x$. As noted in Klein (2009), due to the symmetry of the problem about the middle vertical axis the maximum of the potential temperature perturbation θ' should remain located at the vertical symmetry line. Furthermore, the maximum of θ' should not decrease from its initial value in the

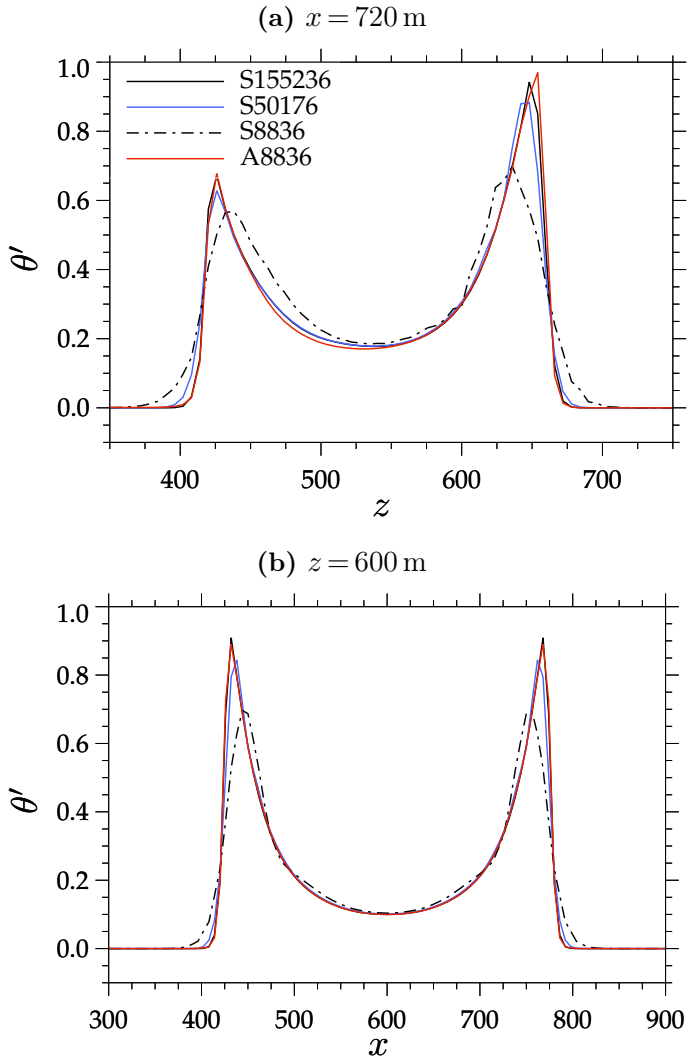

Figure 5.6: Profiles of potential temperature perturbation θ' obtained from various rising thermal flow simulations after $t = 350\,\mathrm{s}$ of integration time: (a) along the vertical direction at $x = 720\,\mathrm{m}$, (b) along the horizontal direction at $z = 600\,\mathrm{m}$; please refer to Figure 5.5 for the relative position of the rising thermal. The various simulations shown differ in the underlying mesh (S: static uniform, A: solution-adaptive), while number following the characters S and A indicates the number of mesh cells N_c used.

present configuration. In Figure 5.5, the static uniform mesh runs in (a) and (b) show two slight extrema of θ' some finite distance away from the symmetry line, while the higher-resolution static uniform mesh run in (c) and the solution-adaptive moving mesh run in (d) maintain a maximum around the centre of the domain. The maximum value of θ' at the initialisation time $t = 0\,\mathrm{s}$ is 1. The higher the resolution of the static uniform mesh runs in Figure 5.5(a)-(c) the more accurate is the preservation of the initial maximum value of θ' and the lower is the overall dissipative error of the solution (i.e. the less smeared does the θ' solution field appear). The

solution-adaptive moving mesh run with $N_c = 94^2 = 8836$ number of mesh cells in Figure 5.5(d) achieves a preservation of the initial θ' maximum that is similar to the static uniform mesh run in Figure 5.5(c), while the latter uses a factor of ~ 17 more mesh cells and a factor of ~ 21 more computing (wall clock) time T_w, respectively. Moreover, the edges of the θ' solution field appear sharper in the solution-adaptive moving mesh run when compared to all static uniform mesh runs.

Figure 5.6 complements the presentation of the results of Figure 5.5 by showing profiles of θ' along vertical and horizontal sections through the rising thermal at the same the integration time $t = 350\,\mathrm{s}$. The profiles in Figure 5.6 were derived using bilinear interpolation of the θ' solution field from the underlying mesh in each of the runs given in Figure 5.5. In both sections of Figure 5.6(a) and Figure 5.6(b), the profiles obtained from the solution-adaptive moving mesh run A8836 match closely the profiles obtained from the highest-resolution static uniform mesh run S155236. In contrast, the profiles obtained from the lower-resolution static uniform mesh run S8836 and also the run S50176 show significantly larger deviations from the profiles of S155236 than the solution-adaptive moving mesh run A8836. The results in Figure 5.6 demonstrate explicitly the ability of the solution-adaptive moving mesh solver to represent the steep gradients and sharp local maxima in the θ' solution field by using only a comparatively low total number of mesh cells.

At the later stage $t = 600\,\mathrm{s}$ of the rising thermal simulation shown in Figure 5.7 the flow has become much more complex. A quantitative assessment of the solution quality at this stage may use the analysis of relevant statistical quantities, which is however not performed here. From a qualitative view, the morphology of the obtained θ' solution field in the solution-adaptive moving mesh run shown in (d) basically resembles the θ' solution field obtained with the high-resolution static uniform mesh run in (c), but the θ' field appears much more smeared in the solution-adaptive moving mesh run in (d). The solution-adaptive moving mesh run is not able to resolve the fine details present in the θ' solution field as obtained with the static uniform mesh run in (c). However, note that the onset of the interfacial shearing instabilities and the transition from the laminar to the turbulent phase is not captured at all in the low resolution static uniform mesh run shown in (a).

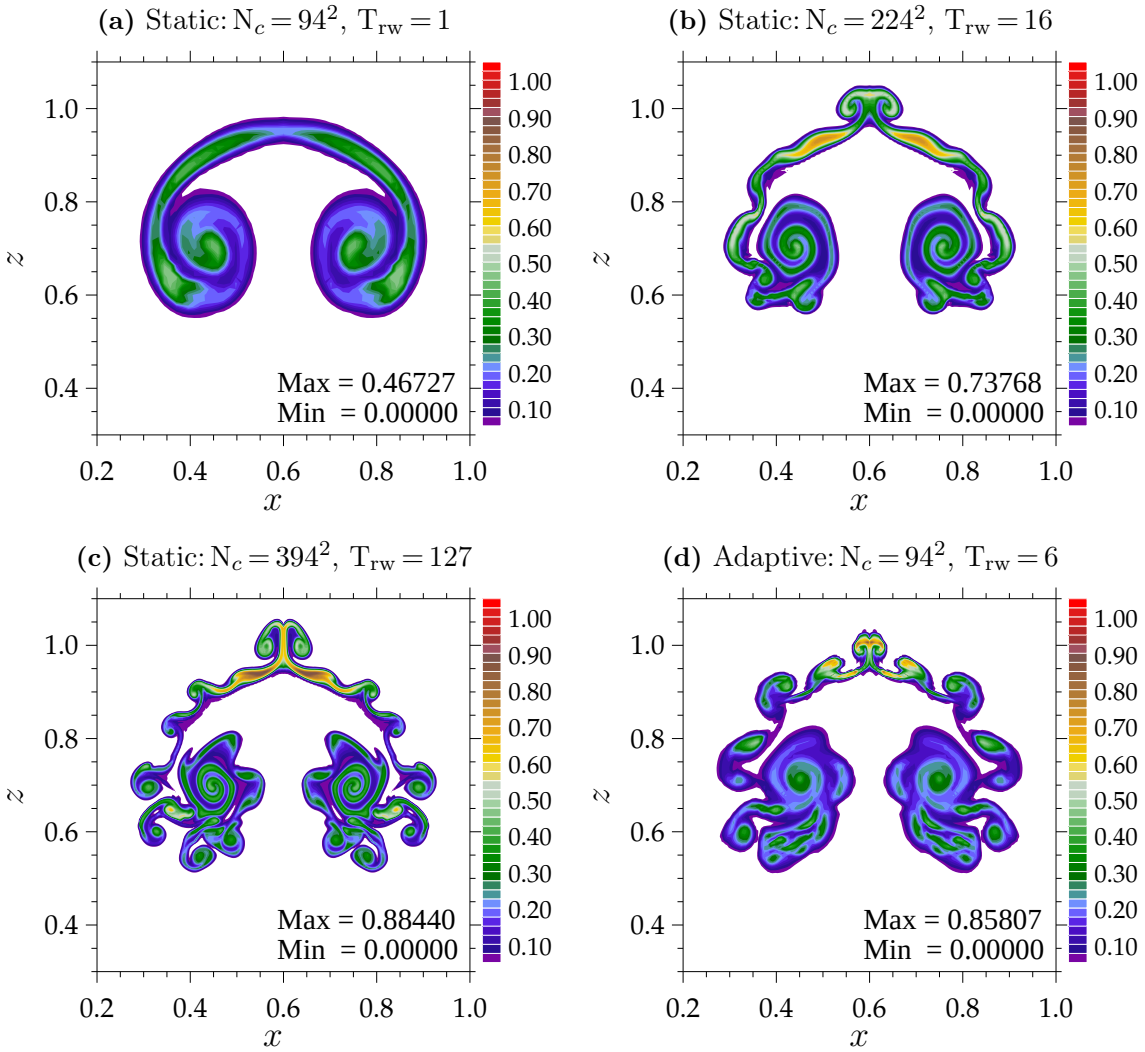

Figure 5.7: Comparison of results from rising thermal flow simulations with a static uniform (non-adaptive) mesh of various resolutions (a)-(c) against the integration that employed solution-adaptive meshing (d), all at the simulation time $t = 600\,\mathrm{s}$. Shown are contours of potential temperature perturbation θ' (K, shaded). Domain maximum and minimum values of θ' are given in the lower right part of the figure. The symbol N_c refers to the number of mesh cells, and T_{rw} is the relative wall clock time with respect to the low-resolution static uniform mesh run with $N_c = 94^2$ in (a). Horizontal distance x and height z are given in km.

5.3 Compatibility of MPDATA with the GMCL

In Section 3.1, the MPDATA scheme has been analysed in terms of the compatibility with the GMCL (3.2). There, the various implementations of MPDATA are discussed on the basis of a theoretical analysis along with elementary numerical experiments using analytically prescribed oscillating moving meshes. Here, the importance of the compatibility of the MPDATA advective scalar transport with

the GMCL is further investigated in the framework of the solution-adaptive moving mesh solver. As in the preceding two sections, the scalar advection and the nonlinear flow of the rising thermal will serve as model problems for the examination.

Scalar advection

Figure 5.8 compares the solution quality in terms of the various MPDATA algorithmic implementations (a) OS, (b) RS, and (c) RP (see Table 3.1), using the scalar advection problem described in Section 5.1. Recall, the scheme RP has been applied in all experiments of Section 5.1 as the default scheme.

The comparison in Figure 5.8 now shows that the MPDATA implementations OS and RS yield considerably larger errors in the L_2 and L_∞ error norms than with the implementation RP. The errors in the solution are largest with the original MPDATA implementation OS. The reduction in the L_2 error norm from the use of the newly developed implementation RP instead of OS is about at a factor of ~ 4 for the present experiment. As in the experiments of Section 3.3, the redefined pseudo-velocities in MPDATA applied in the scheme RS yields a significant improvement over the original MPDATA scheme in the scheme OS. However, full compatibility with GMCL is achieved only with the implementation RP that enforces validity of the discrete GMCL (3.4) by adopting the prognostic approach for correction of the generalised density ρ^{*n+1} in the algorithm. The scheme RP yields L_2 error magnitudes that are reduced by a factor of ~ 3 over RS.

In addition, the MPDATA implementations OS and RS suffer from a major loss of the solution monotonicity. For instance, spurious minima (see the dashed contour lines) exist using the scheme OS in Figure 5.8(a) which undershoot the analytical minimum of the solution at about 5 percent of the main hill's amplitude. Even 15 percent undershoots are observed in slightly modified model configurations, e.g. using only a different number of mesh cells N_c. Note, these significant errors in the solution monotonicity occur despite the FCT enhancement is applied to the MPDATA scheme. In contrast, the MPDATA implementation RP in Figure 5.8(c) provides a solution that is completely free of spurious extrema.

Maximum values of the GMCL error $\|r_{gmcl}\|_\infty$ (3.22) are analysed. As discussed in Section 3.1 (see the consecutive paragraph to the formula (3.4)) and Section 3.3, the standard independent evaluation of the quantities that enter the discrete GMCL (3.4) as applied in the schemes OS and RS does not ensure (3.4) itself to be satisfied. Here, it is found that $\|r_{gmcl}\|_\infty \sim 10^{-2}$ in the simulations with the schemes OS

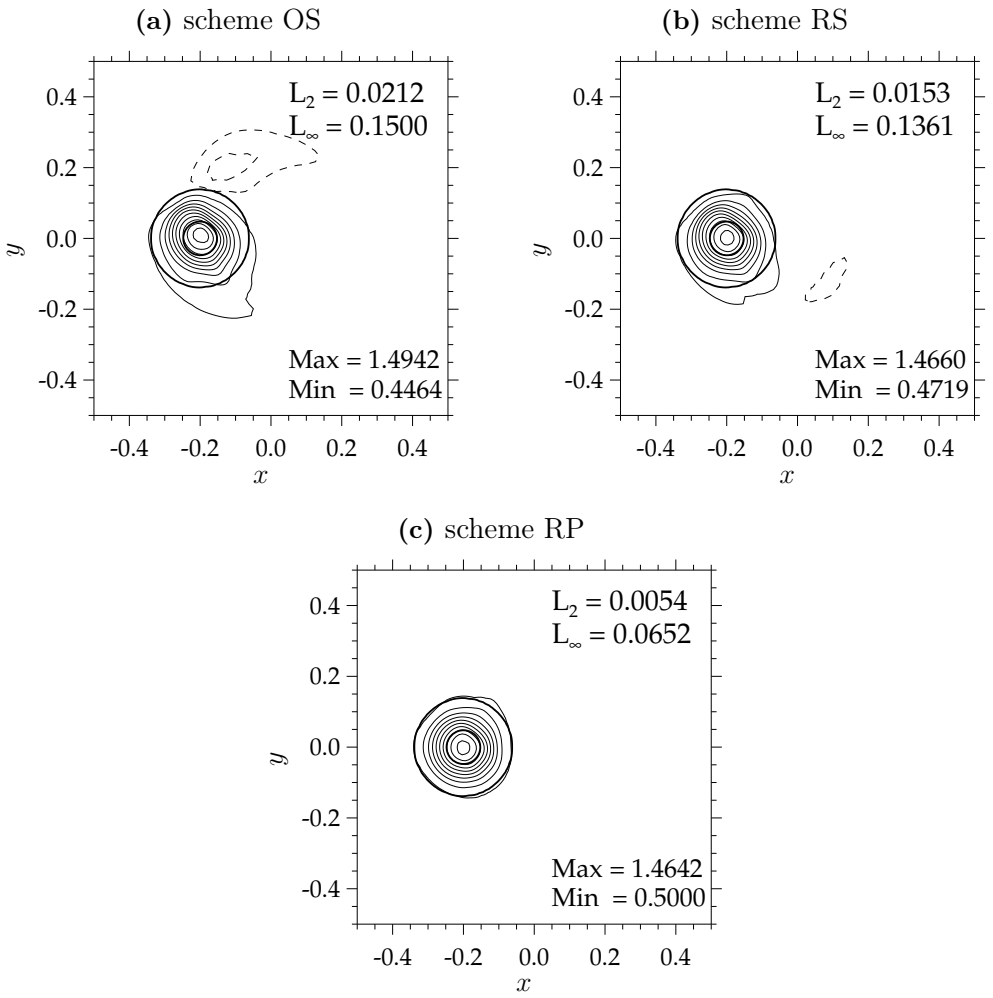

Figure 5.8: Comparison of results between the various MPDATA implementations (a) OS, (b) RS, and (c) RP (see Table 3.1) for the solution-adaptive moving mesh simulation of the scalar advection problem given in Chapter 5.1. As in Figure 5.2, but here contours for ψ lower than the initial minimum value of 0.5 are added (dashed lines; contour values of 0.45 and 0.475).

and RS. This magnitude of $\|r_{gmcl}\|_\infty \sim 10^{-2}$ is considerably larger than the typical values obtained for $\|r_{gmcl}\|_\infty$ under the analytically prescribed oscillating meshes in Table 3.3, which were at the order of 10^{-6}. This explains the relatively larger errors in the MPDATA solution for the present solution-adaptive moving mesh experiments observed in Figure 5.8(a) and Figure 5.8(b).

Rising thermal flow

The discussion of the preceding subsection is continued here by using the rising thermal flow configuration described in Section 5.2. Figure 5.9 compares the θ' so-

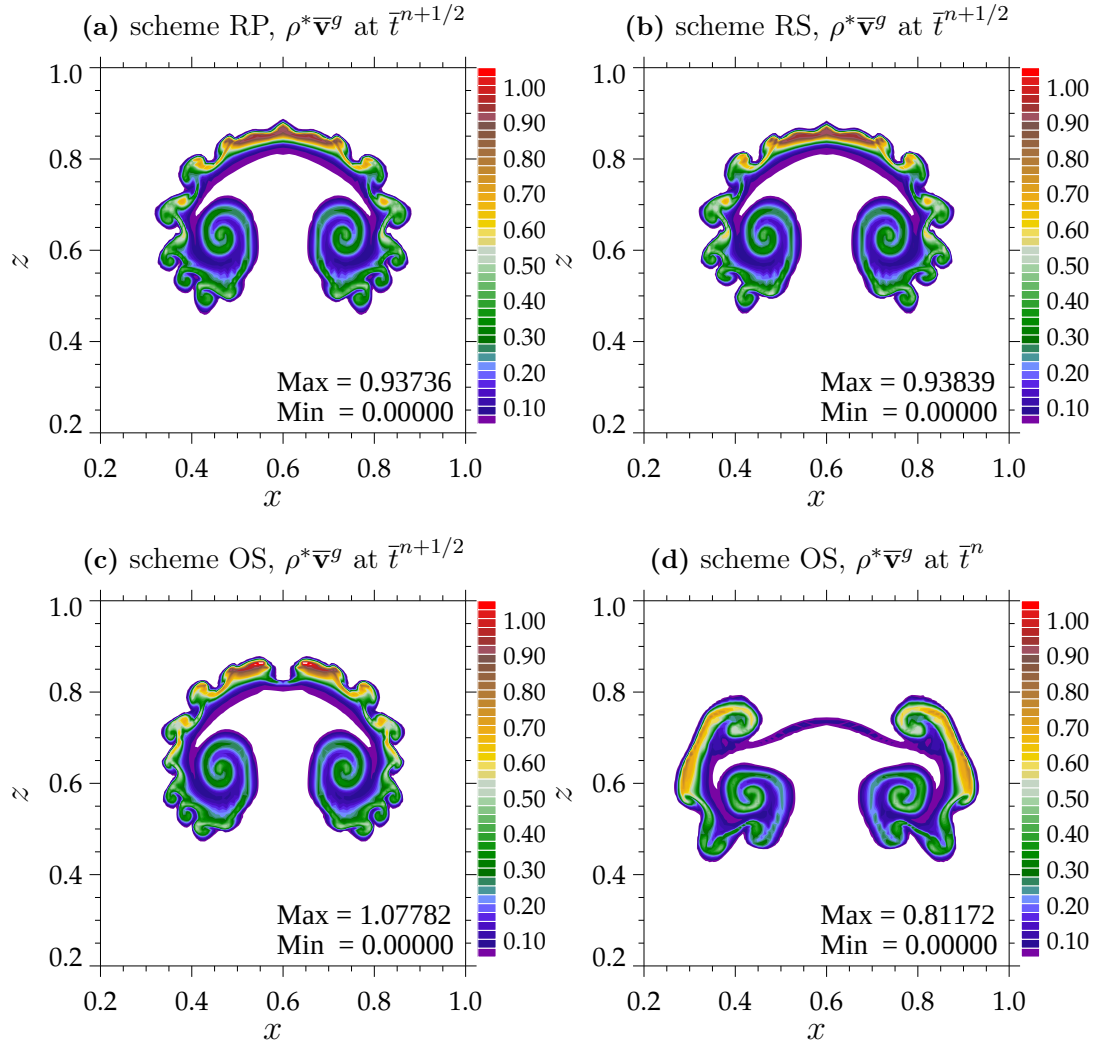

Figure 5.9: Comparison of results between various MPDATA implementations for the solution-adaptive moving mesh simulation of the rising thermal flow given in Chapter 5.2 at the simulation time $t = 500\,\mathrm{s}$. Applied are the schemes RP (a), RS (b), and OS (c) with the procedure (4.25)-(4.28) to approximate the generalised contravariant mass flux $(\rho^*\overline{\mathbf{v}}^*)^{n+1/2}$ in MPDATA, i.e. with $\rho^*\overline{\mathbf{v}}^g$ evaluated at $\overline{t}^{n+1/2}$. The scheme OS in (d) adopts the procedure (4.22)-(4.24) to obtain $(\rho^*\overline{\mathbf{v}}^*)^{n+1/2}$, i.e. with $\rho^*\overline{\mathbf{v}}^g$ evaluated at $\overline{t}^{n}$. See Chapter 3.1 (Table 3.1) and Chapter 4.4 for the detailed specification of the various schemes. Otherwise as in Figure **??**.

lution fields obtained using various MPDATA algorithmic implementations in the integration of the system (5.5). Given are results for the MPDATA implementation (a) RP, (b) RS, and (c) OS. These simulations in (a), (b), and (c) apply the revised procedure (4.25)-(4.28) to approximate the generalised contravariant mass flux $(\rho^*\overline{\mathbf{v}}^*)^{n+1/2}$ in MPDATA, i.e. with the mesh velocity $\rho^*\overline{\mathbf{v}}^g$ evaluated at $\overline{t}^{n+1/2}$. The solution given in Figure 5.9(d) corresponds to the scheme OS of Figure 5.9(c), but $(\rho^*\overline{\mathbf{v}}^*)^{n+1/2}$ instead approximated by means of the procedure (4.22)-(4.24), i.e. with

$\rho^*\overline{\mathbf{v}}^g$ evaluated at $\overline{t}^n$. Note also here, the scheme RP with the revised procedure (4.25)-(4.28) to approximate $(\rho^*\overline{\mathbf{v}}^*)^{n+1/2}$ has been applied as the default scheme in the preceding simulations of Section 5.2.

In Figure 5.9, the θ' solution fields obtained with the schemes RP in (a) and RS (b) appear qualitatively very similar and show the expected evolution of the rising thermal. In contrast, the result obtained with the scheme OS in (c) differs significantly from the results with the schemes RP and RS. In particular, the structure of the rising thermal has started to break apart from the vertical symmetry axis in its upper part, which does not represent an expected solution behaviour for the present flow configuration. Furthermore, unphysically large θ' values greater than $\theta' = 1$ occur with the scheme OS in the upper part of the rising thermal in (c). The θ' solution field in (d) evolves even more different from what is expected, with the thermal completely torn apart from the middle vertical axis.

The computed maximum GMCL error (3.22) in the simulations with the schemes RS and OS both yield $\|r_{gmcl}\|_\infty = 2.03 \times 10^{-3}$. However, the quality of the obtained solution is significantly lower with the original scheme OS in (c) than with redefined scheme RS in (b). This again indicates the advantage of using MPDATA with the redefined pseudo-velocities under moving meshes.

For the simulation in Figure 5.9(d), the computed maximum GMCL error (3.22) amounts to $\|r_{gmcl}\|_\infty = 7.60 \times 10^{-1}$. This value is considerably larger than the value of $\|r_{gmcl}\|_\infty = 2.42 \times 10^{-3}$ observed in the simulation of Figure 5.9(c). Recall, both simulations in (c) and (d) use the identical scheme OS, but adopt the different procedures to approximate the generalised contravariant mass flux $(\rho^*\overline{\mathbf{v}}^*)^{n+1/2}$ in MPDATA. Therefore, the results in (c) and (d) demonstrate the advantage of using the revised procedure (4.25)-(4.28), i.e. evaluating $\rho^*\overline{\mathbf{v}}^g$ at $\overline{t}^{n+1/2}$, instead of using the procedure (4.22)-(4.24), i.e. evaluating $\rho^*\overline{\mathbf{v}}^g$ at $\overline{t}^n$, to approximate $(\rho^*\overline{\mathbf{v}}^*)^{n+1/2}$ in MPDATA under solution-adaptive moving meshes because the former procedure yields considerably lower errors in terms of the discrete GMCL. Note, similar conclusions are drawn from the comparison presented in Figure 5.3.

Finally, the results obtained with the scheme RS in Figure 5.9(b) seem to be fairly insensitive to the large errors $\|r_{gmcl}\|_\infty = 2.42 \times 10^{-3}$. Key aspects for the robustness of the solution in terms of these errors are the enforcement of the anelastic mass continuity $\| (\delta\overline{t}/\rho^*)\, \overline{\nabla} \cdot (\rho^*\overline{\mathbf{v}}^s) \|_\infty < \epsilon$ for the velocity components v^j, and the special sign-preserving property of MPDATA in the transport of θ' that is valid independent of the compatibility of the scheme; see also Section 3.4.

5.4 Summary

In Section 5.1, a solution-adaptive moving mesh NFT solver based on MPDATA for the advection of a passive scalar in a prescribed shear flow was implemented and applied. For the adopted experimental configuration from Blossey and Durran (2008), validation of the results was possible by means of an available analytical solution after each cycle of the time-periodic flow field. It was found that the application of the solution-adaptive moving mesh solver clearly outperforms the solver with a uniform mesh. For example, the solution-adaptive moving mesh solver with $\mathrm{N}_c = 50^2$ mesh cells provided more than 20 % lower L_2 and L_∞ error norms than the solver employing a uniform mesh with $\mathrm{N}_c = 250^2$ mesh cells (Figure 5.2). Thereby, the uniform mesh run required a factor of 26 more wall clock (computing) time T_w than the solution-adaptive moving mesh run. The use of the solution-adaptive moving mesh was essential to resolve the large local gradients in the transported scalar ψ evolving in the time-dependent shear flow. The scalar advection configuration was also employed to demonstrate the higher accuracy of the revised scheme for the approximation of the advective contravariant mass flux $(\rho^* \overline{\mathbf{v}}^*)^{n+1/2}$ in MPDATA as proposed in Section 4.4 (Figure 5.3).

In Section 5.2, an anelastic NFT flow solver with a fully two-dimensional solution-adaptive moving mesh capability in the vertical simulation plane was implemented and applied to the idealised flow of the rising warm thermal. In contrast to the scalar advection configuration of Section 5.1, no analytical solution is available for this flow. A comparison of the solution-adaptive moving mesh solver with the solver employing a uniform mesh was conducted for the laminar phase of the rising thermal. In particular, it was found that the solution-adaptive moving mesh solver preserves the maximum values of the potential temperature perturbation θ' associated with the thermal much better and retains the large gradients of θ' at the interface between the thermal and the ambient air. In these aspects of the solution, the solution-adaptive moving mesh solver with $\mathrm{N}_c = 94^2$ mesh cells provided results comparable to the solver employing a uniform mesh with $\mathrm{N}_c = 394^2$ mesh cells (Figure 5.6). Another noteworthy aspect is that, despite the relatively strong adaptations of the mesh that were applied in the rising thermal flow simulations, the convergence properties of the iterative GCR solver for the elliptic pressure equation in the anelastic system were excellent. Although in the turbulent phase that appears later, the morphology of the θ' solution field obtained from the solution-adaptive moving mesh run with $\mathrm{N}_c = 94^2$ basically resembled the one obtained from the solver employing a uniform mesh with

$N_c = 394^2$ mesh cells, the θ' field appeared smeared in the solution-adaptive moving mesh run (Figure 5.7).

In Section 5.3, the subject of the compatibility of the MPDATA scheme with the GMCL (discussed before in Chapter 3) was investigated in the context of the solution-adaptive moving mesh NFT solver, using the two experimental configurations of Sections 5.1 and 5.2. The conducted tests showed that the original formulation of the Eulerian MPDATA integration suffered unacceptably large errors under numerically-generated solution-adaptive moving meshes (Figure 5.8). The error magnitudes observed were considerably larger than under the prescribed oscillating moving meshes considered in the experiments of Section 3.4. The tests further demonstrated that the extensions to the MPDATA integration developed in Chapter 3 and in Section 4.4 are extremely useful to obtain accurate results under moving meshes.

Chapter 6

Solution-adaptive moving mesh simulations with EULAG

A characteristic example of atmospheric flows is that of synoptic-scale mid-latitude weather systems (i.e. cyclones and anticyclones). The transient weather systems are steered by the smooth large-scale flow of the planetary Rossby waves meandering zonally around the globe. In addition, the weather systems are also coupled with various smaller-scale processes. These include a variety of embedded phenomena such as fronts, jets, internal gravity waves, (organised) moist convection, or microscale phenomena like clear-air turbulence (recall the discussion to Figure 1.1 in the introductory chapter). The task of representing the inherent multiscale interactions in numerical models requires extremely high resolution, and the associated computational costs are huge. Adaptive (moving) meshes can provide a means to significantly improve the representation of these flows without increasing the computational cost.

Here, the solution-adaptive moving mesh solver is applied in EULAG to simulate multiscale interactions in atmospheric flows in an idealised, but realistic, setting. In Section 6.1, dry baroclinic wave life cycle experiments in a periodic zonal channel are conducted that reflect the basic evolution of mid-latitude weather systems in the real atmosphere. The applied model configuration describes the evolution of a baroclinic instability of an initially balanced straight zonal jet flow that is excited by means of a temperature perturbation. The term *baroclinic instability* refers to a hydrodynamic wave instability that arises in rotating stratified fluids that are subject to a horizon-

tal temperature gradient[1]. The baroclinic wave instability extracts its energy from the available potential energy associated with the horizontal temperature gradient of the mean jet flow, see e.g. Gill (1982); Holton (1992). Synoptic-scale mid-latitude weather systems in the real atmosphere are a manifestation of the baroclinic instability of the tropospheric jet streams. The associated north-south temperature gradient is a result of the differential diabatic heating between the poles and the equator.
Idealised dry baroclinic wave life cycles as the one simulated here exhibit many remarkably realistic features. Previous works have used similar configurations to investigate physical aspects like the dynamics of fronts, e.g. Rotunno et al. (1994), the formation of tropopause folds, e.g. Bush and Peltier (1994), the spontaneous generation and propagation of internal gravity waves, e.g. Zhang (2004); Plougonven and Snyder (2005, 2007), the sharpness of the tropopause (Wirth and Szabo, 2007), among others. Typically, uniform mesh solvers or solvers with prescribed grid nesting in certain regions, e.g. Zhang (2004), were applied in the previous works. To the author's knowledge, adaptive moving mesh methods are applied in the present thesis for the first time to simulate a synoptic-scale baroclinic wave life cycle.

The investigation in Section 6.1 is concerned with the question of whether the adaptive moving mesh solver is basically suitable to simulate accurately the complex flow of the baroclinic wave life cycle. For the assessment, the results of the adaptive solver are compared with reference results obtained from high-resolution uniform mesh simulations. The simulated flow is studied in terms of the representation of features like fronts and mesoscale internal gravity waves excited at the later stages of the baroclinic wave evolution. In addition, integral (statistical) measures of kinetic energetics are used for the analysis. It is anticipated that in simulations using a uniform mesh, mesoscale internal gravity waves with a horizontal wave length of ≈ 220 km are only represented at a horizontal mesh increment size $\Delta \approx< 40$ km. Here, it is examined whether an adaptive moving mesh simulation with a lower base resolution can adequately represent the mesoscale internal gravity waves. Moreover, a principal question in the solution-adaptive moving mesh simulations is how to specify mesh refinement criterion. The latter represents a completely open research issue for the adaptive mesh simulation of atmospheric flows.

The essential aspects of the analytical and numerical formulation of EULAG are

[1]The term *baroclinic* indicates a fluid where temperature gradients exist on isobaric, i.e. constant pressure, surfaces. Due to hydrostatic-geostrophic balance, a meridional temperature decrease in the northern hemisphere is associated with an increase of eastward winds (jet flows) with height, see e.g. Holton (1992).

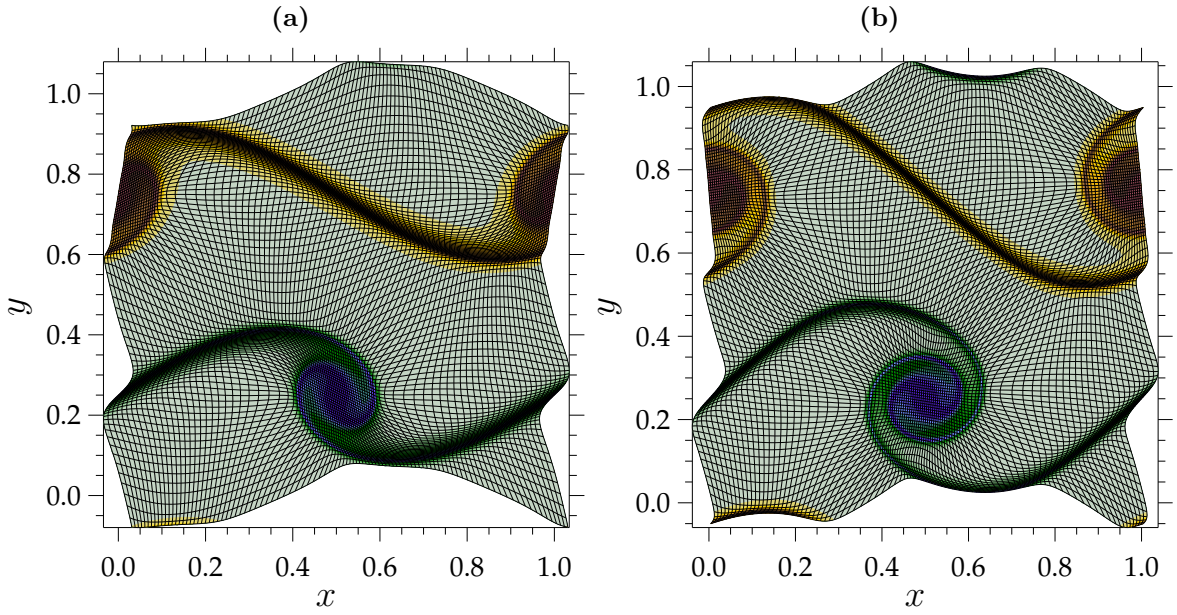

Figure 6.1: Solution-adaptive moving mesh simulation of an inviscid double-shear layer (Kelvin-Helmholtz) instability in a fully periodic domain in x and y using the flow configuration from Bell et al. (1989). The refinement indicator Φ for the solution-adaptive mesh is specified to be proportional to the vorticity $\|\nabla \times \mathbf{v}\|$. Indicated are contours of vorticity (shaded; warmer colours correspond to a larger values of vorticity), superimposed by the solution-adaptive moving mesh (black solid lines) at two selected stages of the flow evolution.

reviewed in Chapter 2. Moreover, the present implementation of EULAG adopts a number of extensions to the default EULAG model developed in the previous chapters of this thesis. These encompass, inter alia, the extension of the Eulerian flux-form advection scheme MPDATA to enable full compatibility with the GMCL under arbitrary moving meshes (Section 3.1), along with the revised predictor scheme for the generalised advective contravariant mass flux in MPDATA (Section 4.4). The MMPDE machinery that performs the solution-adaptive moving mesh generation is described extensively in Chapter 4. Finally, the algorithmic structure that underlies the present implementation, which differs from the default EULAG, is outlined in the flowchart of Figure 4.2.

The development and testing of the above algorithmic elements is conducted in the previous Chapter 5. The incorporation of these elements into the three-dimensional parallel modelling framework of EULAG also underwent numerous test experiments, which are however not discussed here in detail. As only one particular example, Figure 6.1 illustrates the consistent implementation of periodic boundary conditions in the solution-adaptive moving mesh scheme using the double-shear layer instability test problem of Bell et al. (1989).

6.1 Baroclinic wave life cycle experiments

In this section, the nonlinear evolution of a synoptic-scale baroclinically unstable jet flow in a periodic channel on the f-plane[1] is considered as a first application for the solution-adaptive moving mesh solver in EULAG. Apart from assuming dry and inviscid adiabatic dynamics in a rectangular channel geometry, the adopted flow configuration will encompass a fully three-dimensional baroclinic wave life cycle over several days of its evolution.

Description of the model and experimental design

The simulation physical domain $\mathcal{D}_p$ describes a straight channel geometry of length $0 \leq x \leq L_x$ with $L_x = 10000\,\mathrm{km}$ that is periodic in the direction of x. The width of the channel is $L_y = 8000\,\mathrm{km}$ while $-L_y/2 \leq y \leq L_y/2$, and its depth is set to $H = 18\,\mathrm{km}$ with $0 \leq z \leq H$. Rigid free-slip boundaries confine the channel in the transverse direction y and in the vertical direction z. The transformation of the horizontal coordinates x and y assumes the general form as given by (2.9), while the identity transformation $\overline{z} \equiv z$ is applied in the vertical (i.e. no vertical stretching of the coordinate $\overline{z}$).

For the simplicity of the present examination, an inviscid adiabatic fluid is considered, thus adopting only the most basic configuration of EULAG. The specific form of the governing anelastic equations with respect to the transformed space $\mathbf{S}_t$ are given as

$$\frac{\partial(\rho^* u)}{\partial \bar{t}} + \overline{\nabla} \cdot (\overline{\mathbf{v}}^* \rho^* u) = -\rho^* \widetilde{G}_1^1 \frac{\partial \pi'}{\partial \overline{x}} - \rho^* \widetilde{G}_1^2 \frac{\partial \pi'}{\partial \overline{y}} + \rho^* f\,(v - v_e) \tag{6.1a}$$

$$\frac{\partial(\rho^* v)}{\partial \bar{t}} + \overline{\nabla} \cdot (\overline{\mathbf{v}}^* \rho^* v) = -\rho^* \widetilde{G}_2^1 \frac{\partial \pi'}{\partial \overline{x}} - \rho^* \widetilde{G}_2^2 \frac{\partial \pi'}{\partial \overline{y}} - \rho^* f\,(u - u_e) \tag{6.1b}$$

$$\frac{\partial(\rho^* w)}{\partial \bar{t}} + \overline{\nabla} \cdot (\overline{\mathbf{v}}^* \rho^* w) = -\rho^* \frac{\partial \pi'}{\partial \overline{z}} + \rho^* g \frac{\theta'}{\theta_b} - \rho^* \alpha\, w \tag{6.1c}$$

$$\frac{\partial(\rho^* \theta')}{\partial \bar{t}} + \overline{\nabla} \cdot (\overline{\mathbf{v}}^* \rho^* \theta') = -\rho^* \overline{\mathbf{v}}^s \cdot \overline{\nabla} \theta_e - \rho^* \alpha\, \theta' \tag{6.1d}$$

$$\overline{\nabla} \cdot (\rho^* \overline{\mathbf{v}}^s) = 0\ . \tag{6.1e}$$

Terms in (6.1) that do not explicitly appear in the system (2.3) are Rayleigh-type

[1] An f-plane refers to a tangential plane to the Earth's surface on which a constant Coriolis parameter f is assumed.

forces proportional to a relaxation parameter α. These terms in (6.1c) and (6.1d) are used to simulate a gravity wave-absorbing layer near the upper boundary of the model domain. The relaxation parameter α describes an inverse time scale that is specified here to increase linearly from a value of zero at 2 km below the top boundary to $600^{-1}\,\mathrm{s}^{-1}$ at the boundary.

The horizontally-homogeneous hydrostatic basic-state profiles of the density ρ_b and potential temperature θ_b in the system (6.1) are computed using a constant stability parameter $S = N^2/g = 1.2 \times 10^{-5}\, m^{-1}$, where N is the Brunt-Väisälä frequency. The base values for the basic-state profiles at $z = 0\,\mathrm{m}$ are set to $\rho_b(0) = 1.189\,\mathrm{kg\,m}^{-3}$ and $\theta_b(0) = 285\,\mathrm{K}$. Moreover, an ideal gas with constant specific heat capacities $c_p = 1004$ $\mathrm{J\,kg}^{-1}\,\mathrm{K}^{-1}$ and $c_v = 717$ $\mathrm{J\,kg}^{-1}\,\mathrm{K}^{-1}$ is assumed. The gravitational acceleration is specified as $g = 9.80665\,\mathrm{m\,s}^{-2}$. Note furthermore, the Coriolis parameter for the f-plane occurring in (6.1a) and (6.1b) is set to $f = 10^{-4}\,\mathrm{s}^{-1}$.

The ambient state variables θ_e and $\mathbf{v}_e$ in the system (6.1) describe an undisturbed baroclinically unstable jet flow in geostrophic balance, with the direction of the jet flow along the periodic channel in x. For the specification of the ambient state, an x-invariant potential temperature field $\theta_e(y, z)$ is first prescribed adopting the analytical expressions given in Bush and Peltier (1994). The detailed specification is given in Appendix A. The computed distribution of $\theta_e(y, z)$ is depicted as the black contour lines in Figure 6.2. The main feature is the strong baroclinic zone in the y-centre of the channel at tropospheric heights. Note also the increase of static stability from the troposphere into the stratosphere.

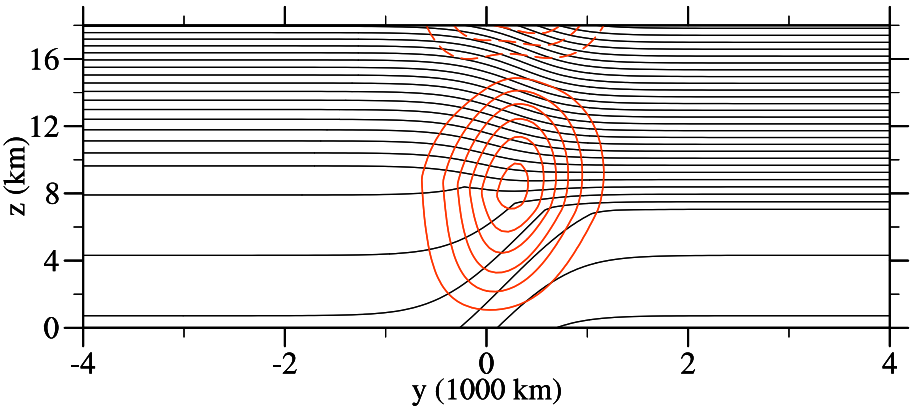

Figure 6.2: Vertical y-z cross section of the undisturbed baroclinically unstable ambient state for potential temperature θ_e (K, black solid contour lines, $\Delta\theta_e = 10\,\mathrm{K}$) and velocity u_e ($\mathrm{m\,s}^{-1}$, red solid contour lines positive, red dashed contour lines negative, $\Delta u_e = 10\,\mathrm{m\,s}^{-1}$, zero contour line not shown) in geostrophic balance. Distance transverse to the channel y and the channel height z.

Given the prescribed thermal field $\theta_e(y,z)$, the inertial flow field $\mathbf{v}_e = (u_e, 0, 0)$ is obtained from the thermal (geostrophic) wind relation

$$\frac{\partial u_e}{\partial \overline{z}} = -\frac{g}{\theta_b\, f}\left(\widetilde{G}_2^1 \frac{\partial \theta_e}{\partial \overline{x}} + \widetilde{G}_2^2 \frac{\partial \theta_e}{\partial \overline{y}}\right), \tag{6.2}$$

which has been derived consistently from the equations (6.1b) and (6.1c) in the anelastic set (6.1). The flow field u_e at $\overline{z} = 0$ is defined to be zero. Then, numerical integration of (6.2) in the vertical direction yields $u_e(y,z)$, as shown by the red contour lines in Figure 6.2. The resulting maximum velocity in the core of the computed jet flow is $\approx 63\,\mathrm{m\,s^{-1}}$ at a height of $z \approx 9\,\mathrm{km}$.

At the initial time $t = 0\,\mathrm{h}$ of the model simulation, the undisturbed baroclinically unstable ambient state of Figure 6.2 is perturbed by means of a thermal anomaly in the tropopause region $z \approx 9\,\mathrm{km}$ around the horizontal centre of the domain $\mathcal{D}_p$. Specifically, the thermal anomaly is prescribed for the prognostic variable θ' as

$$\theta'(0,x,y,z) = \begin{cases} \delta\theta \cos^2\left(\dfrac{\pi_c}{2}\tilde{r}\right), & \tilde{r} \le 1 \\ 0 & \tilde{r} > 1 \end{cases} \tag{6.3}$$

with

$$\tilde{r} = \sqrt{\left(\frac{x - 5000\,\mathrm{km}}{500\,\mathrm{km}}\right)^2 + \left(\frac{y}{500\,\mathrm{km}}\right)^2 + \left(\frac{z - 9\,\mathrm{km}}{2\,\mathrm{km}}\right)^2},$$

and the amplitude set to $\delta\theta = 3\,\mathrm{K}$. The initial flow field $\mathbf{v}$ is set equal to the ambient flow field $\mathbf{v}_e$.

The developed MMPDE machinery as presented in Chapter 4 is applied to achieve solution-dependent adaptation of the mesh in the horizontal plane of the domain $\mathcal{D}_p$, whereupon the mesh mapping function (4.1) is of the form $\mathcal{M} = (x(\overline{t}, \overline{x}, \overline{y}), y(\overline{t}, \overline{x}, \overline{y}))$. This mesh mapping function $\mathcal{M}$ onto the domain $\mathcal{D}_p$ is found by the solution of the two-dimensional MMPDEs (4.6) along with one-dimensional MMPDEs (4.17) for the southern and northern boundary segments of $\mathcal{D}_p$ at $y = \text{-}L_y/2$ and $y = L_y/2$. Periodicity of the mesh geometry is applied in the direction x along the channel. The mesh relaxation time Θ in (4.7) is set to $\Theta = 2.0 \times 10^5\,\mathrm{s}$ (about 55 hours). The smoothing procedure of the monitor function M by means of (4.16) uses a typical number of $K = 15$ passes. The specification of the monitor function M in the form (4.8) with the associated weighting function q according to (4.15) will be given in

the next subsection.

Given the integration procedure described in Section 2.2, the system (6.1) is treated fully implicit with respect to all prognostic quantities $\mathbf{v}$ and θ', plus the pressure variable π'. The preconditioned GCR(3) algorithm is applied for the solution of the elliptic pressure equation (2.23) with the convergence threshold specified as $\| \, (\delta\bar{t}/\rho^*) \, \overline{\nabla} \cdot (\rho^* \overline{\mathbf{v}}^s) \, \|_\infty < \epsilon = 10^{-5}$. Here, an implicit Richardson preconditioner as presented in Smolarkiewicz et al. (2004) with a successive number of 7 iterations is used. The advection module of (2.19) adopts the second-order accurate Eulerian MPDATA advection scheme with FCT enhancement. In addition, the MPDATA scheme uses its extension developed in Section 3.1. Specifically, the implementation RS as given in Table 3.1 is employed. Note, for the present configuration the underlying solution-adaptive moving mesh deformations will be relatively low compared to the tests discussed in Sections 5.1 and 5.2. It is anticipated that maximum residual errors (3.22) of the GMCL (3.2) by using the scheme RS in combination with the procedure (4.25)-(4.28) to approximate the generalised contravariant (advective) mass flux will be $\|r_{gmcl}\|_\infty \sim 10^{-4}$. Therefore, an application of either the prognostic approach or the diagnostic approach of Section 3.3 to control the residual errors of the GMCL (3.2) (respectively the generalised GCL (3.17)) was not performed here.

An evolution of the baroclinic wave instability over an integration period of $T = 288\,\mathrm{h}$ (12 days) is considered in the following. All simulations are conducted in a parallel processing computational environment using the IBM p575 "Power6" cluster of the German climate computing centre DKRZ.

Results of the numerical simulations

To begin the presentation of the simulation results, Figure 6.3 shows the computed evolution of the baroclinic wave using the solution-adaptive moving mesh NFT flow solver. As the mesh adaptation is independent of height, one important question raised with the application of the solver concerns the specification of the spatially two-dimensional monitor function $M(t, x, y)$ in the three-dimensional physical setting of the baroclinic flow evolution. A mesh refinement indicator Φ in the weighting function (4.15) that has been found to work quite satisfactory for the present flow configuration is specified as the vertical average of the Euclidean norm of the horizontal potential temperature gradient given as

$$\Phi(t, x, y) = \frac{1}{H} \int_0^H \|\nabla_h \, \theta(t, x, y, z)\| \, dz \; . \tag{6.4}$$

Basically, the use of (6.4) aims at an increased numerical resolution in regions of baroclinic zones, i.e. the thermal frontal zones characteristic of the baroclinic flow. The regions of these frontal zones can be expected to possess the major small-scale variability occurring in the large-scale environment of the baroclinic wave evolution, and therefore may benefit from an increased local resolution. The average over the depth H of the domain $\mathcal{D}_p$ in (6.4) tries to account for the vertical variation of $\|\nabla_h \theta(t,x,y,z)\|$ with height and to combine the information in the horizontal monitor function $M(t,x,y)$. Other specifications than (6.4) for the monitor function $M(t,x,y)$ will be investigated shortly by the end of the present section. Until then, all presented solution-adaptive moving mesh simulations use (6.4) in the weighting function (4.15). The parameter β in (4.15), which controls the strength of the mesh adaptation, is set to $\beta = 0.4$.

The initial x-invariant field of the potential temperature field θ at $z = 2\,\mathrm{km}$ is displayed in Figure 6.3(a). The MMPDE machinery has been applied at the initial distribution to obtain a higher numerical resolution along the east-west aligned baroclinic zone. Hence, the simulation at $t = 0\,\mathrm{h}$ starts already from an optimised mesh with respect to the specified monitor function M. After the start of the simulation at $t = 0\,\mathrm{h}$, it takes about 6 days of model integration until a disturbance of noticeable amplitude develops, as seen by the model output given in Figure 6.3(b) at $t = 144\,\mathrm{h}$. Then, the amplitude of the baroclinic wave proceeds to increase at an exponential rate in Figure 6.3(c) and Figure 6.3(d), until the growth of the wave saturates after around 10 days of integration time in Figure 6.3(e).

Over the entire course of the simulation from $t = 0\,\mathrm{h}$ until the final integration time $t = 288\,\mathrm{h}$, the solution-adaptive moving mesh NFT flow solver automatically adapts the local resolution with the evolution of the baroclinic wave. Initially, the mesh points are focused in the y-direction along the narrow range of the x-invariant baroclinic zone. As the growth of the baroclinic wave advances, the range of increased resolution widens in the direction of y. Note, for the present configuration the mesh adaptation primarily occurs in the y-direction transverse to the periodic channel. This factor is also reflected in the choice of underlying grid parameters as given in Table 6.1. The solution-adaptive moving mesh run A21340 used a significantly lower number mesh points in the direction of y than in x. The ratio of N_x to N_y in the solution-adaptive moving mesh simulations have been selected to roughly give isotropic local mesh cells for the relevant region of the baroclinic zone. However, the mesh adaptation also takes place in direction along the channel in x, particularly at the later states of the baroclinic flow development. For example, this can be

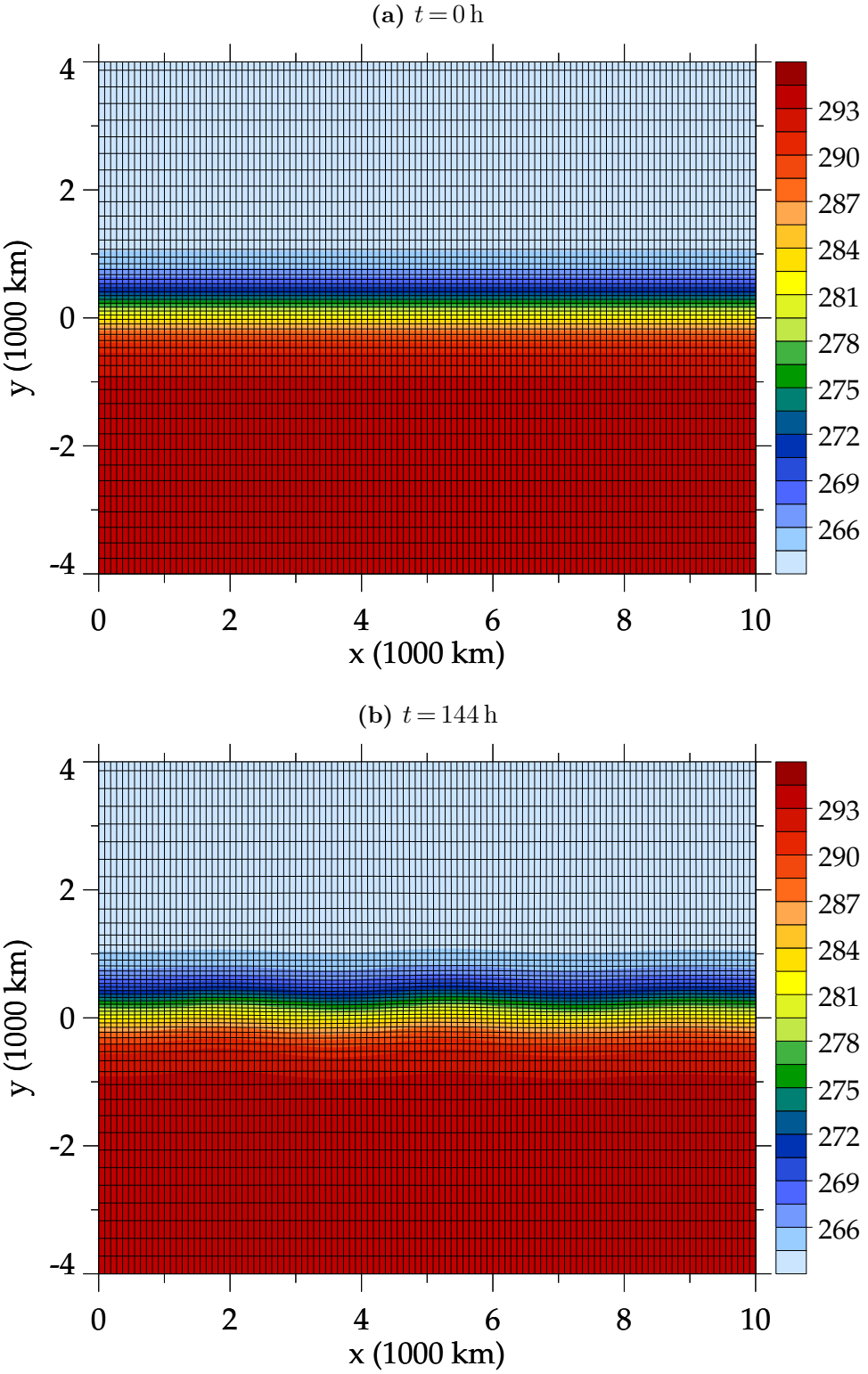

Figure 6.3: Mesh adaptation sequence from the solution-adaptive moving mesh simulation A21340 (see Table 6.1) of the baroclinically unstable jet flow. Depicted are contours of potential temperature θ (K, shaded) in a horizontal cross section at height $z = 2\,\mathrm{km}$, overlaid by the solution-adaptive moving mesh (solid lines; only every 2nd mesh line is drawn) at the selected output times (a) 0 h, (b) 144 h, (c) 192 h, (d) 216 h, (e) 240 h, (f) 264 h.

(c) $t = 192\,\mathrm{h}$

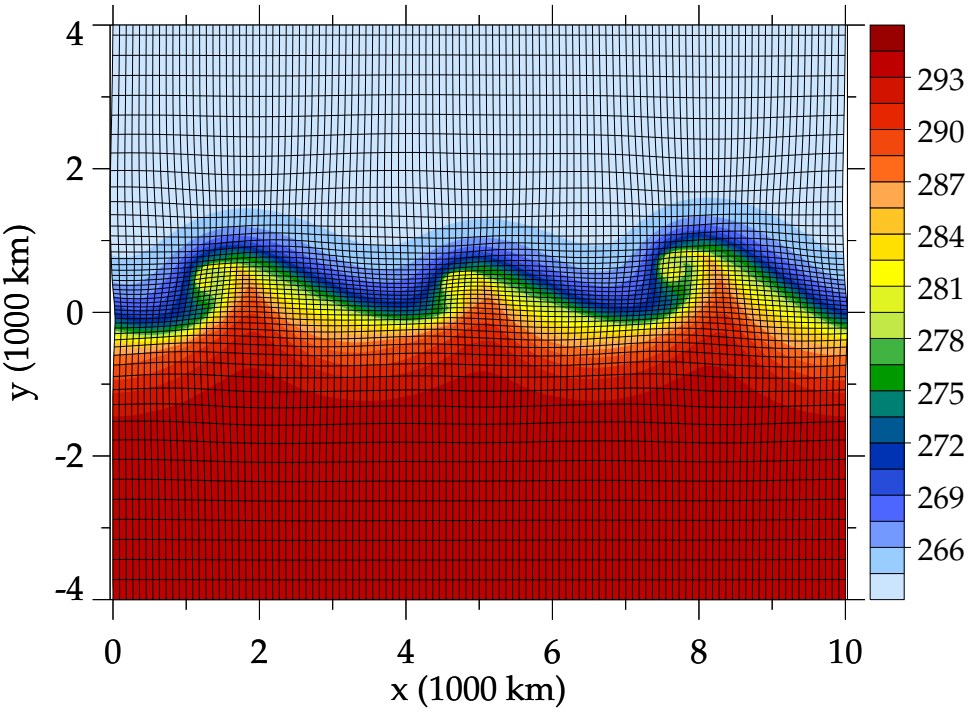

(d) $t = 216\,\mathrm{h}$

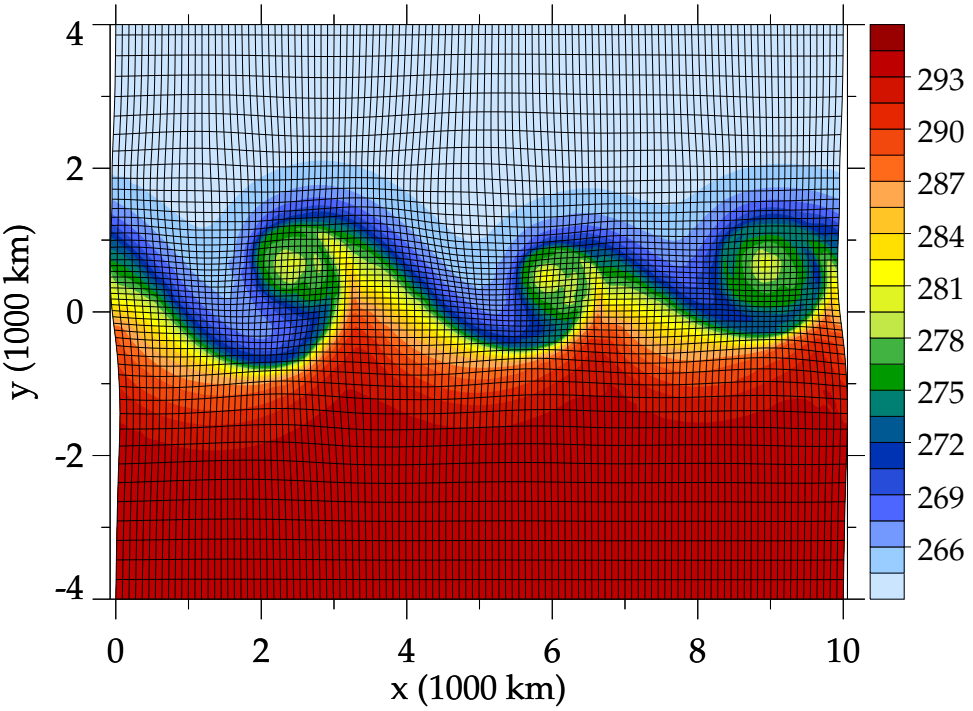

Figure 6.3: (continued)

(e) $t = 240\,\mathrm{h}$

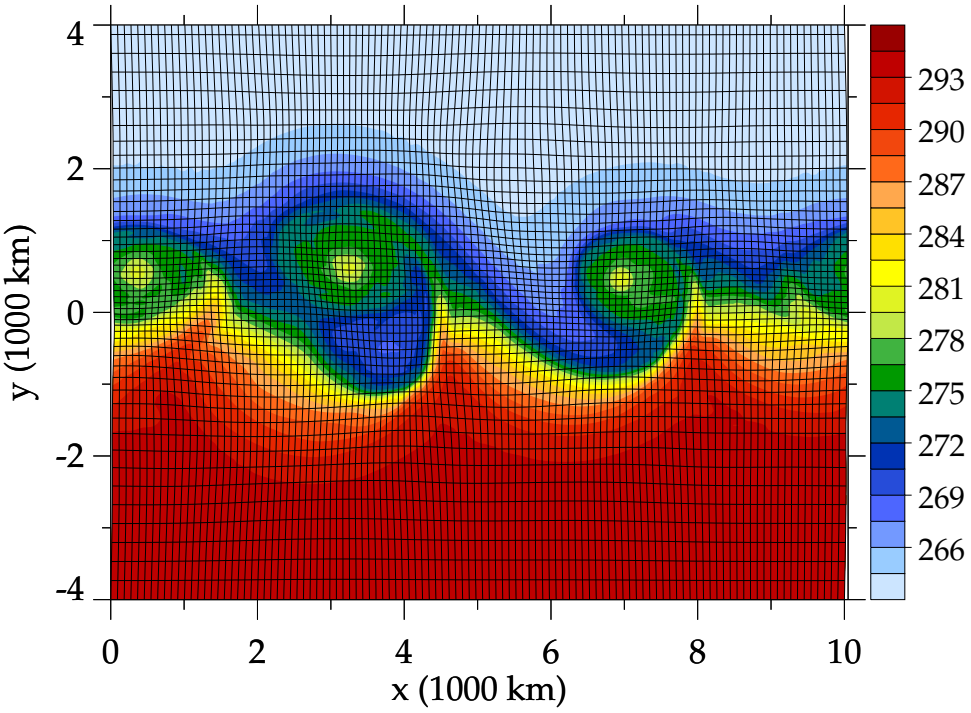

(f) $t = 264\,\mathrm{h}$

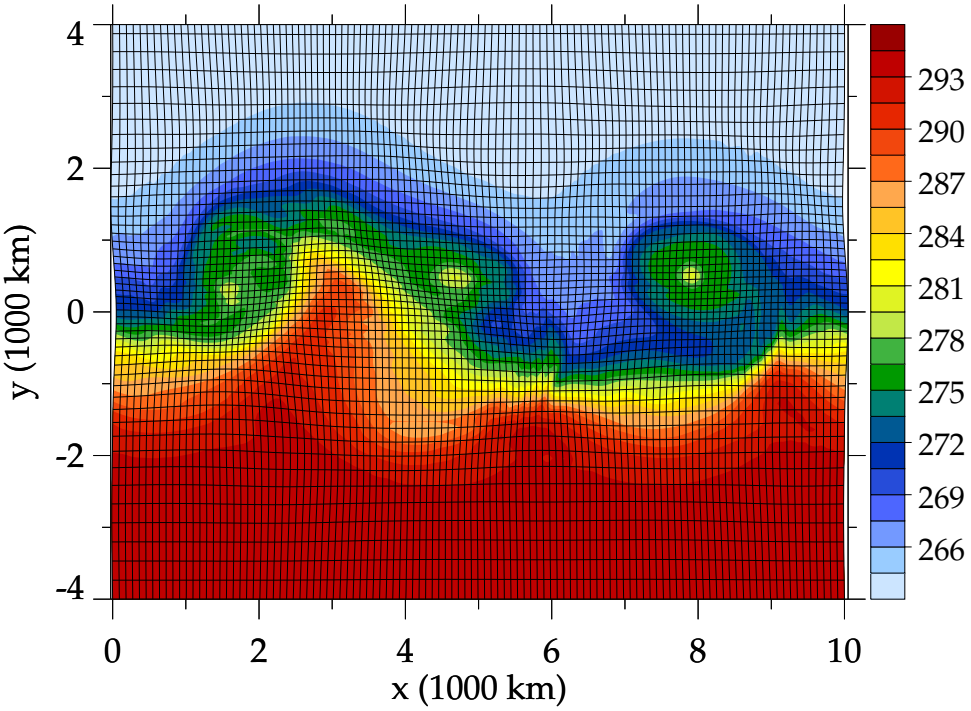

Figure 6.3: (continued)

seen at $t = 240\,\mathrm{h}$ in Figure 6.3(e), where the region of the major cyclone with the pronounced cold pool to the south-west (and the associated cold front ahead) features a higher local resolution than the region directly downstream. Commonly it is observed that a higher resolution exists in the region of and behind the propagating cold front than in the region of the warm sector ahead in Figure 6.3(c)-Figure 6.3(f). The deformation of the mesh geometry along the western and eastern boundaries of the domain; see e.g. Figure 6.3(d); results from the throughout implementation of the assumed periodicity conditions in the MMPDE algorithm. Overall, the skewness of the mesh cells in the present configuration is relatively low.

In the following, the results from the solution-adaptive moving mesh simulation are compared with the results from corresponding static uniform mesh runs. The static uniform mesh runs adopt the identical model as with the solution-adaptive moving mesh run, though the MMPDE machinery being deactivated. The first conducted set of simulations is summarised in Table 6.1. Given are the respective grid parameters along with details of the computational setup. Each of the runs S23213, S54967, and A21340 use a different number of horizontal mesh points N_x and N_y. Note, the total number of horizontal mesh cells used by each run is expressed by the numerical data following the characters S or A in the respective run names. The definition of the parallel processor parameters accounts for the different choices of the horizontal mesh point configurations, i.e. using about the same number of parallel subdomains in x and y. Furthermore, the total number of processors is about the same for all simulations in Table 6.1.

Figure 6.4 compares the potential temperature field θ at $z = 2\,\mathrm{km}$ obtained from the solution-adaptive moving mesh run A21340 in (c) with field obtained from the corresponding static uniform mesh simulations S23213 in (a) and S54967 in (b), after $t = 240\,\mathrm{h}$ of integration time. First of all, the comparison shows that the large-scale structure of the depicted θ field appears very similar for the three different simulations. Differences between the lower-resolution static uniform mesh run S23213 in Figure 6.4(a) and the higher-resolution static uniform mesh run S54967 in Figure 6.4(b) can be discerned in the region of the two main cyclones, which show a more pronounced (low-level) warm core structure in S54967 than in S23213. Smaller differences appear in the alignment of the cold front located at around $x \approx 4300\,\mathrm{km}$, and the minimum value of θ in the cold pool to the west behind the front. The θ field obtained with the solution-adaptive moving mesh run A21340 in Figure 6.4(c) attains very close agreement with the higher-resolution static uniform mesh run S54967 in Figure 6.4(b) even in the aforementioned more detailed solution features.

(a) Static mesh run: S23213

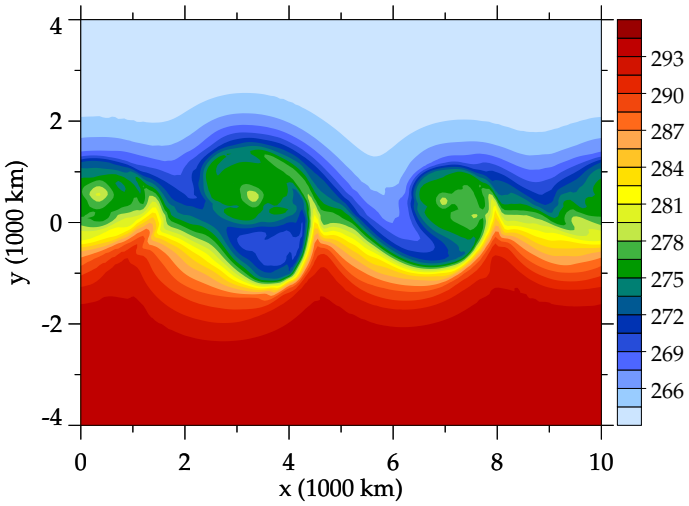

(b) Static mesh run: S54967

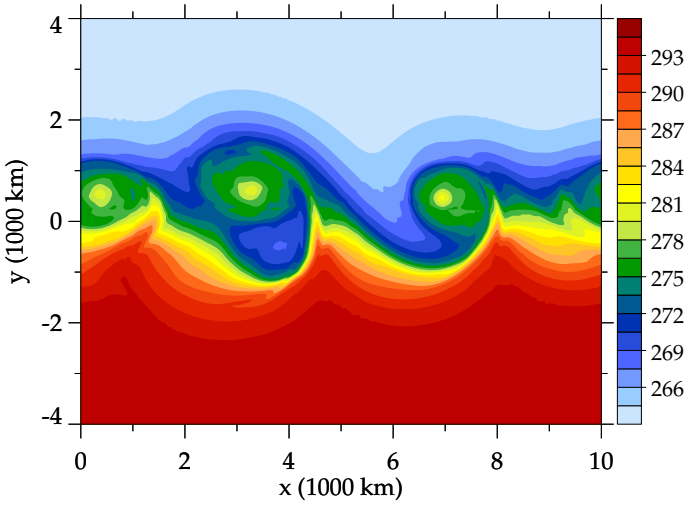

(c) Adaptive mesh run: A21340

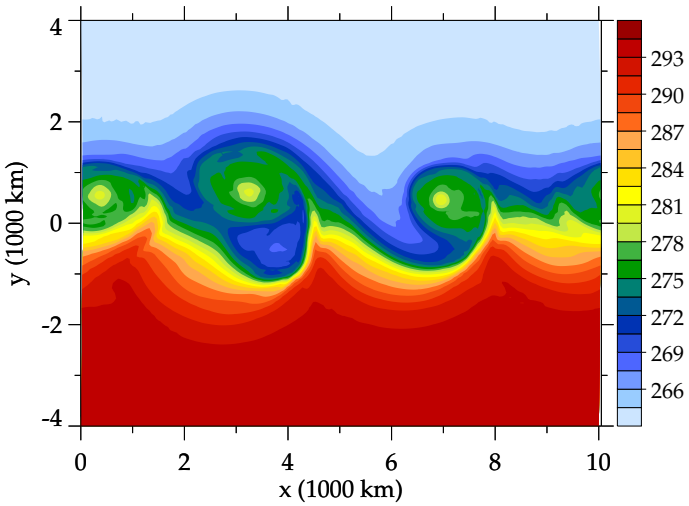

Figure 6.4: Horizontal cross section of the computed potential temperature field θ (K, shaded) at the height $z = 2$ km after $t = 240$ h of simulation time. Comparison of the different mesh configurations (a) S23213, (b) S54967, and (c) A21340 (see Table 6.1 and the main text for a description).

Run	$N_x \times N_y \times N_z$	NPE (NPX×NPY)	$\delta\overline{x} \times \delta\overline{y}$	$\delta\overline{t}$	T_w
S23213	168×140×91	120 (12×10)	≈60 km×60 km	240 s	1077 s
S54967	264×210×91	120 (12×10)	≈38 km×38 km	180 s	3340 s
A21340	221× 98×91	119 (17× 7)	≈45 km×82 km	180 s	1670 s

Table 6.1: Mesh configurations of the conducted simulation runs along with details of the computational setup. First column: assigned name of each run conducted. The symbol S in the run name indicates the use of a static uniform mesh, while A denotes the use of a solution-adaptive moving mesh. The numerical data following the characters S or A indicates the number of horizontal mesh cells used in each run, i.e. $(N_x - 1) \times (N_y - 1)$. Second column: number of mesh points in each coordinate direction $N_x \times N_y \times N_z$. Third column: total number of processors NPE together with the applied arrangement of the horizontal domain decomposition (NPX×NPY). Fourth column: spatial computational grid increment sizes $\delta\overline{x} \times \delta\overline{y}$ in the horizontal. Fifth column: constant time step $\delta\overline{t}$ of each run. Sixth column: total wall clock time T_w required for each simulation on an IBM p575 "Power6" cluster. The vertical grid increment size is $\delta\overline{z} = 200$ m in all runs. The constant time step in the integration has been selected for each run to give a maximum Courant number of $\mathcal{C}_{max} \approx 0.6$.

Representation of mesoscale internal gravity waves

Internal gravity waves are omnipresent in stably-stratified atmospheric flows. These waves can redistribute significant amounts of momentum and energy throughout the atmosphere and are relevant for a wide range of processes, e.g. Dörnbrack et al. (2002); Fritts and Alexander (2003); Lane et al. (2003); Kühnlein (2006). Internal gravity waves originate from many different sources. The most prominent are the flow over topography and moist convection. Evolving large-scale baroclinic flows are known to be important sources of internal gravity waves, too. Previous studies treating the subject of internal gravity wave generation in large-scale baroclinic flows often relate the generation of internal gravity waves to imbalances in the flow field associated with fronts and jet streaks, e.g. Zhang (2004); Kühnlein (2006); Zülicke and Peters (2006). Here, the representation of a particular mesoscale internal gravity wave packet in the solution-adaptive moving mesh simulation of the baroclinic flow evolution is addressed. Note, internal gravity wave generation and propagation in complex three-dimensional baroclinic flows is an area of active research, and it is not commented here on the detailed mechanisms of the wave formation.

Figures 6.5 - 6.6 display the predicted vertical velocity field w at the height $z = 12$ km for the simulation times $t = 240$ h and 246 h. The data in the Figures 6.5 - 6.6 is

shown in a fragment of the full simulation domain that defines the stratospheric region above the major cyclonic development in the troposphere below, cf. Figure 6.4. The most conspicuous feature in both figures is a mesocale internal gravity wave packet that appears through the alternating pattern of positive and negative values of the vertical velocity w and with the phase lines oriented roughly from the north-west to the south-east. At $t = 240\,\mathrm{h}$ in Figure 6.5, the wave packet is located at about the centre of the horizontal cross section, and has drifted slightly towards the east at the later time $t = 246\,\mathrm{h}$ in Figure 6.6.

A comparison between the static uniform mesh configurations in (a) and (b) of Figures 6.5 - 6.6 shows that the signal of the internal gravity wave packet is much weaker in the low-resolution run S23213 than in the higher-resolution run S54967. Also, the horizontal wavelength of the internal gravity wave packet in S23213 is significantly larger than in S54967. Table 6.2 summarises the respective quantitative estimates of the wave packet's characteristics for each run. It is worth to mention that given the values of the horizontal wavelengths λ_h in Table 6.2 and the applied horizontal resolutions for each run (see Table 6.1), the internal gravity waves exist near the cut-off wavelength of the associated numerical grid and are at least partially not adequately resolved. Assuming a representative wavelength λ_h of 240 km, it is covered only by about 4 (6) grid points in the run S23213 (S54967). The varying characteristics of the internal gravity wave packet under different resolutions in the described manner are typical and have been observed similarly in other studies, see e.g. Zhang (2004); Zülicke and Peters (2006); Plougonven and Snyder (2007). The vertical wavelength λ_z of the internal gravity wave packet has been estimated from vertical cross sections (not shown). A value of $\lambda_z \approx 3.5\,\mathrm{km}$ is found for both runs S23213 and S54967 at the output times $t = 240\,\mathrm{h}$ and $t = 246\,\mathrm{h}$. In light of the vertical resolution of $\delta\overline{z} = 200\,\mathrm{m}$ used in the simulations of Table 6.1, this vertical wavelength can be regarded as well resolved. A vertical wavelength of $\lambda_z \approx 3.5\,\mathrm{km}$ is also observed for the internal gravity wave packet in the solution-adaptive moving mesh run A21340 to be addressed next.

The results in Figures 6.5(c) and 6.6(c) indicate that the mesoscale internal gravity wave packet is well represented in the solution-adaptive moving mesh run A21340. The characteristics of the wave packet in A21340 closely match the characteristics obtained in the higher-resolution static uniform mesh run S54967, as exposed in Table 6.2. Only the amplitude in terms of $|w|_{max}$ at $t = 246\,\mathrm{h}$ shows a value that is $\approx 25\,\%$ larger in A21340 than in S54967. This larger amplitude of the internal gravity wave packet in A21340 can be interpreted as a sign for a better resolution

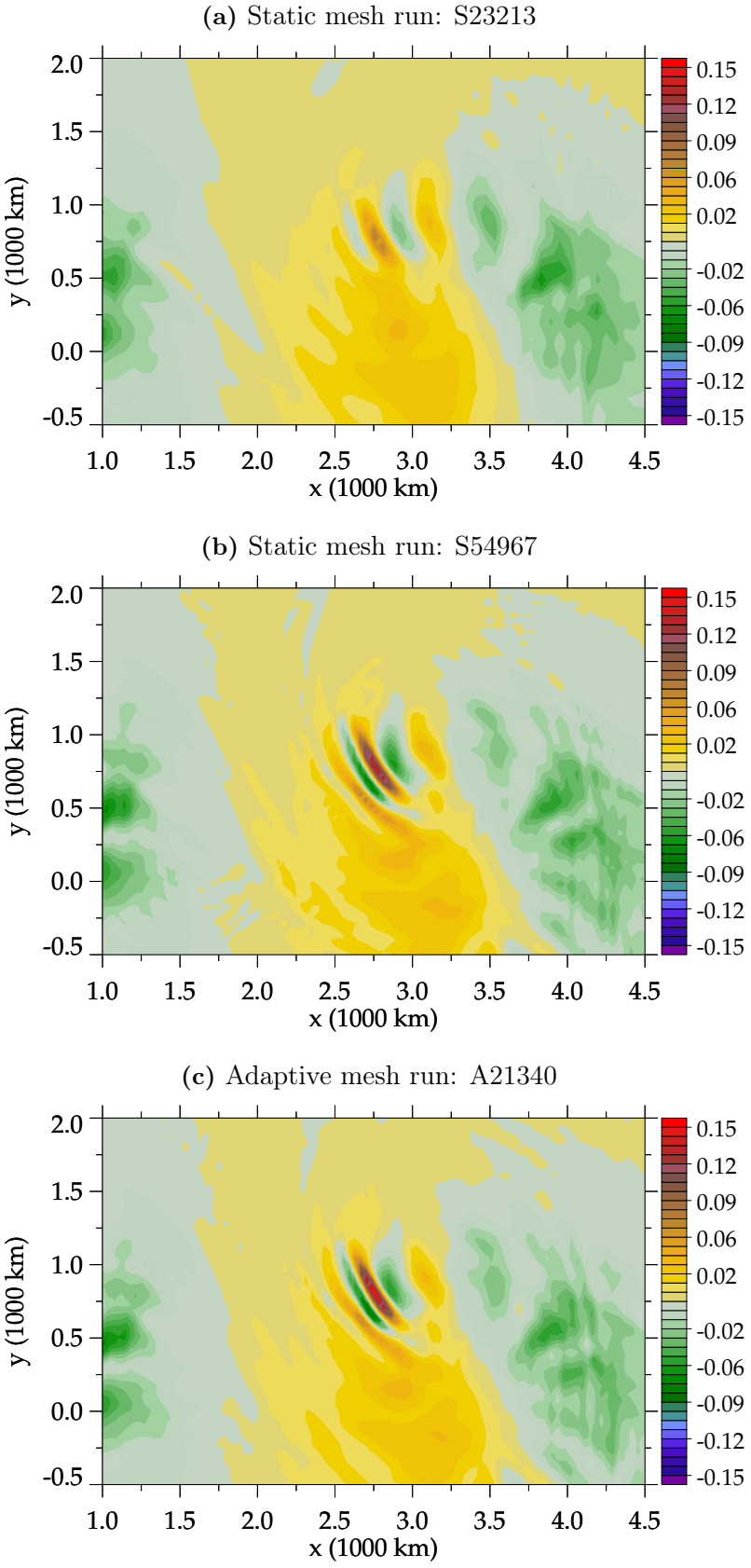

Figure 6.5: Horizontal cross section of the computed vertical velocity field w ($\mathrm{m\,s^{-1}}$, shaded) at the height $z = 12\,\mathrm{km}$ after $t = \mathbf{240\,h}$ of simulation time, shown in a fraction of the full domain. Comparison of the different mesh configurations (a) S23213, (b) S54967, and (c) A21340 (see Table 6.1 and the main text for a description).

(a) Static mesh run: S23213

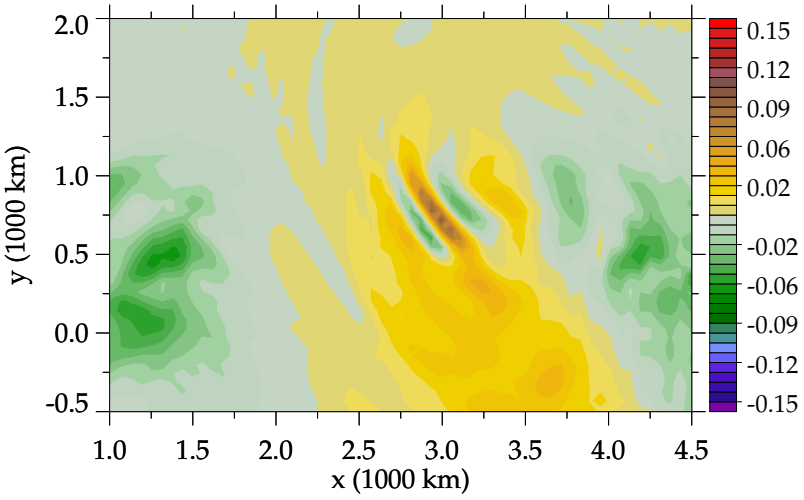

(b) Static mesh run: S54967

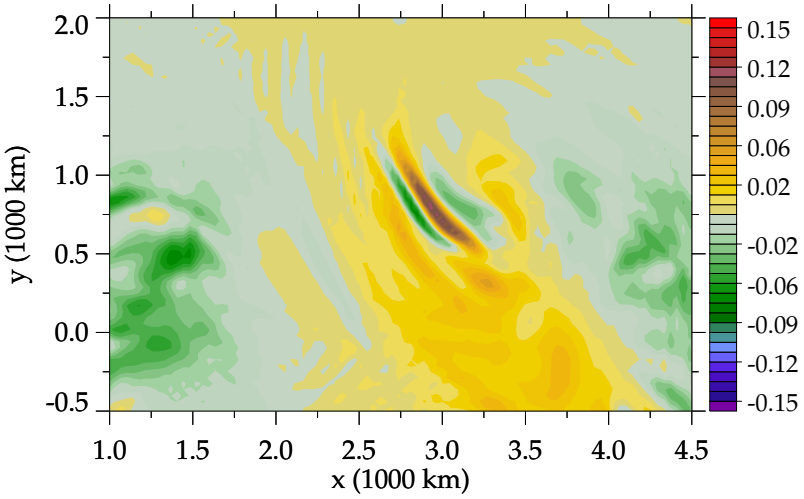

(c) Adaptive mesh run: A21340

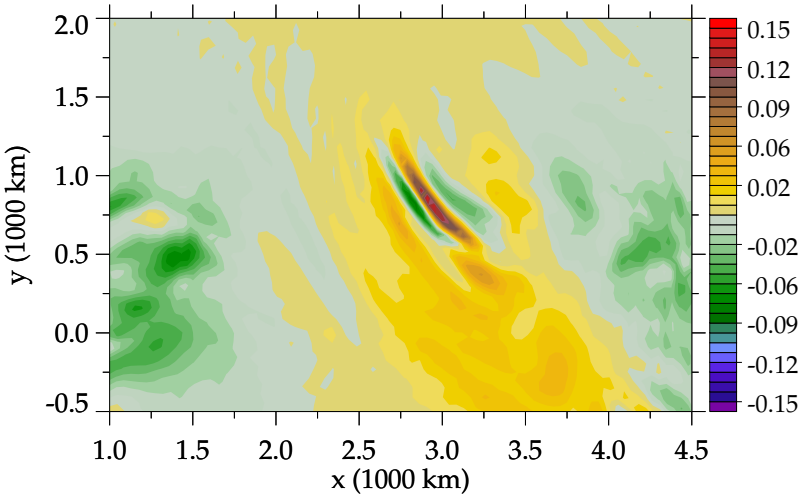

Figure 6.6: Horizontal cross section of the computed vertical velocity field w ($\mathrm{m\,s^{-1}}$, shaded) at the height $z = 12\,\mathrm{km}$ after $t = \mathbf{246\,h}$ of simulation time, shown in a fraction of the full domain. Comparison of the different mesh configurations (a) S23213, (b) S54967, and (c) A21340 (see Table 6.1 and the main text for a description).

Run	$\lvert w\rvert_{max}(t=240\,\mathrm{h})$	$\lambda_h(t=240\,\mathrm{h})$	$\lvert w\rvert_{max}(t=246\,\mathrm{h})$	$\lambda_h(t=246\,\mathrm{h})$
S23213	$\approx 0.06\,\mathrm{m\,s^{-1}}$	$\approx 350\,\mathrm{km}$	$\approx 0.08\,\mathrm{m\,s^{-1}}$	$\approx 300\,\mathrm{km}$
S54967	$\approx 0.15\,\mathrm{m\,s^{-1}}$	$\approx 230\,\mathrm{km}$	$\approx 0.12\,\mathrm{m\,s^{-1}}$	$\approx 230\,\mathrm{km}$
A21340	$\approx 0.16\,\mathrm{m\,s^{-1}}$	$\approx 230\,\mathrm{km}$	$\approx 0.16\,\mathrm{m\,s^{-1}}$	$\approx 220\,\mathrm{km}$

Table 6.2: Estimated values of the maximum vertical velocity magnitude $|w|_{max}$ (second and fourth column) and the horizontal wavelength λ_h (third and fifth column) associated with the discussed mesoscale internal gravity wave packet of Figures 6.5 - 6.6. The results given are for the runs in Table 6.1 at the output times $t=240\,\mathrm{h}$ and $t=246\,\mathrm{h}$.

of the feature, given the discussion of the previous paragraph.

Analysis of the kinetic energetics

The evaluation of the solution-adaptive moving mesh NFT flow solver is continued by conducting an analysis of the statistical quantities of kinetic energetics derived from the predicted velocity fields. A first quantity considered is the total kinetic energy defined as

$$\mathrm{KE} = \frac{1}{2}\,\rho_b\left(u^2+v^2+w^2\right)\ , \tag{6.5}$$

where again u, v, w are the physical velocity components and ρ_b is the horizontally-homogeneous prescribed basic-state density in the anelastic system (6.1). The initial baroclinic jet flow in the present configuration is invariant in the x-direction (in the zonal direction) and $v=w=0$. Therefore, it is convenient to decompose u into a zonally averaged part $\langle u\rangle_x$ and the respective deviation u'' according to

$$u = \langle u\rangle_x + u''\ , \tag{6.6}$$

where

$$\langle u\rangle_x = \frac{1}{L_x}\int_0^{L_x} u\,dx\ . \tag{6.7}$$

A zonal kinetic energy (ZKE) is then defined as

$$\mathrm{ZKE} = \frac{1}{2}\,\rho_b\langle u\rangle_x^2\ , \tag{6.8}$$

while an associated eddy kinetic energy (EKE), i.e. the kinetic energy in terms of the departures from the zonally averaged flow $\langle u\rangle_x$, is defined as

$$\mathrm{EKE} = \frac{1}{2}\,\rho_b\left(u''^2+v^2+w^2\right)\ . \tag{6.9}$$

Finally, volume-averaged measures of KE, ZKE, and EKE according to

$$\langle \psi \rangle_{xyz} = \frac{1}{L_x} \int_0^{L_x} \frac{1}{L_y} \int_0^{L_y} \frac{1}{H} \int_0^{H} \psi \, dx \, dy \, dz \tag{6.10}$$

are discussed. It is added that the analysis of the solution-adaptive moving mesh runs is more involved than the analysis of the uniform mesh simulations, because the data in the former resides on the deformed adaptive mesh geometry. Here, the obtained prognostic variables u, v and w on the deformed solution-adaptive moving mesh are linearly interpolated to a regular uniform mesh in the horizontal at all vertical model levels. Thereby, the uniform mesh is chosen twice as fine as the smallest physical mesh increment of the solution-adaptive mesh in order to maintain the formal second-order accuracy of the computations. The interpolation is also implemented to account for the mesh deformations along the periodic domain boundaries in the x-direction, as seen for instance in Figure 6.3(d). The latter is achieved through a folding of the overlap to the opposite side of the domain.

For an analysis of the kinetic energetics under various mesh configurations, a second set of simulations is considered. The respective simulations are summarised in Table 6.3. The applied mesh increment sizes $\delta\overline{x}$ and $\delta\overline{y}$ are reduced by a factor of 2 between the static uniform mesh runs S3795, S15429, and S62217. The lowest-resolution static uniform run S3795 of Table 6.3 uses horizontal mesh increment sizes $\delta\overline{x} \times \delta\overline{y}$ of $\approx 145\,\mathrm{km} \times 145\,\mathrm{km}$ compared to $\approx 60\,\mathrm{km} \times 60\,\mathrm{km}$ for lowest-resolution run S23213 in the previous set of simulations given in Table 6.1. Hence, the vertical resolution $\delta\overline{z}$ and the number of processors NPE is lowered in the runs of Table 6.3 compared to the runs in Table 6.1. The MMPDE machinery in the solution-adaptive moving mesh runs A3690 and A6254 of Table 6.3 use the same setting as in the previous run A21340 of Table 6.1.

Figure 6.7 shows the temporal evolution of $\langle \mathrm{KE} \rangle_{xyz}$, $\langle \mathrm{ZKE} \rangle_{xyz}$, and $\langle \mathrm{EKE} \rangle_{xyz}$ for the various runs of Table 6.3. The basic behaviour common to all simulations describes the increase of the total kinetic energy $\langle \mathrm{KE} \rangle_{xyz}$ in Figure 6.7(a) due to the conversion of the ambient state's potential energy in the baroclinic instability process. The large amplitude growth of the baroclinic wave that sets in after 6-7 days of model integration is associated with the increase of the eddy kinetic energy $\langle \mathrm{EKE} \rangle_{xyz}$ displayed in Figure 6.7(c). The growth of the $\langle \mathrm{EKE} \rangle_{xyz}$ extracts the potential energy from the baroclinic ambient state, but also (to a lesser extent) from the reservoir of the zonal kinetic energy $\langle \mathrm{ZKE} \rangle_{xyz}$, as seen in Figure 6.7(b) during the time of the initial large-amplitude growth of the instability.

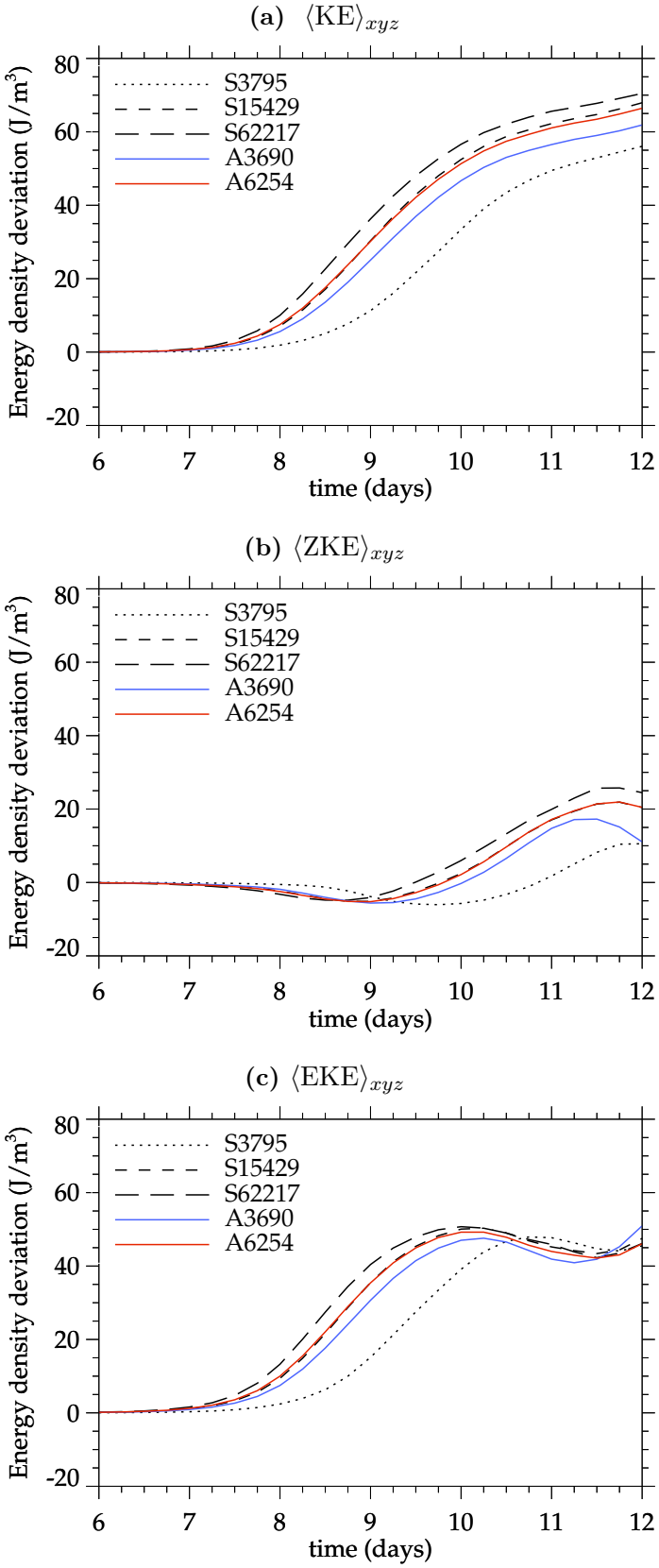

Figure 6.7: Time series analysis of the integral kinetic energetics derived from the results of the baroclinic jet flow instability simulations with the different mesh configurations given in Table 6.3. Drawn are deviations from the initial value at $t = 0$ of (a) total kinetic energy $\langle \mathrm{KE} \rangle_{xyz}$, (b) zonal kinetic energy $\langle \mathrm{ZKE} \rangle_{xyz}$, and (c) eddy kinetic energy $\langle \mathrm{EKE} \rangle_{xyz}$ in the range of day 6 to 12 of the simulations; see the main text for the definitions of the depicted quantities.

Run	$N_x \times N_y \times N_z$	NPE (NPX×NPY)	$\delta\overline{x} \times \delta\overline{y}$	$\delta\overline{t}$	T_w
S3795	70× 56×61	20 (5×4)	≈145 km×145 km	480 s	186 s
S15429	140×112×61	20 (5×4)	≈ 72 km× 72 km	240 s	1480 s
S62217	280×224×61	20 (5×4)	≈ 36 km× 36 km	120 s	13000 s
A3690	91× 42×61	21 (7×3)	≈111 km×195 km	360 s	250 s
A6254	119× 54×61	21 (7×3)	≈ 85 km×151 km	240 s	575 s

Table 6.3: Mesh configurations and details of the computational setup of the simulation runs considered for the kinetic energetics analysis. The vertical grid increment size is $\delta\overline{z} = 300\,\mathrm{m}$ in all runs. The constant time step in the integration is selected for each run in Table 6.3 to give a maximum Courant number of $\mathcal{C}_{max} \approx 0.5$. All other parameters used are as described in Table 6.1.

The more detailed temporal evolution of the kinetic energy measures in Figure 6.7 exhibits significant differences between the various simulations conducted. The static uniform mesh runs S3795, S15429, and S62217 generally predict an earlier onset and a larger growth rate of the instability with an increasing resolution. This can be discerned by inspection of the $\langle \mathrm{EKE} \rangle_{xyz}$ measure in Figure 6.7(c). The lowest-resolution run S3795 shows an onset time of the major growth of $\langle \mathrm{EKE} \rangle_{xyz}$ that is about 1 day delayed in comparison to the highest-resolution run S62217. Also, the slope of the $\langle \mathrm{EKE} \rangle_{xyz}$ line during the period of the major growth is lower in S3795 than in S62217, indicative for the different growth rate. Regarding the total kinetic energy in Figure 6.7(a), larger magnitudes of $\langle \mathrm{KE} \rangle_{xyz}$ are obtained with the higher-resolution runs throughout the integration period from the onset of the finite baroclinic wave growth. After 12 days of model integration, the difference of $\langle \mathrm{KE} \rangle_{xyz}$ between S3795 and S62217 is about 15 $\mathrm{J\,m^{-3}}$. A similar difference in magnitude between S3795 and S62217 is also observed for $\langle \mathrm{ZKE} \rangle_{xyz}$ in Figure 6.7(b) after the 12 days of model integration. Finally, it is remarked that the differences between S3795 and S15429 are significantly larger than between S15429 and S62217, suggesting convergence of the measures $\langle \mathrm{KE} \rangle_{xyz}$, $\langle \mathrm{ZKE} \rangle_{xyz}$, and $\langle \mathrm{EKE} \rangle_{xyz}$.

The solution-adaptive moving mesh run A3690 uses about the same number of mesh cells than the static uniform mesh run S3795. Nevertheless, the onset of the major growth of the instability in terms of $\langle \mathrm{KE} \rangle_{xyz}$ and $\langle \mathrm{EKE} \rangle_{xyz}$ occurs more than 0.5 days earlier in the run A3690 than in S3795, showing a better correlation for A3690 with the higher-resolution static uniform runs S15429 and S62217. Then, the temporal evolution of $\langle \mathrm{KE} \rangle_{xyz}$, $\langle \mathrm{ZKE} \rangle_{xyz}$, and $\langle \mathrm{EKE} \rangle_{xyz}$ obtained from the solution-adaptive moving mesh run A3690 also proceeds closer to the higher-resolution static uniform mesh run S15429 than to S3795. However, the kinetic energy measures in A3690 diverge relatively strong from S15429 after 11 days of integration time,

especially for $\langle \mathrm{ZKE} \rangle_{xyz}$ in Figure 6.7(b). A likely cause for the particular differences at the later stages of the integration is an insufficient number of the mesh points N_y in the y-direction in order to capture completely the dynamics of the growing, i.e. merdionally-extending, baroclinic wave. A similar behaviour is not observed in the higher-resolution solution-adaptive moving mesh run A6254. The measures of $\langle \mathrm{KE} \rangle_{xyz}$, $\langle \mathrm{ZKE} \rangle_{xyz}$, and $\langle \mathrm{EKE} \rangle_{xyz}$ in A6254 show close agreement with the static uniform mesh run S15429 over the entire integration period.

Figure 6.8 finally presents a comparison of different mesh refinement indicators Φ in the solution-adaptive moving mesh simulations with regard to the kinetic energetics. Considered for Φ are the vertical average of the vorticity given as

$$\Phi(t,x,y) = \frac{1}{H} \int_0^H \| \nabla \times \mathbf{v}(t,x,y,z) \| \, dz \ , \tag{6.11}$$

and the horizontal gradient of potential temperature θ

$$\Phi(t,x,y) = \| \nabla_h \, \theta(t,x,y,z_0) \| \tag{6.12}$$

taken at the single height level $z_0 = 600\,\mathrm{m}$ in lower troposphere. The refinement indicators (6.11) and (6.12) are compared to the refinement indicator based on the vertical average of the potential temperature gradient (6.4), that was employed in all previous experiments of this section.

The results for $\langle \mathrm{KE} \rangle_{xyz}$, $\langle \mathrm{ZKE} \rangle_{xyz}$, and $\langle \mathrm{EKE} \rangle_{xyz}$ for the various mesh indicators Φ in Figure 6.8 are practically identical during the early stages of the baroclinic wave growth until about day 9 of the simulations. Thereafter, differences between the various measures $\langle \mathrm{KE} \rangle_{xyz}$, $\langle \mathrm{ZKE} \rangle_{xyz}$, and $\langle \mathrm{EKE} \rangle_{xyz}$ become apparent. With the static uniform mesh run S15429 taken as the reference, the refinement indicator Φ based on the vertical average of the potential temperature gradient (6.4) (indicated by the red solid line in Figure 6.8) provides the best results. The indicator Φ based on the vertical average of the vorticity (6.11), indicated by the blue solid line, shows differences in the measures of $\langle \mathrm{ZKE} \rangle_{xyz}$ and $\langle \mathrm{EKE} \rangle_{xyz}$ against the static uniform mesh run S15429 after day 11. The relatively largest discrepancies are observed with the use of the mesh refinement indicator (6.12) based on the potential temperature gradient at $z = 600\,\mathrm{m}$, displayed by the green solid line in Figure 6.8. For illustration, Figure 6.9 displays the solution-adaptive moving mesh with the refinement indicator (6.12) as applied in the run A6254c of Figure 6.8. Although the mesh aligns nicely with the low-level frontal zone in this run, it draws to many mesh points away from

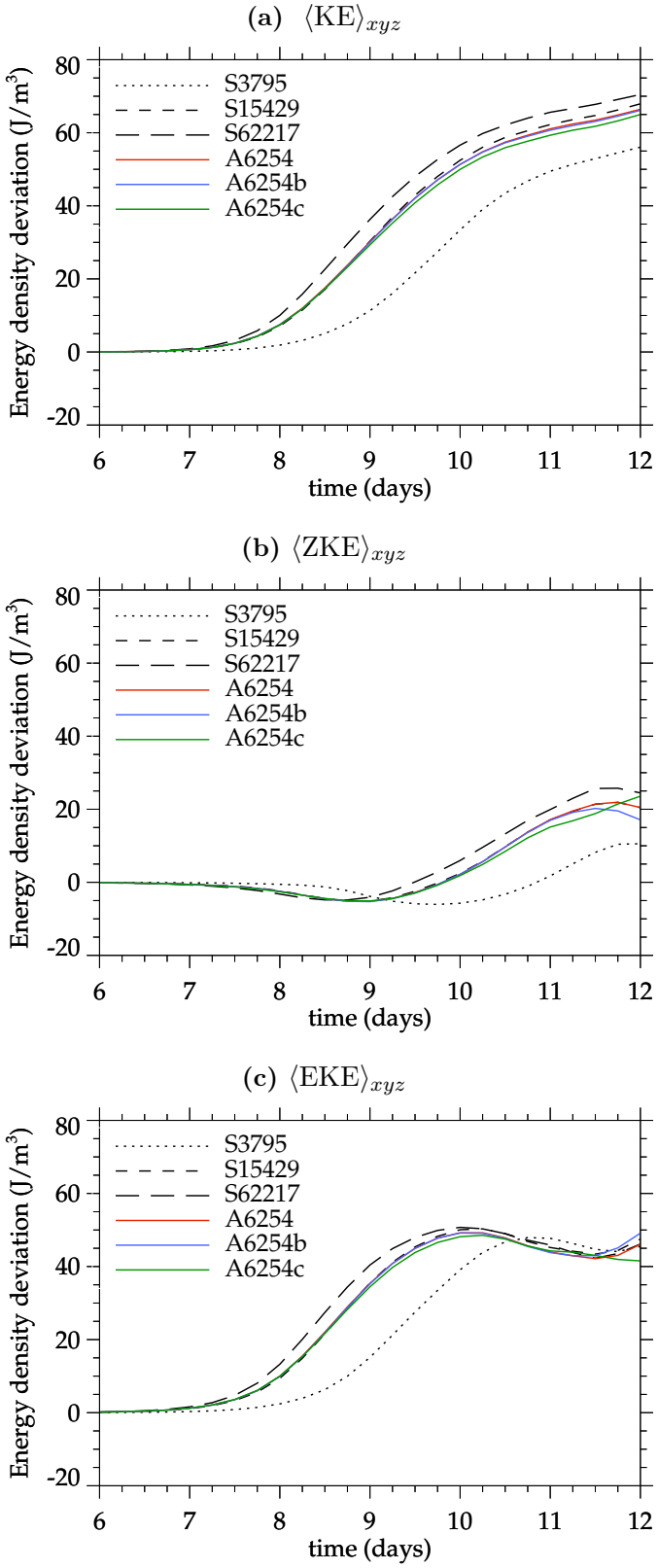

Figure 6.8: Time series analysis of the integral kinetic energetics of the baroclinic jet flow with different specifications of the mesh refinement indicator Φ in the solution-adaptive moving mesh NFT flow solver. The run A6254 corresponds exactly to the run A6254 of Table 6.3 and Figure 6.7, i.e. using the mesh refinement indicator (6.4). The runs A6254b and A6254c use the mesh refinement indicators (6.11) and (6.12), respectively. The static uniform mesh runs S3795, S15429, and S62217 are given for reference.

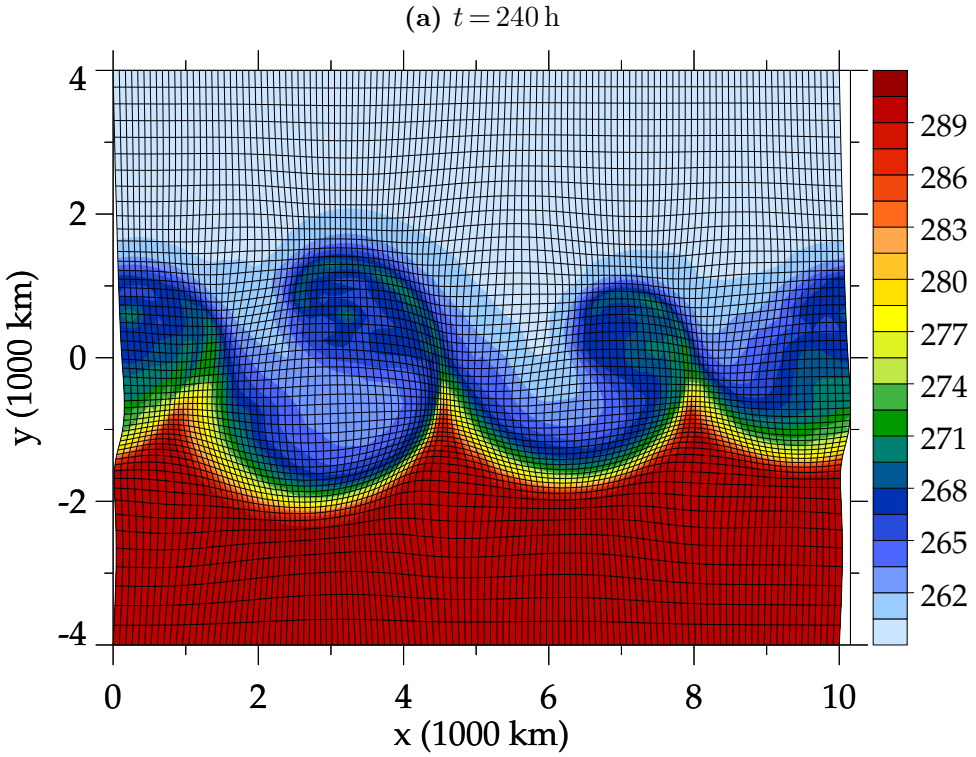

Figure 6.9: Snapshot after 240 h of simulation time from the solution-adaptive moving mesh simulation A6254c (see Table 6.3 and Figure 6.8) with the refinement indicator Φ defined by (6.12). Depicted are contours of potential temperature θ (K, shaded) on a horizontal cross section at height $z = 600$ m, overlaid by the solution-adaptive moving mesh (solid lines; every mesh line is drawn).

the main baroclinic zone and the associated jet flow at higher altitudes.

Discussion

Solution-adaptive moving mesh methods have been applied for the simulation of a synoptic-scale baroclinic wave instability. The results of the numerical experiments demonstrate the capability of the solution-adaptive moving mesh NFT flow solver to reproduce the basic flow evolution of the baroclinic wave life cycle as obtained from high-resolution reference runs with a uniform mesh. The solver runs stable, while producing accurate and reliable results. In addition, the solution-adaptive moving mesh solver can be used to improve the representation of certain flow characteristics compared to static uniform mesh integrations of similar computational effort. This applies to aspects of the large-scale flow development as well as to localised flow features, e.g. the generation and propagation of mesoscale internal gravity waves.

For the global measures of the kinetic energetics given in Figure 6.7, it is found that

the solution-adaptive moving mesh run A6254 evolves similarly as the static uniform mesh run S15429, whereby the latter uses a factor of ~ 2.4 more mesh cells. In terms of the particular marginally-resolved internal gravity wave packet embedded in the evolving large-scale flow, the use of the solution-adaptive moving mesh methodology in the run A23213 significantly improved its representation compared to the static uniform mesh run S21340 with about the same total number of mesh cells. The characteristics of the internal gravity wave packet in A23213 are found to be similar to the wave packet's characteristics in the static uniform mesh run S54967 of a factor of ~ 2.3 times larger total number of mesh cells; cf. Figures 6.5 and 6.6 and Table 6.2.

As typical for nonlinear geophysical flows, an analytical solution is not available for the present flow problem. Converged solutions could be obtained by introducing artificially large viscosity via diffusion terms in the governing equation set (Straka et al., 1993; Polvani et al., 2004). However, this strategy of using artificially large viscosity for converged solutions is not followed here because it is seen as a more stringent (first) test of the solution-adaptive moving mesh solver to work under inviscid conditions[1]. It is that large viscosity might damp possible spurious numerical effects of the solver one wants to detect and, above all, excessive viscosity hampers the examination of marginally-resolved physical phenomena like the mesoscale internal gravity waves discussed above. Regarding possible spurious numerical features, it is added here that a careful examination in terms of the vertical velocity w, horizontal divergence $\nabla_h \cdot \mathbf{v}_h$, and θ' fields at various model levels gave no indication for the existence of any spurious waves of significant amplitude in the solution-adaptive moving mesh simulations. From the preceding paragraph, it is clear that a statement about the value of the solution-adaptive moving mesh flow solver in terms of error norms versus computational effort, e.g. in relation to static uniform mesh runs, is not considered here.

Nevertheless, the respective wall clock times $\mathrm{T_w}$ for all model runs are given in the Tables 6.1 and 6.3. Referring to the discussion of the penultimate paragraph, reductions of $\mathrm{T_w}$ through the use of the solution-adaptive moving mesh methodology in the runs A6254 and A23213 over the static uniform mesh runs S15429 and S54967 are at a factor of ~ 2.57 and ~ 1.55, respectively. Here, it might be of interest to remark that the pure computational benefit from the use of the solution-adaptive mesh technique can be expected to increase with a larger complexity of the modelling system, i.e. with the possible inclusion of additional equations for moist and chemical

[1]It is added that the numerical solution scheme itself features implicit diffusion.

processes plus various sub-grid scale parameterisations. In the present experiments, only the basic dynamical core of EULAG was employed.
The relative portion of T_w that is required for the execution of the mesh adaptation modules in the solution-adaptive moving mesh runs is also given for completeness. In the runs A6254 and A23213, the processing of the MMPDE machinery requires $\sim 5.4\,\%$ and $\sim 6.7\,\%$ of the total wall clock time T_w, respectively. The percentage that is taken by the entire process of the dynamic mesh adaptation, i.e. processing of the MMPDE machinery plus the evaluation of the metric quantities and the ambient fields, amounts to $\sim 16.3\,\%$ and $\sim 14.4\,\%$ of the total wall clock time T_w for the runs A6254 and A23213, respectively.

Despite the restriction of the mesh adaptation to be independent of height, the solution-adaptive moving mesh NFT solver provided significantly improved results within the conducted analysis compared to static uniform mesh computations of similar computational effort. Of the mesh refinement indicators Φ that were tested, the vertically-averaged potential temperature gradient (6.4) provided the best solution quality for this setting in general. A refinement of the mesh along the sharp frontal zones in the lower troposphere (as shown in Figure 6.9) could not be applied without affecting global measures of the flow; see Figure 6.8. Perhaps, to better resolve the sharp frontal zones in the lower troposphere within the framework of the present solver, variants of the mesh refinement indicator (6.4) might be conceivable that assign height-dependent weights in the vertical averaging for a relatively stronger adaptation at lower altitudes, which has yet to be tested.

As discussed before in the previous subsection, the solution-adaptive moving mesh runs A21340 and A6254 were set up for the adapted mesh cells to be roughly isotropic in the dynamically important region of the baroclinic zone, as shown in Figure 6.3. In order to achieve this, a relatively larger number of grid points had to be applied in the direction along the baroclinic zone than in the transverse direction; see the grid parameters N_x and N_y in Tables 6.1 and 6.3. It can be discerned from Figure 6.3 that this specification of the solver inevitably leads to an unnecessary fine spacing of the mesh in the along-channel direction to the north and south away from the region of the baroclinic zone. However, the large number of grid points N_x cannot be avoided without losing the fine resolution in the region of baroclinic zone. This shortcoming of the adopted r-refinement technique in combination with the underlying structured grid arrangement is well known and unavoidable with the present solver. In contrast, an h-refinement method, see e.g. Behrens (2006), is more flexible concerning this matter. The h-refinement method would allow to reduce the number grid points N_x

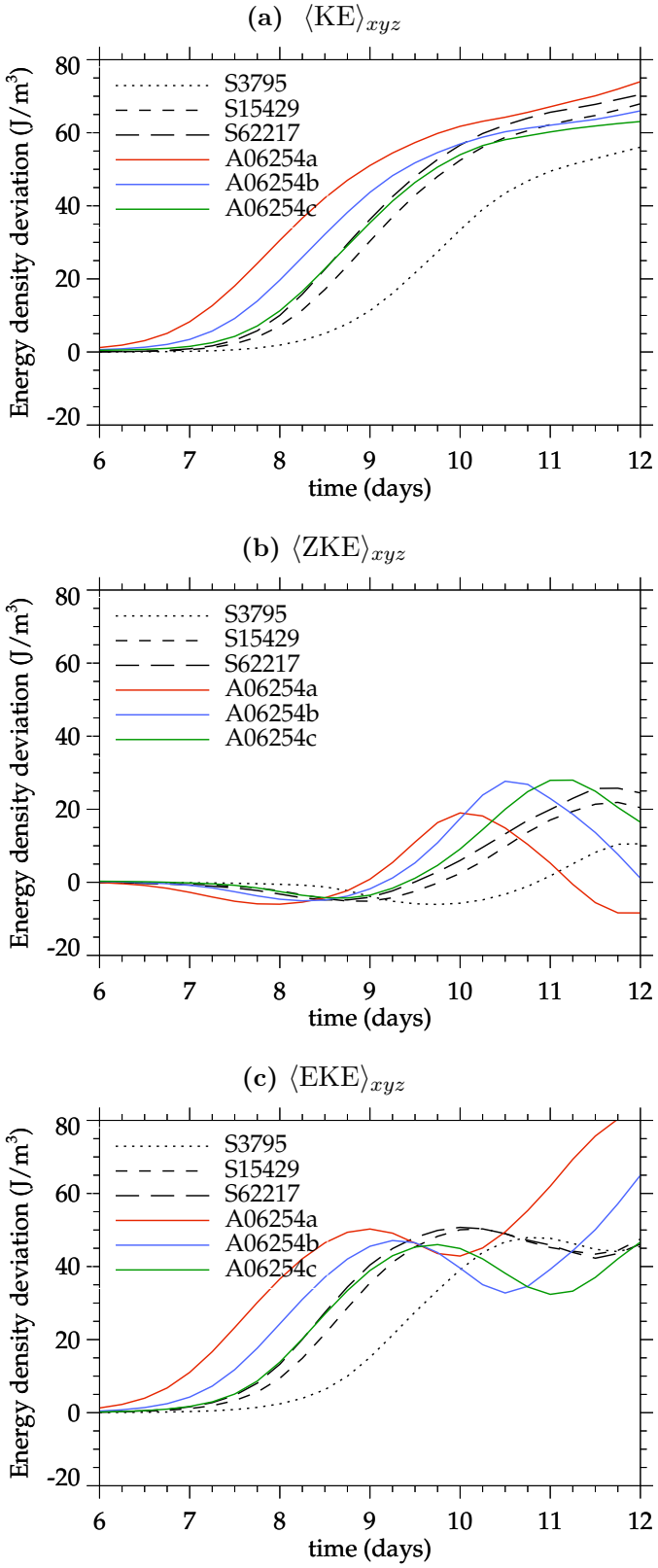

Figure 6.10: Time series analysis of the integral kinetic energetics of the baroclinic jet flow simulations with different mesh configurations. The various runs A06254 are identical to the run A6254 of Table 6.3 but start the integration from a uniform mesh at the initial time $t = 0\,\mathrm{h}$. The individual runs A06254a, A06254b, and A06254c differ in the size of the mesh relaxation time Θ in the MMPDE machinery: $\Theta = 2.0 \times 10^5\,\mathrm{s}$, $\Theta = 4.0 \times 10^5\,\mathrm{s}$, and $\Theta = 1.0 \times 10^6\,\mathrm{s}$, respectively. The static uniform mesh runs S3795, S15429, and S62217 are given for reference.

away from the region of the baroclinic zone, while keeping N_x large in the region of the baroclinic zone. Nevertheless, the present solver based on the moving mesh method achieved a significant reduction in computational cost compared to the static uniform mesh simulations.

It is explained here that the applied mesh adaptation can drastically alter the flow evolution in some situations if not applied carefully. As mentioned before, all previous simulations have been started with an optimised, i.e. adapted, mesh with respect to the monitor function M at the initial time $t = 0\,\mathrm{h}$ of the integration; see e.g. Figure 6.3(a). Figure 6.10 shows results of computed kinetic energetics for a set of solution-adaptive moving mesh simulations A06254 which differ from the previous run A6254 of Figure 6.7 in that they were started from a uniform, i.e. non-adapted, mesh. Hence, with the start of the simulation in the runs A06254, the mesh points immediately begin to move from their positions of the uniform mesh towards the region of the baroclinic zone, as specified by the mesh refinement indicator (6.4) in the monitor function M. The results in Figure 6.10 now indicate that the large-scale evolution of the baroclinic instability flow in terms of the kinetic energy measures $\langle \mathrm{KE} \rangle_{xyz}$, $\langle \mathrm{ZKE} \rangle_{xyz}$, and $\langle \mathrm{EKE} \rangle_{xyz}$ is considerably altered compared to the run A6254 in Figure 6.7. While the results of the run A6254 in Figure 6.7 very closely followed the static uniform mesh run S15429, the major baroclinic wave growth in the runs A06254 of Figure 6.10 is generally excited much earlier (about 1 day for the run A06254a) and the evolution of the measures $\langle \mathrm{KE} \rangle_{xyz}$, $\langle \mathrm{ZKE} \rangle_{xyz}$, and $\langle \mathrm{EKE} \rangle_{xyz}$ occurs differently.
Different mesh relaxation times Θ have been applied in the individual runs A06254a, A06254b, and A06254c in Figure 6.10. The mesh adaptation is fastest in the run A06254a, and this run also shows the largest discrepancies with A6254, respectively S15429. Therefore, the relatively strong mesh adaptation that initially occurs in the runs A06254 disturbs the unstable jet flow, which leads to a different evolution of the baroclinic instability. The faster the moving mesh adaptation the stronger is the perturbation and excitement of the unstable jet flow. In summary, the results demonstrate that one must be careful on how the mesh adaptation is applied, particularly when the flow involves the development of instabilities.

Chapter 7

Summary and conclusions

The present thesis designed, implemented and applied an adaptive mesh algorithm for dynamically variable spatial resolution to the numerical simulation of nonlinear multiscale atmospheric (geophysical) flows. The starting point of the development was the proven geophysical flow solver EULAG. In the recent work by Prusa and Smolarkiewicz (2003), the generic analytical and numerical framework of EULAG for the integration of the non-hydrostatic anelastic equations in time-dependent generalised coordinates was established. Here, this framework of EULAG was modified and extended to enable the application of flow-dependent variable resolution by means of moving curvilinear meshes.

Methodological development

The methodological development of the new solution-adaptive moving mesh anelastic solver in this thesis can be summarised into three tasks:

(i) In Chapter 3, the integration of the anelastic equations in Eulerian conservation form with the NFT advection scheme MPDATA was modified and extended. It was found that the original MPDATA scheme as presented in Smolarkiewicz and Prusa (2002); Smolarkiewicz (2006) is not fully compatible with the generalised anelastic mass conservation law (GMCL) under moving meshes. Violating the numerically implemented compatibility constraint results in significant solution errors under certain moving mesh and flow configurations. As a result, revised formulations of the MPDATA scheme were developed and implemented that provide compatibility with the GMCL under arbitrary moving meshes and flows.
The developed extensions concern two aspects of the MPDATA integration. The

first aspect is the implementation of the error-compensative pseudo-velocities in MPDATA. Therein, a density-correction factor was implemented to permit exact (i.e. with machine precision) preservation of a uniform transported scalar field under a moving mesh (Section 3.2). The original MPDATA scheme does not maintain a uniform scalar field under a moving mesh without the proposed implementation of the density-correction factor. Not maintaining the uniform scalar field violates the MPDATA compatibility with the GMCL. Numerical experiments confirmed that the proposed modified MPDATA scheme preserves the asymptotic second-order accuracy of the original MPDATA.

The second aspect is the implementation of the GMCL in EULAG (Section 3.3). One important finding in the present thesis is the violation of the GMCL in the present implementation of EULAG for moving meshes. In order to satisfy the discrete GMCL in the integration of the anelastic equations for arbitrary moving meshes, a diagnostic and a prognostic approach were developed and presented. The basic idea of the prognostic approach for the geometric conservation law (GCL) was originally proposed in Thomas and Lombard (1979). Here, the approach was adjusted to the anelastic solver based on MPDATA.

However, some issues were discovered with the prognostic approach (see Section 3.3.2 and the last subsection in Section 3.4). Among others, the implemented prognostic approach introduced conservation errors in the flux-form MPDATA solution. Therefore, a new diagnostic approach for the implementation of the GMCL in the MPDATA integration was proposed that conserves the transported quantity with machine precision (as in the original MPDATA scheme). Using a projection method (in the spirit of the anelastic solver), the diagnostic approach corrects the advective contravariant mass flux $(\rho^* \overline{\mathbf{v}}^*)^{n+1/2}$ that enters MPDATA from the approximate predictor scheme rather than correcting the diagnostic generalised density ρ^{*n+1} as in the prognostic approach (see Section 3.3.1).

A detailed numerical comparison study of the developed extensions versus the original form of the MPDATA scheme was conducted using simple scalar advection experiments under a prescribed oscillating mesh in Section 3.4. As mentioned above, the incompatibility of MPDATA with the GMCL in the original formulation generates spurious (i.e. unphysical) extrema in the solution variables. In contrast, spurious extrema were not observed with the herein developed extensions of the MPDATA scheme providing the compatibility with the GMCL (e.g. see Table 3.3). Qualitatively equivalent results were obtained for numerically-generated solution-adaptive moving meshes considered in the experiments of Section 5.3. However, the error magnitudes were considerably larger than for the prescribed oscillating moving meshes

in Section 3.4.

(ii) In Section 4.3, a machinery performing the numerical generation of a solution-adaptive moving curvilinear mesh was designed and implemented. The main ingredient of the machinery is a set of parabolic moving mesh partial differential equations (MMPDEs). The derivation of MMPDEs follows from a standard variational approach. The properties of the generated curvilinear mesh (e.g. local adaptivity) enter the MMPDEs through a monitor function M. Explicit control over the time scale of the moving mesh adaptation is incorporated in the MMPDEs by means of a mesh relaxation time Θ. Practical aspects of the scheme and the implementation were explained in detail in Section 4.3. Furthermore, an efficient and robust numerical solution scheme for the MMPDEs was implemented. First- or second-order implicit temporal discretisations to the MMPDEs were applied, and the resulting elliptic mathematical problem was solved using a generalised conjugate residual (GCR) iterative method. The mesh points at the boundaries of the computational domain may optionally be periodic over the boundaries or governed by the solutions of one-dimensional MMPDEs. The MMPDE machinery for the two-dimensional solution-adaptive moving mesh generation was fully embedded into the parallel coding framework of the three-dimensional solver EULAG.

(iii) In Section 4.4, an efficient computational framework for the overall solution-adaptive moving mesh anelastic NFT flow solver was created. This new framework consists of the anelastic solver based on MPDATA (see penultimate item (i)) and the MMPDE machinery (see the previous item (ii)). The elaborate development and testing of the new framework was conducted using specifically constructed two-dimensional prototype programs applied in a single processor (workstation) computing environment. These prototype programs mimic the numerical formulation of EULAG.
For the effective incorporation of the mesh movement in EULAG, a revised scheme for the approximation of the advective contravariant mass flux $(\rho^*\overline{\mathbf{v}}^*)^{n+1/2}$ in MPDATA was developed. The crux of the revised scheme is that the mesh velocity $\overline{\mathbf{v}}^g$ in the advective contravariant velocity $\overline{\mathbf{v}}^* = \overline{\mathbf{v}}^s + \overline{\mathbf{v}}^g$ is evaluated straightforwardly at the intermediate time level $\bar{t}^{n+1/2}$ by means of a centred difference. The solenoidal velocity $\overline{\mathbf{v}}^s$ is extrapolated to $\bar{t}^{n+1/2}$ using either a linear or nonlinear predictor scheme. This procedure is advantageous for minimising errors associated with the implementation of the discrete GCL in the solver, among others (see the remarks in the last paragraph of Section 4.4).
The incorporation of the revised predictor scheme for $(\rho^*\overline{\mathbf{v}}^*)^{n+1/2}$, as well as the

developed MPDATA extension of Section 3.1, in the NFT solver required a redesign of the algorithmic structure of the default EULAG. The redesigned algorithmic structure of the present adaptive solver is illustrated in Figure 4.2. The use of a variable time step size $\delta\bar{t}$ for efficiency reasons, an option presently not exploited in the default EULAG, was also incorporated in the development.

Results of the applications

The developed solution-adaptive moving mesh solver was thoroughly investigated by simulating a number of relevant atmospheric flow problems.
In Section 5.1, the advection of a passive tracer in a prescribed two-dimensional shear flow was considered. Straightforward validation of the computed results was possible by means of a known exact solution. The results demonstrated the capability of the solver to automatically adapt the local resolution to the evolving fine-scale filamentary structures of the tracer field. It was found that the moving mesh solver adapting locally to the gradient of the tracer field clearly outperforms the solver with a uniform mesh. As an example, the adaptive solver with $\mathrm{N}_c = 50^2$ mesh cells provided more than 20 % lower L_2 and L_∞ error norms than the solver employing a uniform mesh with $\mathrm{N}_c = 250^2$ mesh cells (Figure 5.2). Thereby, the high-resolution uniform mesh simulation required a factor of 26 larger computing time than the simulation with the adaptive solver.
In Section 5.2, an idealised two-dimensional flow of a rising warm thermal was considered. In contrast to the scalar advection problem of Section 5.1, no exact solution is available for this flow. Specifying the mesh adaptation proportional to temperature gradient and vorticity provides a locally high resolution at the interface of the thermal with the ambient air, throughout the entire course of the simulation. As a main result, the adaptive solver preserves very accurately the temperature amplitude of the rising thermal and the large gradients along the interface. Considering these properties of the flow, the adaptive solver with $\mathrm{N}_c = 94^2 = 8836$ mesh cells provided results comparable to the solver employing a uniform mesh with $\mathrm{N}_c = 394^2 = 155236$ mesh cells (Figure 5.6) during the laminar phase of the rising thermal. Another advantage of the adaptive mesh simulations is the appearance of new physical phenomena. In particular, instabilities occurring at the interface of rising thermal with the ambient air could be simulated in much greater detail when compared to the uniform mesh simulation with the same number of mesh points. The representation of the associated mixing processes is of direct relevance for simulating cumulus convection in realistic atmospheric flows. There, the process of fine-scale mixing,

i.e. entrainment and detrainment, between the cloudy and the ambient air could be much better resolved using mesh adaptation.
In Section 6.1, the developed adaptive mesh solver was eventually applied in the three-dimensional parallelised modelling framework of EULAG. For the first time, adaptive moving mesh methods were employed to simulate a synoptic-scale baroclinic wave life cycle. The difficulty in simulating this type of flow are stratification/rotation effects and the nonlinear processes generating a broad motion spectrum. The adaptive solver provided an accurate representation of the synoptic-scale flow and coexisting mesoscale processes, while running stably and without generating any spurious wave effects. The adaptive solver significantly improved the global statistics of kinetic energetics compared to the uniform mesh simulations. Furthermore, focussing the adaptation to the developing frontal zone according to the vertically-integrated gradient of potential temperature revealed the excitation of internal gravity waves at the later stages of the baroclinic wave evolution. These waves were only poorly represented in simulations applying a uniform mesh with about the same number of mesh points. For the present three-dimensional configuration, the adaptive solver reduced the computing time by a factor of ~ 2 compared to (at least) equivalent results of high-resolution reference uniform mesh simulations.

Remarks

The results obtained in this thesis demonstrate the capability and potential of adaptive moving mesh methods to simulate multiscale atmospheric flows with higher fidelity and a much broader coverage of motion scales.
A cumbersome side-effect of the successful and efficient numerical simulations was the extremely time-consuming tuning of the adaptation parameters in the MMPDE machinery. This concerns especially the monitor function and also the mesh relaxation time. In the current state of development, potential users must be aware that finding the optimal choice and combination of these quantities and setting up the solution-adaptive moving mesh solver for a certain flow configuration may require a significant tuning and testing effort. This process clearly exceeds the effort associated with setting up EULAG based on a static mesh. For effective applications of the methodology, an experienced user familiar with the behaviour of adaptive mesh solver is advantageous.
The most crucial part of the moving mesh method is the monitor function. The spatiotemporal distribution of the monitor function directly determines the structure of the mesh. Its specification should detect dynamically relevant regions of the flow

but also ensure a good quality mesh. From the experience gained in this work, one should avoid designing monitor functions on the basis of quantities which are highly irregular, e.g. horizontal velocity divergence or vertical velocity in the synoptic-scale baroclinic wave instability. Such quantities can be used only with considerable smoothing of the monitor function. Otherwise, a highly irregular monitor function requires the iterative GCR solver for the MMPDEs more computational effort to converge. In addition, the resulting poor quality mesh (possibly non-smooth and/or highly-skewed) directly affects the efficacy of the anelastic solver in EULAG.

Atmospheric (geophysical) flow solvers are typically formulated with a horizontal mesh adaptation capability that has no variation with height, see e.g. Bacon et al. (2000). One main reason for this is the dominant balance of hydrostaticity in vertical, which must be correctly represented in the numerical solver[1]. The clue within this framework will be to design appropriate two-dimensional monitor functions that account for the vertical variation of the simulated flows. In this regard, Section 6.1 already provided first ideas by using vertically-averaged quantities of the mesh refinement criteria.

The focus of the present work was on dynamic mesh adaptation. However, it is added that the MMPDE machinery may also be employed in EULAG to perform static mesh adaptation. For instance, the MMPDE machinery may be used to generate an adaptive curvilinear mesh that offers a finer resolution in mountainous regions or along coast lines. This could be achieved by specifying the monitor function M in the MMPDE machinery proportional to the underlying topographic height and its gradient. The finer resolution in the region of topographic features may be key for an improved representation of the flow phenomena such as orographically-generated internal gravity waves, rotors, land-sea circulations. Another aspect in terms of static mesh adaptation is to use the MMPDE machinery in a classical manner to accommodate domains with irregular horizontal boundaries. So far, such a device for static mesh adaptation is not available in EULAG.

Outlook

The developed solution-adaptive moving mesh solver offers a consistent framework for the simulation of multiscale geophysical flow problems. From a purely technical perspective, the solver allows for direct applicability over the full range of

[1]A vertical tilt of the mesh columns with height also complicates the representation of rain processes.

Rossby, Froude, and Reynolds number regimes accessible to the proven flow solver EULAG[1], see also the introductory Section 1.1. Basically, the moving mesh methodology may be beneficial to flow problems that involve locally strongly varying length scales, a situation practically always encountered in geophysical flows thanks to their nonlinear nature. In all possible applications, the appropriate specification of the parameters that enter the MMPDE machinery (the monitor function M and the mesh relaxation time Θ in particular) will be crucial for the success of the solution-adaptive moving mesh method. Therefore, the important subsequent step for the advancement of the technique will be to conduct systematic research in the appropriate adjustment of the MMPDE machinery for a range of applications.

Obvious areas of application are atmospheric flows where the external forcing determines the need of higher local resolution. One example are lee effects of the flow over topography with their different dynamic regimes depending on the Froude number. Also horizontally propagating vortices (from dust devils to polar lows and hurricanes) could profit from the high spatial resolution in their centres. Furthermore, all the nonlinear instability processes occuring in the atmosphere and producing smaller motion scales are a prolific area of application. An important example is the numerical simulation of microphysical processes in the upper atmosphere. The latent heat release of ice nucleation produces small-scale convective motions which require a high spatial resolution. To explore the sensitivity of these instabilities to the spatial resolution while maintaining the mesoscale simulation domain the dynamic mesh adaption might be a beneficial tool.

However, and as often mentioned in this thesis, the effort to apply the full mesh adaptation machinery to a specific problem must be competitive to the use of uniform resolution with huge number of grid points on massively parallel computers. At least, both approaches have to struggle with the same problem: to develop appropriate post-processing tools to deal with the data. On the other hand, the present thesis provides a manageable tool to zoom numerically into regions to search for possible coexisting smaller-scale phenomena not resolved on a coarse mesh.

Currently, the atmospheric and ocean modelling community is vigourously pursuing adaptive mesh methods in order to cope with the demand of much higher resolutions, see e.g. Nikiforakis (2009). To date, applications are largely confined to idealised applications dealing with either synoptic flows in the lowest order long-wave approx-

[1]As noted in Section 4.2, a restriction at the moment is that the MMPDE machinery is not implemented for applications in non-Cartesian, in particular spherical and cylindrical, physical systems $\mathbf{S}_p$, albeit the MMPDE machinery can be extended for this purpose.

imation governed by the shallow water equations, or small-scale buoyant phenomena in neutrally-stratified quiescent atmospheres simulated with derivatives of the incompressible Euler equations (Smolarkiewicz and Szmelter, 2011). Apart from these two diverse classes of motion, there is an abundance of relevant multiscale phenomena scarcely addressed with solution-adaptive mesh methods. The algorithm developed in this thesis is a viable tool to investigate what role *moving mesh methods* can play in the large selection of adaptive techniques considered for the numerical modelling of weather and climate.

Appendix

A Definition of the baroclinic thermal field

Here, the specification of the ambient potential temperature field θ_e as used in the baroclinic instability experiment of Section 6.1 is provided. Adopting the analytical expressions given in Bush and Peltier (1994), the height of the tropopause $H_T(y)$ is defined as

$$H_T(y) = H_{T,0} - \left(\frac{g\,\Delta\theta}{2\,\theta_0}\right)\left(\frac{1}{N_s^2 - N_t^2}\right)\tanh\left[\frac{1}{\delta_\theta}\left(\frac{y}{w_j} + y_0 - \kappa\,z\right)\right] \ . \qquad \text{(A.1)}$$

Then, the potential temperature field θ for tropospheric heights is given as

$$\theta_t(y,z) = \theta_0 + \frac{\theta_0\,N_t^2}{g}\,z - \frac{\Delta\theta}{2}\tanh\left[\frac{1}{\delta_\theta}\left(\frac{y}{w_j} + y_0 - \kappa\,z\right)\right], \quad z < H_T(y)\ , \qquad \text{(A.2)}$$

while for stratospheric heights it reads

$$\begin{aligned}\theta_s(y,z) = \theta_0 + \frac{\theta_0\,N_s^2}{g}\,z \ - \frac{\theta_0\,H_T(y)\,\xi}{g}\left(N_s^2 - N_t^2\right) \qquad \text{(A.3)}\\ -\frac{\Delta\theta\,\xi}{2}\tanh\left[\frac{1}{\delta_\theta}\left(\frac{y}{w_j} + y_0 - \kappa\,H_T(y)\right)\right]\left(1 + \frac{H_T(y) - z}{3}\right), \quad z > H_T(y)\ .\end{aligned}$$

The symbol ξ is a function given as $\xi(y,z) = \sin\left[\pi_c\,(24 - z)/2\,(24 - H(y))\right]$ introduced to smooth the meridional derivative of the potential temperature field θ at a height of 24 km. The parameters in preceding equations are defined as follows. The tropospheric and stratospheric values of the Brunt-Väisälä frequency are $N_t = 10^{-2}\,\mathrm{s}^{-1}$ and $N_s = \sqrt{6}\,N_t$, respectively. The parameter w_j controls the width of the baroclinic zone and is set to $w_j = 1$, and $y_0 = 0\,\mathrm{km}$. The inverse meridional slope of the tropospheric potential temperature field is $\kappa = 70$. The parameter $\Delta\theta = 30\,\mathrm{K}$ is a typical meridional variation of potential temperature over the length

scale $\delta_\theta = 525\,\mathrm{km}$. Base values of the tropopause height and the potential temperature are set to $H_{T,0} = 8\,\mathrm{km}$ and $\theta_0 = 273\,\mathrm{K}$, respectively. The resulting potential temperature field is shown in Figure 6.2.

B On the significance of baroclinic vorticity production in the evolution of wake vortices

The Boussinesq system of flow equations (Spiegel and Veronis, 1960) is often applied for small-scale modelling studies of aircraft wake vortex evolution in stratified atmospheric flows, e.g. Lewellen and Lewellen (1996); Gerz and Holzäpfel (1999). In the Boussinesq system, the pressure gradient term in the momentum equation is linearised and, as a consequence, the solution only provides abbreviated production of baroclinic vorticity. Stated more precisely, the Boussinesq system includes baroclinic vorticity production (BVP) associated with horizontal variations in the thermal field but neglects completely the BVP associated with vertical variations in the thermal field.

Here, a numerical model investigation examines the significance of the abbreviated BVP underlying the Boussinesq system for a descending vortex pair in a stably stratified atmosphere. For this purpose, the solutions obtained from the Boussinesq system are compared to solutions obtained from the incompressible Euler system. The incompressible Euler system is structurally related to the Boussinesq system but uses the general, i.e. unapproximated, form of the momentum equation, and therefore represents the full BVP.

Model formulation

Assuming an inviscid adiabatic non-rotating fluid, the unified model system of equations is given as

$$\frac{D\mathbf{v}}{Dt} = -\,\eta\nabla\pi' - \mathbf{g}\,\frac{\theta'}{\vartheta} \tag{B.1a}$$

$$\frac{D\theta'}{Dt} = -\,w\frac{d\theta_e}{dz} \tag{B.1b}$$

$$\nabla\cdot\mathbf{v} = 0\ . \tag{B.1c}$$

For the choice $(\eta\,,\vartheta)\equiv(\theta_0,\theta_0)$ in (B.1a), the system (B.1) describes the Boussinesq equations, whereas for the choice $(\eta\,,\vartheta)\equiv(\theta,\theta_e)$, the system (B.1) is equivalent to the incompressible Euler equations. The symbol θ_0 in the Boussinesq equations refers to a constant reference value of potential temperature. The symbol $\theta_e(z)$ occurring in both systems describes a horizontally-homogenous ambient profile of potential

temperature in hydrostatic balance with a normalised pressure profile $\pi_e(z)$. The quantities π' and θ' in (B.1) represent deviations from the profiles $\pi_e(z)$ and $\theta_e(z)$ in the respective system.

The unified system (B.1) of the Boussinesq and the incompressible Euler equations is solved in a consistent manner adopting the numerical solution procedure described in Section 2.2. The nonlinear pressure gradient term of the momentum equation (B.1a) in the integration of the incompressible Euler system, i.e. with $(\eta\,,\vartheta) \equiv (\theta, \theta_e)$ in (B.1a), is handled by applying outer iteration of the scheme (2.19), see Smolarkiewicz and Dörnbrack (2008) for a discussion of the implementation. In all simulations conducted here, the Eulerian MPDATA solver is employed in the advection module of the scheme (2.19). Note, in the application of MPDATA for the simulation of the wake vortex flow, a (non-default) nonlinear predictor scheme for the advective velocity is employed instead of a linear predictor scheme of the form (2.35). Assuming static Cartesian coordinates for simplicity, the adopted nonlinear procedure is based on an advective $\mathcal{O}(\delta t^2)$ integral for the physical velocity $\mathbf{v}$ of the form

$$\mathbf{v}^{n+1} = \mathcal{A}[\mathbf{v}^n + \delta t\, \mathbf{R}^n, \mathbf{v}^n]\ , \tag{B.2}$$

where $\mathcal{A}$ symbolically denotes an upwind scheme for the quantity $\mathbf{v}^n + \delta t\, \mathbf{R}^n$ while $\mathbf{R}^n$ being the corresponding momentum forcing. Then, a projection scheme is required at t^{n+1} to control compliance with the divergence constraint (B.1c). The advective velocity at the intermediate time level $t^{n+1/2}$ as required in the MPDATA is then obtained simply by $\mathbf{v}^{n+1/2} = 0.5\,(\mathbf{v}^n + \mathbf{v}^{n+1})$, which completes the procedure.

Experimental design

The numerical simulations consider a two-dimensional domain with $0 \le y \le L_y$ and $0 \le z \le H$, where $L_y = 255\,\mathrm{m}$ and $H = 500\,\mathrm{m}$, respectively. Boundary conditions at the top and bottom boundaries of the model domain are assumed to be rigid free-slip walls for velocity, while a zero normal flux is applied for θ'. Periodicity is applied for all variables at the lateral boundaries of the domain.

A counter-rotating pair of wake vortices is initialised as a superposition of two Lamb-Oseen vortices. The profile of the tangential velocity of each vortex is given by

$$v_t(r) = \frac{\Gamma_0}{2\pi_c\, r}\left\{1 - \exp\left(\frac{-r^2}{r_0^2}\right)\right\}, \quad r_0 = \frac{r_c}{1.12089}\ , \tag{B.3}$$

with the core radius specified as $r_c = 3\,\mathrm{m}$, and Archimedes' trigonometric constant

$\pi_c = 3.14159265$. A root-circulation of $\Gamma_0 = 458.0\,\mathrm{m^2\,s^{-1}}$ is applied along with a vortex spacing of $b_0 = 47.3\,\mathrm{m}$. The initial vertical position of the vortex pair is $z = 0.75\,H$. Varying stratification strengths are prescribed upon the ambient profiles of potential temperature $\theta_e(z)$ (see further below).

The presentation of the results is based on quantities that are non-dimensionalised with the given vortex parameters. A time scale is specified as

$$t_{ref} = \frac{2\pi_c\, b_0^2}{\Gamma_0}\ , \tag{B.4}$$

cf. e.g. Holzäpfel and Gerz (1999). This defines the normalised time $t^* = t/t_{ref}$ and Brunt-Väisälä frequency $N^* = N\,t_{ref}$, with $N = (g\,d(\ln\theta_e)/dz)^{1/2}$.

Among others, the subsequent analysis uses the half-plane total circulation given as

$$\Gamma_{\mathrm{hp}} = \iint_{y \geq L_y/2} \zeta_x\, dydz\ , \tag{B.5}$$

where ζ_x is the component of vorticity in the x-direction.

Finally, in the numerical simulation a uniform mesh spacing of 0.5 m is applied in both the horizontal direction of y and the vertical direction of z. All simulations are run until the normalised time $t^* = 5$.

Results and discussion

Figure B.1 on page 141 compares the results for basic vortex characteristics in (a)-(c) as obtained with either the Boussinesq or the incompressible Euler equations for varying ambient stratifications N^*. As can be seen, for representative values of N^* encountered under tropospheric ($N^* = 0.35$) and stratospheric ($N^* = 0.6$) conditions, the simulation results in Figure B.1(a)-(c) are barely distinguishable. Under a stronger ambient stratification ($N^* = 1.0$), the results obtained with the Boussinesq and incompressible Euler equations show close agreement until an integration time of about $t^* = 3$, but develop some differences for $t^* > 3$. It is argued that these observed differences for $t^* > 3$ might not be of significance in three-dimensional flows with typical background turbulence, where the strength and coherence of the vortices is expected to decrease persistently and at a larger rate than in the two dimensional simulations considered here, cf. Holzäpfel et al. (2001).

In summary, the results suggest that the abbreviated representation of BVP in the

Boussinesq system has no significant influence on the characteristics of the descending vortex pair in relevant stratification regimes. The results obtained here corroborate the examination conducted by Hennemann (2010) (Section 2.5.5 therein).

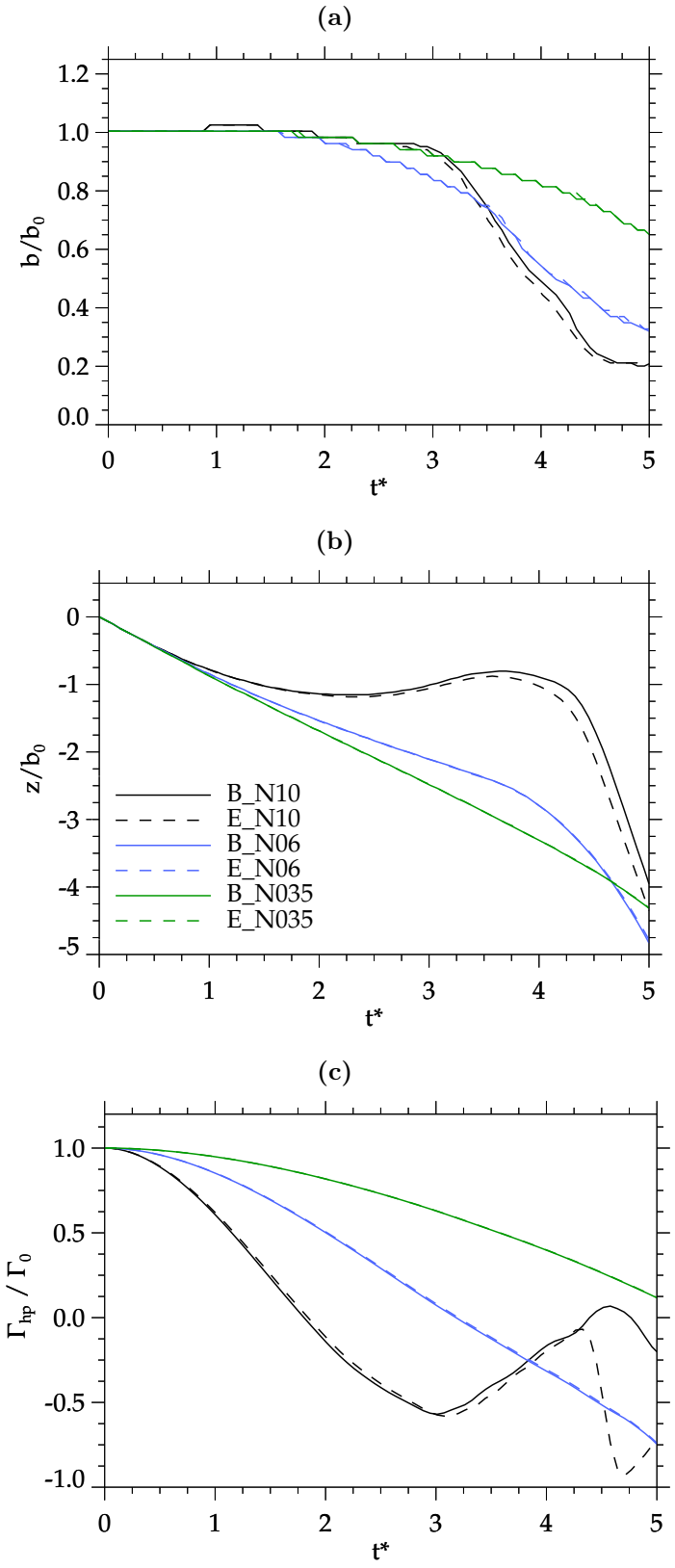

Figure B.1: Comparison of the results for either the Boussinesq (B) or the incompressible Euler (E) equations under varying ambient stratifications $N^* = 0.35$, 0.6, 1.0; see the legend in middle panel (b) for the assignment. Time series analysis of (a) the vortex spacing b normalised by the initial spacing b_0, (b) the vertical descend distance z normalised by b_0, and (c) the half-plane total circulation Γ_{hp} (B.5) normalised by its initial value Γ_0.

Acronyms

AMR adaptive mesh refinement

ALE arbitrary Lagrangian-Eulerian

BVP baroclinic vorticity production

CAT clear-air turbulence

CDGA continuous dynamic grid adaptation

CFL Courant-Friedrich-Lewy

COSMO Consortium for Small-Scale Modelling

CPU central processing unit

DFG Deutsche Forschungsgemeinschaft

DKRZ Deutsches Klimarechenzentrum

DLR Deutsches Zentrum für Luft- und Raumfahrt

DNS direct numerical simulation

ECMWF European Centre for Medium-Range Weather Forecasts

EKE eddy kinetic energy

EULAG Eulerian and semi-Lagrangian flow solver

FCT flux-corrected transport

FT forward-in-time

GCL geometric conservation law

GCM general circulation model

GCR generalized conjugate residual

GMCL generalized anelastic mass conservation law

G-IV Gulfstream-IV

ILES implicit large-eddy simulation

LES large-eddy simulation

LHS left-hand side

MHD magneto-hydrodynamics

MMPDE moving mesh partial differential equation

MPDATA multidimensional positive definite advection transport algorithm

NCAR National Center of Atmospheric Research

NCEP National Center of Environmental Prediction

NFT non-oscillatory forward-in-time

NOAA National Oceanic and Atmospheric Administration

NORPEX North Pacific Experiment

NWP numerical weather prediction

OP Particular MPDATA implementation, see Table 3.1

OS Particular MPDATA implementation, see Table 3.1

RHS right-hand side

RD Particular MPDATA implementation, see Table 3.1

RP Particular MPDATA implementation, see Table 3.1

RS Particular MPDATA implementation, see Table 3.1

ZKE zonal kinetic energy

KE total kinetic energy

Nomenclature

α	relaxation parameter associated with wave-absorbing sponge layers, page 93	$[s^{-1}]$
$\delta\overline{t}$	time step increment, page 19	[s]
$\hat{\mathbf{v}}$	advective contravariant Jacobian-weighted mass flux vector, page 22	
$\mathcal{C}_{max}$	maximum Courant number, page 23	
$\mathcal{D}_p$	physical domain, page 13	
$\mathcal{D}_t$	transformed domain, page 13	
$\overline{\mathbf{v}}^*$	contravariant velocity vector in $\mathbf{S}_t$, page 18	
$\overline{\mathbf{v}}^g$	mesh velocity vector in $\mathbf{S}_t$, page 37	
$\overline{\mathbf{v}}^s$	solenoidal velocity vector in $\mathbf{S}_t$, page 37	
$\mathbf{f}$	Coriolis vector, page 12	$[\mathrm{s}^{-1}]$
$\mathbf{g}$	gravitational acceleration vector, page 12	$[\mathrm{m\,s}^{-2}]$
$\mathbf{S}_p$	physical space, page 13	
$\mathbf{S}_t$	transformed space, page 13	
$\mathbf{v}$	physical velocity vector, page 12	$[\mathrm{m\,s}^{-1}]$
∇	gradient operator, page 13	$[m^{-1}]$
$\overline{\nabla}$	gradient operator with respect to system $\mathbf{S}_t$, page 18	
$\overline{G}$	Jacobian of the transformed system $\mathbf{S}_t$, page 17	
$\overline{G}_{xy}$	Jacobian of the horizontal transformation, page 17	
$\overline{t}, \overline{x}, \overline{y}, \overline{z}$	generalised coordinates, page 13	
$\overline{v}^{*^k}$	contravariant velocity components, page 15	
$\overline{v}^{s^k}$	solenoidal velocity components, page 15	

Φ	mesh refinement indicator function, page 57	
π'	normalised pressure perturbation, page 13	
π_c	Archimedes' trigonometric constant $\pi_c = 3.14159265$, page 33	
ψ	mass-specific variable, page 18	
ρ	fluid density, page 13	$[\mathrm{kg\,m^{-3}}]$
ρ^*	generalised density, page 14	
ρ_b	basic-state fluid density, page 13	$[\mathrm{kg\,m^{-3}}]$
Θ	mesh relaxation time, page 54	
θ	potential temperature, page 13	$[K]$
θ_0	constant reference value of potential temperature, page 132	[K]
θ_b	basic-state potential temperature, page 13	$[K]$
θ_e	ambient-state potential temperature, page 13	$[K]$
$\widetilde{\mathbf{G}}$	renormalised Jacobi matrix, page 20	
$\widetilde{\mathbf{G}}^T$	transpose of the renormalised Jacobi matrix, page 20	
$\widetilde{G}_j^k$	renormalised elements of the Jacobian matrix, page 15	
c_p	specific heat capacity at constant pressure, page 94	$[\mathrm{J\,kg^{-1}\,K^{-1}}]$
c_v	specific heat capacity at constant volume, page 94	$[\mathrm{J\,kg^{-1}\,K^{-1}}]$
D/Dt	Lagrangian derivative, page 13	$[s^{-1}]$
f	Coriolis parameter, page 14	$[\mathrm{s^{-1}}]$
G	Jacobian of the physical system $\mathbf{S}_p$, page 17	
H	upper boundary height of domain, page 16	[m]
M	monitor function, page 51	
N	Brunt-Väisälä frequency, page 94	$[\mathrm{s^{-1}}]$
P	scaling function in the MMPDE, page 53	
q	scalar weighting function, page 56	
R^ψ	source terms of the mass-specific variable ψ, page 18	
S	Stability parameter, page 94	$[\mathrm{m^{-1}}]$
t, x, y, z	physical coordinates, page 13	
v^j, u, v, w	physical velocity components, page 14	$[m\,s^{-1}]$
z_s	lower boundary height of domain, page 16	[m]

Bibliography

Abiodun, B. J., W. J. Gutowski, and J. M. Prusa, 2008: Implementation of a non-hydrostatic, adaptive-grid dynamics core in CAM3. Part II: dynamical influences on ITCZ behavior and tropical precipitation. *Clim. Dyn.*, **31**, 811–822.

Anthes, R. A., 1970: Numerical experiments with a two-dimensional horizontal variable grid. *Mon. Wea. Rev.*, **98**, 810–822.

Bacmeister, J. T. and M. R. Schoeberl, 1989: Breakdown of vertically propagating two-dimensional gravity waves forced by orography. *J. Atmos. Sci.*, **46**, 2109–2134.

Bacon, D. P., et al., 2000: A dynamically adapting weather and dispersion model: The operational multiscale environment model with grid adaptivity (OMEGA). *Mon. Wea. Rev.*, **128**, 2044–2076.

Bannon, P. R., 1996: On the anelastic approximation for a compressible atmosphere. *J. Atmos. Sci.*, **53**, 3618–3628.

Beckett, G., J. A. MacKenzie, A. Ramage, and D. M. Sloan, 2002: Computational solution of two-dimensional unsteady PDEs using moving mesh methods. *J. Comput. Phys.*, **182**, 478–495.

Behrens, J., 2006: *Adaptive atmospheric modeling : key techniques in grid generation, data structures, and numerical operations with applications*. Springer, Berlin, 207 pp.

Behrens, J., K. Dethloff, W. Hiller, and A. Rinke, 2000: Evolution of small-scale filaments in an adaptive advection model for idealized tracer transport. *Mon. Wea. Rev.*, **128**, 2976–2982.

Bell, J. B., P. Colella, and H. M. Glaz, 1989: A second order projection method for the incompressible Navier-Stokes equations. *J. Comput. Phys.*, **85**, 257–283.

Berger, M. J. and J. Oliger, 1984: Adaptive mesh refinement for hyperbolic partial differential equations. *J. Comput. Phys.*, **53**, 484–512.

Blossey, P. N. and D. R. Durran, 2008: Selective monotonicity preservation in scalar advection. *J. Comput. Phys.*, **227**, 5160–5183.

Brackbill, J. U., 1993: An adaptive grid with directional control. *J. Comput. Phys.*, **108**, 38–50.

Brackbill, J. U. and J. S. Saltzman, 1982: Adaptive zoning for singular problems in two dimensions. *J. Comput. Phys.*, **46**, 342–368.

Budd, C. J., W. Huang, and R. D. Russell, 2009: Adaptivity with moving grids. *Acta Numer.*, **18**, 111–241.

Bush, A. B. G. and W. R. Peltier, 1994: Tropopause folds and synoptic-scale baroclinic wave life cycles. *J. Atmos. Sci.*, **51**, 1581–1604.

Cao, W., W. Huang, and R. D. Russell, 1999: A study of monitor functions for two-dimensional adaptive mesh generation. *SIAM J. Sci. Comput.*, **20 (6)**, 1978–1994.

Cao, W., W. Huang, and R. D. Russell, 2003: Approaches for generating moving adaptive meshes: location versus velocity. *Appl. Numer. Math.*, **47 (2)**, 121–138.

Carpenter, R. L., K. K. Droegemeier, P. R. Woodward, and C. E. Hane, 1990: Application of the piecewise parabolic method (PPM) to meteorological modeling. *Mon. Wea. Rev.*, **118**, 586–612.

Chorin, A. J., 1968: Numerical solution of the Navier-Stokes equations. *Mathematics of Computation*, **22 (104)**, 745–762.

Chou, Y. J. and O. B. Fringer, 2009: Consistent discretization for simulations of flows with moving generalized coordinates. *Int. J. Numer. Meth. Fluids*, **62**, 802–826.

Clark, T. L., 1977: A small-scale dynamic model using a terrain-following coordinate transformation. *J. Comput. Phys.*, **24**, 186–215.

Clark, T. L. and R. D. Farley, 1984: Severe downslope windstorm calculations in two and three spatial dimensions using anelastic interactive grid nesting: A possible mechanism for gustiness. *J. Atmos. Sci.*, **41**, 329–350.

Cotter, C. S., P. K. Smolarkiewicz, and I. N. Szczyrba, 2002: A viscoelastic fluid model for brain injuries. *Int. J. Numer. Meth. Fluids*, **40**, 303–311.

Craig, G. C. and A. Dörnbrack, 2008: Entrainment in cumulus clouds: What resolution is cloud-resolving ? *J. Atmos.Sci.*, **65**, 3978–3988.

Cullen, M. J. P., 1990: A test of a semi-implicit integration technique for a fully compressible non-hydrostatic model. *Q. J. Roy. Meteorol. Soc.*, **116**, 1253–1258.

de Boor, C., 1974: Good approximation by splines with variable knots 2. *Springer Lecture Notes in Mathematics*, **363**, 12–20.

Demirdzic, I. and M. Peric, 1988: Space conservation law in finite volume calculations of fluid flow. *Int. J. Numer. Meth. Fluids*, **8**, 1037–1050.

Di, Y., R. Li, T. Tang, and P. Zhang, 2006: Moving mesh methods for singular problems on a sphere using perturbed harmonic mappings. *SIAM J. Sci. Comput.*, **28 (4)**, 1490–1508.

Dietachmayer, G. S., 1992: Application of continuous dynamic grid adaption techniques to meteorological modeling. Part II: efficiency. *Mon. Wea. Rev.*, **120**, 1707–1722.

Dietachmayer, G. S. and K. K. Droegemeier, 1992: Application of continuous dynamic grid adaption techniques to meteorological modeling. Part I: Basic formulation and accuracy. *Mon. Wea. Rev.*, **120**, 1675–1706.

Domaradzki, J. A. and S. Radhakrishnan, 2005: Effective eddy viscosities in implicit modeling of decaying high Reynolds number turbulence with and without rotation. *Fluid Dynamics Research*, **36**, 385–406.

Domaradzki, J. A., Z. Xiao, and P. K. Smolarkiewicz, 2003: Effective eddy viscosities in implicit large eddy simulations of turbulent flows. *Physics of Fluids*, **15**, 3890–3893.

Dorfi, E. A. and L. O. Drury, 1987: Simple adaptive grids for 1-d initial value problems. *J. Comput. Phys.*, **69 (1)**, 175–195.

Dörnbrack, A., T. Birner, A. Fix, H. Flentje, A. Meister, H. Schmid, E. V. Browell, and M. J. Mahoney, 2002: Evidence for inertia-gravity waves forming polar stratospheric clouds over Scandinavia. *J. Geophys. Res. Atmos.*, **107**, 8287–8295.

Dörnbrack, A., C. Kühnlein, and P. Smolarkiewicz, 2010: Modelling flows through canopies with immersed boundary methods. *V European Conference on Computational Fluid Dynamics ECCOMAS CFD, Lisbon, Portugal.*

Dörnbrack, A., M. Leutbecher, H. Volkert, and M. Wirth, 1998: Mesoscale forecasts of stratospheric mountain waves. *Meteorol. Appl.*, **5**, 117–126.

Doyle, J. D., et al., 2010: An intercomparison of T-REX mountain wave simulations and implications for mesoscale predictability. *submitted to Mon. Wea. Rev.*

Drikakis, D. and W. Rider, 2005: *High-resolution methods for incompressible and low-speed flows*. Springer, Berlin.

Durran, D. R., 1989: Improving the anelastic approximation. *J. Atmos. Sci.*, **46**, 1453–1461.

Durran, D. R., 1999: *Numerical methods for wave equations in geophysical fluid dynamics*. Springer, New York.

Durran, D. R., 2008: A physically motivated approach for filtering acoustic waves from the equations governing compressible stratified flow. *J. Fluid Mech.*, **601**, 365–379.

Dutton, J. A. and G. H. Fichtl, 1969: Approximate equations of motion for gases and liquids. *J. Atmos. Sci.*, **26**, 241–254.

Dutton, J. A. and H. A. Panofsky, 1970: Clear air turbulence: A mystery may be unfolding. *Science*, **167**, 937–944.

Dvinsky, A. S., 1991: Adaptive grid generation from harmonic maps on Riemannian manifolds. *J. Comput. Phys.*, **95**, 450–476.

Dwight, R. P., 2008: Goal-oriented mesh adaptation for finite volume methods using a dissipation-based error indicator. *Int. J. Numer. Meth. Fluids*, **56**, 1193–1200.

Eisenstat, S. C., H. C. Elman, and M. H. Schultz, 1983: Variational iterative methods for nonsymmetric systems of linear equations. *SIAM J. Numer. Anal.*, **20 (2)**, 345–357.

Elliott, J. R. and P. K. Smolarkiewicz, 2002: Eddy resolving simulations of turbulent solar convection. *Int. J. Numer. Meth. Fluids*, **39**, 855–864.

Ferziger, J. and M. Peric, 2001: *Computational methods for fluid dynamics*. Springer.

Fiedler, B. H. and R. J. Trapp, 1993: A fast dynamic grid adaption scheme for meteorological flows. *Mon. Wea. Rev.*, **121**, 2879–2888.

Fox-Rabinovitz, M. S., G. L. Stenchikov, M. J. Suarez, and L. L. Takacs, 1997: A finite-difference GCM dynamical core with a variable-resolution stretched grid. *Mon. Wea. Rev.*, **125**, 2943–2968.

Fritts, D. C. and M. J. Alexander, 2003: Gravity wave dynamics and effects in the middle atmosphere. *Reviews of Geophysics*, **41**.

Gal-Chen, T. and R. C. J. Somerville, 1975: On the use of a coordinate transformation for the solution of the Navier-Stokes equations. *J. Comput. Phys.*, **17**, 209–228.

Gelfand, I. and S. Fomin, 1963: *Calculus of variations*. Dover Publications.

Gerz, T. and F. Holzäpfel, 1999: Wing-tip vortices, turbulence, and the distribution of emissions. *AIAA Journal*, **37**, 1270–1276.

Gill, A., 1982: *Atmosphere-ocean dynamics*. Academic Press.

Gopalakrishnan, S. G., et al., 2002: An operational multiscale hurricane forecasting system. *Mon. Wea. Rev.*, **130**, 1830–1847.

Grabowski, W. W. and P. K. Smolarkiewicz, 2002: A multiscale anelastic model for meteorological research. *Mon. Wea. Rev.*, **130**, 939–956.

Gross, E. S., L. Bonaventura, and G. Rosatti, 2002: Consistency with continuity in conservative advection schemes for free-surface models. *Int. J. Numer. Meth. Fluids*, **38**, 307–327.

Held, I. M. and M. J. Suarez, 1994: A proposal for the intercomparison of the dynamical cores of atmospheric general circulation models. *Bull. Am. Meteorol. Soc.*, **75**, 1825–1830.

Hennemann, I., 2010: Deformation und Zerfall von Flugzeugwirbelschleppen in turbulenter und stabil geschichteter Atmosphäre. Ph.D. thesis, Technische Universität München.

Holton, J. R., 1992: *An introduction to dynamic meteorology*. International Geophysics Series, San Diego, New York: Academic Press, 3rd ed.

Holzäpfel, F. and T. Gerz, 1999: Two-dimensional wake vortex physics in the stably stratified atmosphere. *Aerosp. Sci. Technol.*, **5**, 261–270.

Holzäpfel, F., T. Gerz, and R. Baumann, 2001: The turbulent decay of trailing vortex pairs in stably stratified environments. *Aerosp. Sci. Technol.*, **5**, 95–108.

Huang, W., 2001a: Practical aspects of formulation and solution of moving mesh partial differential equations. *J. Comput. Phys.*, **171 (2)**, 753–775.

Huang, W., 2001b: Variational mesh adaptation: isotropy and equidistribution. *J. Comput. Phys.*, **174 (2)**, 903–924.

Huang, W., Y. Ren, and R. D. Russell, 1994: Moving mesh partial differential equations (MMPDEs) based on the equidistribution principle. *SIAM J. Numer. Anal.*, **31 (3)**, 709–730.

Huang, W. and R. D. Russell, 1997: A high dimensional moving mesh strategy. *Appl. Numer. Math.*, **26 (1-2)**, 63–76.

Huang, W. and R. D. Russell, 1999: Moving mesh strategy based on a gradient flow equation for two-dimensional problems. *SIAM J. Sci. Comput.*, **20 (3)**, 998–1015.

Huang, W. and R. D. Russell, 2001: Adaptive mesh movement — the MMPDE approach and its applications. *J. Comput. Appl. Math.*, **128 (1-2)**, 383–398.

Huang, W. and R. D. Russell, 2011: *Adaptive moving mesh methods*, Springer Applied Mathematical Series, Vol. 174.

Hubbard, M. E. and N. Nikiforakis, 2003: A three-dimensional, adaptive, Godunov-type model for global atmospheric flows. *Mon. Wea. Rev.*, **131**, 1848–1864.

Iselin, J. P., W. J. Gutowski, and J. M. Prusa, 2005: Tracer advection using dynamic grid adaptation and MM5. *Mon. Wea. Rev.*, **133**, 175–187.

Iselin, J. P., J. Prusa, and W. Gutowski, 2002: Dynamic grid adaptation using the MPDATA scheme. *Mon. Wea. Rev.*, **130**, 1026–1039.

Jablonowski, C., 2004: Adaptive grids in weather and climate modeling. Ph.D. thesis, University of Michigan.

Jablonowski, C., M. Herzog, J. E. Penner, R. C. Oehmke, Q. F. Stout, B. van Leer, and K. G. Powell, 2006: Block-structured adaptive grids on the sphere: Advection experiments. *Mon. Wea. Rev.*, **134**, 3691–3713.

Jöckel, P., R. von Kuhlmann, M. G. Lawrence, B. Steil, C. A. M. Brenninkmeijer, P. J. Crutzen, P. J. Rasch, and B. Eaton, 2001: On a fundamental problem in implementing flux-form advection schemes for tracer transport in 3-dimensional general circulation and chemistry transport models. *Q. J. Roy. Meteorol. Soc.*, **127**, 1035–1052.

Kalnay, E., S. J. Lord, and R. D. McPherson, 1998: Maturity of operational numerical weather prediction: medium range. *Bull. Am. Meteorol. Soc.*, **79**, 2753–2892.

Klein, R., 2009: Asymptotics, structure, and integration of sound-proof atmospheric flow equations. *Theor. Comput. Fluid Dyn.*, **23**, 161–195.

Klein, R., 2011: On the regime of validity of sound-proof model equations for atmospheric flows. *Proceedings of the ECMWF Workshop on Nonhydrostatic Modelling, Nov 8-10, 2010*, in press.

Klemp, J. B., W. C. Skamarock, and J. Dudhia, 2007: Conservative split-explicit time integration methods for the compressible nonhydrostatic equations. *Mon. Wea. Rev.*, **135**, 2897–2913.

Klemp, J. B. and R. B. Wilhelmson, 1978: The simulation of three-dimensional convective storm dynamics. *J. Atmos. Sci.*, **35**, 1070–1096.

Knupp, P. and S. Steinberg, 1994: *Fundamentals of grid generation.* CRC-Press.

Kühnlein, C., 2006: Clear-air turbulence and gravity waves in a front/jet system. *Diploma thesis, Ludwig-Maximilians-Universität München.*

Lane, T. P., R. D. Sharman, T. L. Clark, and H.-M. Hsu, 2003: An investigation of turbulence generation mechanisms above deep convection. *J. Atmos. Sci.*, **60**, 1297–1321.

Lang, J., W. Cao, W. Huang, and R. D. Russell, 2003: A two-dimensional moving finite element method with local refinement based on a posteriori error estimates. *Appl. Numer. Math.*, **46 (1)**, 75–94.

Laprise, R., 2008: Regional climate modelling. *J. Comput. Phys.*, **227**, 3641–3666.

Läuter, M., D. Handorf, N. Rakowsky, J. Behrens, S. Frickenhaus, M. Best, K. Dethloff, and W. Hiller, 2007: A parallel adaptive barotropic model of the atmosphere. *J. Comput. Phys.*, **223**, 609–628.

Lesieur, M. and O. Metais, 1996: New trends in large-eddy simulations of turbulence. *Annu. Rev. Fluid Mech.*, **28**, 45–82.

Lewellen, D. C. and W. S. Lewellen, 1996: Large-eddy simulations of the vortex-pair breakup in aircraft wakes. *AIAA Journal*, **34**, 2337–2345.

Li, R., T. Tang, and P. Zhang, 2001: Moving mesh methods in multiple dimensions based on harmonic maps. *J. Comp. Phys.*, **170**, 562–588.

Lin, S. and R. B. Rood, 1996: Multidimensional flux-form semi-Lagrangian transport schemes. *Mon. Wea. Rev.*, **124**, 2046–2070.

Lipps, F. B., 1990: On the anelastic approximation for deep convection. *J. Atmos. Sci.*, **47**, 1794–1798.

Lipps, F. B. and R. S. Hemler, 1982: A scale analysis of deep moist convection and some related numerical calculations. *J. Atmos. Sci.*, **39**, 2192–2210.

Liseikin, V., 1999: *Grid generation methods*. Springer, Berlin.

Mani, K. and D. J. Mavriplis, 2010: Error estimation and adaptation for functional outputs in time-dependent flow problems. *J. Comput. Phys.*, **229 (2)**, 415–440.

Margolin, L., P. Smolarkiewicz, and Z. Sorbjan, 1999: Large-eddy simulations of convective boundary layers using nonoscillatory differencing. *Phys. D*, **133 (1-4)**, 390–397.

Margolin, L. and P. K. Smolarkiewicz, 1999: Antidiffusive velocities for multipass donor cell advection. *SIAM J. Sci. Comput.*, **20 (3)**, 907–929.

Nieuwstadt, F. T. M., P. J. Mason, C. H. Moeng, and U. Schumann, 1991: Large-eddy simulation of the convective boundary layer - A comparison of four computer codes. *Thin Solid Films*, **1**, 1–4.

Nikiforakis, N., 2009: Mesh generation and mesh adaptation for large-scale earth-system modelling. *Phil. Trans. R. Soc. A*, **367**, 4473–4481.

Ogura, Y. and N. A. Phillips, 1962: Scale analysis of deep and shallow convection in the atmosphere. *J. Atmos. Sci.*, **19**, 173–179.

Ortiz, P. and P. K. Smolarkiewicz, 2006: Numerical simulation of sand dune evolution in severe winds. *Int. J. Numer. Meth. Fluids*, **50**, 1229–1246.

Piggott, M. D., C. C. Pain, G. J. Gorman, P. W. Power, and A. J. H. Goddard, 2005: h, r, and hr adaptivity with applications in numerical ocean modelling. *Ocean Modell.*, **10**, 95–113.

Piotrowski, Z. P., P. K. Smolarkiewicz, S. P. Malinowski, and A. A. Wyszogrodzki, 2009: On numerical realizability of thermal convection. *J. Comp. Phys.*, **228**, 6268–6290.

Plougonven, R. and C. Snyder, 2005: Gravity waves excited by jets: Propagation versus generation. *Geophys. Res. Lett.*, **32**, 18 802– 4 pp.

Plougonven, R. and C. Snyder, 2007: Inertia-gravity waves spontaneously generated by jets and fronts. Part I: Different baroclinic life cycles. *J. Atmos. Sci.*, **64**, 2502–2520.

Polvani, L. M., R. K. Scott, and S. J. Thomas, 2004: Numerically converged solutions of the global primitive equations for testing the dynamical core of atmospheric GCMs. *Mon. Wea. Rev.*, **132**, 2539–2552.

Power, P. W., M. D. Piggott, F. Fang, G. J. Gorman, C. C. Pain, D. P. Marshall, A. J. H. Goddard, and I. M. Navon, 2006: Adjoint goal-based error norms for adaptive mesh ocean modelling. *Ocean Modell.*, **15**, 3–38.

Prusa, J., P. Smolarkiewicz, and A. Wyszogrodzki, 2001: Simulations of gravity wave induced turbulence using 512 PE Cray T3E. *Int. J. Appl. Math. Comput. Sci*, **11**, 883–897.

Prusa, J. M. and W. J. Gutowski, 2006: MPDATA and grid adaptivity in geophysical fluid flow models. *Int. J. Numer. Meth. Fluids*, **50**, 1207–1228.

Prusa, J. M. and P. K. Smolarkiewicz, 2003: An all-scale anelastic model for geophysical flows: dynamic grid deformation. *J. Comput. Phys.*, **190 (2)**, 601–622.

Prusa, J. M., P. K. Smolarkiewicz, and R. R. Garcia, 1996: Propagation and breaking at high altitudes of gravity waves excited by tropospheric forcing. *J. Atmos. Sci.*, **53**, 2186–2216.

Prusa, J. M., P. K. Smolarkiewicz, and A. A. Wyszogrodzki, 2008: EULAG, a computational model for multiscale flows. *Comput. Fluids*, **37**, 1193–1207.

Purser, R. J. and M. Rančić, 1998: Smooth quasi-homogeneous gridding of the sphere. *Q. J. Roy. Meteorol. Soc.*, **124**, 637–647.

Rančić, M., R. J. Purser, and F. Mesinger, 1996: A global shallow-water model using an expanded spherical cube: Gnomonic versus conformal coordinates. *Q. J. Roy. Meteorol. Soc.*, **122**, 959–982.

Rider, W. J., 2006: The relationship of MPDATA to other high-resolution methods. *Int. J. Numer. Meth. Fluids*, **50**, 1145–1158.

Robert, A., 1993: Bubble convection experiments with a semi-implicit formulation of the Euler equations. *J. Atmos. Sci.*, **50**, 1865–1873.

Rotunno, R., Y. Chen, W. Wang, C. Davis, J. Dudhia, and G. J. Holland, 2009: Large-eddy simulation of an idealized tropical cyclone. *Bull. Am. Meteorol. Soc.*, **90 (12)**, 1783–1788.

Rotunno, R., W. C. Skamarock, and C. Snyder, 1994: An analysis of frontogenesis in numerical simulations of baroclinic waves. *J. Atmos. Sci.*, **51**, 3373–3398.

Saad, Y., 1993: A flexible inner-outer preconditioned GMRES algorithm. *SIAM J. Sci. Comput.*, **14 (2)**, 461–469.

Schär, C. and P. K. Smolarkiewicz, 1996: A synchronous and iterative flux-correction formalism for coupled transport equations. *J. Comput. Phys.*, **128**, 101–120.

Schmidt, H. and U. Schumann, 1989: Coherent structure of the convective boundary layer derived from large-eddy simulations. *J. Fluid Mech.*, **200**, 511–562.

Schumann, U., 1996: Direct and large eddy simulations of stratified shear flows. *Dynam. Atmos. Ocean*, **23**, 81–98.

Skamarock, W., J. Oliger, and R. L. Street, 1989: Adaptive grid refinement for numerical weather prediction. *J. Comput. Phys.*, **80**, 27–60.

Skamarock, W. C., P. K. Smolarkiewicz, and J. B. Klemp, 1997: Preconditioned conjugate-residual solvers for Helmholtz equations in nonhydrostatic models. *Mon. Wea. Rev.*, **125**, 587–599.

Smolarkiewicz, P. and L. Margolin, 1994: Variational solver for elliptic problems in atmospheric flows. *Appl. Math. and Comp. Sci.*, **4**, 527–551.

Smolarkiewicz, P. and L. Margolin, 1997: On forward-in-time differencing for fluids: An Eulerian/semi-Lagrangian non-hydrostatic model for stratified flows. *Atmosphere-Ocean Special*, **35**, 127–152.

Smolarkiewicz, P. and J. Prusa, 2002: Forward-in-time differencing for fluids: simulation of geophysical turbulence. *D. Drikakis, B.J. Geurts Eds., Turbulent Flow Computation, Kluwer Academic Publishers, Dordrecht*, **1**, 207–240.

Smolarkiewicz, P., J. Prusa, and J. Szmelter, 2011: Forward-in-time differencing for fluids: Variable time step integrations. *in preparation.*

Smolarkiewicz, P. K., 1983: A simple positive definite advection scheme with small implicit diffusion. *Mon. Wea. Rev.*, **111**, 479–486.

Smolarkiewicz, P. K., 1984: A fully multidimensional positive definite advection transport algorithm with small implicit diffusion. *J. Comput. Phys.*, **54**, 325–362.

Smolarkiewicz, P. K., 1991: On forward-in-time differencing for fluids. *Mon. Wea. Rev.*, **119**, 2505–2510.

Smolarkiewicz, P. K., 2006: Multidimensional positive definite advection transport algorithm: An overview. *Int. J. Numer. Meth. Fluids*, **50**, 1123–1144.

Smolarkiewicz, P. K. and T. L. Clark, 1986: The multidimensional positive definite advection transport algorithm: further development and applications. *J. Comput. Phys.*, **67 (2)**, 396–438.

Smolarkiewicz, P. K. and A. Dörnbrack, 2008: Conservative integrals of adiabatic Durran's equations. *Int. J. Numer. Meth. Fluids*, **56**, 1513–1519.

Smolarkiewicz, P. K. and W. Grabowski, 1990: The multidimensional positive definite advection transport algorithm: nonoscillatory option. *J. Comput. Phys.*, **86 (2)**, 355–375.

Smolarkiewicz, P. K., V. Grubisic, and L. G. Margolin, 1997: On forward-in-time differencing for fluids: Stopping criteria for iterative solutions of anelastic pressure equations. *Mon. Wea. Rev.*, **125**, 647–654.

Smolarkiewicz, P. K. and L. G. Margolin, 1993: On forward-in-time differencing for fluids - Extension to a curvilinear framework. *Mon. Wea. Rev.*, **121**, 1847–1859.

Smolarkiewicz, P. K. and L. G. Margolin, 1998: MPDATA: a finite-difference solver for geophysical flows. *J. Comput. Phys.*, **140 (2)**, 459–480.

Smolarkiewicz, P. K., L. G. Margolin, and A. A. Wyszogrodzki, 2001: A class of nonhydrostatic global models. *J. Atmos. Sci.*, **58**, 349–364.

Smolarkiewicz, P. K. and J. M. Prusa, 2002: VLES modelling of geophysical fluids with nonoscillatory forward-in-time schemes. *Int. J. Numer. Meth. Fluids*, **39**, 799–819.

Smolarkiewicz, P. K. and J. M. Prusa, 2005: Towards mesh adaptivity for geophysical turbulence: continuous mapping approach. *Int. J. Numer. Meth. Fluids*, **47**, 789–801.

Smolarkiewicz, P. K. and J. A. Pudykiewicz, 1992: A class of semi-Lagrangian approximations for fluids. *J. Atmos. Sci.*, **49**, 2082–2096.

Smolarkiewicz, P. K., R. Sharman, J. Weil, S. G. Perry, D. Heist, and G. Bowker, 2007: Building resolving large-eddy simulations and comparison with wind tunnel experiments. *J. Comput. Phys.*, **227 (1)**, 633–653.

Smolarkiewicz, P. K. and J. Szmelter, 2005: MPDATA: an edge-based unstructured-grid formulation. *J. Comput. Phys.*, **206 (2)**, 624–649.

Smolarkiewicz, P. K. and J. Szmelter, 2009: Iterated upwind schemes for gas dynamics. *J. Comput. Phys.*, **228 (1)**, 33–54.

Smolarkiewicz, P. K. and J. Szmelter, 2011: A nonhydrostatic unstructured-mesh soundproof model for simulation of internal gravity waves. *Acta Geophys.*, submitted.

Smolarkiewicz, P. K., C. Temperton, S. J. Thomas, and A. A. Wyszogrodzki, 2004: Spectral Preconditioners for nonhydrostatic atmospheric models: extreme applications. *In: Proceedings of the ECMWF seminar series on recent developments in numerical methods for atmospheric and ocean modelling. Reading, UK*, p. 203–220.

Soheili, A. R. and J. M. Stockie, 2008: A moving mesh method with variable mesh relaxation time. *Appl. Numer. Math.*, **58 (3)**, 249–263.

Sölch, I. and B. Kärcher, 2010: A large-eddy model for cirrus clouds with explicit aerosol and ice microphysics and Lagrangian ice particle tracking. *Q. J. Roy. Meteorol. Soc.*

Spichtinger, P. and K. M. Gierens, 2009a: Modelling of cirrus clouds – part 1a: Model description and validation. *Atmos. Chem. Phys.*, **9 (2)**, 685–706.

Spichtinger, P. and K. M. Gierens, 2009b: Modelling of cirrus clouds – part 1b: Structuring cirrus clouds by dynamics. *Atmos. Chem. Phys.*, **9 (2)**, 707–719.

Spiegel, E. A. and G. Veronis, 1960: On the Boussinesq approximation for a compressible fluid. *Astrophysical Journal*, **131**, 442–447.

St-Cyr, A., C. Jablonowski, J. M. Dennis, H. M. Tufo, and S. J. Thomas, 2008: A comparison of two shallow-water models with nonconforming adaptive grids. *Mon. Wea. Rev.*, **136**, 1898–1922.

Staniforth, A. N. and H. L. Mitchell, 1978: A variable-resolution finite-element technique for regional forecasting with the primitive equations. *Mon. Wea. Rev.*, **106**, 439–447.

Straka, J. M., R. B. Wilhelmson, L. J. Wicker, J. R. Anderson, and K. K. Droegemeier, 1993: Numerical solutions of a non-linear density current: A benchmark solution and comparisons. *Int. J. Numer. Meth. Fluids*, **17**, 1–22.

Sullivan, P. P., C. Moeng, B. Stevens, D. H. Lenschow, and S. D. Mayor, 1998: Structure of the entrainment zone capping the convective atmospheric boundary layer. *J. Atmos. Sci.*, **55**, 3042–3064.

Synge, J. and A. Schild, 1978: *Tensor calculus*. Dover Publications.

Szmelter, J., M. J. Marchant, A. Evans, and N. P. Weatherill, 1992: Two-dimensional Navier-Stokes equations with adaptivity on structured meshes. *Comput. Methods Appl. Mech. Eng.*, **101 (1-3)**, 355–368.

Szmelter, J. and P. Smolarkiewicz, 2010a: An unstructured mesh framework for simulation of all-scale atmospheric flows. *V European Conference on Computational Fluid Dynamics ECCOMAS CFD, Lisbon, Portugal*.

Szmelter, J. and P. K. Smolarkiewicz, 2006: MPDATA error estimator for mesh adaptivity. *Int. J. Numer. Meth. Fluids*, **50**, 1269–1293.

Szmelter, J. and P. K. Smolarkiewicz, 2010b: An edge-based unstructured mesh discretisation in geospherical framework. *J. Comput. Phys.*, **229 (1)**, 4980–4995.

Tanguay, M., A. Robert, and R. Laprise, 1990: A semi-implicit semi-Lagrangian fully compressible regional forecast model. *Mon. Wea. Rev.*, **118**, 1970–1980.

Taylor, M. A., J. Edwards, and A. St. Cyr, 2008: Petascale atmospheric models for the Community Climate System Model: new developments and evaluation of scalable dynamical cores. *J. Phys. Conf. Ser.*, **125 (1)**.

Thomas, P. and C. Lombard, 1979: Geometric conservation law and its application to flow computations on moving grids. *AIAA Journal*, **17**, 1030–1037.

Tremback, C. J., J. Powell, W. R. Cotton, and R. A. Pielke, 1987: The forward in-time upstream advection scheme: Extension to higher orders. *Mon. Wea. Rev.*, **115**, 540–555.

van Dam, A., 2009: Go with the Flow. Moving meshes and solution monitoring for compressible flow simulation. Ph.D. thesis, Utrecht University, Dept. of Mathematics, Utrecht, The Netherlands.

Vinokur, M., 1974: Conservation equations of gasdynamics in curvilinear coordinate systems. *J. Comput. Phys.*, **14**, 105–125.

Viviand, H., 1974: Formes conservatives des équations de la dynamique des gaz. *La Recherche Aerospatiale*, **1**, 65–66.

Wang, Y., 2002: An explicit simulation of tropical cyclones with a triply nested movable mesh primitive equation model: TCM3. Part II: Model refinements and sensitivity to cloud microphysics parameterization. *Mon. Wea. Rev.*, **130**, 3022–3036.

Warn-Varnas, A., J. Hawkins, P. K. Smolarkiewicz, S. A. Chin-Bing, D. King, and Z. Hallock, 2007: Solitary wave effects north of Strait of Messina. *Ocean Modell.*, **18**, 97–121.

Wedi, N., 2004: Time-dependent boundaries in numerical models. Ph.D. thesis, Ludwig-Maximilians-Universität München.

Wedi, N. P. and P. K. Smolarkiewicz, 2004: Extending Gal-Chen and Somerville terrain-following coordinate transformation on time-dependent curvilinear boundaries. *J. Comput. Phys.*, **193 (1)**, 1–20.

Wedi, N. P. and P. K. Smolarkiewicz, 2005: Laboratory for internal gravity-wave dynamics: the numerical equivalent to the quasi-biennial oscillation (QBO) analogue. *Int. J. Numer. Meth. Fluids*, **47**, 1369–1374.

Wedi, N. P. and P. K. Smolarkiewicz, 2006: Direct numerical simulation of the Plumb McEwan laboratory analog of the QBO. *J. of Atmos. Sci.*, **63**, 3226–3252.

Weller, H., 2009: Predicting mesh density for adaptive modelling of the global atmosphere. *Phil. Trans. R. Soc. A*, **367**, 4523–4542.

Weller, H., T. Ringler, M. Piggott, and N. Wood, 2010: Challenges facing adaptive mesh modeling of the atmosphere and ocean. *Bull. Am. Meteorol. Soc.*, **91**, 105–108.

Wilhelmson, R. and Y. Ogura, 1972: The pressure perturbation and the numerical modeling of a cloud. *J. Atmos. Sci.*, **29**, 1295–1307.

Winslow, A. M., 1981: Adaptive mesh zoning by the equipotential method. *UCID-19062 Lawrence Livermore National Laboratories Report.*

Wirth, V. and T. Szabo, 2007: Sharpness of the extratropical tropopause in baroclinic life cycle experiments. *Geophys. Res. Lett.*, **34**.

Zalesak, S. T., 1979: Fully multidimensional flux-corrected transport algorithms for fluids. *J. Comput. Phys.*, **31**, 335–362.

Zhang, F., 2004: Generation of mesoscale gravity waves in upper-tropospheric jet front systems. *J. Atmos. Sci.*, **61**, 440–457.

Zülicke, C. and D. Peters, 2006: Simulation of inertia gravity waves in a poleward-breaking Rossby wave. *J. Atmos. Sci.*, **63**, 3253–3276.

Acknowledgements

First and foremost, I would like to thank my mentor Dr. Andreas Dörnbrack for his invaluable guidance, constant support and encouragement.

I would like to thank Prof. Ulrich Schumann for supervising this thesis, his constant support, and his helpful comments on the manuscript.

I would also like to thank Prof. George Craig for supervising the thesis as a co-examiner and his valuable suggestions on the manuscript.

I'm deeply grateful that I had the opportunity to work with Dr. Piotr Smolarkiewicz from the National Center of Atmospheric Research (NCAR), Boulder, USA. His invaluable advice and his comments on chapters of the manuscript helped to substantially improve the thesis.

I would like to thank our working group within the DFG priority program Metström, by name Prof. Jochen Fröhlich, Claudia Hertel (TU Dresden) and Prof. Jens Lang, Stefan Löbig (TU Darmstadt), for a pleasant and fruitful collaboration. A discussion about the moving mesh methodology with the applied mathematics group in Darmstadt is appreciated.

Moreover, discussions with Dr. Joseph Prusa (Teraflux Corporation, USA) are gratefully acknowledged. Technical support from Prof. Joanna Szmelter (Loughborough University, UK) and Dr. Andrzej Wyszogrodzki (NCAR, USA) is also gratefully acknowledged. I also thank Dr. Hans Volkert (DLR) for providing me helpful comments.

I would like to thank Winfried Beer and Karl-Ernst Müller who always provided immediate solutions to IT-related problems.

There were also very interesting discussions concerning the simulation of aircraft wake vortices with EULAG. Dr. Thomas Gerz, Dr. Ingo Hennemann, Dr. Frank Holzäpfel, Dr. Takashi Misaka, and Dr. Simon Unterstrasser, many thanks for this.

Lust but not least, I thank all my colleagues at DLR for a pleasant and exciting working atmosphere.